

# Synthesis and Characterization of Multifunctional Metallic and Polymer Composite Coatings on Light Alloys

*Thesis Submitted to AcSIR for the award of the degree of*

**DOCTOR OF PHILOSOPHY**

*in*

**CHEMICAL SCIENCES**



*By*

**JERIN K. PANCRECIOS**

**Registration No: 10CC14J39017**

*Under the guidance of*

**Dr. T.P.D. Rajan and Dr. E. Bhoje Gowd**



***CSIR-National Institute for Interdisciplinary Science and Technology  
Thiruvananthapuram-695019, Kerala, India***

***July 2019***

# Synthesis and Characterization of Multifunctional Metallic and Polymer Composite Coatings on Light Alloys

*Thesis Submitted to AcSIR for the award of the degree of*

**DOCTOR OF PHILOSOPHY**

*in*

**CHEMICAL SCIENCES**



*By*

**JERIN K. PANCRECIOS**

**Registration No: 10CC14J39017**

*Under the guidance of*

**Dr. T.P.D. Rajan and Dr. E. Bhoje Gowd**



***CSIR-National Institute for Interdisciplinary Science and  
Technology***

***Thiruvananthapuram-695019, Kerala, India***

***July 2019***

*Dedicated to my beloved Family...*

## DECLARATION

I hereby declare that the work presented in the thesis entitled as “**Synthesis and Characterization of Multifunctional Metallic and Polymer Composite Coatings on Light Alloys**” is the result of investigations carried out by me at Materials Science and Technology Division, CSIR- National Institute for Interdisciplinary Science and Technology (CSIR-NIIST), Thiruvananthapuram, under the supervision of Dr. T.P.D. Rajan and Dr. E. Bhoje Gowd. The same has not been submitted elsewhere for any other degree.

Thiruvananthapuram

19<sup>th</sup> July 2019

  
19/07/19  
**Jerin K. Pancrecious**

*Council of Scientific & Industrial Research*  
**CSIR- NATIONAL INSTITUTE FOR INTERDISCIPLINARY SCIENCE  
AND TECHNOLOGY (CSIR-NIIST)**

Industrial Estate P.O., Trivandrum - 695 019, India



**CERTIFICATE**

This is to certify that the work embodied in the thesis entitled as “**Synthesis and Characterization of Multifunctional Metallic and Polymer Composite Coatings on Light Alloys**” has been carried out by Ms. Jerin K. Pancrecius under our supervision and guidance at Materials Science and Technology Division, CSIR-National Institute for Interdisciplinary Science and Technology (CSIR-NIIST), Trivandrum and the same has not been submitted elsewhere for any other degree. Research material obtained from other sources has been duly acknowledged in the thesis. Any text, illustration, table etc., used in the thesis from other sources, have been duly cited and acknowledged. It is also certified that this work done by the student, under our supervision, is plagiarism free.

Dr. T.P.D. Rajan  
Principal Scientist  
CSIR-NIIST  
Trivandrum

Dr. E. Bhoje Gowd  
Principal Scientist  
CSIR- NIIST  
Trivandrum

Jerin K. Pancrecius  
(Student)

Trivandrum  
19 July 2019

## **Acknowledgements**

*I would like to take this opportunity to extend my sincere gratitude and appreciation to all those who have helped me for doing the work and made this Ph.D. thesis possible.*

*With deep regards and respect, I would like to express my profound gratitude to my research supervisors Dr. T.P.D. Rajan and Dr. E. Bhoje Gowd, Principal Scientists of Materials Science and Technology Division, CSIR-National Institute for Interdisciplinary Science and Technology (CSIR-NIIST), Thiruvananthapuram, for suggesting this exciting area, their sustained enthusiasm, creative suggestions, dedicated help, encouragement, advice, and useful corrections of this research work.*

*I am thankful to Dr. A. Ajayaghosh, and Dr. Suresh Das, present and former Directors of the CSIR-NIIST, Thiruvananthapuram for providing me all the necessary facilities for carrying out the work.*

*I extend my sincere gratitude towards Dr. S. Savithri, Dr. K. Harikrishna Bhat, Dr. P. Prabhakar Rao, and Dr M.L.P. Reddy present and former heads of the Materials Science and Technology division for all the help and support. I thank Dr. C. H. Suresh, Dr. Luxmi Varma and Dr. Mangalam S. Nair present and former AcSIR co-ordinators, for the timely conduction of course work, valuable help and encouragement.*

*I wish to acknowledge Dr. S. Ananthakumar, Dr. U.S. Hareesh, Dr. M. Vasundhara my doctoral advisory committee members for their insightful comments and discussions which helped me to widen my research from various perspectives.*

*I gratefully acknowledge all the scientists and staffs in CSIR-NIIST, Thiruvananthapuram, for their help, support and encouragement.*

*My wholehearted thanks to Mr. V. Antony, Mr. Kiran Mohan, Mr. M.R. Chandran, Mr. Chandrakanth C.K., Mr. Harish Raj V., Ms. Soumya, Mr. Peer Mohamed Mr. Prithviraj, Ms. Aju Thara, Mrs. Aswathi, Mr. Aswin, Ms. Anju P., Mr. Rajeev, Mr. Vibhu, Ms. Anjali, Mr. Madhu, Mr. Merin for their technical support by extending different instrumental facilities.*

*Words are insufficient to express my gratitude to my seniors, colleagues and friends who made my life at CSIR-NIIST as enjoyable and memorable. Dr. T.P.D.R. group members: Dr. Deepa J. P., Dr. Resmi V. G., Dr. Lakshmi V., Dr Annu Raju, Mrs. Praseeda S. Nair, Dr. Akhil S. Karun, Dr. Sreemanu K.M., Ms. Sarah Bill Ulaeto, Ms.*

*Ramya R., Ms. Suja P., Ms. Arsha A.G., Mr. Akhil M. G., Mr. Vishnu R.L., Mr. N. Anand; Dr. E.B.G. group: Dr. Shaiju P., Dr. B. Nagendra., Mr. Sivaprasad, Ms. Praveena, Mr. Amal raj R.B, Mr. Vipin G. Krishnan, Mr. G. Virat., Ms. Sruthi are greatly acknowledged for the stimulating discussions, constant help, advice, support.*

*My sincere thanks to my colleague and friend Mr. Jithu Jayaraj for his scientific inputs, paper correction and personal helps at CSIR-NIIST. I extend my gratitude to all the members of MMM group: Mr. Rajesh Kumar, Dr. Athul K.R., Mr. Abhilash Viswanath, Mr. Hari S., Mr. Rajesh K.R., Mr. Arun Kumar, Mr. Gowtham, Mr. Ajayraag, Mr. Sreeraj; and Members of workshop for all their generous help for metal sample preparation and good companionship. I thank Dr. J.D. Sudha group members for all the scientific suggestions and motivation.*

*I express my heartfelt thanks to Master's project students Ms. Varanya Jayan, Ms. Gopika P.S., Ms. Vineetha S. V. and Ms. Savithry K.N., for their friendship, help and useful discussions during the work.*

*It's my pleasure to thank my best friends: Ms. Molji C., Ms. Shuhailath K.A, Ms. Sijla Rosely C. V., Ms. Deepthi Krishnan at NIIST, Ms. Marilyn Mary Xavier, Ms. Roniya Joseph and Ms. Chinju Govind for always being with me, caring me, standing beside me at difficult times.*

*I would like to acknowledge my other friends at NIIST Mr. A. Aashish, Ms. Nimisha G, Ms. Sajitha S, Ms. Salfeena, Ms. Aswathi, Ms. Parvathy, Ms. Sumitha, for their moral support, motivation and to make my life at NIIST memorable.*

*I feel a deep sense of gratefulness to my parents, sister, and brother-in-law, those who are my strengths and part of my vision. They dreamed good things and showed good values in life for me. Their unfailing love, care, pain, support, patience and sacrifice will remain my inspiration throughout my life. I greatly acknowledge Fr. Biju Vettukallel for his prayers and support. I take this opportunity to thank Geetha aunty and Sukumaran uncle, house owners for their love and caring, like our parents.*

*I would like to acknowledge the Council of Scientific and Industrial Research, New Delhi for providing me the financial support.*

*I owe all the blessings to god ALMIGHTY including good health and strength during the research period and for giving confidence to undertake this Ph. D. work.*

***Jerin K. Pancrecius***

# CONTENTS

|  | <b>Page No.</b> |
|--|-----------------|
| <b>List of Tables</b>  | xiii            |
| <b>List of Figures</b>   | xiv             |
| <b>List of Abbreviation</b>  | xix             |
| <b>Preface</b>   | xxi             |
| <br>   |                 |
| <b>Chapter 1 Introduction: Multifunctional Composite Coatings-an overview.</b> |                 |
| <i>Abstract</i>  | 1               |
| 1.1. Introduction  | 1               |
| 1.2. Electroless metal composite coatings                                      | 3               |
| 1.2.1. Basic aspects of electroless composite coatings                         | 4               |
| 1.2.2. Reinforcements  | 6               |
| 1.2.3. Pretreatments and surface activation                                    | 6               |
| 1.2.4. Composite coating mechanisms  | 8               |
| 1.3. Nickel composite coatings   | 13              |
| 1.3.1. Surface morphology and structural characteristics                       | 13              |
| 1.3.2. Corrosion resistance  | 15              |
| 1.3.3. Mechanical and tribological characteristics                             | 20              |
| 1.3.4. Industrial applications   | 31              |
| 1.4. Polymer composite coatings  | 32              |
| 1.4.1. Polymer composite coatings for corrosion protection                     | 33              |
| 1.4.1.1. Inhibitor loaded polymer composite coatings                           | 34              |
| 1.4.1.2. Container based corrosion inhibitor loading                           | 35              |
| 1.4.1.3. Layered double hydroxide (LDH)  | 38              |
| 1.5. Corrosion sensing   | 39              |
| 1.6. Scope and objectives  | 41              |
| References   | 42              |

## **Chapter 2: Effect of nanoceria in electroless nickel boride coating on Aluminium A356 alloy**

|   |    |
|---|----|
| <i>Abstract</i>   | 51 |
| 2.1. Introduction   | 52 |
| 2.2. Material and methods   | 53 |
| 2.2.1. Materials  | 53 |
| 2.2.2. Coating preparation  | 54 |
| 2.2.3. Characterizations  | 55 |
| 2.2.3.1. Structural analyses  | 55 |
| 2.2.3.2. Electrochemical measurements                                 | 55 |
| 2.2.3.3. Hardness measurements  | 56 |
| 2.2.3.4. Pin on disc wear testing                                     | 56 |
| 2.3. Results and Discussion   | 56 |
| 2.3.1. Surface morphology and elemental composition                   | 56 |
| 2.3.2. AFM analysis   | 58 |
| 2.3.3. X-ray diffraction studies                                      | 59 |
| 2.3.4. XPS analysis   | 60 |
| 2.3.5. Electrochemical characterization for corrosion analyses        | 63 |
| 2.3.6. Hardness behaviour   | 67 |
| 2.3.7. Tribological Characteristics                                   | 68 |
| 2.3.8. Ni-B-CeO <sub>2</sub> nanocomposite coatings on cylinder liner | 70 |
| 2.4. Conclusions  | 71 |
| References  | 72 |

## **Chapter 3: Morphology and characteristics of electroless nickel boride-Layered double hydroxide composite coating on Aluminium A356 alloy**

|                   |    |
|-------------------|----|
| <i>Abstract</i>   | 75 |
| 3.1. Introduction | 76 |
| 3.2. Experimental | 77 |
| 3.2.1. Materials  | 77 |

|          |  |    |
|----------|--|----|
| 3.2.2.   | Ni-Al LDH Synthesis                    | 78 |
| 3.2.3.   | Coating preparation                    | 78 |
| 3.2.4.   | Sample analysis                        | 79 |
| 3.2.4.1. | Surface characterizations              | 79 |
| 3.2.4.2. | Contact angle measurements             | 79 |
| 3.2.4.3. | Corrosion analysis                     | 80 |
| 3.2.4.4. | Pin on disc wear analysis              | 80 |
| 3.3.     | Results and discussion                 | 80 |
| 3.3.1.   | Ni-Al LDH reinforcement                | 80 |
| 3.3.1.1. | Morphology                             | 80 |
| 3.3.1.2. | Structural analysis                    | 81 |
| 3.3.2.   | Ni-B-LDH composite coating             | 82 |
| 3.3.2.1. | Coating morphology                     | 82 |
| 3.3.2.2. | XRD analysis                           | 83 |
| 3.3.2.3. | XPS analysis                           | 84 |
| 3.3.2.4. | Surface roughness                      | 86 |
| 3.3.2.5. | Contact angle measurements             | 87 |
| 3.3.2.6. | Electrochemical corrosion measurements | 88 |
| 3.3.2.7. | Anti-corrosion mechanism               | 91 |
| 3.3.2.8. | Wear analysis                          | 92 |
| 3.4.     | Conclusions                            | 94 |
|          | References                             | 95 |

## **Chapter 4: Layered double hydroxide-Ceria hybrid Reinforced Epoxy Composite Coating for corrosion resistance**

|        |                             |     |
|--------|-----------------------------|-----|
|        | <i>Abstract</i>             | 99  |
| 4.1.   | Introduction                | 100 |
| 4.2.   | Experimental                | 103 |
| 4.2.1. | Materials                   | 103 |
| 4.2.2. | Substrate preparation       | 103 |
| 4.2.3. | Ni-Al Nitrate LDH Synthesis | 104 |
| 4.2.4. | Vanadate intercalation      | 104 |

|  |     |
|--|-----|
| 4.2.5. Ceria decoration  | 104 |
| 4.2.6. Epoxy LDH composite coating   | 104 |
| 4.2.7. Characterizations   | 104 |
| 4.2.7.1. Structural analysis   | 104 |
| 4.2.7.2. Electrochemical measurements                                      | 104 |
| 4.2.7.3. Immersion Test  | 105 |
| 4.3. Results and Discussion  | 105 |
| 4.3.1. SEM Analysis  | 105 |
| 4.3.2. FTIR  | 107 |
| 4.3.3. Raman analysis  | 108 |
| 4.3.4. XRD analysis  | 109 |
| 4.3.5. Corrosion analysis  | 110 |
| 4.3.5.1. Effect of ceria nanoparticles decoration on Ni-Al Nitrate LDH     | 110 |
| 4.3.5.2. Effect of nanoceria decoration on Ni-Al vanadate LDH              | 111 |
| 4.3.5.3. Immersion test  | 115 |
| 4.3.5.4. Raman analysis  | 117 |
| 4.3.6. Corrosion Mechanism   | 117 |
| 4.3.7. Corrosion Protection of Epoxy- LDH Composite Coatings on A356 alloy | 118 |
| 4.4. Conclusions   | 120 |
| References   | 121 |

## **Chapter 5: Layered double hydroxide for corrosion sensing applications on light metal alloys**

|                                      |     |
|--------------------------------------|-----|
| <i>Abstract</i>                      | 125 |
| 5.1. Introduction                    | 126 |
| 5.2. Experimental                    | 128 |
| 5.2.1. Materials                     | 128 |
| 5.2.2. Zn-Al phph LDH synthesis      | 128 |
| 5.2.3. Acrylic-LDH composite coating | 128 |

|   |     |
|---|-----|
| 5.2.4. Sample analysis                                | 129 |
| 5.2.4.1. Zn-Al phph LDH characterization              | 129 |
| 5.2.4.2. Corrosion analysis                           | 129 |
| 5.2.4.3. Corrosion sensing                            | 129 |
| 5.3. Results and Discussions                          | 130 |
| 5.3.1. SEM Analysis                                   | 130 |
| 5.3.2. XRD Analysis                                   | 131 |
| 5.3.3. FTIR   | 132 |
| 5.3.4. XPS Analysis                                   | 134 |
| 5.3.5. Corrosion Studies                              | 136 |
| 5.3.5.1. Potentiodynamic polarization measurements    | 136 |
| 5.3.5.2. Electrochemical Impedance Spectroscopy (EIS) | 137 |
| 5.3.6. Corrosion sensing                              | 139 |
| 5.4. Conclusion                                       | 141 |
| References  | 142 |
| Summary   | 145 |
| Future perspectives                                   | 147 |
| List of publications                                  | 149 |
| List of conference presentations                      | 150 |

## List of Tables

|                   |   |  | Page No. |
|-------------------|---|--|----------|
| <b>Table 1.1.</b> | Commonly used sources of metal ions, reducing and complexing agents.                                      |  | 5        |
| <b>Table 1.2.</b> | Commonly used reinforcements and their properties.  |  | 6        |
| <b>Table 1.3.</b> | Corrosion resistant characteristics of electroless nickel composite coatings.                             |  | 19       |
| <b>Table 1.4.</b> | Hardness and tribological behaviour of electroless nickel composite coatings.                             |  | 28       |
| <b>Table 1.5.</b> | List of different container loaded corrosion inhibitor systems in the polymer coatings.                   |  | 37       |
| <b>Table 1.6.</b> | Corrosion sensing polymer composite coatings  |  | 40       |
| <b>Table 2.1.</b> | Electroless Ni-B-CeO <sub>2</sub> bath constituents and parameters.                                       |  | 54       |
| <b>Table 2.2.</b> | $E_{corr}$ , $\beta_c$ , $\beta_a$ and $i_{corr}$ values obtained from potentiodynamic polarization scan. |  | 64       |
| <b>Table 2.3.</b> | The fitted values of EIS measurements of the samples using equivalent circuits shown in the Figure 2.9.   |  | 67       |
| <b>Table 3.1.</b> | Ni-B LDH bath parameters and constituents.  |  | 79       |
| <b>Table 3.2.</b> | $E_{corr}$ Vs. SCE and $i_{corr}$ values calculated from the Tafel plot                                   |  | 90       |
| <b>Table 4.1.</b> | $E_{corr}$ , and $i_{corr}$ values obtained from potentiodynamic polarization scan.                       |  | 111      |
| <b>Table 4.2.</b> | The fitted values of the samples corresponding to the equivalent circuits given as Figure 4.8.            |  | 113      |
| <b>Table 5.1.</b> | $E_{corr}$ and $i_{corr}$ values obtained from potentiodynamic polarization scan given in Figure 5.5.     |  | 137      |

## List of Figures

|                    |   | Page<br>No. |
|--------------------|---|-------------|
| <b>Figure 1.1</b>  | Schematic representation of electroless gold plating process on a nickel coated poly acrylonitrile (PAN) nano fibers after tin-palladium activation.  | 5           |
| <b>Figure 1.2</b>  | Schematic representation of Guglielmi's model electroless composite coatings.   | 9           |
| <b>Figure 1.3</b>  | Schematic representation of various stages of electroless nanocomposite coatings.   | 11          |
| <b>Figure 1.4</b>  | Schematic representation of ion adsorption mechanism.   | 12          |
| <b>Figure 1.5</b>  | Back scatter scanning electron microscopy images of (a) Ni-P, Ni-P/nanometer diamond depositions at various concentrations of nano-diamond in electroless solution: (b) 0.5, (c) 1.0, (d) 4.0 g L <sup>-1</sup> . | 13          |
| <b>Figure 1.6</b>  | Potentiodynamic polarization curves of Ni-P and Ni-P-SiC coatings at varying concentrations of SiC.   | 16          |
| <b>Figure 1.7</b>  | Nyquist plots for Ni-P coatings containing different concentration of diamond nano particle (DNP) in 3.5% NaCl solution; $f_{max}$ of semicircles was given. Inset: equivalent circuits.                          | 17          |
| <b>Figure 1.8</b>  | Schematics of coatings cross-section: (a) Ni-P and (b) Ni-P/DNP elucidates the corrosion prevention by diamond nanoparticles  | 18          |
| <b>Figure 1.9</b>  | SEM images of the coatings cross-section: (a) Ni-P and (b) Ni-P/DNP   | 18          |
| <b>Figure 1.10</b> | Effect of heat treatment and particle concentration on the microhardness of electroless Ni-P-Al <sub>2</sub> O <sub>3</sub> coatings  | 22          |
| <b>Figure 1.11</b> | Microhardness of substrate, Ni-B coating and the composite coatings with different secondary particles  | 23          |
| <b>Figure 1.12</b> | Friction Coefficient of Ni-P-Si <sub>3</sub> N <sub>4</sub> nanowire electroless composite coating with varying nanowire concentration  | 24          |
| <b>Figure 1.13</b> | Schematic representation of lubricious tribolayer   | 26          |

formation during the sliding motion.

|                    |  |    |
|--------------------|--|----|
| <b>Figure 1.14</b> | Three major steps involved in the dip coating process.   | 32 |
| <b>Figure 1.15</b> | Microcapsule based self-healing mechanism with encapsulated monomer and a solid catalyst.  | 36 |
| <b>Figure 1.16</b> | Structure of layered double hydroxide  | 38 |
| <b>Figure 1.17</b> | Schematic illustration of microcapsule encapsulated phenolphthalein with pH, an indication of corrosion  | 40 |
| <b>Figure 2.1</b>  | SEM micrograph of the surface and Energy-dispersive X-ray spectroscopy: (a & c) Ni-B alloy, (b & d) Ni-B-CeO <sub>2</sub> composite coatings.  | 57 |
| <b>Figure 2.2</b>  | Cross-sectional SEM image of Ni-B-CeO <sub>2</sub> nanocomposite coating and the EDS mapping.  | 58 |
| <b>Figure 2.3</b>  | AFM height images: (a) Ni-B alloy and (b) Ni-B-CeO <sub>2</sub> nanocomposite coatings.  | 59 |
| <b>Figure 2.4</b>  | XRD of Ni-B and Ni-B-CeO <sub>2</sub> nanocomposite coatings. Enlarged portion of Ni(111) peak is shown as inset.  | 60 |
| <b>Figure 2.5</b>  | XPS survey spectrum of NiB-CeO <sub>2</sub> (a), high-resolution spectrum of Ni 2p (b), B 1s (c), Ce 3d (d), O 1s (e).   | 62 |
| <b>Figure 2.6</b>  | Tafel plots of (a) A356 alloy, (b) Ni-B coatings and (c) Ni-B-CeO <sub>2</sub> composite coatings at a scan rate of 1mV/s.   | 64 |
| <b>Figure 2.7</b>  | Tafel plots of Ni-B-CeO <sub>2</sub> composite coatings at different concentrations of 0.2 gL <sup>-1</sup> and 0.5 gL <sup>-1</sup> at a scan rate of 1mV/s.  | 65 |
| <b>Figure 2.8</b>  | Nyquist (a) and Bode, phase angle vs. log f (b) plots of A356 alloy, Ni-B coatings and Ni-B-CeO <sub>2</sub> composite coatings at their OCP with amplitude of 10 mV in the frequency range from 10 <sup>4</sup> to 10 <sup>-1</sup> Hz. | 66 |
| <b>Figure 2.9</b>  | Equivalent electrical circuit model used to fit the EIS data; (a) A356 alloy and Ni-B coatings and (b) Ni-B-CeO <sub>2</sub> composite coatings.   | 67 |
| <b>Figure 2.10</b> | Vickers microhardness values of the samples under the indentation of 50 gf with a speed 50 μm/s  | 68 |

|                    |   |    |
|--------------------|---|----|
| <b>Figure 2.11</b> | (a) Wear rate as a function of load applied (b) SEM micrograph of the worn surface of A356 (c) Ni-B and (d) Ni-B-CeO <sub>2</sub> coating after pin-on-disk wear testing.   | 69 |
| <b>Figure 2.12</b> | Friction coefficients of A356, NiB and NiB-CeO <sub>2</sub> coatings during sliding at 0.4 m/s velocity under 2N load.  | 70 |
| <b>Figure 2.13</b> | (a) Uncoated and (b) electroless NiB-CeO <sub>2</sub> coated A356 Piston cylinders.   | 71 |
| <b>Figure 3.1</b>  | (a) SEM and (b) TEM micrographs of synthesised Ni-Al LDH.   | 81 |
| <b>Figure 3.2</b>  | (a) FTIR and (b) XRD of synthesised Ni-Al LDH.  | 82 |
| <b>Figure 3.3</b>  | SEM micrographs of the surface texture of (a) A356 alloy, (b) electroless Ni-B, (c) Ni-B-0.5% LDH, (d) Ni-B-1% LDH, (e) Ni-B-2% LDH and (f) Ni-B-5% LDH composite coatings. | 83 |
| <b>Figure 3.4</b>  | X-ray diffraction patterns: (a) Ni-Al LDH and (b) Ni-B-LDH coating.   | 84 |
| <b>Figure 3.5</b>  | XPS (a) survey spectrum of Ni-B-LDH and high-resolution spectra of (b) Ni 2p, (c) B 1s, (d) Al 2p, and (e) N 1s.  | 85 |
| <b>Figure 3.6</b>  | Average surface roughness of aluminium alloy and composite coatings containing 0 to 5 % of LDH.   | 87 |
| <b>Figure 3.7</b>  | Water contact angle of aluminium alloy and composite coatings containing 0 to 5 % of LDH.   | 88 |
| <b>Figure 3.8</b>  | Tafel plots of aluminium alloy, Ni-B and Ni-B-LDH (0.5 - 5 wt% of LDH) composite coatings.  | 89 |
| <b>Figure 3.9</b>  | Nyquist plots of aluminium alloy, Ni-B and Ni-B-LDH (0.5-5 wt% of LDH) composite coatings.  | 91 |
| <b>Figure 3.10</b> | Schematic demonstration of the anti-corrosion mechanism of Ni-B-LDH composite coating.  | 91 |
| <b>Figure 3.11</b> | Wear rates of aluminium alloy and composite coatings containing 0 to 5 % of LDH samples as a function of applied load.  | 92 |

|                    |  |     |
|--------------------|--|-----|
| <b>Figure 3.12</b> | SEM micrographs of the worn out surface aluminium alloy and composite coatings containing 0 to 5 % of LDH at an applied load 2 N.  | 93  |
| <b>Figure 3.13</b> | EDS spectra of the worn out surface aluminium alloy and composite coatings containing 0 to 5 % of LDH at an applied load 2 N.  | 94  |
| <b>Figure 4.1</b>  | Schematic representation of inhibitor loaded LDH modification.   | 103 |
| <b>Figure 4.2</b>  | SEM and EDS analysis of (a,c) Ni-Al nitrate, (b,d) Ni-Al vanadate, (e,g) Ni-Al nitrate-CeO <sub>2</sub> and (f,h) Ni-Al vanadate-CeO <sub>2</sub> .  | 106 |
| <b>Figure 4.3</b>  | Infrared spectra of (a) Ni-Al nitrate and (b) Ni-Al vanadate. The enlarged portion of the peaks corresponding to anionic species from 1650 cm <sup>-1</sup> to 1150 cm <sup>-1</sup> is shown as an inset. | 107 |
| <b>Figure 4.4</b>  | Raman spectra of (a) ammonium vanadate, (b) Ni-Al Nitrate and (c) Ni-Al Vanadate.  | 108 |
| <b>Figure 4.5</b>  | X-ray diffractions patterns of (a) Ni-Al Nitrate, (b) Ni-Al Vanadate and (c) Ni-Al Nitrate -CeO <sub>2</sub> LDHs.   | 109 |
| <b>Figure 4.6</b>  | Tafel plots of A356 alloy in different inhibitor added 3.5% NaCl solution at a scan rate of 1mV/s.   | 110 |
| <b>Figure 4.7</b>  | Nyquist plots of the samples at their open circuit potential with a peak-to-peak amplitude of 10 mV in the frequency range from 10 <sup>4</sup> to 10 <sup>-2</sup> Hz.                                    | 112 |
| <b>Figure 4.8</b>  | Equivalent electrical circuit for A356 corrosion behavior in 3.5 wt% NaCl alone (a) and LDH added solution (b).  | 113 |
| <b>Figure 4.9</b>  | Bode plots of A356 corrosion behaviour in 3.5 wt% NaCl alone and LDH added solutions (a) log Z vs. log f and (b) phase angle vs. log f.  | 114 |
| <b>Figure 4.10</b> | Corrosion rate of A356 alloy in different electrolytes calculated from weight loss measurement after 32 days immersion test.   | 115 |

|                    |  |     |
|--------------------|--|-----|
| <b>Figure 4.11</b> | SEM images of the A356 surface after Immersion test for 32 days (after the removal of corrosion products).   | 116 |
| <b>Figure 4.12</b> | Raman spectra of (a) NiAl-Vanadate and (b) A356 alloy surface after immersion  | 117 |
| <b>Figure 4.13</b> | Schematic representation of the proposed corrosion protection mechanism.   | 118 |
| <b>Figure 4.14</b> | Cross-sectional SEM image of (a) Epoxy and (b) Epoxy LDH composite coating   | 119 |
| <b>Figure 4.15</b> | Bode plots of epoxy composite coated A356 alloy corrosion behaviour in 3.5 wt% NaCl solution.  | 120 |
| <b>Figure 5.1</b>  | SEM image and EDS spectra of Zn-Al LDH (a <sub>1</sub> &b <sub>1</sub> ) and Zn-Al phph LDH (a <sub>2</sub> &b <sub>2</sub> ).   | 130 |
| <b>Figure 5.2</b>  | XRD pattern of Zn-Al LDH and Zn-Al phph LDH synthesized at different pH.   | 132 |
| <b>Figure 5.3</b>  | FTIR spectra of Zn-Al LDH, Zn-Al phph LDH synthesized at different pH and phenolphthalein.   | 133 |
| <b>Figure 5.4</b>  | XPS survey spectrum of (a) Zn-Al phph LDH, high-resolution spectrum of (b) Zn 2p, (c) Al 2p, (d) C 1s, and (e) O 1s.   | 135 |
| <b>Figure 5.5</b>  | Tafel plot of (a) A356 alloy in 3.5 wt% and (b) AAZ31 alloy in 1wt% NaCl alone, NaCl solution containing 0.05 wt% of Zn-Al LDH, and NaCl solution containing 0.05 wt% of Zn-Al phph LDH.   | 137 |
| <b>Figure 5.6</b>  | Nyquist plots of the samples at their open circuit potential with a peak-to-peak amplitude of 10 mV in the frequency range from (a) 10 <sup>4</sup> to 10 <sup>-2</sup> Hz for A356 and (b) 10 <sup>4</sup> to 10 <sup>-1</sup> Hz for AZ31. | 138 |
| <b>Figure 5.7</b>  | Bode plots of (a) A356 corrosion behaviour in 3.5 wt% NaCl and (b) AZ31 in 1 wt% NaCl alone and LDH added solutions (log Z vs. log f)  | 139 |
| <b>Figure 5.8</b>  | Photographs of corroding surfaces of AZ31 alloy after (a) 2 minutes (b) 10 minutes and (c) A356 alloy after 24 hours.  | 140 |
| <b>Figure 5.9</b>  | Acrylic paint in 1% NaOH solution: (a) 0 minutes, (b) 5 minutes, and (c) acrylic coating on AZ31 in 1% NaCl solution: After 48 hours.  | 141 |

## List of Abbreviation

|                           |  |
|---------------------------|--|
| °C                        | Degree Celsius   |
| A                         | Ampere   |
| AFM                       | Atomic force microscopy                                |
| ATR-FTIR                  | Attenuated total reflection-Fourier transform Infrared |
| BE                        | Binding energy   |
| <i>C</i>                  | Capacitance  |
| CeO <sub>2</sub>          | Ceria  |
| cm                        | Centimetre   |
| CPE                       | Constant phase element                                 |
| <i>d</i>                  | Diameter   |
| DGEBA                     | Diglycidyl ether of bisphenol-A                        |
| <i>E</i> <sub>break</sub> | Breakdown potential                                    |
| <i>E</i> <sub>corr</sub>  | Corrosion potential                                    |
| EDS                       | Energy-dispersive X-ray spectroscopy                   |
| EIS                       | Electrochemical impedance spectroscopy                 |
| eV                        | Electron volt  |
| <i>f</i>                  | Frequency  |
| FT-IR                     | Fourier-Transform Infrared                             |
| FWHM                      | Full width at half maximum                             |
| g                         | Gram   |
| gf                        | Gram-force   |
| HY951                     | Araldite HY 951 epoxy hardener                         |
| Hz                        | Hertz  |
| <i>i</i>                  | Current density  |
| <i>i</i> <sub>corr</sub>  | Corrosion current density                              |
| IR                        | Infrared   |
| <i>L</i>                  | Inductance   |

|               |  |
|---------------|--|
| L             | Litter                                       |
| LDH           | Layered double hydroxide                     |
| min           | Minute                                       |
| mm            | Millimeter                                   |
| mM            | Millimolar                                   |
| N             | Newton                                       |
| $n$           | CPE constant                                 |
| Ni-B          | Nickel boride                                |
| nm            | Nanometer                                    |
| OCP           | Open circuit potential                       |
| phph          | Phenolphthalein                              |
| $R_{ct}$      | Charge transfer resistance                   |
| $R_p$         | polarization resistance                      |
| $R_q$         | Root mean square average of height deviation |
| $R_s$         | solution resistance                          |
| s             | Second                                       |
| SCE           | Standard calomel electrode                   |
| SEM           | Scanning electron microscopy                 |
| V             | voltage                                      |
| $VHN$         | Vickers hardness                             |
| Vs.           | Versus                                       |
| Wt%           | Weight percentage                            |
| XPS           | X-ray photoelectron spectroscopy             |
| XRD           | X-ray diffraction                            |
| $Z$           | Impedance                                    |
| $\beta_a$     | Anodic slope                                 |
| $\beta_c$     | Cathodic slope                               |
| $\mu\text{m}$ | Micrometer                                   |
| $\Omega$      | ohm  |

## PREFACE

Surface modifications and coatings of metallic materials and structures are one of the most important techniques for improving the functional performance of the engineering components in real time applications and service in extreme environmental conditions. Surface properties of a material decide its applicability and durability regarding corrosion resistance, surface hardness, antibacterial activity, mechanical stability, etc. Therefore, chemical or physical modifications of surfaces to achieve superior performance have been widely used to attain the benchmark for different applications. The surface coating is an important process with wide acceptance to give a better appearance, properties, and advanced functionalities. Pure metal or alloy, polymer, ceramic, and composite coatings with the addition of micro or nano sized secondary particles can enhance strength and stability of the material. The development of composite/nanocomposite coatings on various surfaces based on electroless process has much interest among researchers due to their enhanced mechanical, electrical, and magnetic properties compared with their metallic or alloy counterparts. However, properties of the product depend upon not only on the nature of secondary particle used but also the specific characteristics of the matrix. Polymer matrix composite coatings are widely used to improve the corrosion resistance of the metal. Depending on the requirement of an end product, different reinforcements can be selected.

The first chapter gives a general introduction about recent developments in micro and nanostructured metallic and polymeric composite coatings formed by electroless and dip coating techniques, respectively. Main focus of the chapter is on the properties of electroless nickel based metallic composite coatings as well as commonly used polymer composite coatings. Metal/polymeric systems with various reinforcements including micro or nano particles, one dimensional wires and layered materials have been discussed.

In chapter 2 electroless Ni-B alloy and Ni-B-CeO<sub>2</sub> nanocomposite coatings were formed on 356 aluminium alloy surfaces. Ceria incorporation to Ni-B coating reduces the average nodular grain size from 1150 nm to 650 nm and Ni crystallite size from 15 nm to 9.97 nm. Ni-B-CeO<sub>2</sub> nanocomposite shows remarkable improvement in microhardness of 684 VHN compared to pure Ni-B coating with

424 VHN. Enhanced wear resistance and reduction in friction coefficient are observed for the nanocomposite coatings compared to 356 Al alloy and Ni-B alloy coating. Potentiodynamic polarization measurements show a remarkable reduction in the corrosion current density for ceria added nanocomposite coating ( $2.48 \times 10^{-6} \text{Acm}^{-2}$ ) than that of the particle-free counterpart ( $11.18 \times 10^{-6} \text{Acm}^{-2}$ ). Uniform Ni-B-CeO<sub>2</sub> composite coating was obtained on centrifugally cast A356 aluminium alloy cylinder liners which have potential applications in automotive systems.

Chapter 3: A nickel boride-layered double hydroxide (Ni-B-LDH) hydrophobic surface has fabricated on A356 aluminium alloy surface by electroless method. The anti-corrosion and anti-wearing performances were studied with varying amount, from 0 to 5 wt %, of LDH in the nickel boride matrix. The composite coating with highest water contact angle having the value of 120° was observed for Ni-B containing 0.5 wt % of LDH. This could be attributed to the increased surface roughness offered by the LDH layers. Potentiodynamic polarization measurements in 3.5 wt % NaCl solution indicate significant decrease in the corrosion current density ( $i_{\text{corr}}$ ) values for LDH added composite coating with a lowest of  $3.96 \times 10^{-6} \text{A cm}^{-2}$  for 0.5 wt% of LDH. This may be due to the combined effect of both coating hydrophobicity and feasibility for chloride ion intake by ion exchange mechanism of LDH. Improved wear resistance was obtained for composite coated aluminium with minimum wear rate for 1% LDH added coating. Stable tribolayer formation in presence of LDH gave higher wear resistance.

Chapter 4 introduces a modified layered double hydroxides (LDH) based system for corrosion inhibition on dual actions by both active and passive mechanism. Nickel aluminium layered double hydroxide (Ni-Al LDH) intercalated with vanadate ion was further decorated with ceria nanoparticles to enhance the corrosion protection efficiency. The corrosion inhibition efficiency of vanadate-ceria modified LDH on A356 aluminum alloy was investigated by electrochemical impedance spectroscopy (EIS) and immersion test. The bare metallic substrates in 3.5 wt % sodium chloride solution containing inhibitor loaded LDH were tested to understand the inhibition mechanism. The modified LDH loaded epoxy composite coatings were also made on A356 alloy to study the corrosion resistance in the real

application. The results show that an enhancement of the corrosion protection can be achieved by vanadate as well as ceria modification. Presence of stable ceria nanoparticles passively protects the metal from corrosive anions and water molecules. The release of vanadate ion during anion exchange of LDH with chloride ion in the corrosive environment and formation of polymeric vanadate on the surface actively protects the metal from further corrosion. The combined effect of both vanadate and ceria incorporated with LDH exhibit the best anti-corrosion property in the electrolyte as well as composite coating.

In chapter 5, phenolphthalein loaded Zn-Al layered double hydroxide (Zn-Al LDH) was prepared and their corrosion sensing property was analysed. The colour-change or fluorescing compounds were found to be sensitive to corrosion processes by indicating the pH change associated with the cathodic or anodic reaction that accompanies corrosion. The precise corrosion monitoring can be achieved by the controlled release of corrosion sensing compounds from a nano container at the beginning of corrosion process. LDH is a versatile material for corrosion sensing compound loading with tuneable properties. The synthesized LDH was characterized by scanning electron microscopy (SEM), Fourier transform infrared (FT-IR) spectroscopy, Energy-dispersive X-ray spectroscopy (EDS), X-ray photoelectron spectroscopy (XPS), and X-Ray Diffraction (XRD) analysis, which confirm the formation of phenolphthalein modified LDH. Corrosion resistance investigations by both potentiodynamic polarization analysis and electrochemical impedance spectroscopy (EIS) indicate the applicability of modified LDH without prompting the metallic corrosion. Pink coloration on the cathodic reaction sites on metal surface indicate the feasibility of phenolphthalein loaded LDH as corrosion sensing material. The modified LDH dispersed acrylic coated AZ91 alloy shows pink colour formation during corrosion.

Summary of the thesis work is given in the 6<sup>th</sup> chapter which also includes the future perspectives.

# Chapter 1

## Introduction: Multifunctional Composite Coatings-An overview

---

### ***Abstract***

*The development of composite/nanocomposite coatings on metallic surfaces based on various techniques has much interest among researchers due to their enhanced mechanical, tribological, electrical, magnetic, optical and anti-corrosive properties compared to the bare counterparts. These coatings have shown many applications in automotive, aerospace and industrial fields with unique characteristics obtained by the incorporation of secondary particles as reinforcement at micro or nanoscale in the matrix. However, properties of the product depend upon not only the nature of secondary particle used but also the specific characteristics of the matrix. Pure metal or alloy, polymer, and ceramic matrix composite coatings with the addition of secondary particles can enhance strength and stability of the material. This chapter reviews the recent developments in micro and nanostructured metallic and polymeric composite coatings formed by electroless coating and solution blending methods, respectively. The protective behavior of different coating systems has surveyed. Finally, the scope and objectives of the present work are defined at the end of this chapter.*

### **1.1. Introduction**

The surface properties of a material decide its applicability and durability regarding corrosion resistance, surface hardness, antibacterial activity, and mechanical stability towards wear and erosion. Therefore, chemical or physical modifications of surfaces to achieve superior performance have been widely used to attain the benchmark for different applications. Nowadays, several methods like surface hardening, heat treatment, surface coatings, etc. are available to improve the

exterior characteristics. However, the surface coating is an important process with wide acceptance to give a better appearance, properties, and advanced functionalities. Pure metal or alloy, polymer, ceramic, and composite coatings with the addition of micro or nano sized secondary particles can enhance strength and stability of the material.

Electroless process is a coating technique in which there is deposition of metal, alloy or a composite on an activated surface by autocatalytic reduction of metallic ions from the salt solution containing a reducing agent. Most of substrates can be plated by this method, irrespective of their conductivity due to the nature of deposition, without an external source of electrical current. Moreover, it is a better way for the complex parts to plate completely over sharp edges and deep recesses, which is hard to plate with electrolytic processes because of current density variations across the surface.<sup>1</sup> Electroless deposition is different from other metal depositions such as displacement deposition and contact deposition that are carried out without an outside electrical current source.<sup>2</sup> Displacement deposition is a galvanic process in which the noble metal ions (with more positive reduction potential) are reduced and deposited on the surface of an active metal, without any reducing agent, by the dissolution of that metal. Contact deposition is like electrochemical deposition with the exception that the current is derived from the chemical reaction and not from an external current.

Polymeric coatings are made up of natural or synthetic polymers on the substrate formed by curing or polymerization of resins, in the form of powder or liquid, to the thin surface film. The coatings can be applied on any type of substrate material to provide desired properties and protection. Epoxy, acrylics, polyurethane, poly vinyl chloride, rubber, cellulose and silicone are commonly used for various applications like corrosion resistance, household and biomedical appliances, packaging, energy devices and decorative purposes. Different coating techniques have been employed for the polymer coating. Dip coating, spin coating, spray coating, printing and casting are some among them.<sup>3</sup>

## **1.2. Electroless Metal Composite Coatings**

Electroless process is a coating technique in which there is deposition of metal, alloy or a composite on an activated surface by autocatalytic reduction of metallic ions from the salt solution containing a reducing agent. Most of substrates can be plated by this method, irrespective of their conductivity due to the nature of deposition, without an external source of electrical current. Moreover, it is a better way for the complex parts to plate completely over sharp edges and deep recesses, which is hard to plate with electrolytic processes because of current density variations across the surface <sup>1</sup>.

The electroless coating process was first noted by Liebig in 1835 related to the reduction of Ag ion to Ag metal using aldehydes. In 1844, Wurtz observed a nickel deposition from an aqueous salt solution in the presence of hypophosphite ion.<sup>2</sup> However, it has gained the acceptance in various engineering sectors after Brenner and Riddell, who introduced the term electroless metal deposition in 1946, made nickel-tungsten alloy plating on inner walls of tubes.<sup>4</sup> Later, many researchers studied the feasibility and usefulness of electroless metallic coatings such as Ni, Co, Cu, Ag, Au, and Pd on different substrates. While most of the coatings were obtained as alloy coating instead of pure metal owing to the presence of another element(s) derived from the reducing agents and bath additives. It seems that most of the alloy coatings got industrial embrace with many applications due to their improved mechanical properties.

Electroless composite coatings are obtained by the co-deposition of second phase particles along with the metal matrix on an activated substrate. Earlier, the composite coatings had been made by incorporating micrometer size particles of Al<sub>2</sub>O<sub>3</sub> or SiC. However, the initial attempts at producing such deposits were unsuccessful owing to the agglomeration of fine particles. Later, with the help of suitable surfactants, stabilizers, and better stirring facility, electroless composite coatings were prepared successfully. Synthesis of electroless composite coatings using a variety of particles such as diamond for higher hardness<sup>5</sup>, ZrO<sub>2</sub> and Al<sub>2</sub>O<sub>3</sub> for superior wear resistance and microhardness<sup>6,7</sup>, B<sub>4</sub>C and Si<sub>3</sub>N<sub>4</sub> for wear and corrosion resistance<sup>8</sup>, etc. have been explored.

The possibility to incorporate smaller particles of nano size, within a metal/alloy matrix has initiated a new generation of composite coatings referred to as electroless nanocomposite coatings. These coatings exhibit enhanced mechanical, physical and functional properties due to large interface and nanoscale effects.<sup>9</sup> However, an extensive study is needed to understand the role of secondary particles for protective application and their formation mechanism.

### 1.2.1. Basic aspects of electroless composite coatings

Autocatalytic deposition is a metal deposition process by controlled chemical reaction that is catalyzed by the material being deposited in the presence of a reducing agent. The chemical reactions occurring during electroless deposition are described in equations (1.1) and (1.2):



Where, 'R' and 'M' indicate reducing agent and the metal. The composite coatings involve co-deposition of reinforcements during the autocatalytic deposition process onto a substrate. The deposition process can be simply written as:

Metal ion +Reduction solution +Reinforcement  $\rightarrow$  Composite solid +Oxidation solution

Since it is necessary to obtain the deposition at a desired surface, the substrate material should be activated before immersion in the electroless bath. Depending on the requirement of an end product, different metals can be selected for the deposition on the substrate including multilayer coatings. For example, an electroless gold coating on a nickel plated polyacrylonitrile (PAN) nanofibers improves the surface texture for the potential application in wearable textile containing antibacterial and wound healing properties.<sup>10</sup> The schematic representation of surface activation and deposition process is shown in Figure 1.1. The precise and detailed mechanisms of co-deposition are discussed in section 1.2.4. Typical electroless plating baths of composite coatings include a source of metal ions, a reducing agent(s), complexing agent(s), stabilizer, buffering agent, reaction inhibitors and reinforcements. Commonly used sources of metal ions, reducing and complexing agents are given in

Table 1.1. The process is also controlled by certain parameters like temperature and pH.

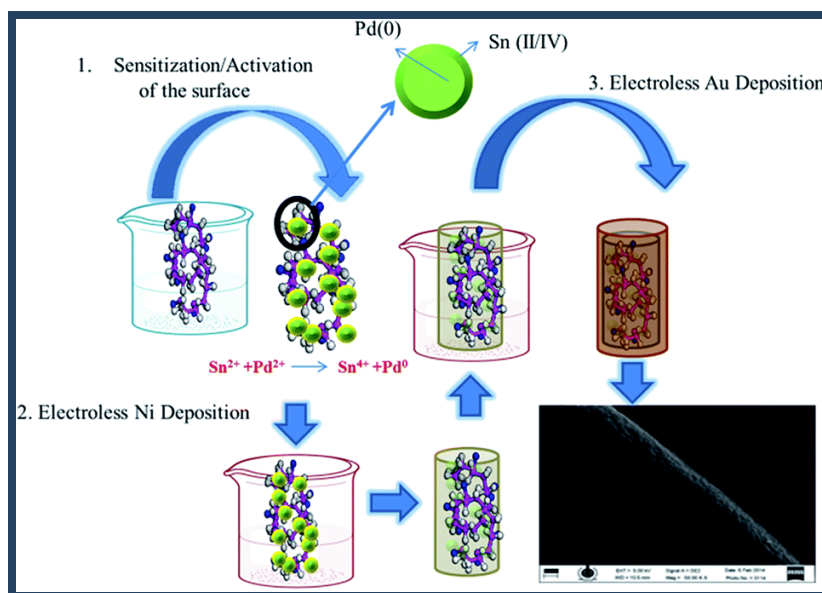


**Figure 1.1:** Schematic representation of electroless gold plating process on a nickel coated poly acrylonitrile (PAN) nano fibers after tin-palladium activation.<sup>10</sup>

**Table 1.1:** Commonly used sources of metal ions, reducing and complexing agents.

| Metal | Salts used as metal source  | Reducing agents  | Complexing agents   |
|-------|---|--|---|
| Ni    | NiSO <sub>4</sub> , NiCl <sub>2</sub> , Ni(CH <sub>3</sub> COO) <sub>2</sub> , Ni(H <sub>2</sub> PO <sub>2</sub> ) <sub>2</sub> | Sodium hypophosphite, Amino boranes, Sodium borohydride, Hydrazine | EDTA, citric, lactic, glycolic acids, sodium citrate, succinic acid, sodium pyrophosphate |
| Cu    | CuSO <sub>4</sub> , CuCl <sub>2</sub> , Cu(CN) <sub>2</sub>   | Formaldehyde, Sodium hypophosphate                                 | EDTA, glycolic acid, Triethyl amine, cyanide  |
| Co    | CoSO <sub>4</sub> , CoCl <sub>2</sub>   | Sodium hypophosphite, Amino boranes, Sodium borohydride, Hydrazine | EDTA, citric acid, sodium citrate, succinic acid, sodium pyrophosphate, aminoacetate      |
| Au    | KAu(CN) <sub>2</sub> , KAuCl <sub>4</sub> , Na <sub>3</sub> Au(SO <sub>3</sub> ) <sub>2</sub>                                   | Formaldehyde, Hydrazine  | Cyanide, citrate, ethanolamine  |
| Ag    | AgNO <sub>3</sub> , NaAg(CN) <sub>2</sub>   | Hydrazine, Rochelle salt, glucose                                  | Cyanide, ammonium   |

### 1.2.2. Reinforcements

A wide range of particles such as synthetic and natural diamond, graphite, graphene, multi/single walled carbon nanotube (CNT), polytetrafluoroethylene (PTFE), MoS<sub>2</sub>, oxides of Al, Ce, Si, Ti, Th, and Zr; carbides of Si, B, Ti, W, and Cr; nitrides of Si and B; and borides of Ti and Zr have been incorporated in the matrix.<sup>11</sup> However, size, shape, concentration, and dispersion of particles would influence the surface morphology and characteristic properties of the plated material. Uneven distribution of particles may give non-uniform, porous coatings. Therefore, selection of particles and their uniform dispersion by proper agitation are needed to get required properties. Frequently used reinforcements are given in Table 1.2.

**Table 1.2:** Commonly used reinforcements and their properties.

| Category            | Reinforcements   | Characteristics  |
|---------------------|--|--|
| Carbon based        | CNTs, Graphite, Graphene   | Low electrical resistivity, Low friction coefficient, Hydrophobicity, Corrosion resistance |
|                     | Diamond  | High hardness, Good polishing properties   |
| Inorganic           | Oxides (ZrO <sub>2</sub> , CeO <sub>2</sub> , Al <sub>2</sub> O <sub>3</sub> )<br>Carbides (SiC, B <sub>4</sub> C) | Corrosion resistance, Wear resistance, Microhardness                                       |
|                     | Other systems (Si <sub>3</sub> N <sub>4</sub> , TiN, WS <sub>2</sub> )   | Low friction coefficient, Corrosion resistance   |
| Polymer/<br>Organic | PTFE   | Wear resistance, Low friction coefficient,   |

### 1.2.3. Pretreatments and surface activation

The electroless process differs from other metallic coating techniques (electroplating, spray coating, vacuum metalizing, conversion coating and hot-dip galvanizing) with the unique feature that the substrate itself initiates the autocatalytic metal ion reduction process. Among a vast number of substrate materials, some of the metals such as steel and aluminum become catalytic by the formation of a metal

deposit in the electroless plating solution. While, other materials like plastics, ceramics and certain metals (copper) are passive in nature. But, even naturally active surfaces may become passive when contaminated by some residues or oxide layers. Therefore proper surface preparation is required to initiate the electroless plating process. Moreover, the properties of coated materials are associated with the efficiency of the electroless process. Uniformity of final coating with required thickness and properties show the effectiveness. These criteria can be achieved by the choice of activated substrate material at suitable metal ion concentration and bath parameters. On the other hand, electroless plating solutions are metastable; thus the metal deposition is restricted to the catalytically active surface which lowers the activation barrier of the reduction reaction.<sup>12</sup> Surface cleaning prior to the activation is necessary to eliminate unwanted dust particles and impurities like oxides on the sample to be coated.

Many researchers studied the influence of pretreatment since the early stages of electroless plating progress. Surface-to-coating bonds with high adhesion values require thorough surface preparation.<sup>13</sup> Pretreatment steps for any substrate material include machining, polishing, washing, and etching in general. After polishing, parts of heavy solid particles like machine oil, grease, SiC particles, and buffering compounds are washed with acetone. The remaining contaminants are removed by chemical etching such as alkaline treatment/soak and acid pickling. Alkaline treatment with sodium hydroxide can easily remove many of the superficial contaminants as their hydroxides leading to the formation of a clean and activated surface for coating. During the acid pickling, oxide films and other corrosion products of the metal are removed by chemical reaction. Conventional pretreatment with chromium(VI)-containing solution, followed by activation in a hydrofluoric acid solution contains some species harmful to human health and environment.<sup>14</sup> Nowadays, hydrochloric acid or sulphuric acid is used as the pickling agent. In certain cases, nitric, hydrofluoric or phosphoric acid, or mixtures of acids are used.

Surface sensitization and activation are further steps of substrate preparation. In general, this activation is done by depositing any catalytically active metal on the

surface. However, different approaches are used with respect to the nature of the substrate and the metal to be coated. Etching in hydrochloric acid solution is enough to activate steel samples.<sup>15,16</sup> Zincation is necessary for good adhesion prior to autocatalytic or electrolytic metal plating, especially for the surfaces of aluminium. The principle behind the process is the formation of a deposit of zinc on the aluminum surface by displacement from an alkaline zincate solution. The basic mechanism can be explained by equation (1.3):



Sensitization by immersing the parts in an acidic stannous chloride solution, then rinsing and activation with an acidic solution of palladium chloride is also a widely accepted procedure for aluminium. Fluoride activation in HF<sup>17</sup> or (Chromium + HF)<sup>8</sup> is the general practice for magnesium alloys.

Surface activation of ceramics and polymers provide wettability of the surface as a prerequisite for subsequent void-less covering and good adhesion of metal layers. The surface cleaned particles or substrates are sensitized with Sn<sup>2+</sup> ions followed by activation with Pd<sup>2+</sup> to enhance the bondability between ceramic/polymer phases and metallic ions. The activation process can be represented by the following equation;



Other promising materials like carbon nanotubes and carbon fibers are activated by a similar process.<sup>18-20</sup>

#### **1.2.4. Composite coating mechanisms**

Electroless composite coatings on a catalytic surface are formed by the controlled chemical reduction of metallic ions by a reducing agent and co-deposition of the dispersoids along with it. The deposit itself is catalytic enough for further reduction reaction, and the reaction continues as long as either the surface remains in contact with the bath solution or the entire solution gets depleted.<sup>21</sup> Co-deposition by electroless process with pure metal/ alloy coating can be made using various dispersoids based on micro or nano-sized particles, short fibers, whiskers and platelets.<sup>22</sup>

Different mechanisms are proposed for particle incorporation in the electroless metal matrix as in the case of electrodeposition. Guglielmi's model<sup>23</sup> for the co-deposition process occurring during electrolytic deposition is the widely accepted one. According to this model, the co-deposition of particles is governed by a two-step adsorption mechanism as shown in Figure 1.2. First step is the physical adsorption of particles on the substrate surface. The dispersed particles in the bath are transported to the surface by mechanical action and are loosely adsorbed. It is determined by the particle flux at the interface of the substrate and the electrolyte, which is a function of their concentration, size, and density.

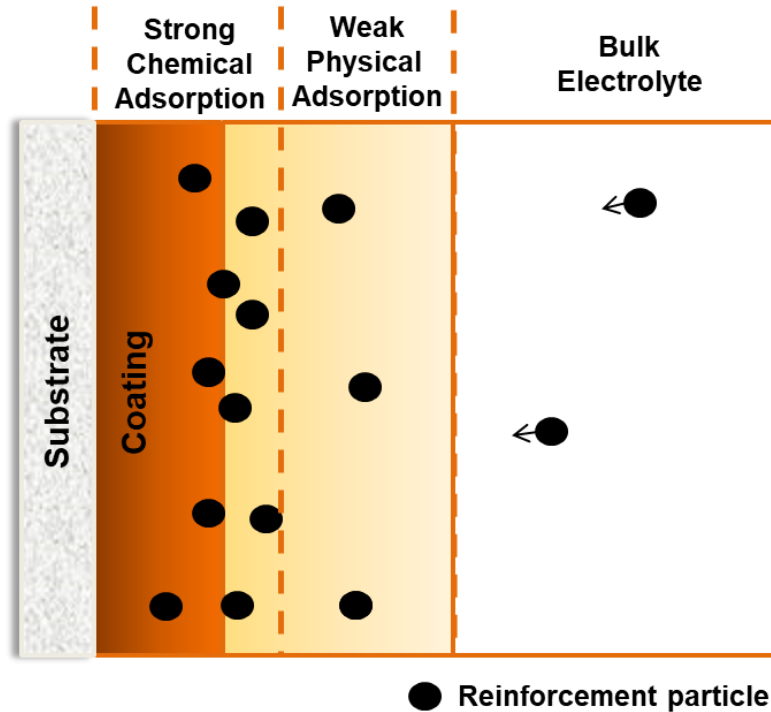


**Figure 1.2:** Schematic representation of Guglielmi's model electroless composite coatings.

Physical adsorption of the particles is explained using the Langmuir adsorption isotherm. Therefore, the surface coverage can be written as equation (1.5):

$$\sigma = kC_v / (1 + kC_v) (1 - \theta) \quad (1.5)$$

Where,  $\sigma$  is surface coverage,  $k$  is adsorption coefficient,  $C_v$  is the volume of the solid particles in the suspension bath, and  $\theta$  is the degree of the cathode surface coverage with the particles finally embedded into the coating. In the second step, the

particles are strongly adsorbed on the substrate in association with the electrochemical reduction of metal matrix. This strong irreversible chemical adsorption can be explained by Temkin adsorption.

However, Guglielmi's co-deposition model does not discuss many relevant factors, such as the type and size of the particles and the hydrodynamic conditions. The studies to determine the impact of bath stirring with particles such as PTFE into the nickel matrix<sup>24</sup> reveal its importance. If the stirring is too weak or too intense, the suspension may become heterogeneous due to the sedimentation or the centrifugal force. Their effective concentration in the suspension may become lower and the obtained coating will contain a smaller amount of the co-deposited particles.

The co-deposition mechanism for the micro and nano-sized particles in the metal matrix is different. The micrometer-sized particles are deposited at the borders and the edges of the metal crystallites, while the nanoparticles are incorporated inside the metal crystals besides the borders and edges. Hence, the embedding mechanism of the micro and nanoparticles could be characterized as "intercrystalline" and "intracrystalline" respectively.<sup>25</sup>

According to the Kariapper and Foster's<sup>26</sup> model co-deposition mechanism, the metal ion adsorption on particles is the most important step, and it practically determines the possibility of obtaining a composite coating. The authors assumed that it was necessary to get a positive charge on the particle for its deposition process. Celis et al.<sup>27</sup> and Fransaer et al.<sup>28</sup> also considered the fact that the production of composite coatings required adsorption of ions on solid particles in the plating bath and the reduction of some ions of the deposited metal adsorbed on the particles of the solid phase. This concept has been used to explain the nanoparticle co-deposition. The schematic representation of the various stages of electroless nanocomposite coatings is shown in Figure 1.3. When the nanoparticles are added to the plating bath, they will be covered by an ionic cloud. The ion-adsorbed nanoparticles transport towards the electrode surface by means of convection and diffusion. Finally, the ion-adsorbed nanoparticles are reduced similarly as that of the metal ions and they get incorporated

into the growing metal matrix. In addition to that most of the nanoparticles are in the form of clusters following their agglomeration in the plating.

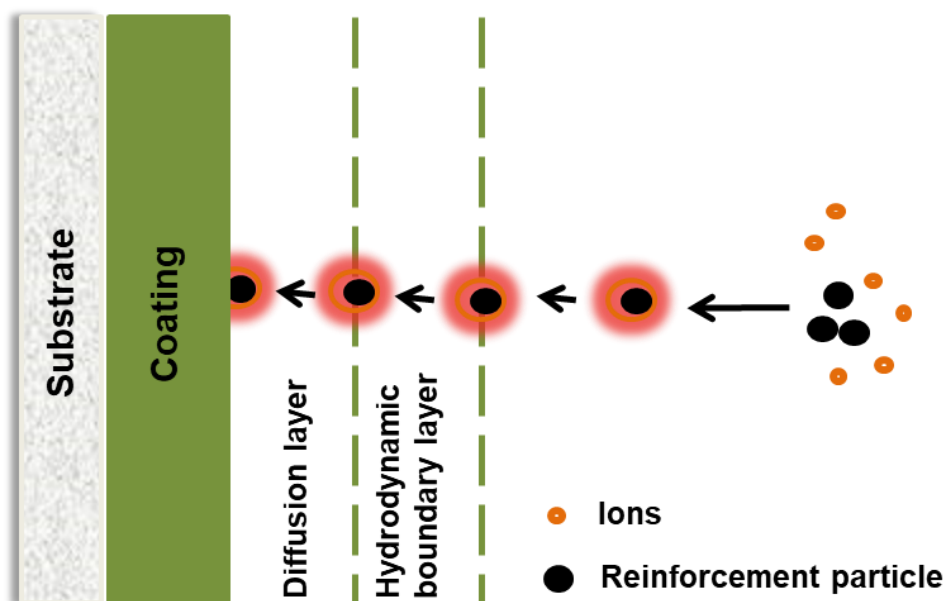


**Figure 1.3:** Schematic representation of various stages of electroless nanocomposite coatings.

The above mechanisms have been derived for electrodeposition of composite coatings and, which is extended to electroless composite coating process. Few studies particularly for electroless co-deposition behavior and mechanism of ultrafine particles were also described below. Co-deposition of nanodiamond with the very large specific surface area was investigated by Matsubara et al.<sup>29</sup> The schematic representation is given in the Figure 1.4. If the nanodiamond particles are adsorbed by a large number of Ni-complex (a), the co-deposition becomes more because of the higher incorporation of particles in the Ni-complex. On the contrary (b), if the ion adsorption is less, the amount of co-deposition of particles becomes less. Such adsorption of metal on the surface of a particle is a kind of interaction between a particle and a metal ion. The high surface energy of the nanoparticle may enhance the ion adsorption mechanism.

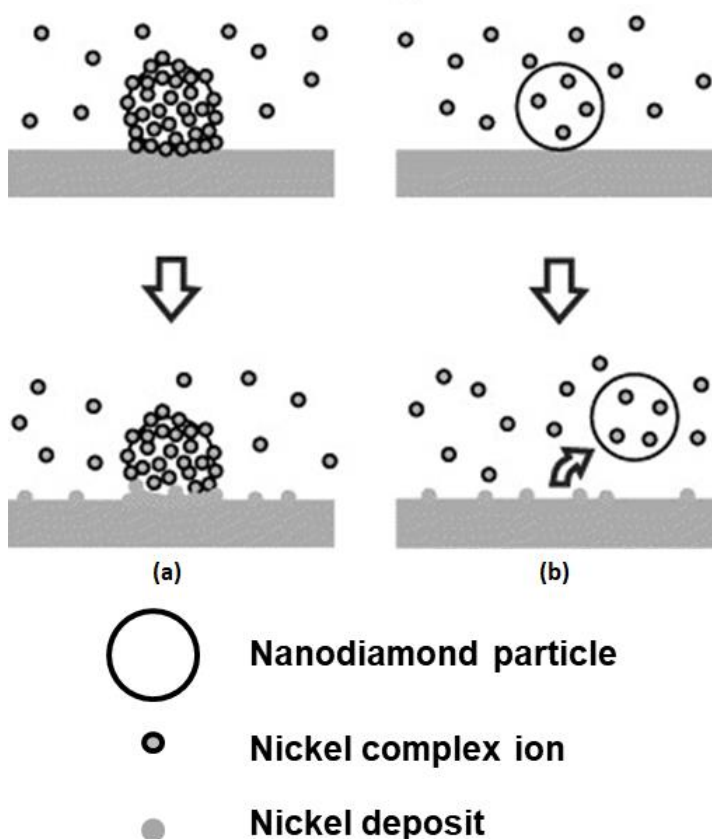


**Figure 1.4:** Schematic representation of ion adsorption mechanism.<sup>29</sup>

The mechanism for the deposition of Ni-P-TiO<sub>2</sub> nanocomposite was studied by Hosseini et al.<sup>30</sup> It is also in agreement with the above explained mechanisms behind the co-deposition of nanoparticles. The process includes three stages: (i) the particles are transferred primarily by forced convection (ii) the ion-adsorbed particles are adsorbed loosely at the substrate surface and (iii) the particles are incorporated irreversibly into the metal matrix by the reduction of some of the adsorbed ions on the particle surface. As a result, when the inert nanoparticles of TiO<sub>2</sub> are absorbed by metal ions, acquire positive surface charge and are possibly adsorbed on the electrode surface. Further reduction of these metal ions results in strong adsorption of the particles onto the metal matrix and the substrate.<sup>31</sup> However, actual depositing process can be far more complex than these assumptions due to the presence of intermediate reactants and other adsorbed species such as organic surfactant, which strongly influences the depositing process.

### 1.3. Nickel composite coatings

#### 1.3.1. Surface morphology and structural characteristics

Co-deposition of secondary particles along with metal matrix may or may not change the surface morphology. The structure of electroless Ni-P-Si<sub>3</sub>N<sub>4</sub> composite coating was not influenced by the incorporation of particles in the matrix.<sup>32</sup> A similar observation has been observed by many researchers. X-ray diffraction pattern, transmission electron micrograph, selected area electron diffraction pattern and energy dispersive X-ray analysis of Ni-P/Ni-P composite coatings have shown the insignificance of Si<sub>3</sub>N<sub>4</sub>, CeO<sub>2</sub> and TiO<sub>2</sub> particles addition in the structure of the electroless Ni-P deposits.<sup>33</sup> On the other hand, the higher percentage of particles co-deposition would lead to the additional peaks in the XRD pattern of composite coating. Apachitei et al.<sup>34</sup> observed the presence of SiC in as-plated electroless Ni-P-SiC composite coating by XRD analysis.

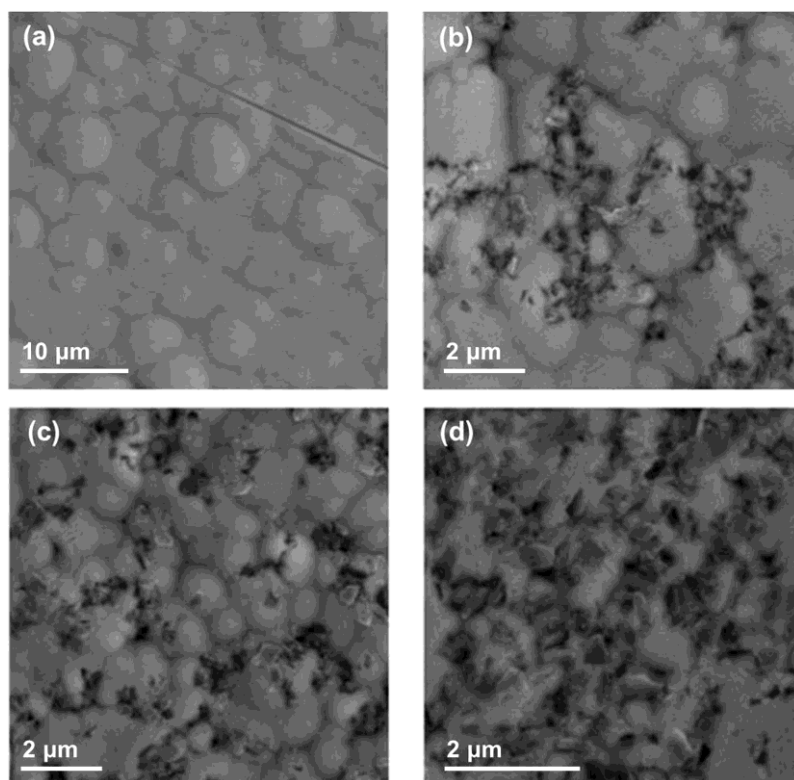


**Figure 1.5:** Back scatter scanning electron microscopy images of (a) Ni-P, Ni-P/nanometer diamond depositions at various concentrations of nano-diamond in electroless solution: (b) 0.5, (c) 1.0, (d) 4.0 g L<sup>-1</sup>.<sup>5</sup>

Ni-P/nano-diamond composite deposition shows the consistency of surface morphologies (Figure 1.5) with incorporated nanodiamond particles in Ni-P matrix.<sup>5</sup> On the other hand, incorporation of micro/nano size particles into the electroless coating can lead to the grain refinement by an increase in the number of nucleation sites. Surface roughness occurs by the presence of many nodular protrusions over the surfaces and changes the orientation of metal crystallites without influencing the crystallite dimensions.<sup>35</sup> These features can be altered by the size, shape, and concentration of the second phase particle. Rabizadeh and Allahkaram observed a spherical nodule formation on the Ni-P coating upon the addition of SiO<sub>2</sub> nanoparticles.<sup>36</sup> Addition of TiO<sub>2</sub> nanoparticles induced a considerable reduction of the nodular features Ni-P-TiO<sub>2</sub> nanocomposite coating. Depending on an increase in the concentration of TiO<sub>2</sub> nanoparticles in the bath, sub-micrometer nodules were formed for 3 to 5 g L<sup>-1</sup> solution and for 7 to 9 g L<sup>-1</sup> bath, the size of the nodules was again decreased.<sup>37</sup> Effect of varying concentrations of nano-sized TiC in the surface morphology of Ni-P coating on the low carbon steel substrate was studied by Afroukhteh et al.<sup>38</sup> It was observed that the morphology of coatings became smoother in the presence of small quantity of TiC particles (0.01-0.1 g L<sup>-1</sup>) with a drastic decrease of nodule size from 12 μm to 2 μm with particle free counterpart. Plating rate was also influenced by the particle concentration. The highest deposition rate was obtained for 0.3 g L<sup>-1</sup> TiC in Ni-P coating, and it was very slow with lower amounts of TiC (less than 0.1 g L<sup>-1</sup>). Particles deposition can also influence the surface energy along with the surface roughness which in turn modifies the material characteristics. The influence of surface energy components of substrates versus bacterial adhesion has been investigated on Ni-P-TiO<sub>2</sub>-PTFE nanocomposite coatings with different surface-energy components made by the electroless plating technique. The results demonstrated that there was a strong correlation between bacterial attachment/removal and the CQ ratio (ratio of Lifshitz-van der Waals (LW) a polar to electron donor surface-energy components of substrates). The coatings with the lowest CQ ratio showed the most inferior bacterial adhesion or the highest removal.<sup>39</sup>

The co-deposition of second phase particle depends not only on the concentration but also their dispersion in the electroless bath. It can be achieved by proper stirring or agitation of the electroless bath and the use of surfactants to prevent agglomeration. Surfactants are often introduced to the solution containing the particles to get a better dispersion, uniformity, and stability. Ionic (both cationic and anionic), non-ionic and polymeric surfactants have been used for several studies. Sodium dodecyl sulfate (SDS), cetyltrimethyl ammonium bromide (CTAB)<sup>40</sup> and 1,3-toloyl tri-ethanol ammonium chloride (TTAC)<sup>41</sup> are generally utilized for the electroless deposition. Primarily surfactants act as dispersing agent for the secondary particle. However, they could perform different roles when incorporated during composite coating: a) modification of the surface charge by the surfactant monomers or hemimicelle adsorbed on particles, b) wettability by the reduction in the surface tension between the substrate and particles and, c) enhancement of the electrostatic adsorption of suspended solids on the substrate. Electroless deposition of Ni-P-nano-ZrO<sub>2</sub> composite coatings in the presence of cationic, anionic, and nonionic surfactants was investigated by Zielinska et al.<sup>42</sup> showing that surfactant type have a significant effect on the deposition process. The addition of the cationic surfactant, DTAB, as the suspension stabilizer reduces the number of free anions in the solution and practically inhibits the conversion of hypophosphite ions to elementary phosphorus. In addition to the influence of surfactant, composite coating in the presence of ultrasonication would increase the uniform particle dispersion in the entire electrolyte.<sup>43</sup>

### **1.3.2. Corrosion resistance**

Corrosion resistance of electroless composite coatings highly depends on the nature of co-deposited particles. Enhanced corrosion resistance has been observed by the addition of certain particles like SiC, CeO<sub>2</sub>, TiO<sub>2</sub>, and SiO<sub>2</sub>. Corrosion resistance properties of the SiC added composite coatings had been subjected to many studies. Farzaneh et al.<sup>44</sup> made a Ni-P-SiC nanocomposite coating like Ni-P for use in saline corrosive environments to improve the corrosion resistance of mild steel. Potentiodynamic polarization curves (Figure 1.6) of the coatings reveal that the corrosion performance of the Ni-P layer was improved by co-deposition of the SiC

nanoparticles. However, SiC concentration higher than  $2 \text{ g L}^{-1}$  was negatively affected. Heat treatment also enhanced the property of the Ni-P-SiC coating. The coating heat treated at  $400^\circ\text{C}$  had the best performance of corrosion resistance compared to the as-deposited and the heat treated samples at  $700^\circ\text{C}$ .

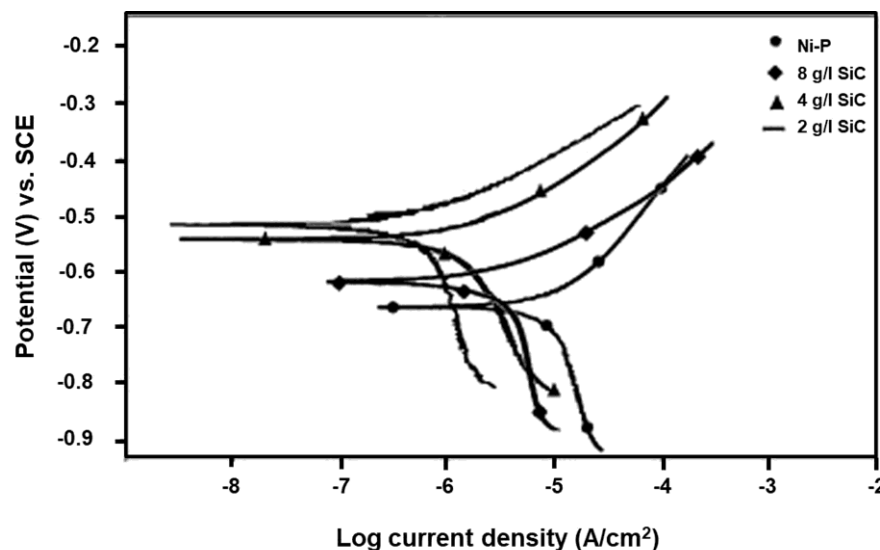


**Figure 1.6:** Potentiodynamic polarization curves of Ni-P and Ni-P-SiC coatings at varying concentrations of SiC.<sup>44</sup>

Electrochemical measurements showed that the annealed Ni-P/nano-TiO<sub>2</sub> coatings had excellent corrosion resistance in 3.5 wt.% NaCl solution compared to Ni-P coatings.<sup>45</sup> Reduction of corrosion with Ni-P-TiO<sub>2</sub> nanocomposite coatings prepared by Hosseini et al.<sup>30</sup> at optimized condition ( $10 \text{ g L}^{-1}$  TiO<sub>2</sub>) were 15 times better than that of the pure copper substrate. Cheng-Kuo Lee<sup>46</sup> made electroless Ni-P/nano-TiO<sub>2</sub> and Ni-P/CNT composite coatings on 5083 aluminum alloy. The efficiency for corrosion prevention of nanocomposite coatings was the maximum at  $10 \text{ g L}^{-1}$  nano-TiO<sub>2</sub> and nano-CNT addition. Moreover, the property exhibited by Ni-P/CNT was superior to the nano-TiO<sub>2</sub> co-deposited coating. Studies on the corrosion resistance of electroless Ni-P and Ni-P composite coatings with Si<sub>3</sub>N<sub>4</sub>, CeO<sub>2</sub> and TiO<sub>2</sub> particles by electrochemical impedance spectroscopy revealed that the coatings with Si<sub>3</sub>N<sub>4</sub> and CeO<sub>2</sub> have better properties than the TiO<sub>2</sub>.<sup>47</sup>

The corrosion resistance of NiP-Al<sub>2</sub>O<sub>3</sub> ( $4 \text{ g L}^{-1}$ ) coating is believed to be improved by the rapid formation of continuous Ni hydroxide passive films at surface

defects.<sup>48</sup> According to Yu et al.<sup>49</sup> Ni-P-SiO<sub>2</sub> and Ni-P-CeO<sub>2</sub> composite coatings were formed with strong corrosion and tarnish resistance. Less porosity density by accommodation of nanoparticles in the matrix promoted the corrosion resistance. The optimum concentration of nanodiamond particle in nickel phosphate coating exhibited significant anticorrosive properties. Figure 1.7 shows the Nyquist representation of electrochemical impedance spectroscopy studies and corresponding equivalent circuit. Stable passive film formation in the presence of nanoparticles especially at 100 mg L<sup>-1</sup> concentration gave highest charge transfer resistance<sup>50</sup>.

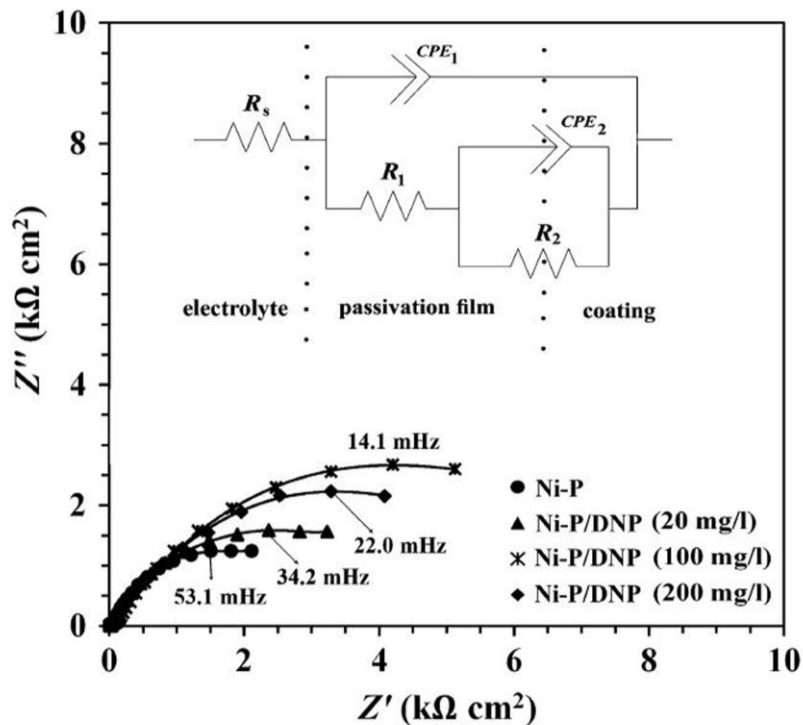


**Figure 1.7:** Nyquist plots for Ni-P coatings containing different concentration of diamond nano particle (DNP) in 3.5 wt.% NaCl solution;  $f_{\text{max}}$  of semicircles was given. Inset: equivalent circuits.<sup>50</sup>

Influence of particles added in electroless nickel composite coatings for corrosion resistance has been explained in several reports. Schematic representation of corrosion prevention mechanism by the addition of diamond nanoparticles in Ni-P matrix and the corresponding SEM images of coating cross section were given in Figure 1.8 and 1.9 respectively.<sup>50</sup> The Ni-P coating cross-section exhibited long and

straight grain boundaries which shorten the way of corroding agents to reach the metallic surface. On the other hand, co-deposited nanoparticles act as obstacles in the corrosion paths and stop the columnar growth.<sup>51</sup> As much as the nanoparticle content higher in the coating the corrosion paths become less straight and which result in higher corrosion resistance of the composite coating.

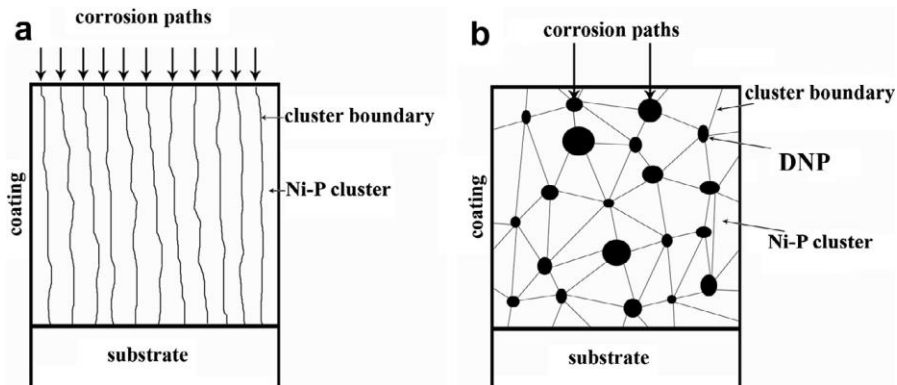


**Figure 1.8:** Schematics of coatings cross-section: (a) Ni-P and (b) Ni-P/DNP elucidates the corrosion prevention by diamond nanoparticles.<sup>50</sup>

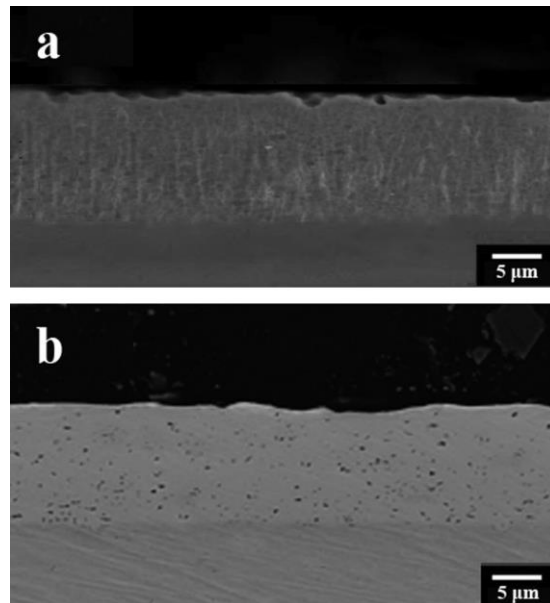


**Figure 1.9:** SEM images of the coatings cross-section: (a) Ni-P and (b) Ni-P/DNP.<sup>50</sup>

Table 1.3 provides an overall understanding of the corrosion resistance of different reinforcements in the nickel matrix. Higher values of corrosion potential ( $E_{corr}$ ), polarization resistance ( $R_p$ ) and lower values for corrosion current density ( $i_{corr}$ ) of each composite coating compared with the particle-free coating reveals the

anticorrosion efficiency. Some of them have better properties while the others have less which depends on the particles and coating stability. Although, the values may vary for the same composite coating made by different groups owing to the changes in the conditions and chosen substrate.

**Table 1.3:** Corrosion resistant characteristics of electroless nickel composite coatings.

| Coating                             | Optimum conc. of reinforcement | $E_{corr}$ (V vs SCE) | $i_{corr}$ ( $\mu\text{A}\cdot\text{cm}^{-2}$ ) | $R_p$ ( $\text{ohm}\cdot\text{cm}^2$ ) | Reference |
|-------------------------------------|--------------------------------|-----------------------|---|--|-----------|
| Ni-P                                | -                              | - 0.662               | 2.51  | 29455                                  | 44        |
| Ni-P-SiC                            | 2 g L <sup>-1</sup>            | - 0.512               | 0.56  | 59784                                  | 44        |
| Ni-P-TiO <sub>2</sub>               | 10 g L <sup>-1</sup>           | - 0.260               | 0.34  | -                                      | 30        |
| Ni-P                                | -                              | - 0.838               | 6.36  | -                                      | 46        |
| Ni-P-TiO <sub>2</sub>               | 10 g L <sup>-1</sup>           | - 0.654               | 4.87  | -                                      | 46        |
| Ni-P-CNT                            | 10 g L <sup>-1</sup>           | - 0.514               | 2.95  | -                                      | 46        |
| Ni-P-SiO <sub>2</sub>               | 2 g L <sup>-1</sup>            | -                     | -   | 3.14×10 <sup>8</sup>                   | 52        |
| Ni-P-ZrO <sub>2</sub>               | 25 mL L <sup>-1</sup> sol      | - 0.321               | 0.37  | -                                      | 53        |
| Ni-P-ZrO <sub>2</sub>               | 5 wt.%                         | - 0.361               | 0.96  | 61593                                  | 54        |
| Ni-P-Al <sub>2</sub> O <sub>3</sub> | 6 g L <sup>-1</sup>            | - 0.354               | 0.59  | 32920                                  | 55        |
| Ni-P-nano diamond                   | 100 mg L <sup>-1</sup>         | - 0.380               | 0.85  | 12650                                  | 50        |
| Ni-P-CeO <sub>2</sub>               | 8.10 wt.%                      | -                     | 0.37  | 90700                                  | 47        |
| Ni-P-Si <sub>3</sub> N <sub>4</sub> | 7.44 wt.%                      | -                     | 0.33  | 90525                                  | 47        |
| Ni-P-TiO <sub>2</sub>               | 5.42 wt.%                      | -                     | 0.66  | 58991                                  | 47        |
| Ni-P-PTFE                           | 6-8 g L <sup>-1</sup>          | -0.384                | 3.70  | -                                      | 56        |
| Ni-P-MoS <sub>2</sub>               | 6-8 g L <sup>-1</sup>          | -0.555                | 25.8  | -                                      | 56        |
| Ni-P-PTFE-MoS <sub>2</sub>          | 6-8 g L <sup>-1</sup> each     | -0.681                | 85.8  | -                                      | 56        |
| NiP                                 | -                              | -0.808                | 7   | -                                      | 8         |
| Ni-P-B <sub>4</sub> C               | 4 g L <sup>-1</sup>            | -1.031                | 84  | -                                      | 8         |
| Ni-B                                | -                              | -0.469                | 19  | -                                      | 57        |
| Ni-B-SiC                            | 1 g L <sup>-1</sup>            | -0.386                | 8.30  | -                                      | 57        |

**1.3.3. Mechanical and tribological characteristics**

The enhancement in mechanical and tribological properties of the coatings depends on the type of second phase particles incorporated. Surface texture, coating thickness, reinforcement, adhesion on the base material, compatibility between metal matrix and the reinforcement, etc. would contribute to the specific properties of every coating. It is well known that the wear resistance of the material is mainly affected by the hardness, strength and friction coefficient. The wear resistance is proportional to the hardness of coatings under the lower load. The relation between surface hardness and wear resistance can be expressed using Archard's equation (1.6):<sup>58</sup>

$$W = kLSH \quad (1.6)$$

Where  $W$  is the wear volume,  $L$  is the applied load,  $S$  is the sliding distance,  $k$  is the wear coefficient and  $H$  is the hardness of the materials. Hence higher hardness and lower friction coefficient of the coating can help in improving the wear resistance.

Surface hardness is a major factor in components and semi-finished products to control wear and tear process for practical uses. Electroless nickel has recognized as a hard coating for tribology based applications. Since Ni-P and Ni-B are the major contributors in industrial applications; the influence of phosphorous and boron in nickel-based coatings are well established. During electroless Ni-P coatings, random capturing of phosphorus along with nickel atoms occurs and the variation in the rate of segregation of nickel and phosphorus atoms determines the crystallinity of the resultant coating and which in turn decide the microhardness.<sup>59</sup> If the required phosphorus segregation is substantial, it will prevent the nucleation of face-centered cubic nickel phase and this result in a disordered amorphous structure in as-deposited condition.

Heat treatment of the coated samples allows the transformation of electroless Ni-P coating from the disordered structure to an ordered arrangement of face-centered cubic Ni and body-centered tetragonal  $Ni_3P$  and  $Ni_5P_2$  hard phases. The phosphides prevent the dislocation movement, thereby increasing the hardness further. Hence, the hardness of electroless nickel coating is found to be increased with the heat treatment up to a certain temperature above which the hardness is found to

be decreased.<sup>60</sup> The excessive annealing at very high temperature causes film degradation with grain coarsening, which leads to surface brittleness and enhanced dislocation propagation followed by the decrease in hardness of Ni-P.<sup>61</sup> Borohydride reduced Ni-B coatings show better hardness and wear resistance even in as-deposited condition. Krishnaveni et al.<sup>62</sup> observed that the Ni-B coating in as-plated condition had the microhardness of the order of 570 (HV<sub>100</sub>) and it was increased by heat treatment up to a maximum of 908 (HV<sub>100</sub>) at 450°C for one hour. The increase in hardness was obtained due to the precipitation of nickel borides, Ni<sub>3</sub>B and Ni<sub>2</sub>B.

The hardness of composite coating can be altered by both heat treatment and the properties of secondary particles. Co-deposition of hard particles during electroless coating is a general trend to obtain the surface with better hardness and wear resistance. The properties are influenced by particle size, shape and concentration. Wear resistance of Ni-P-Diamond coatings, with varying particles sizes (3-6, 6-12, 20-40 micrometer) at different annealing temperatures (230, 350, and 400°C) for 2h was investigated by Reddy et al.<sup>63</sup> It was observed that Ni-P-C composite coatings with finer diamond particles were more wear resistant than the larger particles, since the bigger ones were less firmly held by the coatings. Heat treatment of the coated sample shows high wear resistance after heating at 350°C due to the diffusion of nickel into the substrate. The entire amorphous portion of the deposited nickel gets converted into crystalline nickel and nickel phosphides. In a study of Ni-P-Al<sub>2</sub>O<sub>3</sub> coatings done by Alirezaei et al.<sup>64</sup> detected that, while increasing the particles content to 15 g L<sup>-1</sup> in the bath, the co-deposited particles increased to the maximum value of 29 vol.% and consequently maximum hardness obtained approximately 1050 HV<sub>0.05</sub> (Figure 1.10).

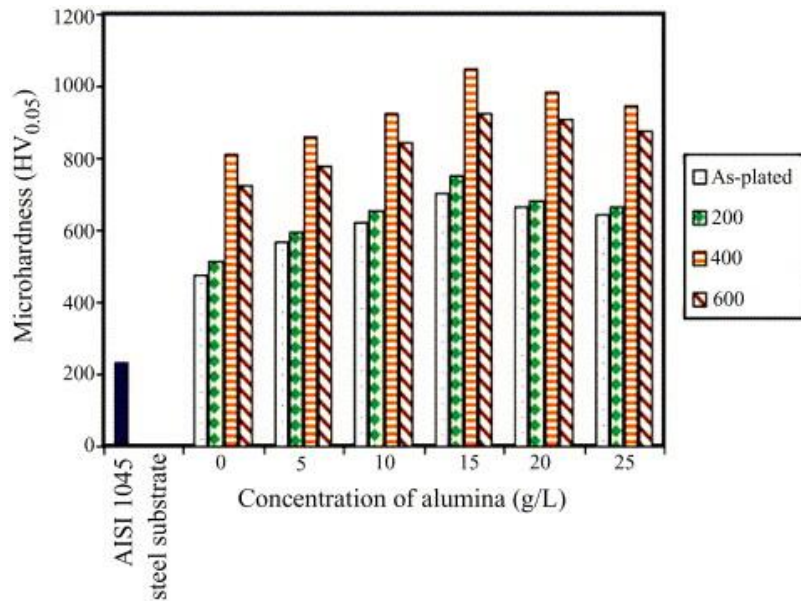


**Figure 1.10:** Effect of heat treatment and particle concentration on the microhardness of electroless Ni-P-Al<sub>2</sub>O<sub>3</sub> coatings.<sup>64</sup>

Makkar et al.<sup>65,66</sup> studied the effect of TiO<sub>2</sub> nanoparticles, obtained by both chemical synthesis and mechanical milling, in the Ni-P matrix. The coefficient of friction and specific wear rate of nanocomposite coatings was observed to be lower than Ni-P coatings. SiC added electroless nickel composite coating also show superior mechanical properties compared to particle free electroless nickel coating in both as-deposited and heat-treated conditions.<sup>67,68</sup> Incorporation of Si<sub>3</sub>N<sub>4</sub> particles in the composite coatings significantly improves the hardness and wear resistance.<sup>69</sup> Electroless Ni-P-gold nanocomposite coatings exhibited higher hardness, corrosion resistance and uniformity than the particle-free coatings.<sup>70</sup> Mechanical properties of nickel boride coatings can significantly improve by the incorporation of TiO<sub>2</sub> nanopowder. The maximum Knoop microhardness was obtained with 2 g L<sup>-1</sup> TiO<sub>2</sub> nanopowder addition. Further addition of TiO<sub>2</sub> powder leads to a deterioration of mechanical property due to the agglomeration of nanoparticles and break of coating integrity<sup>71</sup>. Incorporation of WC nanoparticles in composite coatings elevates the wear resistance and microhardness with the increase of WC weight percentage<sup>72,73</sup> The influence of various particles in nickel boride coating to mechanical properties was studied by Ekmekci et al.<sup>74</sup> SiO<sub>2</sub>, Al<sub>2</sub>O<sub>3</sub>, TiO<sub>2</sub>, and CuO nanoparticles dispersed

electroless Ni-B coated AISI-304 steel substrates showed an increase in the surface nodularity. The nanocomposite coatings tend to have higher microhardness compared with the coating without nanoparticles owing to the effect of dispersion strengthening of ceramic particles in the matrix. Among the four particles,  $\text{Al}_2\text{O}_3$  added composite coating had the highest microhardness (Figure 1.11).

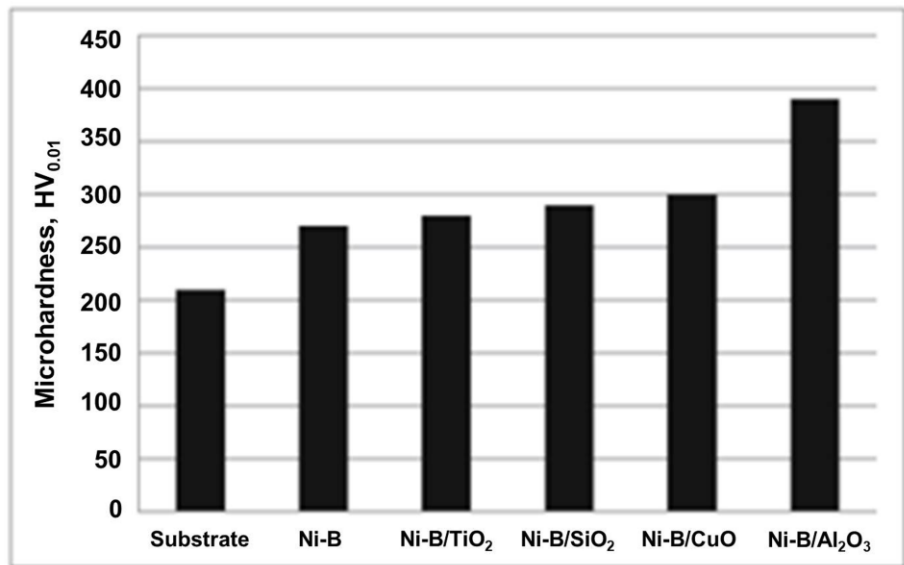


**Figure 1.11:** Microhardness of substrate, Ni-B coating and the composite coatings with different secondary particles.<sup>74</sup>

Friction and wear are two kinds of responses from one tribosystem exactly related to each other in each state of contact, although a whole, simple relationship should not be expected.<sup>75</sup> Hence, the friction coefficient of any material highly influences the wear behavior and followed by their mechanical properties. The presence of soft and layered materials along with metal deposition gives a broad range of properties due to their precise behavior. Wang et al.<sup>76</sup> found that under an unlubricated condition, Ni-based CNT composite coatings exhibited higher wear resistance and lower friction coefficient than Ni-P electroless coating. The self-lubricating behavior of CNTs due to the short and tubular shape would allow easier sliding or be rolling between the mating metal surfaces, resulting in the decrease in the friction coefficient of the composite coatings. Percentage of particles added and their distribution in the matrix was found to be the key factors in improving the

frictional behavior of this composite coating. Ni-P-Si<sub>3</sub>N<sub>4</sub> nanowire electroless composite deposited on AZ31 Mg alloy showed a lower coefficient of friction and wear rate in comparison with the conventional Ni-P coating (Figure 1.12). At an optimum concentration of Si<sub>3</sub>N<sub>4</sub> nanowires (1.5 g L<sup>-1</sup>), the composite coating had minimum friction coefficient ~0.25 (Figure 1.12), which indicated the surface suffered a small frictional shear force during wear test. Hence, it possesses the desirable wear resistance. While, the nanowire concentrations exceeds 1.5 g L<sup>-1</sup>, the wear resistance of composite coating decrease rapidly because of their agglomeration, which is easy to occur brittle flaking off under external force.<sup>77</sup>

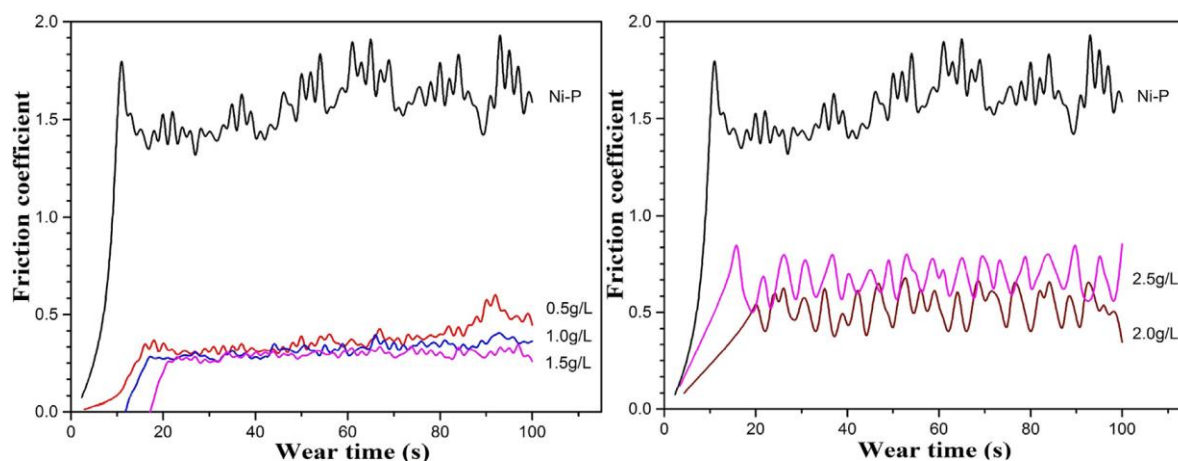


**Figure 1.12:** Friction Coefficient of Ni-P-Si<sub>3</sub>N<sub>4</sub> nanowire electroless composite coating with varying nanowire concentration.<sup>77</sup>

Use of WS<sub>2</sub> particles in the Ni-P coating decreased the hardness and modified the wear behavior. As-plated Ni-P-WS<sub>2</sub> possess both abrasive and adhesive wear mechanisms instead of severe adhesive wear for as-plated Ni-P coating. For heat treated samples, the presence of WS<sub>2</sub> in composite coating brings mild abrasive wearing. Additionally, the coefficient of friction was reduced from above 0.6 to about 0.1 owing to the lubricating nature of the particle.<sup>78</sup> Incorporation of graphene oxide (GO) and reduced graphene oxide (rGO) in electroless nickel decreased the hardness due to their soft nature.<sup>79</sup> Tribology of the composite coating may vary with the temperature of the system. For example, the average friction coefficient of Ni-P-MoS<sub>2</sub> composite coating dropped at 500°C, and then slightly increased at 600°C. Higher coefficient of friction at room temperature was explained by the presence of higher

surface roughness due to the addition of the MoS<sub>2</sub>, which exceeds the lubrication effect of MoS<sub>2</sub>. In addition to that, the wear rates of Ni-P-MoS<sub>2</sub> composite coatings vary little between 10<sup>-5</sup> and 10<sup>-4</sup> and the properties were the best at 400°C. The improvement of tribological properties of the composite coatings at higher temperature was attributed to the formation of lubricious oxide film composed of NiO and MoO.<sup>80</sup> This type of “lubricious” coatings can be used as dry- low friction coatings between sliding components, like a small-caliber automatic weapon, instead of using liquid lubricants with an affinity of dirt, dust and fine sand to the surface.<sup>81</sup>

Better wear resistance offered by the composite coatings based on layered materials can be explained by their self-lubricating behavior. The schematic representation in Figure 1.13 shows the lubricious tribolayer formation in composite coating and its influence during the sliding motion in comparison with metallic coating. While applying a load to the moving metallic coated sample, the surface comes in contact with the counter disc resulting in a plastic deformation and coating delamination. Moreover, the composite coating exhibits a modified wearing mechanism. As soon as the coating gets in contact with the hard surface, layered reinforcements are partially transferred to the surface by adhesion. Due to adhesion effects, some layers are dragged towards the contact area and prevent the direct contact of the two sliding surfaces. A slight lift of the adhered layers induces a sliding behavior with a lower coefficient of friction. Moreover, the elastic recovery of compressed reinforcement after the stroke enhances the wear resistance.<sup>82</sup>

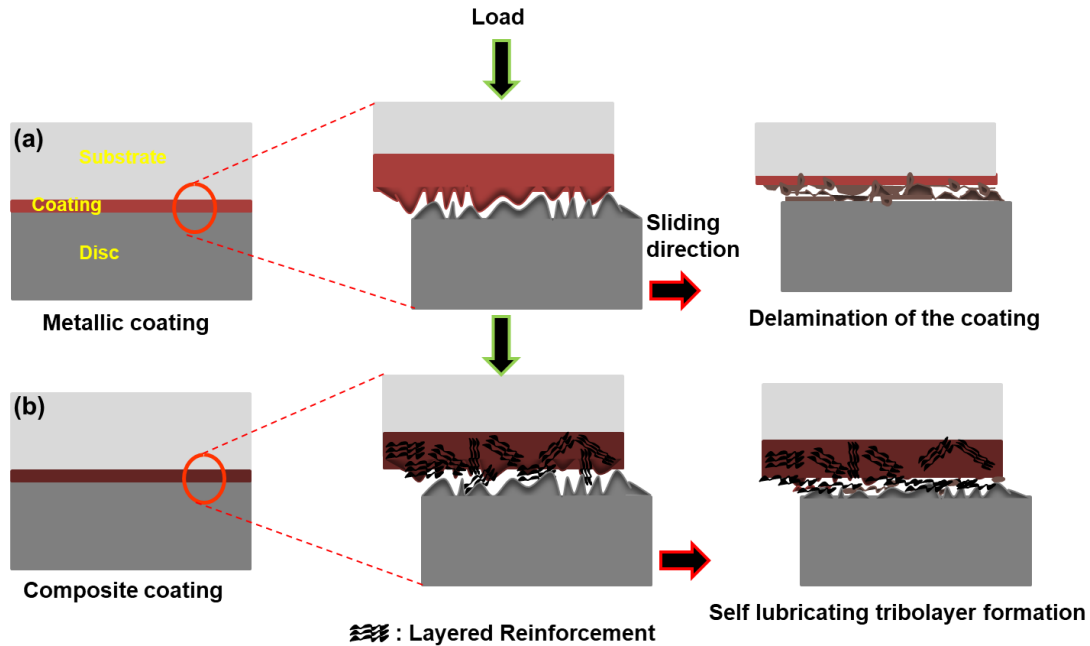


**Figure 1.13:** Schematic representation of lubricious tribolayer formation during the sliding motion.

### ***Role of hybrid particles***

The combination of two different particles can incorporate in the same composite coating to attain a broad range of features for various applications. Wu et al.<sup>83,84</sup> studied the tribological behavior of electroless Ni-P-Graphite-SiC along with Ni-P-SiC and Ni-P-Gr. Ni-P-Gr had lowest friction coefficient, and Ni-P-SiC had a higher hardness. As a combined effect, Ni-P-Gr-SiC possessed excellent wear resistance among the three composite coatings. It maintains the combination of unique advantages of Ni-P-SiC with high load-bearing capacity and Ni-P-Gr with a low friction coefficient. The graphite-rich mechanical mixed layer formed on the worn surface during the analysis was responsible for the better antifriction properties, and SiC particles mixed with graphite played a load-bearing role in protection from shearing easily.

Mechanical properties of Ni-P-B<sub>4</sub>C-PTFE hybrid coating were investigated by Dooz et al.<sup>85</sup> Ni-P, Ni-P-PTFE, Ni-P-B<sub>4</sub>C and Ni-P-B<sub>4</sub>C-PTFE coatings were created on Aluminum samples. Ni-P-PTFE composite coating had the lowest friction coefficient,

and Ni-P-B<sub>4</sub>C composite coating had the highest hardness, and the Ni-P-B<sub>4</sub>C-PTFE hybrid coatings showed the best wear resistance. Adding Teflon particles leads to reduced friction coefficient, and it is useful for slippery applications. Hard boron carbide particles increased the coating hardness to 1260 Vickers, and it results in improved wear resistance. PTFE particles are very soft so that they cannot prevent dislocations as ceramic particles such as boron carbide do. Since the dislocations easily peel particles from the surface. Therefore, plastic deformation (in micrometer-scale) of PTFE composite becomes easier than coatings without particles. Besides, boron carbide particles addition resulted in increased corrosion resistance while PTFE particles decreased the corrosion resistance. Co-deposition of polytetrafluoroethylene (PTFE) and MoS<sub>2</sub> particles with electroless nickel enhanced their tribological properties. The particles contained in the composite coating were increased by changing the specimen orientation from vertical to the horizontal configuration. Moreover, change in phase structure during heat treatment improves the wear resistance.<sup>86</sup>

The following table (Table1.4) explains the features of different nickel-based composite coatings in terms of tribology.

**Table 1.4:** Hardness and tribological behaviour of electroless nickel composite coatings.

| Coating   | Thickness ( $\mu\text{m}$ )                         | Hardness (various units)  | Coefficient of friction (average)  | Remarks  | References |
|---|---|---|--|--|------------|
| Ni-P-Diamond  | 20  | -   | -  | Finer diamond particles addition and annealing at $350^{\circ}\text{C}$ can give more wear resistance. | 63         |
| Ni-P-Gr-SiC along with Ni-P-SiC and Ni-P-Gr   | -   | Ni-P-SiC > Ni-P > Ni-P-Gr-SiC ( $\approx 830$ $\text{HV}_{50}$ at $400^{\circ}\text{C}$ ) > Ni-P-Gr   | Ni-P-SiC (0.23) > Ni-P (0.15) > Ni-P-Gr-SiC (0.1) > Ni-P-Gr (0.06)                           | Ni-P-Gr-SiC coating show excellent wear resistance.  | 83,84      |
| Ni-P-CNT  | 25  | Ni-P (1095 $\text{HV}_{50}$ )<br>Ni-P-CNT <sub>11.2</sub> vol.% (1524 $\text{HV}_{50}$ )  | Ni-P > Ni-P-CNT  | Self-lubrication of CNTs improves the wear resistance.   | 76         |
| Ni-P-B <sub>4</sub> C-PTFE hybrid coating<br>Ni-P, Ni-P-PTFE, Ni-P-B <sub>4</sub> C | 40  | Ni-P 454 (1076 <sub>HT</sub> )<br>Ni-P-PTFE 190 (375 <sub>HT</sub> )<br>Ni-P-B <sub>4</sub> C 804 (1260 <sub>HT</sub> ) (at 200 grams)                        | Ni-P 0.44<br>Ni-P-PTFE 0.18<br>Ni-P-B <sub>4</sub> C 0.48<br>Ni-P-B <sub>4</sub> C-PTFE 0.32 | Ni-P-B <sub>4</sub> C-PTFE hybrid coatings showed the best wear resistance.                            | 85         |
| Ni-P-Al <sub>2</sub> O <sub>3</sub>   | 25-30<br>Ni-P > Ni-P-Al <sub>2</sub> O <sub>3</sub> | Ni-P $\approx 850$ $\text{HV}_{0.05}$ Ni-P-Al <sub>2</sub> O <sub>3</sub> $\approx 1050$ $\text{HV}_{0.05}$ for 15 g L <sup>-1</sup> at $400^{\circ}\text{C}$ | -  | Abrasive wear is the most dominant mechanism of wear for Ni-P-Al <sub>2</sub> O <sub>3</sub> coatings. | 64         |

|  |   |   |  |  |    |
|--|---|---|--|--|----|
| NiB-TiO <sub>2</sub>                         | 10-15<br>NiB< NiB-TiO <sub>2</sub>          | Knoop microhardness NiB≈ 629 HK(25 g), NiB-TiO <sub>2</sub> ≈ 735 HK(25 g) for 2 g L <sup>-1</sup> TiO <sub>2</sub>   | NiB-TiO <sub>2</sub> <NiB                        | TiO <sub>2</sub> nano-powder changes the surface morphology from smooth nodular-like structure to rough nodules.                                   | 71 |
| Ni-P/SiO <sub>2</sub> nanocomposite          | 25-30                                       | Ni-P ≈830 HV <sub>0.3</sub> Ni-P-SiO <sub>2</sub> (10 g/L) ≈700 HV <sub>0.3</sub> at 270°C  | Ni-P>Ni-P-SiO <sub>2</sub> (0.4-0.45)            | Ni-P-SiO <sub>2</sub> shows better wear resistance.  | 87 |
| NiP-WC                                       | ≈16 μm                                      | NiP-WC 19% higher than NiP (as deposited) and 1150 HV <sub>5N</sub> at 400°C  | NiP 0.5<br>NiP-WC 0.13 (at 400°C)                | Formation of Ni <sub>3</sub> P phase and trapping of the reinforced nanoparticles gave higher mechanical properties for annealed coating at 400°C. | 73 |
| Ni-P-Si <sub>3</sub> N <sub>4</sub>          | ≈15   | Ni-P 612 HV <sub>100</sub><br>Ni-P-Si <sub>3</sub> N <sub>4</sub> 784 HV <sub>100</sub> (as-plated) and 1078 HV <sub>100</sub> and 1173 HV <sub>100</sub> respectively at 400°C | Ni-P<<br>Ni-P-Si <sub>3</sub> N <sub>4</sub>     | Abrasion wear mechanism was observed for the coatings.   | 69 |
| NiP-SiC                                      | NiP 30-35<br>NiP-SiC <sub>18g/L</sub> 40-45 | NiP ≈ 350HK0.1<br>NiP-SiC <sub>18g/L</sub> ≈ 500HK0.1   | -  | Surface roughness of the composite coating was smaller than cast Al-Si substrate.  | 67 |
| Ni-P-Si <sub>3</sub> N <sub>4</sub> nanowire | ~ 40-45                                     | Ni-P ~650 HV <sub>200</sub> Ni-P-Si <sub>3</sub> N <sub>4</sub> nanowire 1.5 g/L ~790HV <sub>200</sub> ,  | Ni-P ~1.5<br>Ni-P-Si <sub>3</sub> N <sub>4</sub> | Si <sub>3</sub> N <sub>4</sub> nanowire in the composite coating induce  | 77 |

|   |       |  |  |   |    |
|---|-------|--|--|---|----|
|   |       |  | nanowire 1.5<br>g/L~0.25   | low frictional shear force during wear test, hence it possesses the desirable wear resistance.  |    |
| Ni-P-TiO <sub>2</sub>                               | ~ 20  | Ni-P 414 VHN & 815 VHN (HT at 400°C)<br>Ni-P-TiO <sub>2</sub> 510 VHN & 935 VHN (HT at 400°C)                  | Ni-P 0.35<br>Ni-P-TiO <sub>2</sub> 0.25<br>(load:100gm<br>velocity: 0.1 m/s) | The friction coefficient of Ni-P-TiO <sub>2</sub> nanocomposites increases with increasing load and rotational speed                          | 66 |
| Ni-P-WS <sub>2</sub>                                | ~15   | Ni-P 850 HV <sub>50</sub><br>Ni-P-WS <sub>2</sub> 480 HV <sub>50</sub> (HT at 400°C)                           | Ni-P 0.5-0.7<br>Ni-P-WS <sub>2</sub> 0.1                                     | Soft WS <sub>2</sub> particles act as solid lubricant and reduce friction coefficient and hardness.   | 78 |
| Ni-P-graphene oxide and Ni-P-reduced graphene oxide | ~16.7 | (100 g for 10 s) Ni-P 523 HV and 806 HV (HT)<br>Ni-P- GO 235 HV & 530 HV (HT)<br>Ni-P-rGO 250 HV & 560 HV (HT) | -  | Soft material reinforcement led to decrease in hardness. rGO reinforced EN composite coating offer better corrosion resistance.               | 79 |
| Ni-P-MoS <sub>2</sub> at elevated temperatures      | ~40   | -  | Ni-P-MoS <sub>2</sub> 0.78 (RT)<br>0.27 (at 500°C)                           | Lubricious oxide film composed of NiO and MoO <sub>3</sub> at high temperature improves the tribological properties of the composite coating. | 80 |

#### **1.3.4. Industrial applications**

Electroless metal and composite coatings are commonly used for industrial applications due to formation of coating with uniform thickness regardless of components geometry without any post finishing processes. Hence it is an economically and industrially viable method for coating engineering components and structures, especially with electroless nickel based alloy and composite coatings. These functional deposits are practically applied for many applications in a wide range of industries which include aerospace, automotive, chemical and petroleum, electrical and electronics, marine, military, and mining.

In automotive industry, electroless nickel based composites are coated on parts made of iron, steel, aluminum, copper, brass and other alloys; to protect them from corrosion, to improve their abrasion and wear resistance, and to reduce friction resistance. Hence it is applied on brakes, injectors, clutch, etc. In aerospace industry, it is commonly used on fuel injection pumps, carburetors, ABS systems and clutch systems, defrosting valves, aircraft engines, pump bodies, bolts etc. Recently black electroless nickel plating has developed to serve the vital function of light and energy absorption. It is also used for aesthetic purposes whenever an attractive black finish is required. Since electroless nickel has a wide range of chemical resistance, it can be used in chemical, petroleum and gas industries on different parts such as reactor vessels, retaining rings, gaskets, separator parts, fasteners, bolts, compressor blades, gas turbine absorption equipment, and pumps. Corrosion and abrasion resistance of electroless nickel based coatings is used to make boring equipment and drill bits in mining industry.

Electroless technique is also used to form metallic or composite deposits on non-conducting materials like plastic and ceramics in electronic and computer components. Especially, nickel coatings is suitable to protect the surfaces that contact with cooling water against corrosion, plastic molds against abrasion, on maintenance kits, conducting surfaces, and magnetic memory disks.

## 1.4. Polymer Composite Coatings

Polymeric coatings are made up of natural or synthetic polymers on the substrate formed by curing or polymerization of resins in the form of powder or liquid to the thin surface film. The coatings can be applied on any type of substrate material to provide desired properties and protection. Epoxy, acrylics, polyurethane, poly vinyl chloride, rubber, cellulose and silicone are commonly used in various fields such as protective coatings, household and biomedical appliances, packaging, energy devices and decorative purposes. Different coating techniques have been employed for the polymer coating. Dip coating, spin coating, spray coating, printing and casting are some among them.<sup>3</sup>

Dip coating is a widely used technique for uniform polymer coating on the substrate, which includes dipping of the substrate in resin or polymer melt followed by pulled up in a controlled speed and finally drying. Figure 1.14 shows the steps involved in the dip coating process. The coating thickness and properties can be adjusted by changing resin concentration, dipping time, velocity, number of dips. More the withdrawal speed, the evaporation rate of the solvent is greater than that of the film shrinkage and more will be the coating thickness. At low rates, the trend is inverted due to the drainage of the solution by gravitational force and better adhesion to the substrate.<sup>88</sup>

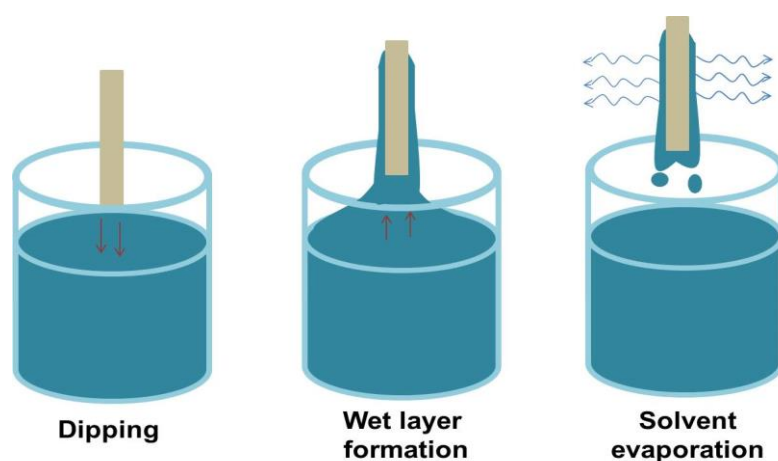


**Figure 1.14:** Three major steps involved in the dip coating process.

The polymer coatings exhibit low barrier properties, low hardness, low scratch resistance, and high flammability compared to metallic and ceramic coatings that restricts their applicability. Similarly, for outdoor coatings, the stability of polymers is inadequate owing to the photodegradation in presence of sunlight. The major disadvantage of polymer covering is their characteristic porousness to allow diffusion of gases and water molecules towards the metal surface. To overcome this scenario, polymer matrix composite coatings reinforced with hard and stiff materials metal oxides.

Polymer composite coatings are applied on the material to achieve functional or decorative layers on the surface. Acrylic, polypyrrole, polyamide, epoxy based coatings for corrosion protection;<sup>89-91</sup> polyurethane for abrasion resistance;<sup>92</sup> nylon for textile and protection from chemicals;<sup>93</sup> polyethylene, polyester, polypropylene, poly vinyl chloride, nylon, etc. for packaging and biocompatible polymers for disease diagnosis and therapy<sup>94</sup> have been developed. The reinforcements based on carbides and silicates, carbon nanotubes and layered materials have been emerged to make polymer composite coatings. The particles of TiO<sub>2</sub>, and ZnO in polyurethane/acrylic silicone rubber coatings are used as UV blocking agents.<sup>95,96</sup> Nuraje et al.<sup>97</sup> introduced graphene to polyurethane coating for improved weathering. Results revealed that the addition of graphene increased resistance to UV degradation.

#### **1.4.1. Polymer composite coatings for corrosion protection**

Polymeric composite coatings have been known for corrosion protection. Protective polymeric coatings are given to the metals and alloys to reduce the corrosion process. The basic concepts of corrosion resistance improved by secondary particles addition are similar to the nickel composite coatings, which are described in previous section 1.3.2. However, depending on the nature of polymer matrix the extent of activity as well as the anti-corrosion mechanism can be varied. Conductive polymers such as polyaniline (PANI), polystyrene, polypyrrole, and polythiophene provide anodic protection to the metal.<sup>98</sup> Polyaniline-clay nanocomposite synthesized by chemical oxidative polymerization showed better barrier properties than the PANI coating.<sup>99</sup> Additionally, the coupling between conducting polymer and metal led to an

improved corrosion resistance. However, most of the polymeric coatings are integrally porous after curing mainly due to solvent evaporation that fails to prevent the corrosive species. Moreover, the coating damage by scratch, wearing or peeling can trigger the corrosion protection failure. Incorporation of nano or micro materials in polymer matrix can significantly improve their performance. These materials can completely or moderately inhibit or heal the coating damages.

Different types of secondary particles have been used for the passive corrosion protection by applying as polymer composite coating. A study on the corrosion resistance of steel by polyaniline-glass flake (10%) composite in epoxy binder indicates the passivation capacity of polyaniline highly influences the coating property.<sup>100</sup> 0.5% of functionalized graphite nanoplatelets (20-40 nm) in epoxy nano-coating with physical barrier characteristics gave an impressive corrosion inhibition on carbon steel.<sup>101</sup> ZrO<sub>2</sub> nanoparticles,<sup>102</sup> silica nanoparticles-covered graphene oxide nanohybrids (SiO<sub>2</sub>-GO),<sup>103</sup> 3-aminopropyltriethoxysilane functionalized GO sheets anchored on Al<sub>2</sub>O<sub>3</sub> nanoparticles<sup>104</sup> and amino functionalized graphene oxide (FGO)<sup>105</sup> considerably improved the corrosion performance of epoxy composite coating. The sacrificial performance zinc rich epoxy coating was enhanced in presence of PANI modified GO. GO-PANI species enhanced the electrical conductivity between steel substrate and zinc particles.<sup>106</sup> The epoxy coatings containing 3-aminopropyltriethoxysilane functionalized fullerene C60 (FC60) and graphene (FG) were evaluated for the tribological as well as anti-corrosion performances. FC60-epoxy coatings showed better tribological behavior than FG-epoxy coating while, corrosion performance was just opposite.<sup>107</sup> Epoxy-MWCNT (multiwalled carbon nanotubes) coating on Al alloy possessed higher wear and corrosion resistance.<sup>108</sup>

#### **1.4.1.1. Inhibitor loaded polymer composite coatings**

The corrosion process on polymer coated metal involves oxidation of metal as anodic reaction and both polymer and oxygen reduction as cathodic reaction. Upon polymer reduction, the release of doped anions and inhibitors can happen, which improve the corrosion resistance of the coatings.<sup>3</sup> The organic adsorptive inhibitors such as 8-hydroxyquinoline, salicylaldehyde, and quinaldic acid can form a thin film of

insoluble complexes in the corrosive environment, which suppress the release of ions from the active intermetallic zones.<sup>109</sup> Williams et al.<sup>110</sup> showed that 2,5-dimercapto-1,3,4- thiadiazolate (DMTD) was effective for inhibiting pitting corrosion of AA2024. In another study by Poznyak et al.<sup>111</sup> explicated the effective corrosion inhibition by quinaldate and 2-mercaptobenzothiazolate owing to the stable layer formation on copper-rich phases of AA2024 alloy. However, the organic compounds are prone to photodegradation, which reduces the inhibiting properties upon time.<sup>112</sup>

Corrosion inhibition efficiency of inorganic anions, transition metal and rare earth oxides were widely investigated. Iron-molybdate complex film generated from PANI-MoO<sub>4</sub><sup>2-</sup> coating on steel substrate offer higher corrosion resistance.<sup>113</sup> Optimum concentration of vanadates in alkyd composite coating contains vanadate loaded Al-Zn-hydrotalcite showed corrosion inhibition.<sup>114</sup> Yasakau et al.<sup>115</sup> investigated the inhibition efficiency of cerium molybdate nanowires added sol-gel coating on aluminium alloy in NaCl solution. The release of both cerium and molybdate ions from the coating reduced the corroding defects. The use of lithium salts has been proposed as a potential replacement for chromates in organic coatings. Lithium salts have shown protective properties on aluminium alloys by the formation of continuous polycrystalline layer of Li-Al layered double hydroxide along with lithium aluminate, which can act as pore filler on the surface under neutral salty environment.<sup>116,117</sup>

#### **1.4.1.2. Container based corrosion inhibitor loading**

One of the ideal strategies to increase the efficiency of inhibitors is that the encapsulation of the healing or inhibiting agents in micro or nanostructured capsules, which are distributed in the polymeric matrix. The capsules actively release the reactive agent and the released species repairs the coating. Different types of containers and methodologies have been used for the corrosion inhibitor loading.

Formerly the polymerization of healing agents loaded in the microcapsules was developed for active corrosion prevention. Dicyclopentadien and epoxy resin are some of the examples. The catalysts for the reaction are distributed in the polymer. When a scratch is formed, the container breaks and the healing agent will be released.<sup>118,119</sup> The schematic representation of healing mechanism is given in Figure 1.15.

Unfortunately, once it gets released and polymerized, further supply of healing agents for long time cannot be achieved. Hence, other external stimuli or the corrosion process itself triggering inhibitor delivery systems were established.

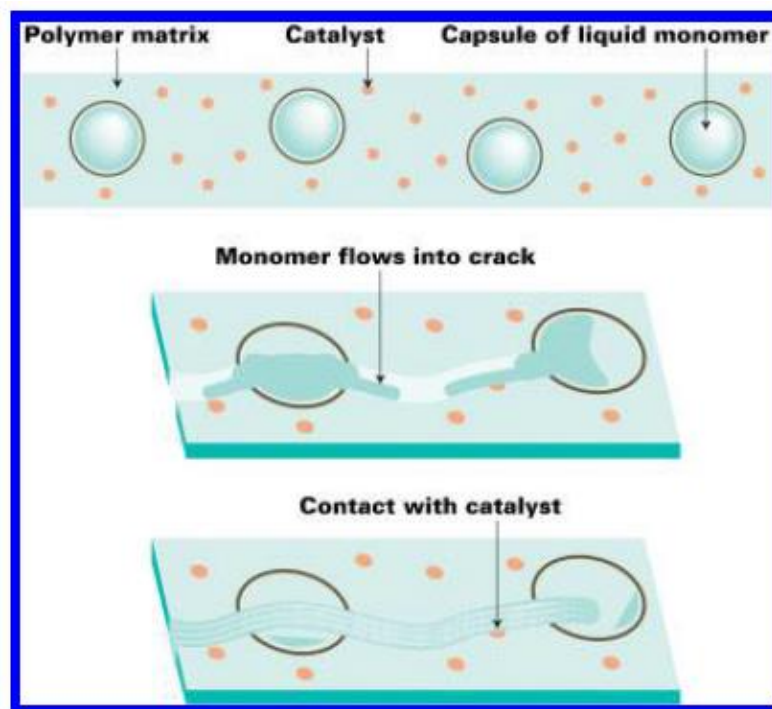


**Figure 1.15:** Microcapsule based self-healing mechanism with encapsulated monomer and a solid catalyst.<sup>120</sup>

In the last decade, different types of containers for controlled releasing of corrosion inhibitor has been established.<sup>121,122</sup> Mesoporous silica,<sup>123,124</sup> polyurethane microcapsules,<sup>125</sup> natural clays<sup>126,127</sup> and layered double hydroxides<sup>128</sup> are widely used. Some of the inhibitor loaded container systems are given in Table 1.5.

**Table 1.5:** List of different container loaded corrosion inhibitor systems in the polymer coatings.

| Coating  | Container   | Inhibitor   | Reference |
|--|---|---|-----------|
| Epoxy  | Poly(urea-formaldehyde)   | endo- dicyclopentadiene tungsten (VI) chloride catalyst with a co-activator (phenylacetylene) | 129       |
| Epoxy on steel   | Poly(urea-formaldehyde)   | Epoxy resin   | 130       |
| Acrylic and polyurethane On copper                             | Halloysite clay nanotubes   | Benzotriazole, 2-mercaptobenzimidazole, and 2-mercaptobenzothiazole                           | 131       |
| Epoxy on steel   | Urea-formaldehyde   | Linseed oil   | 132       |
| PEO coatings on Mg   | Halloysite nanotubes  | Benzotriazole   | 133       |
| Epoxy on steel   | Polystyrene-highly branched polyethylenimine                          | Benzotriazole   | 134       |
| Epoxy and sol-gel coating on aluminium                         | Layered double hydroxides   | Vanadate,phosphate,and2-mercaptobenzothiazolate   | 135       |
| Hybrid sol-gel film on aluminium                               | Layered double hydroxides   | Quinaldate and 2-mercaptobenzothiazolate  | 111       |
| Hybrid SiO <sub>x</sub> /ZrO <sub>x</sub> sol-gel on Al alloy. | Mesoporous Silica Nanoparticles                                       | 1H-benzotriazole  | 136       |
|  | Mesoporous silica nanoparticles modified by supramolecular nanovalves | Benzotriazole   | 137       |
| Silica-zirconia hybrid film on Al                              | SiO <sub>2</sub> -Polyelectrolyte multilayers                         | Benzotriazole   | 138       |
|  | Hollow mesoporous zirconia nanospheres                                | 2-Mercaptobenzothiazole   | 139       |

### 1.4.1.3. Layered double hydroxide (LDH)

Layered double hydroxides (LDH) are synthetic lamellar compounds and commonly known as anionic or hydrotalcite-like clays. The basic chemical formula can be written as  $[M_{1-x}^{2+}M_x^{3+}(OH)_2]^{x+}[(A^{n-})_{\frac{x}{n}} \cdot mH_2O]^{x-}$ , where  $M^{2+}$  is divalent, and  $M^{3+}$  is trivalent cations,  $A^{n-}$  represents anions.<sup>140,141</sup>

$M^{2+}$ : Divalent cation-  $Ca^{2+}$ ,  $Mg^{2+}$ ,  $Zn^{2+}$ ,  $Co^{2+}$ ,  $Ni^{2+}$  etc. ( $Li^{1+}$  can also be used)

$M^{3+}$ : Trivalent cation-  $Al^{3+}$ ,  $Cr^{3+}$ ,  $Fe^{3+}$ ,  $Co^{3+}$ ,  $Ni^{3+}$ ,  $Mn^{3+}$  etc.

$A^{n-}$ : Inter layer anion-  $Cl^-$ ,  $NO_3^-$ ,  $ClO_4^-$ ,  $CO_3^{2-}$ ,  $SO_4^{2-}$  etc.

The overall charge of host layers is positive and hydrated exchangeable anions for charge neutralization located in the interlayer gallery. The LDH structure consists of edge-sharing  $M(OH)_6$  octahedral and the vertexes containing hydroxide group connect to form two dimensional sheets. Figure 1.16 represents the typical brucite like structure of LDH.

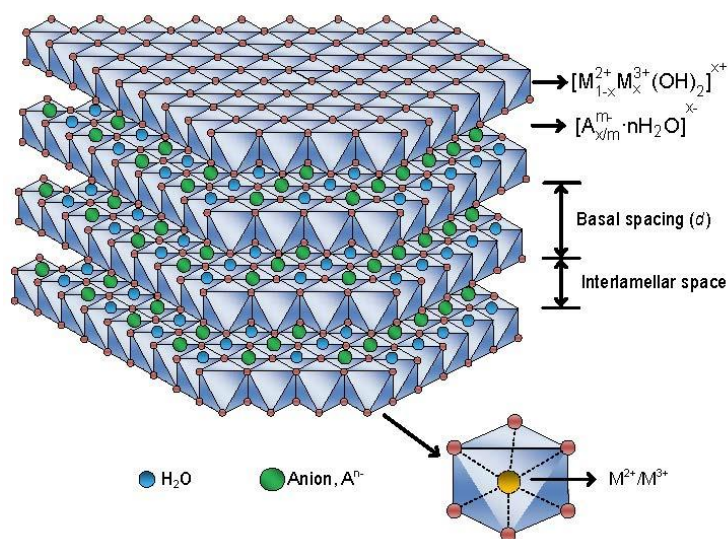


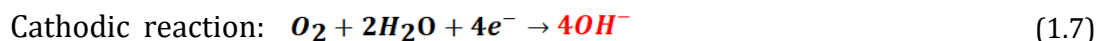
**Figure 1.16:** Structure of layered double hydroxide.<sup>142</sup>

LDH has wide applications as catalyst, precursors, acid absorbents, energy storage materials, optics, and bio-active nano composites owing to their flexibility to tune the metal-anion combinations within the layered structures. Corrosion protection is one of the major applications, especially with Zn-Al, Ni-Al and Mg-Al

based LDHs.<sup>143-147</sup> Mechanical and flame retardant properties can be achieved by the addition of halogen-free and environmental-friendly LDH as reinforcement.<sup>148</sup> Nano-Mg-Al-layered double hydroxide on cotton gained enhanced mechanical, UV protection and flame retardancy at low cytotoxicity level.<sup>149</sup> LDH-poly(lactide-co-glycolic acid) (PLGA) film composite is relevant for the controlled release of antibiotics.<sup>150</sup> Controlled drug delivery is possible by the release of drugs intercalated between LDH layers by easy preparation method and good biocompatibility.<sup>151</sup> LDH has been investigated frequently for textile dye effluent removal<sup>152</sup> and fiber-based flexible super-capacitors or energy storage devices.<sup>153</sup>

### 1.5. Corrosion Sensing

Corrosion sensing is one of the most effective corrosion protection strategies like corrosion retardation or inhibition. Corrosion sensing coatings are a type of active coatings, which monitor the corrosion process on a material at the early stages of deterioration. The material deterioration by corrosion is an electrochemical process that influences local pH change on the material. Electrochemical reactions associated with corrosion process are given as equations 1.7-1.9.



At the cathodic region, reduction reaction takes place and OH<sup>-</sup> will be released, which increases the local pH. At the anodic region, oxidation reactions take place and H<sup>+</sup> will be released, which decreases the local pH. Sensing of these reactions by pH indicators can be utilized for the early detection of corrosion process. Fluorescent pH indicators are also been developed for corrosion sensing applications.<sup>154</sup>

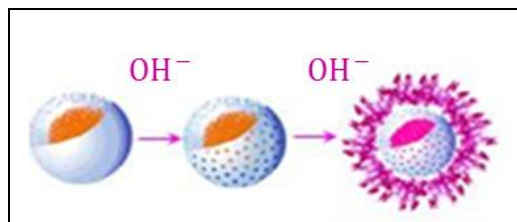
The pH-sensing compounds accompanied by colour change are generally used to identify the pH increase related to cathodic reaction. Phenolphthalein is one of the suitable examples for acid-base indicator, which show pink coloration at the alkaline pH starting from 8.2 and bright purple at very high pH. Different corrosion sensing indicators used to develop the polymer composite coatings on metals are given in

Table 1.6. The sensing compound should be uniformly distributed as well as compatible to the polymer matrix without reducing the barrier properties. However, as in the case of corrosion inhibitors, the direct contact between pH indicators and the matrix could reduce the coatings properties and trigger the corrosion.

**Table 1.6:** Corrosion sensing polymer composite coatings.

| Substrate             | Indicator/Inhibitor  | Coating                              | References |
|-----------------------|--|--------------------------------------|------------|
| Aluminum<br>AA2024-T3 | Phenolphthalein,<br>Bromothymol blue   | Acrylic                              | 155        |
| Aluminum              | 8-hydroxyquinoline-5-sulfonic acid   | Polyester,<br>epoxy,<br>Polyurethane | 155        |
| Aluminum<br>Al7075    | 8-hydroxyquinoline (oxine)   | Acrylic, epoxy                       | 156        |
| Mg-AZ31,<br>Al-2024   | Phenolphthalein  | Acrylic                              | 157        |
| Aluminum<br>Al2024T3  | Lumogallion, <i>N,N'</i> -bis-(salicylidene)-<br>2,3-diaminobenzofuran (SABF) and<br>Phen Green™ | Epoxy/polyami<br>de coating          | 158        |

Container based composite coating system developed by encapsulation of active compounds in the container can provide a sensible on-time response. Porous silica, polyurea, urea-formaldehyde, and melamine-formaldehyde microcapsules have been used for encapsulation of phenolphthalein.<sup>157,159</sup> Schematic representation of corrosion sensing by microcapsule loaded phenolphthalein is given in Figure 1.17.



**Figure 1.17:** Schematic illustration of microcapsule encapsulated phenolphthalein with pH, an indication of corrosion.<sup>160</sup>

## **1.6. Scope and Objectives**

Light metals and alloys are used in automotive, aerospace, structural and industrial fields owing to their unique characteristics of low weight and high specific strength. Though, the deterioration of materials followed by the properties during continuous usage has substantial social and economic impact. Surface modifications and coatings of metallic materials and structures are one of the most important techniques for improving the functional performance of the engineering components in real time applications and service in extreme environmental conditions. Currently, several methods like surface hardening, heat treatment, and surface coatings are available to improve the exterior characteristics. However, the surface coating is an important process with wide acceptance to give a better appearance, properties, and advanced functionalities. Multifunctional coatings with the primary objectives of wear and corrosion resistance can be achieved by applying thin layers of less reactive metals, alloys, polymers or composites on the metal surface. Different methods have been adopted to develop the coatings such as electroless process, electroplating, physical and chemical vapour deposition, dip coating, spray coating etc.

The development of composite/nanocomposite coatings on various surfaces based on electroless process has much interest among researchers due to their enhanced mechanical, tribological, electrical, and anti-corrosive properties compared with their metallic or alloy counterparts. However, properties of the product depend upon both the nature of secondary particle and the specific characteristics of the matrix used. Electroless nickel as well as polymeric matrix composite coatings are widely used to improve the properties of the metal. Depending on the requirement of an end product, different reinforcements can be selected. The reinforcement can be a one, two, three or zero dimensional species. Among the nanoparticle secondary materials, ceria ( $\text{CeO}_2$ ) shows remarkable role in improving both mechanical and electrochemical properties. On the other hand, two dimensional layered double hydroxide (LDH) is well known for their anti-corrosive properties due to unique anion exchange behavior. In the present thesis, few composite coatings are aimed based on metal and polymer matrix systems for various applications and studied the

characteristics based on morphological, structural, tribological, anti-corrosive and corrosion sensing properties.

The major objectives are:

- Development of electroless Nickel boride (Ni-B) alloy and Ni-B-CeO<sub>2</sub> composite coating on aluminium A356 alloy (composition: Al-7Si-0.35Mg in wt.%) to investigate the surface morphology, coating composition, corrosion resistance, microhardness, and tribology.
- Formation of Ni-B-LDH composite coating on A356 alloy and optimisation of coating parameters to get better wear and corrosion resistance.
- Synthesis of inhibitor loaded LDH by vanadate intercalation followed by nanoceria decoration for higher anti-corrosive properties.
- Development of phenolphthalein loaded LDH container to make polymer composite coating on light alloys for corrosion sensing applications.

## References

- 1 C. Kang, H. Lu, S. Yuan, D. Hong, K. Yan and B. Liang, *Chem. Eng. J.*, 2012, **203**, 1–8.
- 2 S. S. Djokić, in *Modern Aspects of Electrochemistry*, Kluwer Academic Publishers, Boston, pp. 51–133.
- 3 A. Kausar, *J. Macromol. Sci. Part A*, 2018, **55**, 440–448.
- 4 A. Brenner, inventor; Riddell Grace E, *United States Pat.*
- 5 H. Mazaheri and S. R. Allahkaram, *Appl. Surf. Sci.*, 2012, **258**, 4574–4580.
- 6 S. B. Sharma, R. C. Agarwala, V. Agarwala and S. Ray, *Mater. Manuf. Process.*, 2002, **17**, 637–649.
- 7 G. Jiaqiang, W. Yating, L. Lei and H. Wenbin, *Mater. Lett.*, 2005, **59**, 391–394.
- 8 A. Araghi and M. H. Paydar, *Mater. Des.*, 2010, **31**, 3095–3099.
- 9 M. Roy, in *Surface Engineering for Enhanced Performance against Wear*, Springer Vienna, Vienna, 2013, pp. 45–78.
- 10 R. Yadav and K. Balasubramanian, *RSC Adv.*, 2015, **5**, 24990–24996.
- 11 T. S. N. Sankara Narayanan, S. K. Seshadri, T. S. N. Sankara Narayanan and S. K. Seshadri, in *Wiley Encyclopedia of Composites*, John Wiley & Sons, Inc., Hoboken, NJ, USA, 2012.

- 12 F. Muench, A. Eils, M. E. Toimil-Molares, U. H. Hossain, A. Radetinac, C. Stegmann, U. Kunz, S. Lauterbach, H.-J. Kleebe and W. Ensinger, *Surf. Coatings Technol.*, 2014, **242**, 100–108.
- 13 G. O. Mallory, J. B. Hajdu and American Electroplaters and Surface Finishers Society., *Electroless plating : fundamentals and applications*, The Society, 1990.
- 14 Z.-H. Xie, F. Chen, S.-R. Xiang, J.-L. Zhou, Z.-W. Song and G. Yu, *J. Electrochem. Soc.*, 2014, **162**, D115–D123.
- 15 V. Vitry, A.-F. Kanta, J. Dille and F. Delaunois, *Surf. Coatings Technol.*, 2012, **206**, 3444–3449.
- 16 A.-F. Kanta, M. Poelman, V. Vitry and F. Delaunois, *J. Alloys Compd.*, 2010, **505**, 151–156.
- 17 R. Ambat and W. Zhou, *Surf. Coatings Technol.*, 2004, **179**, 124–134.
- 18 F. Wang, S. Arai and M. Endo, *Carbon N. Y.*, 2005, **43**, 1716–1721.
- 19 S. Arai, M. Endo, S. Hashizume and Y. Shimojima, *Electrochem. commun.*, 2004, **6**, 1029–1031.
- 20 J. H. Kim, J. D. Kim, H. M. Park, S. B. Lee, J. W. Yi and S. Il Jung, *Appl. Surf. Sci.*, 2013, **265**, 527–531.
- 21 R. C. Agarwala and V. Agarwala, *Sadhana*, 2003, **28**, 475–493.
- 22 J. Sudagar, J. Lian and W. Sha, *J. Alloys Compd.*, 2013, **571**, 183–204.
- 23 N. Guglielmi, *J. Electrochem. Soc.*, 1972, **119**, 1009.
- 24 P. Berçot, E. Peña-Muñoz and J. Pagetti, *Surf. Coatings Technol.*, 2002, **157**, 282–289.
- 25 P. Gyftou, M. Stroumbouli, E. A. Pavlatou, P. Asimidis and N. Spyrellis, *Electrochim. Acta*, 2005, **50**, 4544–4550.
- 26 A. M. J. Kariapper and J. Foster, *Trans. IMF*, 1974, **52**, 87–91.
- 27 J. P. Celis, *J. Electrochem. Soc.*, 1987, **134**, 1402.
- 28 J. Fransaer, *J. Electrochem. Soc.*, 1992, **139**, 413.
- 29 H. Matsubara, Y. Abe, Y. Chiba, H. Nishiyama, N. Saito, K. Hodouchi and Y. Inoue, *Electrochim. Acta*, 2007, **52**, 3047–3052.
- 30 J. Hosseini and A. Bodaghi, *Surf. Eng.*, 2013, **29**, 183–189.

- 31 C. S. Lin, C. Y. Lee, C. F. Chang and C. H. Chang, *Surf. Coatings Technol.*, 2006, **200**, 3690–3697.
- 32 R. K. Balaraju JN, *Electroless deposition and characterization of high phosphorus13; Ni-P-Si3N4 composite coatings.*, Electrochemical Science Group, 2007.
- 33 J. N. Balaraju, T. S. N. S. Narayanan and S. K. Seshadri, *Mater. Res. Bull.*, 2006, **41**, 847–860.
- 34 I. Apachitei, F. . Tichelaar, J. Duszczyk and L. Katgerman, *Surf. Coatings Technol.*, 2002, **149**, 263–278.
- 35 B. Bozzini, C. Martini, P. L. Cavallotti and E. Lanzoni, *Wear*, 1999, **225–229**, 806–813.
- 36 T. Rabizadeh and S. R. Allahkaram, *Mater. Des.*, 2011, **32**, 133–138.
- 37 M. Momenzadeh and S. Sanjabi, *Mater. Corros.*, 2011, **63**, n/a-n/a.
- 38 S. Afroukhteh, C. Dehghanian and M. Emamy, *Appl. Surf. Sci.*, 2012, **258**, 2597–2601.
- 39 C. Liu and Q. Zhao, *Langmuir*, 2011, **27**, 9512–9519.
- 40 P. Sahoo and S. K. Das, *Mater. Des.*, 2011, **32**, 1760–1775.
- 41 Z. Abdel Hamid and M. . Abou Elkhair, *Mater. Lett.*, 2002, **57**, 720–726.
- 42 K. Zielińska, A. Stankiewicz and I. Szczygieł, *J. Colloid Interface Sci.*, 2012, **377**, 362–367.
- 43 F. F. Xia, C. Liu, F. Wang, M. H. Wu, J. D. Wang, H. L. Fu and J. X. Wang, *J. Alloys Compd.*, 2010, **490**, 431–435.
- 44 A. Farzaneh, M. Mohammadi, M. Ehteshamzadeh and F. Mohammadi, *Appl. Surf. Sci.*, 2013, **276**, 697–704.
- 45 M. A. Shoeib, M. M. Kamel, S. M. Rashwan and O. M. Hafez, *Surf. Interface Anal.*, 2015, **47**, 672–680.
- 46 C.-K. Lee, *Int. J. Electrochem. Sci*, 2012, **7**, 12941–12954.
- 47 J. Balaraju, T. Sankara Narayanan and S. Seshadri, *J. Solid State Electrochem.*, 2001, **5**, 334–338.
- 48 X. T. Yuan, Z. Q. Hua, L. Wang, D. B. Sun and S. L. Chen, *Appl. Mech. Mater.*, 2011,

- 66–68, 1668–1675.
- 49 X. Yu, H. Wang, Z. Yang, P. Yin and X. Xin, *Appl. Surf. Sci.*, 2000, **158**, 335–339.
- 50 H. Ashassi-Sorkhabi and M. Es'haghi, *Corros. Sci.*, 2013, **77**, 185–193.
- 51 R. Arghavanian and N. Parvini-Ahmadi, *J. Solid State Electrochem.*, 2011, **15**, 2199–2204.
- 52 M. Islam, M. R. Azhar, N. Fredj, T. D. Burleigh, O. R. Oloyede, A. A. Almajid and S. Ismat Shah, *Surf. Coatings Technol.*, 2015, **261**, 141–148.
- 53 X. Shu, Y. Wang, C. Liu, A. Aljaafari and W. Gao, *Surf. Coatings Technol.*, 2015, **261**, 161–166.
- 54 Y. W. Song, D. Y. Shan and E. H. Han, *Electrochim. Acta*, 2008, **53**, 2135–2143.
- 55 J. N. Balaraju, Kalavati and K. S. Rajam, *Surf. Coatings Technol.*, 2006, **200**, 3933–3941.
- 56 M. Mohammadi and M. Ghorbani, *J. Coatings Technol. Res.*, 2011, **8**, 527–533.
- 57 E. Georgiza, V. Gouda and P. Vassiliou, *Surf. Coatings Technol.*, 2017, **325**, 46–51.
- 58 J. F. Archard, *J. Appl. Phys.*, 1953, **24**, 981–988.
- 59 A. Szasz, D. J. Fabian, Z. Paal and J. Kojnok, *J. Non. Cryst. Solids*, 1988, **103**, 21–27.
- 60 B. Oraon, G. Majumdar and B. Ghosh, *Mater. Des.*, 2008, **29**, 1412–1418.
- 61 M. Palaniappa and S. K. Seshadri, *Wear*, 2008, **265**, 735–740.
- 62 S. S. Krishnaveni K, Narayanan TS, *Mater Chem Phys.*, 2006, **99**, 300–308.
- 63 V. V. . Reddy, B. Ramamoorthy and P. K. Nair, *Wear*, 2000, **239**, 111–116.
- 64 S. Alirezai, S. M. Monirvaghefi, M. Salehi and A. Saatchi, *Wear*, 2007, **262**, 978–985.
- 65 P. Makkar, R. C. Agarwala and V. Agarwala, *Ceram. Int.*, 2013, **39**, 9003–9008.
- 66 P. Makkar, R. C. Agarwala and V. Agarwala, *Adv. Powder Technol.*, 2014, **25**, 1653–1660.
- 67 M. Franco, W. Sha, S. Malinov and R. Rajendran, *Surf. Coatings Technol.*, 2013, **235**, 755–763.
- 68 M. Franco, W. Sha, S. Malinov and H. Liu, *Wear*, 2014, **317**, 254–264.
- 69 U. Matik, *Surf. Coatings Technol.*, 2016, **302**, 528–534.
- 70 H. Ma, Z. Liu, F. Tian and H. Sun, *J. Alloys Compd.*, 2008, **450**, 348–351.

- 71 X. Shu, Y. Wang, C. Liu and W. Gao, *Mater. Technol.*, 2015, **30**, A41–A45.
- 72 C. Zhao and Y. Yao, *J. Mater. Eng. Perform.*, 2014, **23**, 193–197.
- 73 Y. Y. Liu, J. Yu, H. Huang, B. H. Xu, X. L. Liu, Y. Gao and X. L. Dong, *Surf. Coatings Technol.*, 2007, **201**, 7246–7251.
- 74 D. EKMEKÇİ and F. BÜLBÜL, *Bull. Mater. Sci.*, 2015, **38**, 761–768.
- 75 K. Kato, *Wear*, 2000, **241**, 151–157.
- 76 L. Y. Wang, J. P. Tu, W. X. Chen, Y. C. Wang, X. K. Liu, C. Olk, D. H. Cheng and X. B. Zhang, *Wear*, 2003, **254**, 1289–1293.
- 77 S. Wang, X. Huang, M. Gong and W. Huang, *Appl. Surf. Sci.*, 2015, **357**, 328–332.
- 78 I. Sivandipoor and F. Ashrafizadeh, *Appl. Surf. Sci.*, 2012, **263**, 314–319.
- 79 M. H. Sadhir, M. Saranya, M. Aravind, A. Srinivasan, A. Siddharthan and N. Rajendran, *Appl. Surf. Sci.*, 2014, **320**, 171–176.
- 80 Z. Li, J. Wang, J. Lu and J. Meng, *Appl. Surf. Sci.*, 2013, **264**, 516–521.
- 81 S. J. Shaffer and M. J. Rogers, *Wear*, 2007, **263**, 1281–1290.
- 82 L. Reinert, F. Lasserre, C. Gachot, P. Grützmacher, T. MacLucas, N. Souza, F. Mücklich and S. Suarez, *Sci. Rep.*, 2017, **7**, 42873.
- 83 Y. Wu, B. Shen, L. Liu and W. Hu, *Wear*, 2006, **261**, 201–207.
- 84 Y. T. Wu, L. Lei, B. Shen and W. B. Hu, *Surf. Coatings Technol.*, 2006, **201**, 441–445.
- 85 A. P. Dooz, S. Akhavan and A. Tahviliyan, *Int. J. Eng. Innov. Res.*, **3**, 2277–5668.
- 86 M. Mohammadi, M. Ghorbani and A. Azizi, *J. Coatings Technol. Res.*, 2010, **7**, 697–702.
- 87 Y. de Hazan, D. Zimmermann, M. Z'graggen, S. Roos, C. Aneziris, H. Bollier, P. Fehr and T. Graule, *Surf. Coatings Technol.*, 2010, **204**, 3464–3470.
- 88 P. Nguyen-Tri, T. A. Nguyen, P. Carriere and C. Ngo Xuan, *Int. J. Corros.*, 2018, **2018**, 1–19.
- 89 S. Sathiyarayanan, S. S. Azim and G. Venkatachari, *Appl. Surf. Sci.*, 2006, **253**, 2113–2117.
- 90 V. Q. Trung, P. Van Hoan, D. Q. Phung, L. M. Duc and L. T. T. Hang, *J. Exp. Nanosci.*, 2014, **9**, 282–292.

- 91 X. Shi, T. A. Nguyen, Z. Suo, Y. Liu and R. Avci, *Surf. Coatings Technol.*, 2009, **204**, 237–245.
- 92 R. P. Singh, N. S. Tomer and S. V. Bhadraiah, *Polym. Degrad. Stab.*, 2001, **73**, 443–446.
- 93 P. S. Hess, *U.S. Pat.*
- 94 N. Wang, K. Burugapalli, W. Song, J. Halls, F. Moussy, A. Ray and Y. Zheng, *Biomaterials*, 2013, **34**, 888–901.
- 95 M. S. Lowry, D. R. Hubble, A. L. Wressell, M. S. Vratsanos, F. R. Pepe and C. R. Hegedus, *J. Coatings Technol. Res.*, 2008, **5**, 233–239.
- 96 F. Madidi, G. Momen and M. Farzaneh, *Adv. Mater. Sci. Eng.*, 2016, **2016**, 1–8.
- 97 N. Nuraje, S. Khan, ... H. M.-I. P. and undefined 2013, *downloads.hindawi.com*.
- 98 M. Rohwerder, *Int. J. Mater. Res.*, 2009, **100**, 1331–1342.
- 99 J.-M. Yeh, S.-J. Liou, C.-Y. Lai, P.-C. Wu and T.-Y. Tsai, *Chem. Mater.*, 2001, **13**, 1131–1136.
- 100 S. Sathiyarayanan, S. Syed Azim and G. Venkatachari, *Electrochim. Acta*, 2008, **53**, 2087–2094.
- 101 S. Mohammadi, F. Afshar Taromi, H. Shariatpanahi, J. Neshati and M. Hemmati, *J. Ind. Eng. Chem.*, 2014, **20**, 4124–4139.
- 102 M. Behzadnasab, S. M. Mirabedini, K. Kabiri and S. Jamali, *Corros. Sci.*, 2011, **53**, 89–98.
- 103 B. Ramezanzadeh, Z. Haeri and M. Ramezanzadeh, *Chem. Eng. J.*, 2016, **303**, 511–528.
- 104 Z. Yu, H. Di, Y. Ma, L. Lv, Y. Pan, C. Zhang and Y. He, *Appl. Surf. Sci.*, 2015, **351**, 986–996.
- 105 B. Ramezanzadeh, S. Niroumandrad, A. Ahmadi, M. Mahdavian and M. H. M. Moghadam, *Corros. Sci.*, 2016, **103**, 283–304.
- 106 B. Ramezanzadeh, M. H. Mohamadzadeh Moghadam, N. Shohani and M. Mahdavian, *Chem. Eng. J.*, 2017, **320**, 363–375.
- 107 D. Liu, W. Zhao, S. Liu, Q. Cen and Q. Xue, *Surf. Coatings Technol.*, 2016, **286**, 354–364.

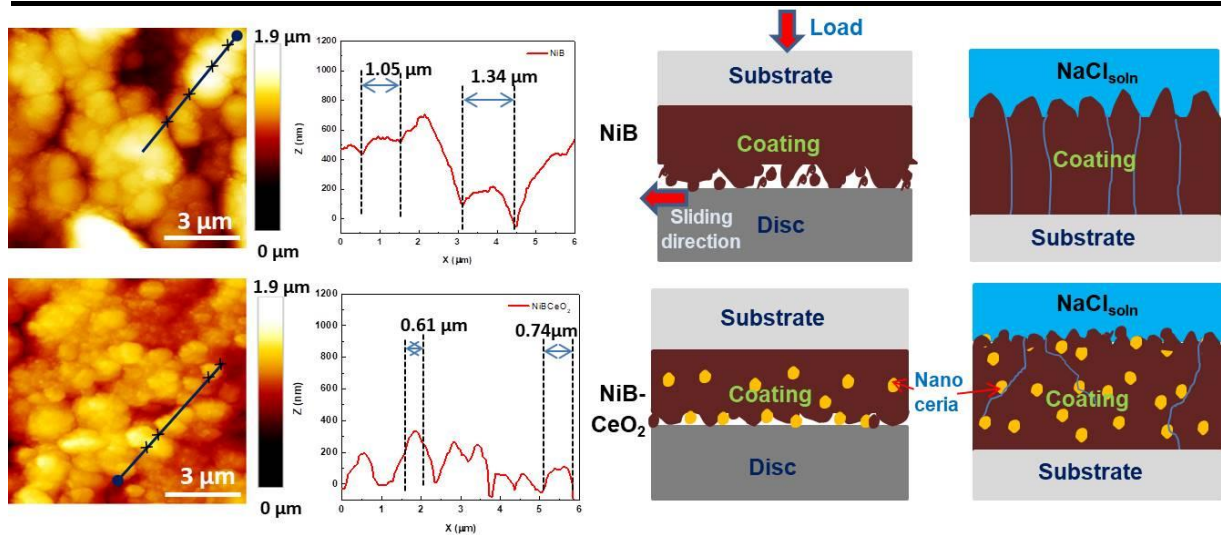
- 108 N. W. Khun, B. C. R. Troconis and G. S. Frankel, *Prog. Org. Coatings*, 2014, **77**, 72–80.
- 109 M. L. Zheludkevich, K. A. Yasakau, S. K. Poznyak and M. G. S. Ferreira, *Corros. Sci.*, 2005, **47**, 3368–3383.
- 110 G. Williams, A. J. Coleman and H. N. McMurray, *Electrochim. Acta*, 2010, **55**, 5947–5958.
- 111 S. K. Poznyak, J. Tedim, L. M. Rodrigues, A. N. Salak, M. L. Zheludkevich, L. F. P. Dick and M. G. S. Ferreira, *ACS Appl. Mater. Interfaces*, 2009, **1**, 2353–2362.
- 112 D. Snihirova, S. V. Lamaka and M. F. Montemor, in *Smart Composite Coatings and Membranes*, Elsevier, 2016, pp. 85–121.
- 113 V. Karpakam, K. Kamaraj, S. Sathiyarayanan, G. Venkatachari and S. Ramu, *Electrochim. Acta*, 2011, **56**, 2165–2173.
- 114 J. M. Vega, N. Granizo, D. de la Fuente, J. Simancas and M. Morcillo, *Prog. Org. Coatings*, 2011, **70**, 213–219.
- 115 K. A. Yasakau, S. Kallip, M. L. Zheludkevich and M. G. S. Ferreira, *Electrochim. Acta*, 2013, **112**, 236–246.
- 116 R. G. Buchheit, M. D. Bode and G. E. Stoner, *CORROSION*, 1994, **50**, 205–214.
- 117 P. Visser, Y. Liu, X. Zhou, T. Hashimoto, G. E. Thompson, S. B. Lyon, L. G. J. van der Ven, A. J. M. C. Mol and H. A. Terry, *Faraday Discuss.*, 2015, **180**, 511–526.
- 118 S. R. White, N. R. Sottos, P. H. Geubelle, J. S. Moore, M. R. Kessler, S. R. Sriram, E. N. Brown and S. Viswanathan, *Nature*, 2001, **409**, 794–797.
- 119 S. H. Cho, S. R. White and P. V. Braun, *Adv. Mater.*, 2009, **21**, 645–649.
- 120 T. C. Mauldin and M. R. Kessler, *Int. Mater. Rev.*, 2010, **55**, 317–346.
- 121 E. V. Skorb, A. G. Skirtach, D. V. Sviridov, D. G. Shchukin and H. Möhwald, *ACS Nano*, 2009, **3**, 1753–1760.
- 122 D. G. Shchukin, *Polym. Chem.*, 2013, **4**, 4871.
- 123 D. Borisova, H. Möhwald and D. G. Shchukin, *ACS Nano*, 2011, **5**, 1939–1946.
- 124 E. V. Skorb, D. Fix, D. V. Andreeva, H. Möhwald and D. G. Shchukin, *Adv. Funct. Mater.*, 2009, **19**, 2373–2379.
- 125 V. V. Gite, P. D. Tatiya, R. J. Marathe, P. P. Mahulikar and D. G. Hundiware, *Prog.*

- Org. Coatings*, 2015, **83**, 11–18.
- 126 E. Abdullayev, R. Price, D. Shchukin and Y. Lvov, *ACS Appl. Mater. Interfaces*, 2009, **1**, 1437–1443.
- 127 A. Ghazi, E. Ghasemi, M. Mahdavian, B. Ramezanzadeh and M. Rostami, *Corros. Sci.*, 2015, **94**, 207–217.
- 128 J. Tedim, S. K. Poznyak, A. Kuznetsova, D. Raps, T. Hack, M. L. Zheludkevich and M. G. S. Ferreira, *ACS Appl. Mater. Interfaces*, 2010, **2**, 1528–1535.
- 129 L. Haiyan, W. Rongguo and L. Wenbo, *J. Reinf. Plast. Compos.*, 2012, **31**, 924–932.
- 130 Y. Zhao, W. Zhang, L. Liao, S. Wang and W. Li, *Appl. Surf. Sci.*, 2012, **258**, 1915–1918.
- 131 E. Abdullayev, V. Abbasov, A. Tursunbayeva, V. Portnov, H. Ibrahimov, G. Mukhtarova and Y. Lvov, *ACS Appl. Mater. Interfaces*, 2013, **5**, 4464–4471.
- 132 A. Pilbáth, T. Szabó, J. Telegdi and L. Nyikos, *Prog. Org. Coatings*, 2012, **75**, 480–485.
- 133 M. Sun, A. Yerokhin, M. Y. Bychkova, D. V. Shtansky, E. A. Levashov and A. Matthews, *Corros. Sci.*, 2016, **111**, 753–769.
- 134 G. L. Li, M. Schenderlein, Y. Men, H. Möhwald and D. G. Shchukin, *Adv. Mater. Interfaces*, 2014, **1**, 1300019.
- 135 J. Tedim, S. K. Poznyak, A. Kuznetsova, D. Raps, T. Hack, M. L. Zheludkevich and M. G. S. Ferreira, *ACS Appl. Mater. Interfaces*, 2010, **2**, 1528–1535.
- 136 D. Borisova, H. Möhwald and D. G. Shchukin, *ACS Nano*, 2011, **5**, 1939–1946.
- 137 T. Chen and J. Fu, *Nanotechnology*, 2012, **23**, 235605.
- 138 M. L. Zheludkevich, D. G. Shchukin, K. A. Yasakau, H. Möhwald and M. G. S. Ferreira, *Chem. Mater.*, 2007, **19**, 402–411.
- 139 A. Chenan, S. Ramya, R. P. George and U. Kamachi Mudali, *Ceram. Int.*, 2014, **40**, 10457–10463.
- 140 V. R. L. Constantino and T. J. Pinnavaia, *Inorg. Chem.*, 1995, **34**, 883–892.
- 141 S. P. Newman and W. Jones, *New J. Chem.*, 1998, **22**, 105–115.
- 142 J. Tronto, A. Cludia, Z. Naal and J. Barros Valim, in *Materials Science - Advanced Topics*, InTech, 2013.

- 143 M. Zhou, L. Yan, H. Ling, Y. Diao, X. Pang, Y. Wang and K. Gao, *Appl. Surf. Sci.*, 2017, **404**, 246–253.
- 144 M. L. Zheludkevich, S. K. Poznyak, L. M. Rodrigues, D. Raps, T. Hack, L. F. Dick, T. Nunes and M. G. S. Ferreira, *Corros. Sci.*, 2010, **52**, 602–611.
- 145 T. Stimpfling, F. Leroux and H. Hintze-Bruening, *Colloids Surfaces A Physicochem. Eng. Asp.*, 2014, **458**, 147–154.
- 146 L. Wang, Q. Zong, W. Sun, Z. Yang and G. Liu, *Corros. Sci.*, 2015, **93**, 256–266.
- 147 J. Tedim, A. Kuznetsova, A. N. Salak, F. Montemor, D. Snihirova, M. Pilz, M. L. Zheludkevich and M. G. S. Ferreira, *Corros. Sci.*, 2012, **55**, 1–4.
- 148 C. M. Becker, A. D. Gabbardo, F. Wypych and S. C. Amico, *Compos. Part A Appl. Sci. Manuf.*, 2011, **42**, 196–202.
- 149 S. Barik, A. Khandual, L. Behera, S. K. Badamali and A. Luximon, *Cellulose*, 2017, **24**, 1107–1120.
- 150 M. Chakraborti, J. K. Jackson, D. Plackett, S. E. Gilchrist and H. M. Burt, *J. Mater. Sci. Mater. Med.*, 2012, **23**, 1705–13.
- 151 S. Hasan, H. Al Ali, M. Al-Qubaisi, M. Zobir Hussein, M. Ismail, Z. Zainal and M. Nazrul Hakim, *Int. J. Nanomedicine*, 2012, **7**, 3351–63.
- 152 F. Z. Mahjoubi, A. Khalidi, M. Abdennouri and N. Barka, *Desalin. Water Treat.*, 2016, **57**, 21564–21576.
- 153 P. Guoxiang, X. Xinhui, L. Jingshan, C. Feng, Y. Zhihong and F. Hongjin, *Appl. Clay Sci.*, 2014, **102**, 28–32.
- 154 A. Augustyniak and W. Ming, *Prog. Org. Coatings*, 2011, **71**, 406–412.
- 155 J. Zhang and G. S. Frankel, *CORROSION*, 1999, **55**, 957–967.
- 156 R. E. Johnson, M. G. Durrett and V. S. Agarwala, .
- 157 F. Maia, J. Tedim, A. C. Bastos, M. G. S. Ferreira and M. L. Zheludkevich, *RSC Adv.*, 2014, **4**, 17780.
- 158 M. P. Sibi and Z. Zong, *Prog. Org. Coatings*, 2003, **47**, 8–15.
- 159 F. Maia, J. Tedim, A. C. Bastos, M. G. S. Ferreira and M. L. Zheludkevich, *Nanotechnology*, 2013, **24**, 415502.
- 160 W. Li, J. W. Buhrow, S. T. Jolley, L. M. Calle, J. S. Hanna and J. W. Rawlins, .

## Chapter 2

### *Effect of nanoceria in electroless nickel boride coating on Aluminium A356 alloy*



#### **Abstract**

*Nickel-based coatings on aluminium with specific surface properties are of great interest for anti-corrosive, anti-wearing, and self-lubricating applications. In the present study electroless Ni-B alloy and Ni-B-CeO<sub>2</sub> nanocomposite coatings were formed on 356 aluminium alloy surfaces. Ceria incorporation to Ni-B coating reduces the average nodular grain size from 1150 nm to 650 nm and Ni crystallite size from 15 nm to 9.97 nm. Ni-B-CeO<sub>2</sub> nanocomposite shows remarkable improvement in microhardness of ~ 684 VHN compared to pure Ni-B coating with ~ 424 VHN. Enhanced wear resistance and reduction in friction coefficient are observed for the nanocomposite coatings compared to 356 Al alloy and Ni-B alloy coating. Potentiodynamic polarization measurements show a remarkable reduction in the corrosion current density for ceria added nanocomposite coating ( $2.48 \times 10^{-6} \text{ A cm}^{-2}$ ) than that of the particle-free counterpart ( $11.18 \times 10^{-6} \text{ A cm}^{-2}$ ). Uniform Ni-B-CeO<sub>2</sub> composite coating was obtained on centrifugally cast A356 (Al-7Si-0.35Mg wt.%) aluminium alloy cylinder liners which have potential applications in automotive systems.*

## **2.1. Introduction**

Aluminium alloys are used extensively in various sectors with a range of products from basic infrastructure to aerospace applications. However, the degradation of them by continuous use and under the influence of aggressive environment like sea water has significant social and economic concern. It is a global issue that severely affects a large number of industries such as construction, automotive, oil refinery, shipping, and general engineering. The protection of them from corrosion and wear has been an active area of research under materials science for many years. Surface coatings with thin layers of less reactive metals, alloys or composites can act as a protective barrier. Various techniques like electroplating, electroless deposition, physical or chemical vapour deposition, and spray coating have been used with varying success. Unfortunately, most of the metallic coatings are inherently porous and uneven with a little shielding against corrosion and wearing. These issues have largely been overcome with the development of electroless nickel plating.<sup>1,2</sup> Electroless nickel coatings possess improved tribological properties as well as corrosion resistance.<sup>3,4</sup> Moreover, this is a favourable method to plate any material with complex shapes.

Borohydride-reduced electroless nickel coating has been widely accepted due to its advantages like uniformity in thickness, significant resistance to wear and corrosion,<sup>5</sup> electrical properties,<sup>6</sup> ductility, and lubricating behaviour over other coatings. As-deposited nickel boride coatings composed of amorphous Ni-B and microcrystalline nickel, and the amorphous nature increases with increase in boron content.<sup>7</sup> The difference in boron content as low, mid and high concentrations can alter the hardness and wear process.<sup>8</sup>

Development of nickel boride composite coatings by co-deposition of secondary particles (reinforcements) from electroless bath has received a great interest owing to the enhancement of properties over electroless nickel-boron alloy coating.<sup>9,10</sup> The electroless composite coatings formed using different particles has different effects. Accordingly, diamond for higher hardness and wear resistance,<sup>11,12</sup> TiO<sub>2</sub> for improved wear resistance and microhardness,<sup>13</sup> SiC and Si<sub>3</sub>N<sub>4</sub> for wear and

corrosion resistance<sup>14,15</sup> have been investigated. Ni-B-SiC composite coatings from alkaline bath had higher corrosion resistance.<sup>16</sup>

Most of the coating properties like microhardness, hydrophobicity, hydrophilicity, corrosion resistance and scratch resistance depend on the surface texture. Uniformly distributed nanoparticles can induce significant grain refinement in coatings. Studies show that microhardness of Ni-P-SiO<sub>2</sub> increases with decrease in grain size of the matrix.<sup>17</sup> The presence of SiC nanoparticles in electrodeposited Ni coatings influences the nickel grain growth and led to the grain refinement and higher erosion-corrosion resistance.<sup>18</sup> Addition of Al<sub>2</sub>O<sub>3</sub> into Ni matrix gave significant enhancement of wear resistance and mechanical properties.<sup>19,20</sup> Though there are many reinforcement choices, CeO<sub>2</sub> shows remarkable role in improving both mechanical<sup>21</sup> and electrochemical properties.<sup>22</sup> Electrodeposited Ni-B/Ni-P-CeO<sub>2</sub> coatings exhibited superior hardness and corrosion protection efficiency.<sup>23</sup> However, the influence of CeO<sub>2</sub> nanoparticles on the properties of electroless nickel-boride coatings has not yet studied well. In the present study, the effect of CeO<sub>2</sub> particles on nickel-boride coating by electroless deposition of Ni-B-CeO<sub>2</sub> on aluminium 356 alloy surfaces was investigated concerning the surface morphology, coating composition, corrosion resistance, microhardness, and tribology. The composite coatings are deposited over the cylinder liners for evaluating its uniformity in engineering components.

## **2.2. Material and Methods**

### **2.2.1. Materials**

Nickel chloride (98%), ceria (99.95%), thiourea (99%), ferric chloride (96%), lactic acid (85%), sodium chloride (99%) and ammonia (30%) used were purchased from Sigma-Aldrich Co. Ltd., USA. Other chemicals; disodium ethylenediaminetetraacetate dihydrate (Na<sub>2</sub>EDTA-98%), sodium sulphite (97%), NaOH (97%), and sodium borohydride (98%) were obtained from S D Fine-Chem Ltd., India. The chemicals were used without purification for all the studies.

### 2.2.2. Coating preparation

Aluminium (A356) alloy substrates with 30×20×3 mm dimension were used for electroless deposition. The aluminium alloy pieces were polished with SiC abrasive paper (to 1000 grit) and ultrasonically cleaned in acetone. The cleaned substrate was etched with basic (20 g L<sup>-1</sup> NaOH) and acidic (100 g L<sup>-1</sup> H<sub>2</sub>SO<sub>4</sub> and 25 g L<sup>-1</sup> HCl) solutions (1 minute each) for the removal of surface impurities and metal oxides. Surface cleaned strips were introduced to a zincate solution containing zinc oxide (62.5 g L<sup>-1</sup>), sodium potassium tartrate (7.5 g L<sup>-1</sup>), sodium sulphite (0.25 g L<sup>-1</sup>), anhydrous ferric chloride (5 g L<sup>-1</sup>), and sodium hydroxide (6.25 g L<sup>-1</sup>) for 1 minute and dipped in a diluted nitric acid solution to remove the excess surface adsorbed Zn<sup>2+</sup> ions. The zincation was repeated for 20 seconds to provide better activation. The surface was further sensitized using acidic SnCl<sub>2</sub> (5 g L<sup>-1</sup> SnCl<sub>2</sub> and 30 mL L<sup>-1</sup> HCl) solution followed by activation with acidic PdCl<sub>2</sub> (0.01 g L<sup>-1</sup> PdCl<sub>2</sub> and 5 mL L<sup>-1</sup> HCl) solution. The sensitized substrate was introduced into the electroless plating solution for 1 hour at pH 8.5 to get a uniform surface coating with a considerable thickness under ultrasonic agitation (40 Hz). Ammonia solution was used to attain the alkaline pH of 8.5. The bath constituents and process parameters used for coating are given in Table 2.1.

**Table 2.1:** Electroless Ni-B-CeO<sub>2</sub> bath constituents and parameters.

| Bath constituents and parameters | Concentration / values |
|----------------------------------|------------------------|
| Nickel chloride                  | 9 g L <sup>-1</sup>    |
| Na <sub>2</sub> EDTA             | 10 g L <sup>-1</sup>   |
| Sodium borohydride               | 4 g L <sup>-1</sup>    |
| Lactic acid                      | 10 mL L <sup>-1</sup>  |
| Thiourea                         | 0.4 g L <sup>-1</sup>  |
| Ceria                            | 0.1 g L <sup>-1</sup>  |
| Bath temperature                 | 60°C                   |

### 2.2.3. Characterizations

#### 2.2.3.1. Structural analyses

The surface morphologies of electroless Ni-B and Ni-B-CeO<sub>2</sub> coatings were observed with scanning electron microscopy, SEM (JEOL, Japan). The elemental composition was identified using energy-dispersive X-ray spectroscopy, EDS (Hitachi) attached with SEM (Zeiss EVO 18 cryo-SEM). Further, changes in surface texture and roughness were analysed with atomic force microscopy (AFM) analysis under ambient conditions using the Bruker Multimode AFM-3COCF (Germany) in the tapping mode. X-ray diffraction, XRD (PANalytical, Netherlands) in the range from 20° to 70° (2θ angles) by Cu Kα radiation used to determine the crystallite size of nickel. The chemical composition was studied using X-ray photoelectron spectroscopy, XPS (PHI 5000 Versa Probe II) with Al Kα radiation. CasaXPS software was used to calculate the relative percentage of each element present in the coating. The binding energy (BE) was measured with reference to the C 1s line of the adventitious carbon at 285.0 eV. All the surface studies were carried out on a 5×5 mm sample taken from the coated substrate. Coating thickness was measured from the SEM image of the coating cross-section. The samples were vertically mounted in the acrylic polymer and polished to a mirror finished surface.

#### 2.2.3.2. Electrochemical measurements

Corrosion behaviour was measured by electrochemical impedance spectroscopy (EIS) and potentiodynamic polarization test at room temperature in 3.5 wt% NaCl solution with a three-electrode electrochemical cell (CHI608E). The coated specimen with 1 cm<sup>2</sup> exposed surface was used as the working electrode; saturated calomel and a platinum grid were taken as the reference and counter electrodes respectively. The specimens were kept in the electrolyte for 20 min prior to the experiment for attaining their stable open circuit potential (OCP). The potentiodynamic scan was done at a rate of 1 mV/s from -200 mV to +200 mV concerning the OCP values. The corrosion potential ( $E_{\text{corr}}$  vs. SCE) and corrosion current density ( $i_{\text{corr}}$ ) of each sample were obtained from the applied potential vs.

current (Tafel) plot. EIS measurements were done at their OCP in the frequency from 10<sup>4</sup> to 10<sup>-1</sup> Hz with amplitude of 10 mV. The data were fitted by EC-Lab software with corresponding equivalent electrical circuits.

#### *2.2.3.3. Hardness measurements*

The Vickers micro-hardness tester (Clemex) was used to measure hardness on the coated A356 alloy surface under the indentation of 50 gf with an indentation speed of 50 μm/s and 15 s dwell time. Hardness measurements at five different locations of the specimen were done and the average value was taken.

#### *2.2.3.4. Pin on disc wear testing*

Pin on disc wear testing machine (TR-20, DUCOM) was used to measure the wear rate and coefficient of friction at the dry condition. The measurements were done for coated samples as well as bare A356 alloy surface after heat-treatment (300°C for 2hrs). The pins with 6 mm diameter and 30 mm length were used against EN31 high carbon alloy steel disc (d = 80 mm). The A356 alloy pins were coated with Ni-B alloy and Ni-B-CeO<sub>2</sub> composite followed by heat treatment at 300°C. Wear tests were done at a sliding velocity of 0.4 m/s under 5, 10 and 20 N standard loads up to 500 m distance at room temperature.

## **2.3. Results and Discussion**

### **2.3.1. Surface morphology and elemental composition**

SEM micrographs of electroless Ni-B alloy and Ni-B-CeO<sub>2</sub> nanocomposite coatings deposited on A356 aluminium alloy are given in Figure 2.1a and Figure 2.1b, respectively. The deposits exhibit similar morphologies with a typical nodular surface texture. However, the dimension of nodules in the nanocomposite coating is smaller than that in the Ni-B, which indicates the induced grain refinement during the co-deposition of ceria nanoparticles with nickel boride. The addition of CeO<sub>2</sub> particles influences the deposition mechanism by increasing the number of active sites to start the metal matrix deposition as the nucleation centre for electroless process.<sup>24</sup> Simultaneously, the incorporation of nanoparticles at the boundaries of nickel

crystallites can reduce the nodular grain size and become denser than the electroless Ni-B coating. Elemental composition analysis (Figure 2.1c & 2.1d) of Ni-B alloy possesses nickel (~ 90%) as the major elemental contribution and boron (~ 3.5%) with relatively low concentration. The composite coating surface gave additional peak corresponding to cerium from ceria along with nickel and boron. Approximately 0.3% cerium present in the coating by co-deposition of ceria nanoparticles. It has been confirmed that the nanoparticles were successfully incorporated into the nanocomposite coating surface. Figure 2.2 represents the cross-sectional SEM image of Ni-B-CeO<sub>2</sub> composite coatings depicting the average coating thickness of 40  $\mu\text{m}$  and EDS mapping gives the elemental distribution of nickel, boron, and cerium in the coating.

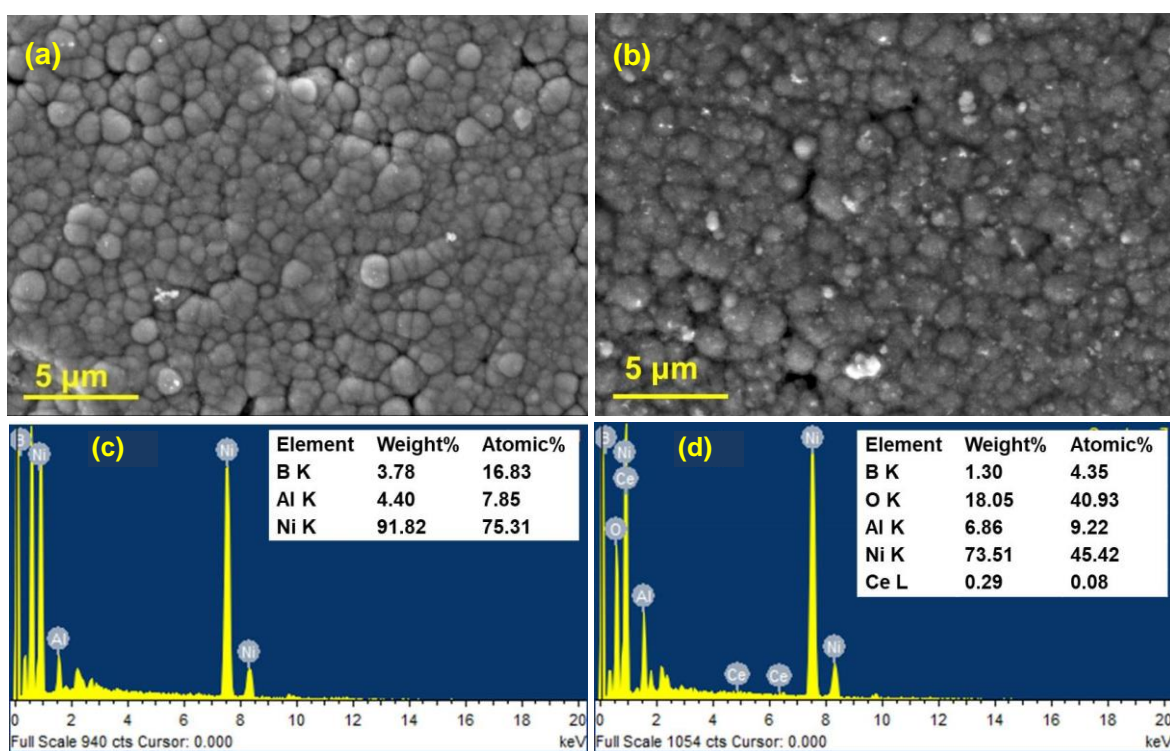


**Figure 2.1:** SEM micrograph of the surface and Energy-dispersive X-ray spectroscopy: (a & c) Ni-B alloy, (b & d) Ni-B-CeO<sub>2</sub> composite coatings.

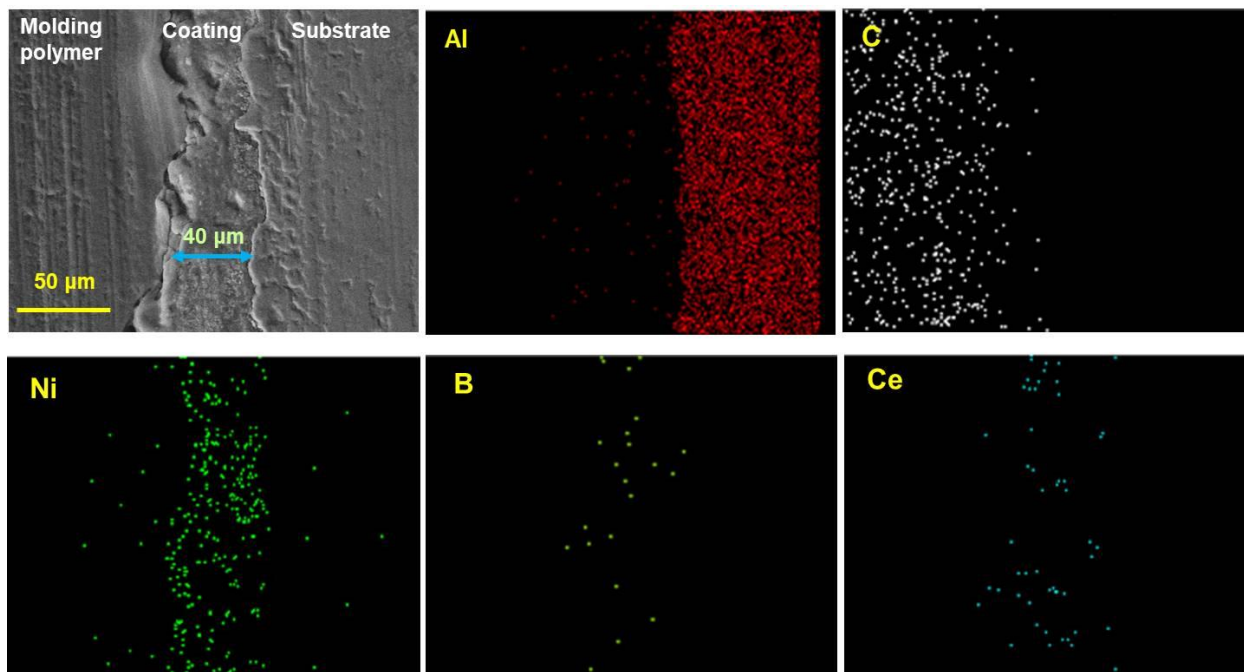


**Figure 2.2:** Cross-sectional SEM image of Ni-B-CeO<sub>2</sub> nanocomposite coating and the EDS mapping.

### 2.3.2. AFM analysis

The AFM images of Ni-B and Ni-B-CeO<sub>2</sub> composite coated surfaces are shown in Figure 2.3a and 2.3b, respectively. It gives clear evidence for the changes in surface roughness and grain refinement for the nanocomposite coatings. The section profile through the nodular grains on the coated surface provides the accurate measurement of their size. The typical height topography measurement along the line drawn is displayed in the AFM image. The grain size was measured between two cross marks in the image. Measurements at various locations are made, and the average size is determined. The average nodular grain size of Ni-B coating is 1150 nm, and it has significantly reduced to 650 nm for the nanoparticle added coating. The surface roughness of the nanocomposite coating got reduced by co-depositing 0.1 g L<sup>-1</sup> of CeO<sub>2</sub> in compared with the alloy coating. The Rq values are 239 nm and 154 nm for Ni-B alloy and Ni-B-CeO<sub>2</sub> coatings respectively. Uniform distribution of co-deposited CeO<sub>2</sub> nanoparticles brings smooth, uniform, compact and less porous nanocomposite coating compared to Ni-B coating. At higher concentrations of ceria in the coating,

surface roughness value increased to 199 nm and 294 nm for 0.2 g L<sup>-1</sup> and 0.5 g L<sup>-1</sup> of CeO<sub>2</sub> concentration respectively.

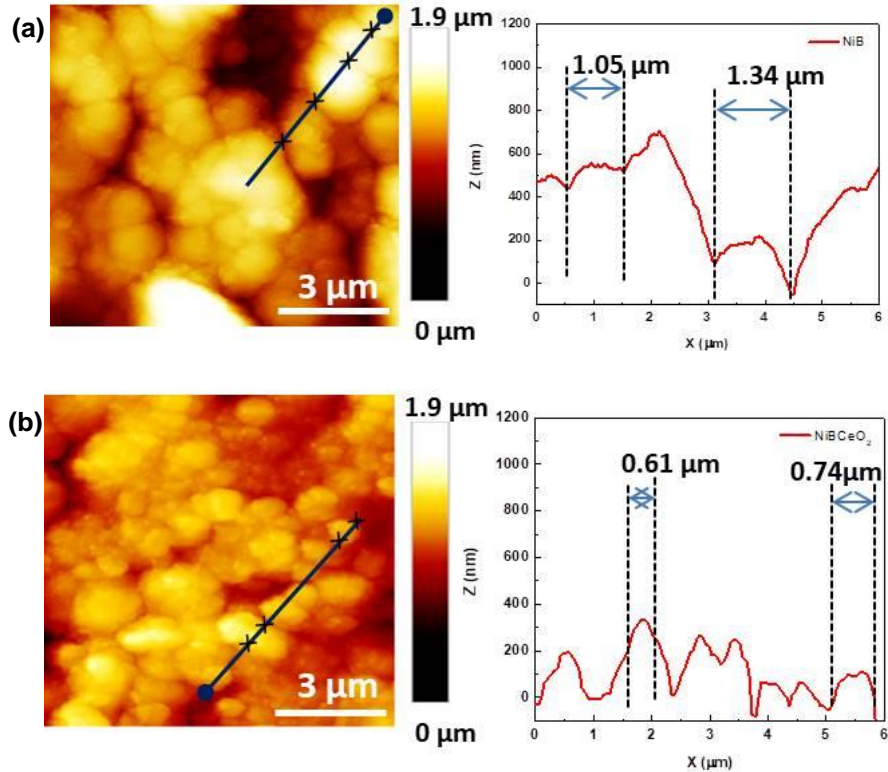


**Figure 2.3:** AFM height images: (a) Ni-B alloy and (b) Ni-B-CeO<sub>2</sub> nanocomposite coatings.

### 2.3.3. X-ray diffraction studies

X-ray diffraction patterns of Ni-B and Ni-B-CeO<sub>2</sub> after heat treatment (300°C) are shown in Figure 2.4 to analyse the crystallite size of nickel deposit. The characteristic reflection corresponding to Ni (111) plane is observed at  $2\theta=44.7^\circ$ . Formation of microcrystalline Ni<sub>3</sub>B phases at  $49.21^\circ$ ,  $52.88^\circ$  was also identified to the crystal planes (113), (212). The peaks at  $38.44^\circ$  and  $65.09^\circ$  represent the crystal planes (111), and (220) of aluminium substrate.<sup>25,26</sup> Presence of CeO<sub>2</sub> in the nanocomposite coating cannot be observed with X-ray diffraction patterns owing to their low concentration. Crystallite size (grain size) of the coatings was calculated by the Scherrer equation (Equation (2.1)) using the diffraction peak of Ni (111).

$$D_p = (K \lambda) / (\beta \cos \theta) \quad (2.1)$$

Where,  $D_p$  = Average crystallite size,  $K = 0.9$  is the Scherrer constant,  $\beta$  = full width at half maximum of the peak,  $\theta$  = Bragg angle,  $\lambda$  = X-ray wavelength. The grain size measurements indicate that Ni-B coatings (14.96 nm) have large grain size compared to Ni-B- CeO<sub>2</sub> composite coatings (9.97 nm). Incorporation of ceria particles into the Ni-B matrix refines its crystallite size by providing many heterogeneous nucleation sites for the crystal growth.<sup>27</sup>

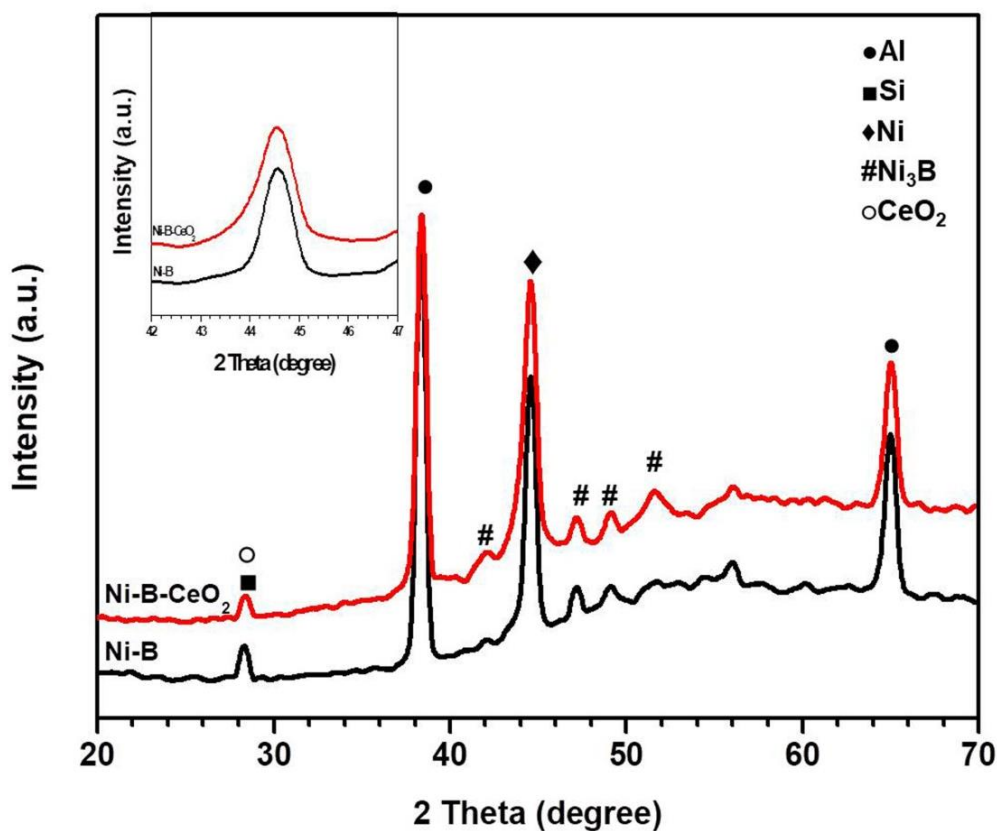


**Figure 2.4:** XRD of Ni-B and Ni-B-CeO<sub>2</sub> nanocomposite coatings. Enlarged portion of Ni(111) peak is shown as inset.

#### 2.3.4. XPS analysis

X-ray photoelectron spectroscopy (XPS) technique was employed to find the chemical states of all elements in composite coated (as-deposited) sample. The survey spectrum of Ni-B-CeO<sub>2</sub> (Figure 2.5a) also certifies the presence of Ni, B, Ce, and O;

which is consistent with the SEM and EDS results. Percentage of elements calculated by CasaXPS software indicates the presence of ~ 73% of nickel, ~ 3.7% of boron, ~ 18% of oxygen, and 0.79% of cerium in composite coating. Three broad peaks in the range of 600 eV to 800 eV represent Ni auger peaks corresponding to Ni LMM, Ni LMM1, and Ni LMM2 transitions.<sup>28,29</sup> The high-resolution spectrum of Ni 2p (Figure 2.5b) shows the primary and secondary peaks corresponding to Ni 2p<sub>3/2</sub> and Ni 2p<sub>1/2</sub> spin-orbit energy levels and hence the Ni ion is in zero oxidation state. The secondary peaks observed at higher binding energies represent the satellite peaks. Boron present as both zero (189 eV) and '+3' (192 eV) states, as amorphous borides and oxidized states (Figure 2.5c) similar to the previous reports on sodium borohydride-reduced nickel system.<sup>30</sup> The XPS spectrum of cerium (Ce 3d) in Ni-B-ceria film is given in Figure 2.5d. The spectrum is complex instead of four characteristic peaks for 3d<sub>3/2</sub> and 3d<sub>5/2</sub> states of Ce(IV) and Ce(III) owing to the spin-orbit splitting.<sup>31</sup> Therefore, six and four peaks assigned for Ce<sup>4+</sup> and Ce<sup>3+</sup> respectively.<sup>32</sup> According to Burroughs et al.,<sup>33</sup> the peaks named as v, v'', v''' and u, u'', u''' represent 3d<sub>5/2</sub> and 3d<sub>3/2</sub> of Ce(IV) and the peaks titled v<sub>0</sub>, v' and u<sub>0</sub>, u' for 3d<sub>5/2</sub> and 3d<sub>3/2</sub> of Ce(III) oxidation state respectively. The existence of both oxidation states indicates the presence of non-stoichiometric cerium oxide, mainly as CeO<sub>2</sub> and Ce<sub>2</sub>O<sub>3</sub>. Figure 2.5e shows the XPS spectrum of O 1s region. The broad peak consists of lattice oxygen in both Ce(IV) and Ce(III) oxides, and adsorbed oxygen in different forms on the surface.<sup>34</sup>

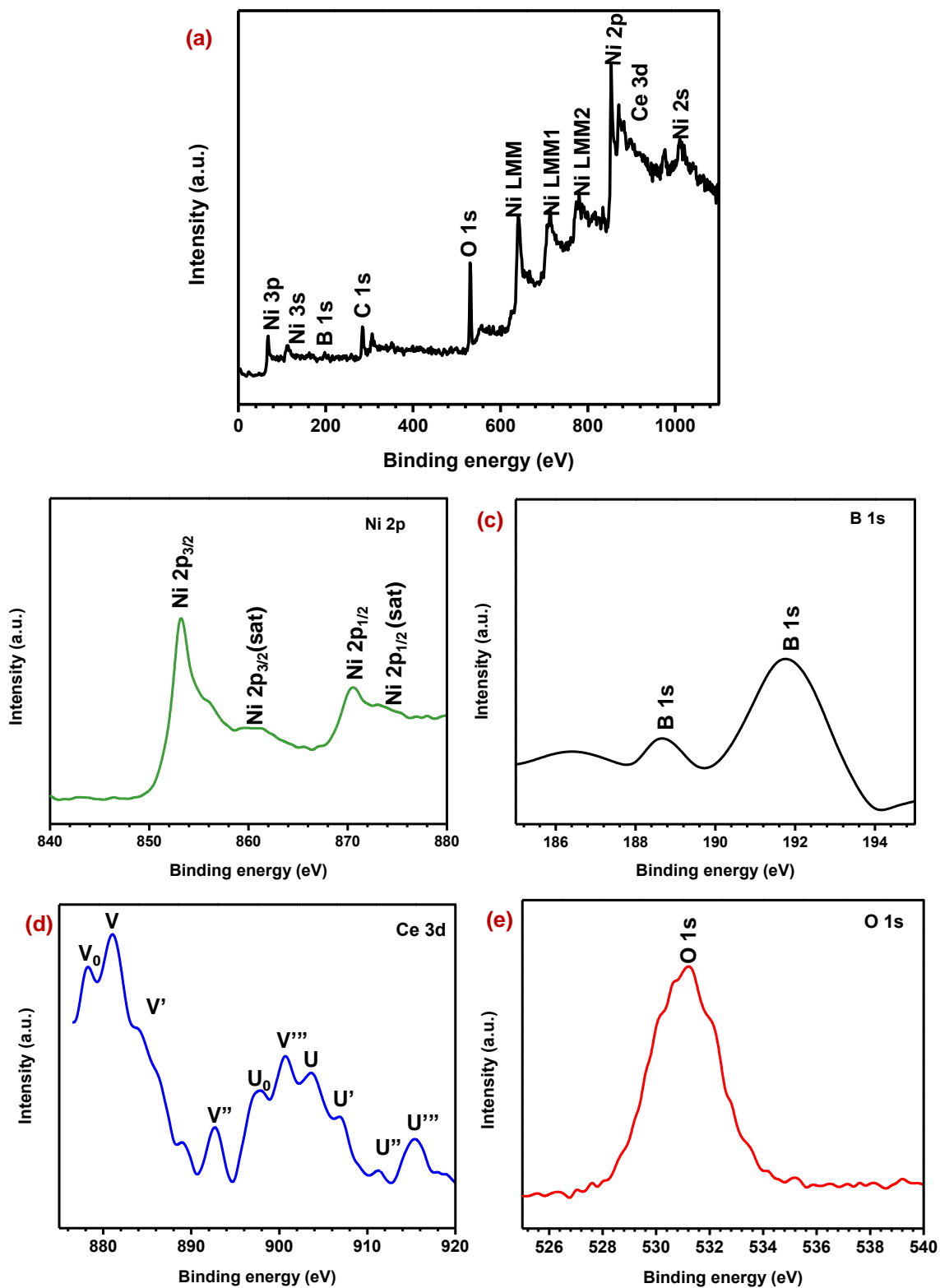


**Figure 2.5:** XPS survey spectrum of NiB-CeO<sub>2</sub> (a), high-resolution spectrum of Ni 2p (b), B 1s (c), Ce 3d (d), O 1s (e).

### 2.3.5. Electrochemical characterization for corrosion analyses

Figure 2.6 shows the potentiodynamic polarization curves (Tafel plots) of samples by plotting the potential scanned from cathodic region to the anodic region vs. logarithm of current density. The values of corrosion current density ( $i_{\text{corr}}$ ) and corrosion potential ( $E_{\text{corr}}$ ), obtained by the extrapolation of cathodic and anodic sides are given in Table 2.2. Variation of  $E_{\text{corr}}$  value towards more positive direction and the lower  $i_{\text{corr}}$  indicates the corrosion prevention of coatings, especially for the composite plating. Presence of ceria nanoparticles in the coating leads to a substantial reduction in the  $i_{\text{corr}}$  values of the Ni-B from  $11.18 \times 10^{-6} \text{ A cm}^{-2}$  to  $2.482 \times 10^{-6} \text{ A cm}^{-2}$ . The corresponding shift of the graph towards the left-hand side was observed. The reduction in  $i_{\text{corr}}$  values of the coated samples indicates the decreased ionic diffusion on the surface during the corrosion process.<sup>35</sup> The anodic polarization curves of bare aluminium and nickel boride coating exhibited an active dissolution phenomenon whereas the ceria added sample had significant passivation behaviour. Moreover, the composite coating is more cathodic to the other samples and possesses excellent corrosion protection. Influence of ceria concentration in corrosion resistance shows that the higher concentration of  $0.2 \text{ gL}^{-1}$  and  $0.5 \text{ gL}^{-1}$  nanoparticles slightly reduces the corrosion resistance with an increase in corrosion current density of  $7.58 \times 10^{-6} \text{ A cm}^{-2}$  and  $12.56 \times 10^{-6} \text{ A cm}^{-2}$  respectively (Figure 2.7).

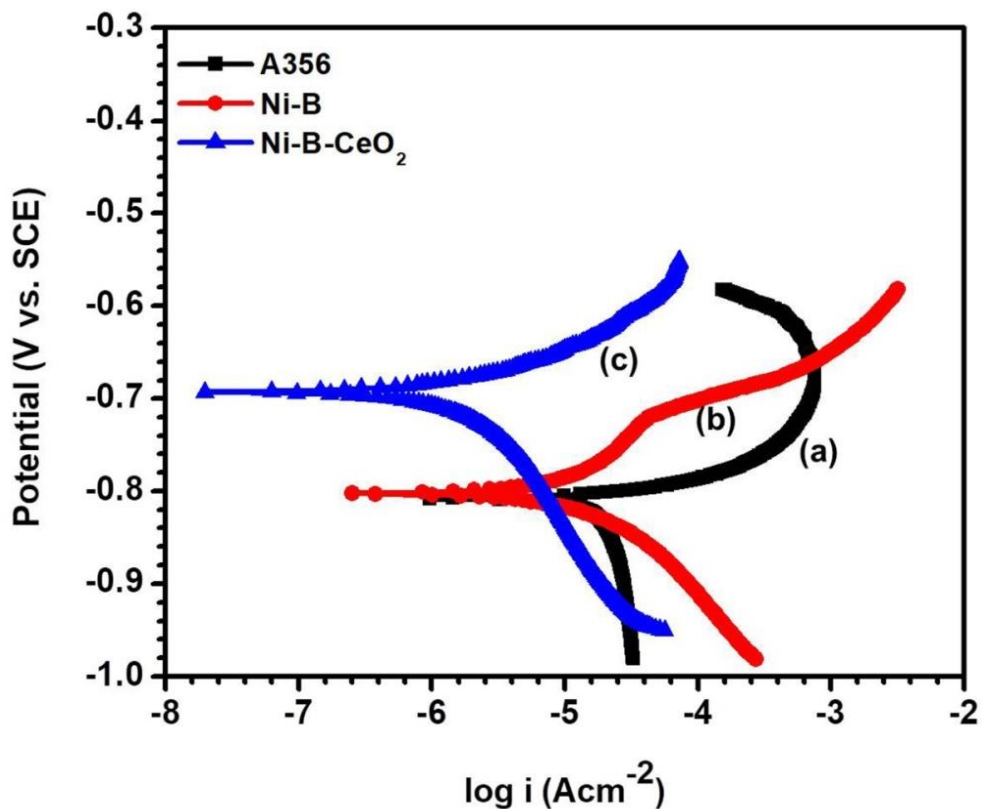


**Figure 2.6:** Tafel plots of (a) A356 alloy, (b) Ni-B coatings and (c) Ni-B-CeO<sub>2</sub> composite coatings at a scan rate of 1mV/s.

**Table 2.2:**  $E_{\text{corr}}$ ,  $\beta_c$ ,  $\beta_a$  and  $i_{\text{corr}}$  values obtained from potentiodynamic polarization scan.

| Sample ID             | $E_{\text{corr}}$ (V vs. SCE) | $\beta_c$ (mV/decade) | $\beta_a$ (mV/decade) | $i_{\text{corr}}$ (A cm <sup>-2</sup> ) |
|-----------------------|-------------------------------|-----------------------|-----------------------|---|
| A356                  | -0.808                        | 1.257                 | 4.412                 | 16.87 x 10 <sup>-6</sup>                |
| Ni-B                  | -0.802                        | 6.658                 | 17.57                 | 11.18 x 10 <sup>-6</sup>                |
| Ni-B-CeO <sub>2</sub> | -0.693                        | 5.063                 | 9.748                 | 2.482 x 10 <sup>-6</sup>                |

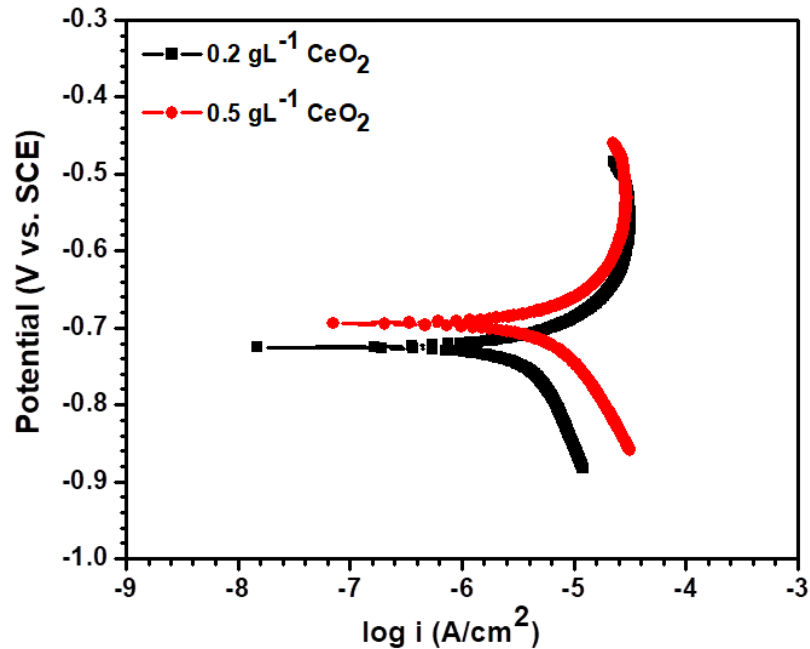


**Figure 2.7:** Tafel plots of Ni-B-CeO<sub>2</sub> composite coatings at different concentrations of 0.2 gL<sup>-1</sup> and 0.5 gL<sup>-1</sup> at a scan rate of 1mV/s.

EIS measurements are represented as Nyquist plot (Figure 2.8a) and Bode plots (Figure 2.8b). From the Nyquist plot, loops correspond to aluminium alloy surface and Ni-B coating show single capacitive arc at all range of frequencies. The capacitive arc is observed by the presence of double layer capacitance formation at the sample-electrolyte interface and metal dissolution, and the diameter represents the charge transfer resistance ( $R_{ct}$ ). At higher frequencies, the resistance is attributed to the solution resistance ( $R_s$ ). Non-homogeneous double layer capacitance is represented as the constant phase element (CPE), instead of a pure capacitor. The corresponding equivalent electrical circuit used for the fitting is given in Figure 2.9, and the values of each component are specified in Table 2.3. Ni-B-CeO<sub>2</sub> nanocomposite coating has an additional capacitive loop at high to middle frequencies due to the protective film containing nanostructured cerium oxide particles.<sup>36</sup> Since the low-frequency region is associated with the corrosion process, the largest loop diameter for composite coating reveal the improvement in corrosion resistance of Ni-B-CeO<sub>2</sub>. However, the  $R_{ct}$  of Ni-B doesn't have any considerable improvement in comparison with the bare material. The secondary particle added coating have the highest charge transfer resistance ( $R_{ct}$

values: Al - 1358.5 ohm, Ni-B - 1525.16 ohm and Ni-B-CeO<sub>2</sub> - 6054.9 ohm) compared with the particle-free counterpart and aluminium alloy, implying increased corrosion resistance of the composite coating.

To investigate in detail, bode plots of the samples are shown in Figure 2.8b, phase angle vs.  $\log f$ . The phase angle plot of nickel boride coating has single phase maximum as for bare aluminium alloy. But the frequency range has shifted towards the lower value due to the presence of relatively noble Ni-B alloy. For nanocomposite coated sample, the capacitance behaviour exhibited for a wide frequency range with two time constants overlying at medium and low frequencies. The asymmetry of the peak may due to the overlapping of two relaxation processes with similar capacitance values as explained with the equivalent circuit. Additional barrier property exhibited by ceria added coatings may be due to the inert characteristics of the particles towards the corrosive ions and the water molecules. This particle could induce zig-zagging of the path for ion movement towards the metallic surface.<sup>37</sup> Grain refinement offered by the nanoparticles further increases the path length of aggressive ionic species. Moreover, conversion of oxygen deficient ceria nanoparticle with the Ce<sup>3+</sup> ion to more stable Ce<sup>4+</sup> in the presence of corrosive environment can attribute to the anti-corrosion behaviour.

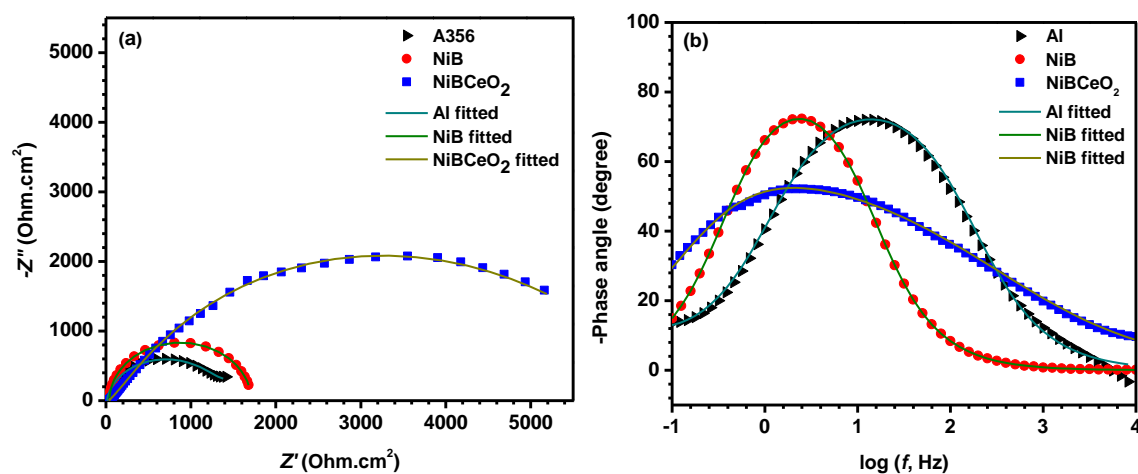


**Figure 2.8:** Nyquist (a) and Bode, phase angle vs.  $\log f$  (b) plots of A356 alloy, Ni-B coatings and Ni-B-CeO<sub>2</sub> composite coatings at their OCP with amplitude of 10 mV in the frequency range from  $10^4$  to  $10^{-1}$  Hz.

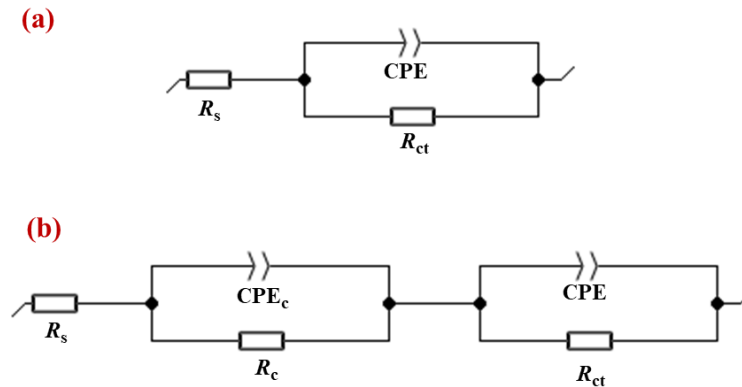


**Figure 2.9:** Equivalent electrical circuit model used to fit the EIS data; (a) A356 alloy and Ni-B coatings and (b) Ni-B-CeO<sub>2</sub> composite coatings.

**Table 2.3:** The fitted values of EIS measurements of the samples using equivalent circuits shown in the Figure 2.9.

| Sample ID  | A356                   | Ni-B                  | Ni-B-CeO <sub>2</sub> |
|--|------------------------|-----------------------|-----------------------|
| $R_s$ ( $\Omega \text{ cm}^2$ )                  | 11.84                  | 41.37                 | 30.72                 |
| $R_{ct}$ ( $\Omega \text{ cm}^2$ )               | 1289                   | 1669                  | 4386                  |
| $R_c$ ( $\Omega \text{ cm}^2$ )                  | -                      | -                     | 2754                  |
| CPE ( $S^n / \Omega \text{ cm}^2$ )              | $13.21 \times 10^{-5}$ | $26.1 \times 10^{-5}$ | $25.4 \times 10^{-5}$ |
| CPE <sub>c</sub> ( $S^n / \Omega \text{ cm}^2$ ) | -                      | -                     | $21.7 \times 10^{-5}$ |
| n  | 0.919                  | 1                     | 0.804                 |

### 2.3.6. Hardness behaviour

The microhardness obtained for ceria added composite coating shows exceptional high hardness values of  $\sim 684$  VHN compared to base alloy and pure Ni-B coating with the Vickers hardness of  $\sim 105$  VHN and  $\sim 424$  VHN respectively (Figure 2.10). Grain boundary immobilization by the nanoparticles and the dispersion

strengthening may improve the hardness for composite coating.<sup>38</sup> However, Ni-B coating itself gave a considerable enhancement in the hardness due to the random incorporation of boron with nickel. Microhardness values of the samples increase in the order of base alloy < pure Ni-B < Ni-B-CeO<sub>2</sub> composite coating.

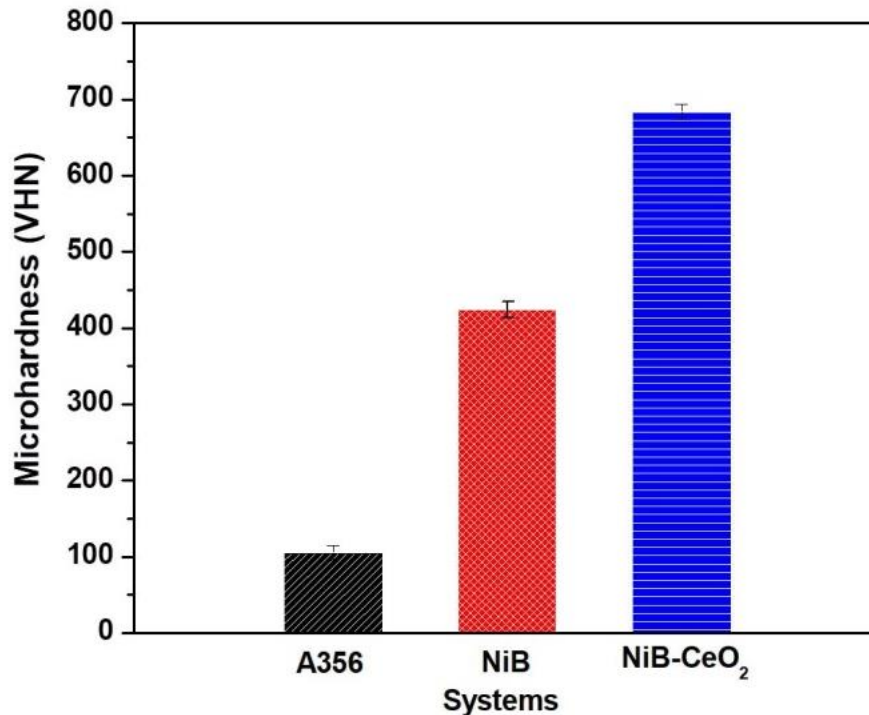


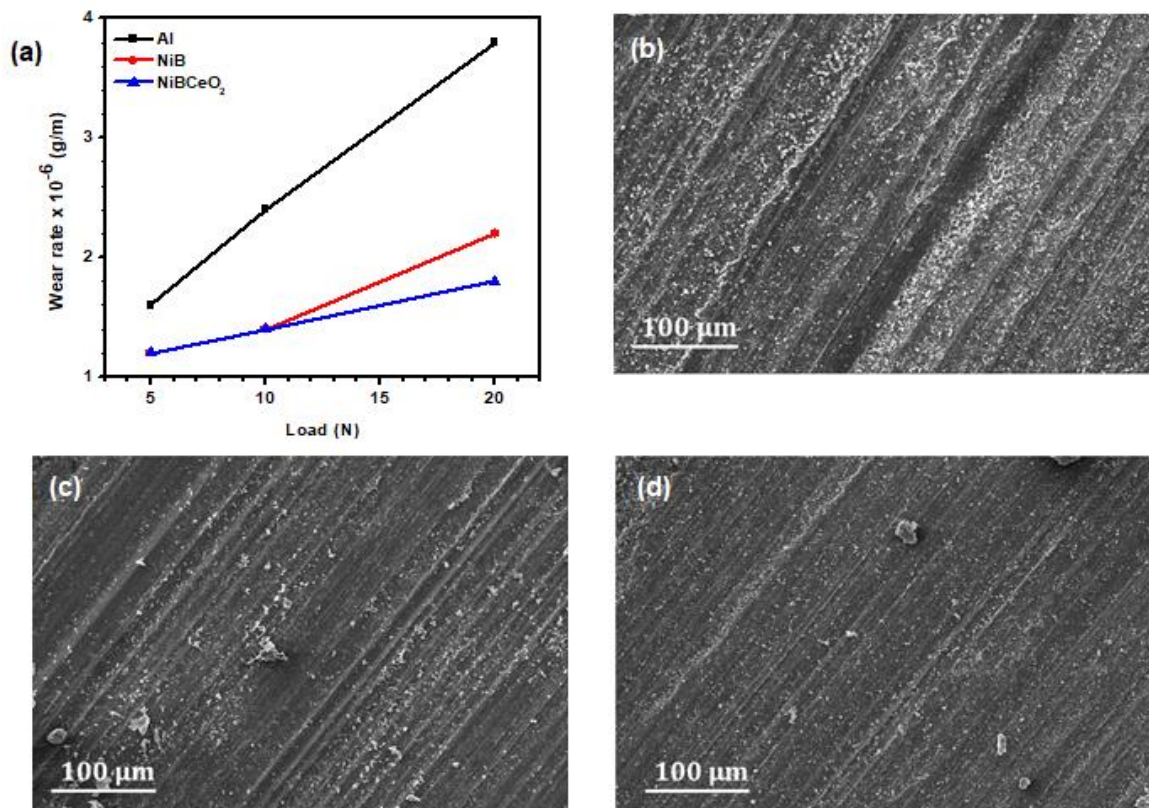
**Figure 2.10:** Vickers microhardness values of the samples under the indentation of 50 gf with a speed 50  $\mu\text{m/s}$ .

### 2.3.7. Tribological Characteristics

Variation in the wear rates of samples with different loadings by the pin on disc method is given in Figure 2.11a. It is observed that the nanocomposite coating system exhibits the lowest wear rate when compared with nickel coating, which is smaller than the bare aluminium alloy. Wear rates of all the samples increases with increase in loading. At higher loads, ceria added nanocomposite exhibits significantly lower wear rate. The fragments of nickel matrix and reinforcements from the coating along with iron debris from the counter surface may lead to the formation of a mechanically mixed or an intermediate layer at higher loads. Presence of mechanically mixed layer over the mating disc during sliding results in avoiding direct contact with the alloy,

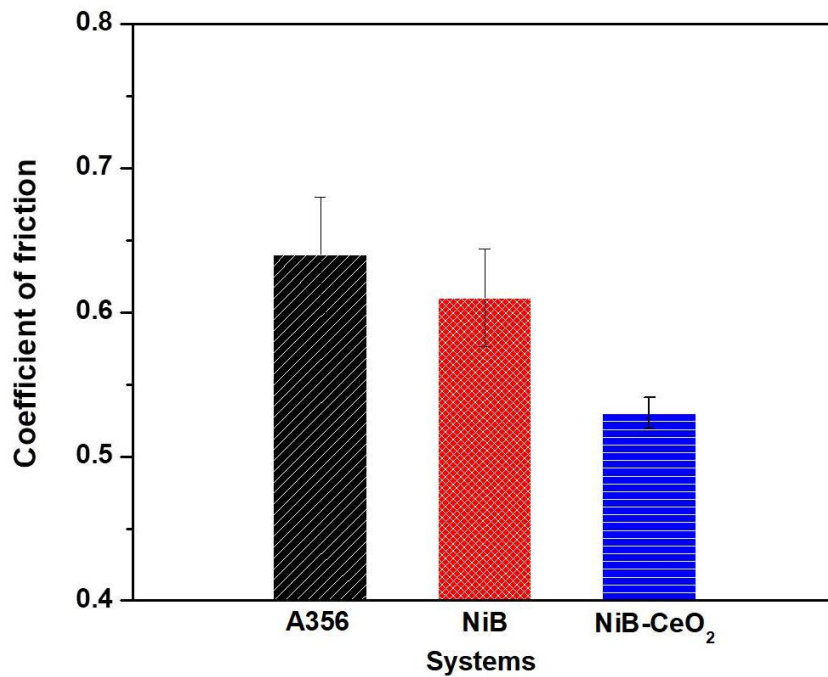
which reduces material removal from the sample under the steady state of wear. Moreover, the interfacial bond strength between the Ni-B and the particles play a vital role in the wear process.<sup>39</sup> Therefore, the lower wear rate under higher load could be explained by the decreased grain size of the matrix, reinforcement hardening effect and better integrity of ceria particle in the matrix as compared to the alloy.

Figure 2.11b, 2.11c, and 2.11d show the worn surface morphology corresponding to A356 alloy, Ni-B and Ni-B-CeO<sub>2</sub> nanocomposite coatings. Long and deep grooves formed on the surface of the aluminium alloy due to continuous abrasion from a large fragment adhered to the counter face from the specimen. Sliding wear debris is present along the sliding direction on the surface of A356, which has resulted from the high wear rate by cutting or plastic deformation. On the other hand, the nanocomposite coated surface after sliding becomes smoother, and the grooves are smaller and fewer, resulting in a decrease in the wear rate.



**Figure 2.11:** (a) Wear rate as a function of load applied (b) SEM micrograph of the worn surface of A356 (c) Ni-B and (d) Ni-B-CeO<sub>2</sub> coating after pin-on-disk wear testing.

Ni-B-CeO<sub>2</sub> nanocomposite coatings show the lowest coefficient of friction (COF) values (0.531) as given in Figure 2.12. The Ni-B and aluminium alloy samples show relatively higher values with an average of 0.610 and 0.639 respectively. The presence of nanoparticles and grain refinement observed in the deposited nanocomposite may provide the lowest coefficient of friction values for them compared with their particle free counterpart.



**Figure 2.12:** Friction coefficients of A356, NiB and NiB-CeO<sub>2</sub> coatings during sliding at 0.4 m/s velocity under 2N load.

### 2.3.8. Ni-B-CeO<sub>2</sub> nanocomposite coatings on cylinder liner

The developed ceria nanocomposite coating has been applied successfully on the cylinder liners by the electroless process under ultrasonication. Figure 2.13 shows the photographs of uncoated (2.13a) and Ni-B-CeO<sub>2</sub> coated (13b) aluminium A356 alloy cylinder liners. A silvery grey colored composite coating was obtained uniformly on the entire surface of the cylinder liner.

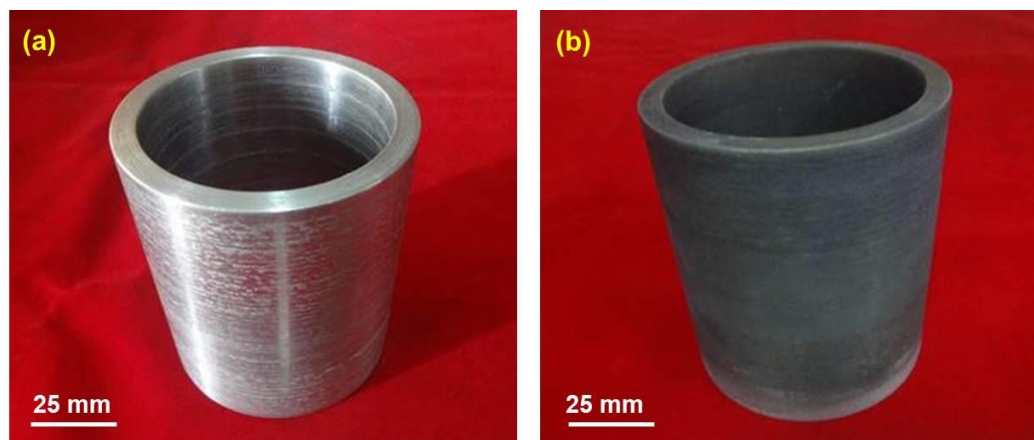


**Figure 2.13:** (a) Uncoated and (b) electroless NiB-CeO<sub>2</sub> coated A356 Piston cylinders.

## 2.4. Conclusions

Ni-B and Ni-B-CeO<sub>2</sub> nanocomposite films were effectively deposited on A356 aluminium alloy by the electroless process. Ni-B-CeO<sub>2</sub> composite coating shows finer nodular grain size and Ni crystallite size than the particle-free coatings as the grain growth starts from the ceria particles. XPS studies confirmed the co-existence of Ce<sup>4+</sup> and Ce<sup>3+</sup> oxides in the nanocomposite coating. The nanocomposite coating exhibited better barrier effect in a corrosive environment in the presence of ceria nanoparticles, and the corrosion current density was reduced to  $2.48 \times 10^{-6}$  A cm<sup>-2</sup> from that of the particle-free counterpart  $11.18 \times 10^{-6}$  A cm<sup>-2</sup>. Grain refinement offered by the nanoparticles could induce zig-zagging of the path for ion movement towards the metallic surface. Additionally, oxidation of ceria nanoparticle with Ce<sup>3+</sup> ion present in the coating to more stable Ce<sup>4+</sup> in the corrosive environment can attribute the anti-corrosion behaviour. Higher microhardness ( $\sim 684$  VHN for composite coating and  $\sim 424$  VHN for pure Ni-B), enhanced wear resistance and low friction coefficient are observed for the nanocomposite coating. Smaller grain size and better integrity effect of ceria particle in the matrix has contributed to the coating stability. Nickel boride composite coatings are uniformly applied over the centrifugally cast aluminium alloy cylinder liner.

## References

- 1 J. Sudagar, J. Lian and W. Sha, *J. Alloys Compd.*, 2013, **571**, 183–204.
- 2 P. Sahoo and S. K. Das, *Mater. Des.*, 2011, **32**, 1760–1775.
- 3 A. Araghi and M. H. Paydar, *Mater. Des.*, 2010, **31**, 3095–3099.
- 4 A.-F. Kanta, M. Poelman, V. Vitry and F. Delaunois, *J. Alloys Compd.*, 2010, **505**, 151–156.
- 5 Y. . Huang, X. . Zeng, X. . Hu and F. . Liu, *Electrochim. Acta*, 2004, **49**, 4313–4319.
- 6 C. Kang, H. Lu, S. Yuan, D. Hong, K. Yan and B. Liang, *Chem. Eng. J.*, 2012, **203**, 1–8.
- 7 F. Bulbul, *Met. Mater. Int.*, 2011, **17**, 67–75.
- 8 L. B. V. Vitry, *Surf. Coatings Technol.*, 2017, **311**, 164–171.
- 9 T. S. N. Sankara Narayanan and S. K. Seshadri, *J. Alloys Compd.*, 2004, **365**, 197–205.
- 10 M. D. B. Kaya, T. Gulmez, *Proc. world Congr. Eng. Comput. Sci.*, 2008, 22–24.
- 11 K. Krishnaveni, T. S. N. Sankara Narayanan and S. K. Seshadri, *Surf. Coatings Technol.*, 2005, **190**, 115–121.
- 12 H. Mazaheri and S. R. Allahkaram, *Appl. Surf. Sci.*, 2012, **258**, 4574–4580.
- 13 X. Shu, Y. Wang, C. Liu and W. Gao, *Mater. Technol.*, 2015, **30**, A41–A45.
- 14 A. Farzaneh, M. Mohammadi, M. Ehteshamzadeh and F. Mohammadi, *Appl. Surf. Sci.*, 2013, **276**, 697–704.
- 15 J. N. Balaraju, V. Ezhil Selvi and K. S. Rajam, *Mater. Chem. Phys.*, 2010, **120**, 546–551.
- 16 E. Georgiza, V. Gouda and P. Vassiliou, *Surf. Coatings Technol.*, 2017, **325**, 46–51.
- 17 S. Sadreddini, Z. Salehi and H. Rassaie, *Appl. Surf. Sci.*, 2015, **324**, 393–398.
- 18 J. A. Calderón, J. E. Henao and M. A. Gómez, *Electrochim. Acta*, 2014, **124**, 190–198.
- 19 W. G. R.A. Shakoor, R. Kahraman, U. Waware, Y. Wang, *Mater. Des.*, 2014, **64**, 127–135.
- 20 Z. P. C. Li, Y. Wang, *Mater. Des.*, 2013, **47**, 443–448.
- 21 R. A. Shakoor, R. Kahraman, U. S. Waware, Y. Wang and W. Gao, *Mater. Des.*,

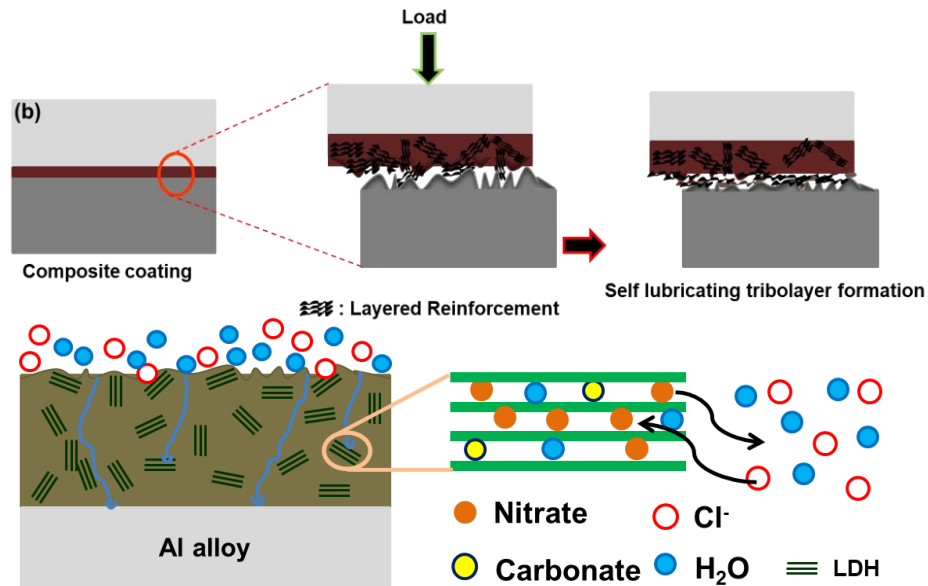
- 2014, **59**, 421–429.
- 22 N. S. Qu, W. H. Qian, X. Y. Hu and Z. W. Zhu, *Int. J. Electrochem. Sci. Int. J. Electrochem. Sci.*, 2013, **8**, 11564–11577.
- 23 M. M. Yusuf, A. B. Radwan, R. A. Shakoor, M. Awais, A. M. Abdullah, M. F. Montemor and R. Kahraman, *J. Appl. Electrochem.*, 2018, **48**, 391–404.
- 24 S. Singh, M. Sribalaji, N. P. Wasekar, S. Joshi, G. Sundararajan, R. Singh and A. K. Keshri, *Appl. Surf. Sci.*, 2016, **364**, 264–272.
- 25 P. S. Kumar and P. K. Nair, *Nanostructured Mater.*, 1994, **4**, 183–198.
- 26 V. Vitry, A.-F. Kanta, J. Dille and F. Delaunois, *Surf. Coatings Technol.*, 2012, **206**, 3444–3449.
- 27 R. Shakoor, U. Waware, K. Ali, R. Kahraman, A. Popelka, M. Yusuf and A. Hasan, *Coatings*, 2017, **7**, 161.
- 28 Z. Wu, X.-L. Huang, Z.-L. Wang, J.-J. Xu, H.-G. Wang and X.-B. Zhang, *Sci. Rep.*, 2014, **4**, 3669.
- 29 J. R. Zeng, M. Y. Gao, Q. B. Zhang, C. Yang, X. T. Li, W. Q. Yang, Y. X. Hua, C. Y. Xu and Y. Li, *J. Mater. Chem. A*, 2017, **5**, 15056–15064.
- 30 A. J. Friedrich, C. E. Joseph and T. J. Strathmann, *Appl. Catal. B Environ.*, 2009, **90**, 175–183.
- 31 E. Stoyanova, D. Guergova, D. Stoychev, I. Avramova and P. Stefanov, *Electrochim. Acta*, 2010, **55**, 1725–1732.
- 32 D. R. Mullins, *Surf. Sci. Rep.*, 2015, **70**, 42–85.
- 33 P. Burroughs, A. Hamnett, A. F. Orchard and G. Thornton, *J. Chem. Soc. Dalton Trans.*, 1976, **0**, 1686.
- 34 R. Jain, A. Dubey, M. K. Ghosalya and C. S. Gopinath, *Catal. Sci. Technol.*, 2016, **6**, 1746–1756.
- 35 J. Jayaraj, S. Amruth Raj, A. Srinivasan, S. Ananthakumar, U. T. S. Pillai, N. G. K. Dhaipule and U. K. Mudali, *Corros. Sci.*, 2016, **113**, 104–115.
- 36 T. Ishizaki, Y. Masuda and M. Sakamoto, *Langmuir*, 2011, **27**, 4780–4788.
- 37 H. Ashassi-Sorkhabi and M. Es'haghi, *Corros. Sci.*, 2013, **77**, 185–193.
- 38 R. Srinivasu, A. Sambasiva Rao, G. Madhusudhan Reddy and K. Srinivasa Rao,

*Def. Technol.*, 2015, **11**, 140–146.

39 V. V. . Reddy, B. Ramamoorthy and P. K. Nair, *Wear*, 2000, **239**, 111–116.

## Chapter 3

# *Morphology and characteristics of electroless nickel boride-Layered double hydroxide composite coating on Aluminium A356 alloy*



### **Abstract**

A nickel boride-layered double hydroxide (Ni-B-LDH) hydrophobic surface has fabricated on A356 aluminium alloy surface by electroless method. The anti-corrosion and anti-wearing performances were studied with varying amount, from 0 to 5 wt.%, of LDH in the nickel boride matrix. The composite coating with highest water contact angle having the value of 120° was observed for Ni-B containing 0.5 wt.% of LDH. This could be attributed to the increased surface roughness offered by the LDH layers. Potentiodynamic polarization measurements in 3.5 wt.% NaCl solution indicate significant decrease in the corrosion current density ( $i_{corr}$ ) values for LDH added composite coating with a lowest of  $3.96 \times 10^{-6} \text{ A cm}^{-2}$  for 0.5 wt.% of LDH. This may be due to the combined effect of both coating hydrophobicity and feasibility for chloride ion intake by ion exchange mechanism of LDHs. Improved wear resistance was obtained for composite coated aluminium with minimum wear rate for 1% LDH added coating. Stable tribolayer formation in presence of LDH gave higher wear resistance.

### **3.1. Introduction**

Aluminium alloys are potential lightweight materials used for multifunctional applications including structural, automotive, aerospace, building, and household sectors owing to their characteristic features of low density, high specific strength and flexibility. However, these materials and their components experience failures during service owing to wearing and corrosion.<sup>1</sup> High wear rate and deterioration of passive aluminium oxide film by aggressive environments have great concern.<sup>2,3</sup> Surface protective coatings based on electroless nickel boride (Ni-B) can provide improved wear resistance, controlled frictional behaviour and resistance to corrosion.<sup>4-8</sup> The columnar morphology of Ni-B deposit helps to retain liquid lubricants under adhesive wearing conditions.<sup>9</sup> However, wear debris and dust particles from the surroundings entrapped in the lubricants can trigger the material removal.<sup>10</sup> To avoid this situation, solid state lubricious nickel-based coatings have been established.<sup>11-14</sup>

Metallic composite coating in presence of secondary particles (metal oxides, carbides and nitrides), nanotubes, layered materials etc. have been developed for improvement in tribological behaviour and corrosion resistance.<sup>15</sup> Electrochemical redox reaction occurring in presence of an electrolyte on the metal surface is the main reason for corrosion mechanism. Hence, reducing the availability of moisture or any electrolyte at the metal surface has the major concern regarding corrosion process. The coatings with thin layers of hydrophobic behaviour can successfully prevent electrolyte path towards base substrate. Hydrophobic nickel film by electrodeposition method can reach the water contact angle as high as  $160.3 \pm 1.5^\circ$ . Rough cauliflower/thorn-like surface texture allow trapping air below the water droplet and can prevent the liquid to reach the copper substrate.<sup>16-19</sup> Secondary modification of nickel coating with stearic acid<sup>20,21</sup> or myristic acid<sup>22</sup> possess super-hydrophobic property showing excellent self-cleaning as well as anticorrosion performance. Hydrophobic composite coatings of Nickel- polytetrafluoroethylene (PTFE)<sup>23</sup> and an anticorrosive three-layer Ni-P, TiO<sub>2</sub>/ZnO and octadecyltrimethoxysilane (ODS)<sup>24</sup> are also been developed.

Layered double hydroxide is one of the prospective reinforcements to make multifunctional composite coatings. LDH reinforced polymer matrix composite coatings exhibit anti-corrosive nature due to their anion-exchange behaviour<sup>25,26</sup> and anti-wearing by sliding of nanoplatelets.<sup>27</sup> Besides, in-situ bare LDH deposits on metal surfaces are also studied.<sup>28</sup> However, the studies on LDH metallic nanocomposite coatings are very few. Zn-Al LDH nanoplatelets incorporated in the nickel matrix by electrodeposition exhibit higher corrosion resistance than pure nickel.<sup>29</sup> A water-based lubricant made up of oleylamine-modified Ni-Al LDH nanoplatelets give excellent tribological properties. The nanoplatelets form an interlayer of lubricating film at the contact area to avoid direct collision.<sup>27</sup> LDH-based polymer matrix composite coating resulted in an outstanding resistance to stone chips for automotive applications.<sup>30</sup> LDH-polyurethane powder coating shows higher hardness, resistance to cupping and scratch with other properties like higher contact angle and lower surface free energy.<sup>31</sup>

In the present work, a metallic composite coating composed of nickel boride matrix and Ni-Al LDH as the reinforcement was aimed to get more reliable wear and corrosion resistance. The effect of Ni-Al LDH on Ni-B coating was investigated by electroless deposition of nickel-boride alloy and nickel-boride-LDH composite coatings on aluminium A356 alloy (Al-7Si-0.35Mg) with varying percentages of LDH. The coating morphology was determined by scanning electron microscopy (SEM). X-ray photoelectron spectroscopy (XPS) and X-ray diffraction (XRD) were used for elemental composition and structural characterisations, respectively. Water contact angle measurements were done to find out the hydrophobicity of the coatings. Potentiodynamic polarisation measurements and electrochemical impedance spectroscopy were carried out for corrosion resistance studies.

## **3.2. Experimental**

### **3.2.1. Materials**

Nickel chloride (98%), aluminium nitrate (98.5%), nickel nitrate (98%), ammonia (30%), thiourea (99%), lactic acid (85%), ferric chloride (96%), and sodium chloride (99%) were bought from Sigma-Aldrich Co. Ltd., USA. Sodium dodecyl

sulfonate and NaCl (99%) were purchased from Merck, India. Other chemicals; sodium borohydride (98%), disodium ethylenediaminetetraacetate dehydrate ( $\text{Na}_2\text{EDTA}$ -98%), sodium sulphite (97%), and NaOH (97%), were procured from SD Fine chemicals, India. The chemicals as obtained were used for the synthesis and coatings.

### **3.2.2. Ni-Al LDH Synthesis**

Ni-Al LDH synthesis was carried out in a two-neck round bottom flask under nitrogen atmosphere by the co-precipitation method. Aluminium nitrate, nickel nitrate, and urea were dissolved in distilled water to get the concentrations of 5, 10 and 35 mM, respectively. Then the round bottom flask containing the solution was kept at 100 °C under continuous stirring for 24 h. The precipitate obtained was washed with hot distilled water to remove unreacted ions and vacuum dried for 24 h at 60 °C.

### **3.2.3. Coating preparation**

Ni-B-LDH composite coatings and Ni-B alloy coating were done on 30×20×3 mm A356 aluminium alloy strip. The strips were polished up to 1000 grit size SiC abrasive paper and cleaned under ultrasonication with acetone. Alkaline etching (20 g/L NaOH) and acid pickling (100 g/L  $\text{H}_2\text{SO}_4$  and 25 g/L HCl) were done for 1 minute to remove the other impurities and aluminium oxide. The washed alloy were kept for zincation in a solution containing zinc oxide- 62.5 g/L, sodium sulphate-0.25 g/L, sodium potassium tartrate-7.5 g/L, NaOH-6.25 g/L, and anhydrous ferric chloride-5 g/L for 2 minute and rinse with dilute  $\text{HNO}_3$  for eliminating the excess  $\text{Zn}^{2+}$  ions from the surface. Further, the Zn-activated alloy was treated with  $\text{SnCl}_2$  solution (5 g/L  $\text{SnCl}_2$  dissolved in 25 g/L HCl) and  $\text{PdCl}_2$  solution (0.01 g/L  $\text{PdCl}_2$  dissolved in 5 g/L HCl). The zinc and palladium activated substrate was used for electroless plating. Sodium borohydride,  $\text{NaBH}_4$  (4 g/L) was added as drops for 1 h at pH 8.5 under agitation by magnetic stirring. The alkaline pH was attained by adding ammonia solution to the bath. All the coating parameters and constituents of Ni-B LDH bath are given in Table 3.1.

**Table 3.1:** Ni-B LDH bath parameters and constituents.

| Bath constituents / parameters | Concentration / values |
|--------------------------------|------------------------|
| Nickel chloride                | 10 g/L                 |
| Na <sub>2</sub> EDTA           | 10 g/L                 |
| Sodium borohydride             | 4 g/L                  |
| Lactic acid                    | 10 mL/L                |
| Thiourea                       | 0.4 g/L                |
| LDH                            | 0.1, 0.2, 0.4 & 1g/L   |
| Bath temperature               | 60°C                   |
| pH of solution                 | 8.5                    |
| Magnetic stirring              | 1000 rpm               |

### 3.2.4. Sample analysis

#### 3.2.4.1. Surface characterizations

The surface morphology of LDH, Ni-B coating and LDH co-deposited Ni-B coatings by the electroless process were studied using SEM, TEM (JEOL 2010 transmission electron microscope), X-ray diffraction (XEUSS SAXS/WAXS system, Germany), EDS, and FTIR. The instrumental specifications are given in section 2.2.3.1 of chapter 2. All the characterizations on the coated surface were carried out on a 5×5 mm sample taken from the coated material. The coating surface roughness was measured using profilometer (Bruker DektakXT profilometer, Germany).

#### 3.2.4.2. Contact angle measurements

Hydrophobicity of the coated specimens was measured by KRUSS drop shape analyzer (DSA30) using distilled water of 4 μL drop size with automatic multi-liquid dispenser, monochromatic cold light source and accompanying software. The average of three droplets at different places of a sample has been used to get the contact angle.

### **3.2.4.3. Corrosion analysis**

Corrosion performance of the coated as well as uncoated samples at ambient conditions in 3.5 wt.% NaCl solution was measured by a conventional three-electrode cell using CH Instruments electrochemical workstation (CHI608E) as explained in chapter 2.

### **3.2.4.4. Pin on disc wear analysis**

Dry wear rate of the composite coatings were measured by a pin on disc wear analysis machine (TR-20, DUCOM). Aluminium substrate, Ni-B alloy and Ni-B-LDH composite coated (as deposited) pins with 30 mm length and 6 mm diameter were the specimens. High carbon EN31 steel alloy disc was the moving counter surface. The disc was cleaned with acetone prior to each test. The tests were conducted with applied loads of 1, 2 and 5 N at sliding speed of 0.4 m/s upto 500 meters at laboratory conditions. The wear rates were calculated by weighing the pins after and before the test. The equation used was, specific wear rate,  $k = \Delta P/FL$ . Where  $\Delta P$  is the change in weight (kg), F is the load given (N) and L is the sliding distance (m).

## **3.3. Results and discussion**

### **3.3.1. Ni-Al LDH reinforcement**

#### **3.3.1.1. Morphology**

Scanning electron micrograph and transmission electron micrograph of synthesised LDH are given in Figure 3.1. Two-dimensional plate-like layered structure with 600-700 nm diameter and 10-15 nanometres thickness was obtained. The EDS analysis (given as inset of Figure 3.1a) shows the Ni-Al LDH composed of Ni, Al, N and O. Aluminium and nickel are in the ratio of 1:2 as for a typical layered double hydroxide.<sup>32</sup> Presence of nitrogen is due to the intercalated nitrate ion and the oxygen from nitrate ion as well as water molecules between the layers.

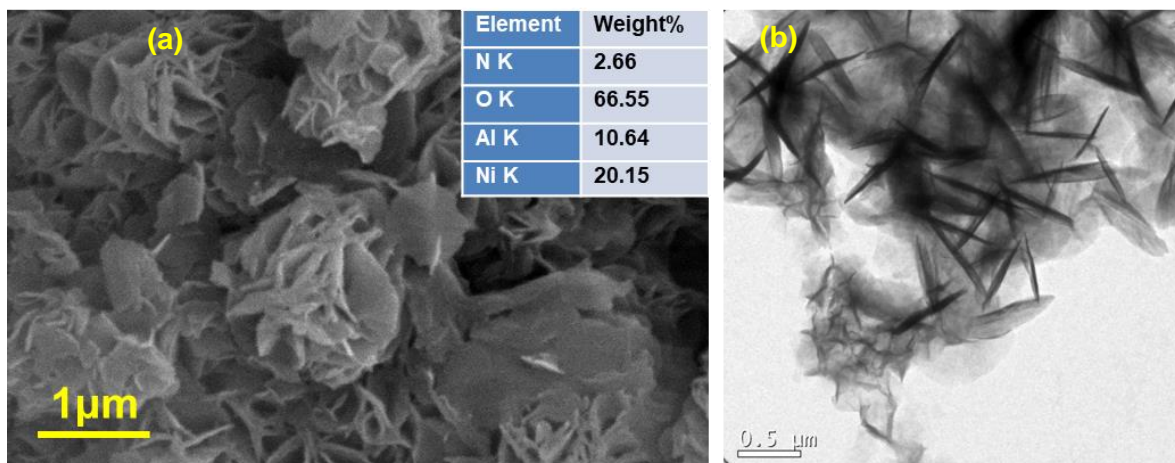


**Figure 3.1:** (a) SEM and (b) TEM micrographs of synthesised Ni-Al LDH.

### 3.3.1.2. Structural analysis

Fourier-transform infrared spectrum and X-ray diffraction pattern of synthesised Ni-Al LDH are shown in Figure 3.2a and Figure 3.2b, respectively. The IR spectrum consist of a broad band at  $3468\text{ cm}^{-1}$  corresponds to the hydroxyl stretching mode of metal hydroxide host layer and water molecules present in the gallery space. A low intensity band at  $1630\text{ cm}^{-1}$  represents H-O-H bending mode of interlayer  $\text{H}_2\text{O}$ .<sup>33</sup> Existence of nitrate ion can be detected as the sharp band at  $1383\text{ cm}^{-1}$  by the antisymmetric stretching vibrations.<sup>34</sup> The peak at  $610\text{ cm}^{-1}$  is attributed to the bending of M-OH bond. From the XRD pattern, the crystalline layered structure with characteristic peaks corresponding to (003), (006) and (012) planes are observed. Based on the Bragg's law, the d-spacing calculated from points of fundamental reflection (003) is 0.76 nm, which indicate the nitrate ions are lying parallel to the metal-hydroxide layer.<sup>35</sup>

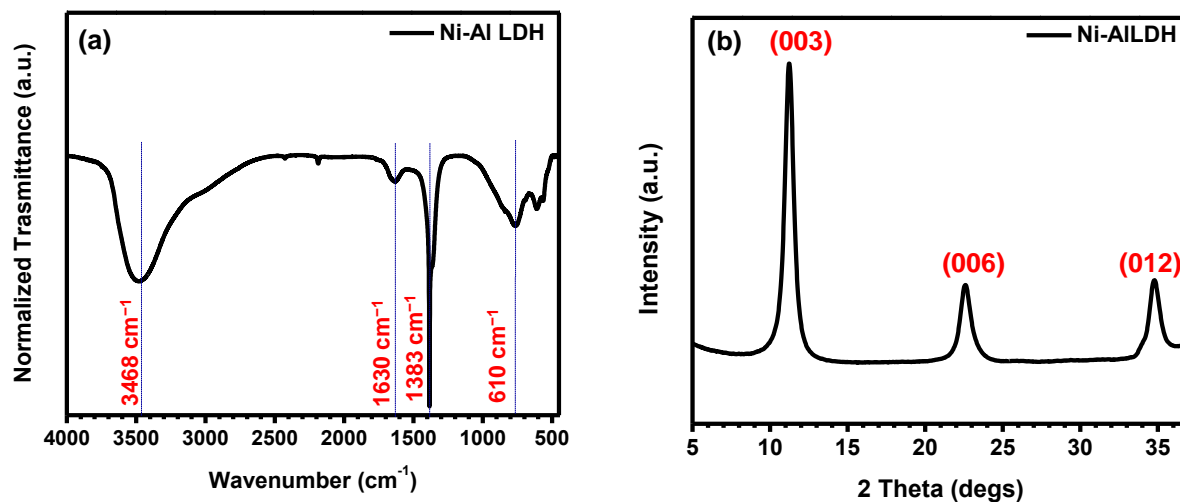


**Figure 3.2:** (a) FTIR and (b) XRD of synthesised Ni-Al LDH.

### 3.3.2. Ni-B-LDH composite coating

#### 3.3.2.1. Coating morphology

Figure 3.3 shows the SEM images of aluminium substrate (a), Ni-B coating (b) and Ni-B-LDH composite coatings with varying percentages of LDH (c-f). The Ni-B coating exhibit typical nodular surface same as the previous studies.<sup>15</sup> 0.5 wt.% of LDH addition in Ni-B matrix doesn't give significant change in the surface morphology. However, the co-deposition of LDH increases the number of nucleation centers to begin the deposition process. Additionally, it is important to give a final Ni-B covering on top of the composite deposit to get more compactable surface. Otherwise some of the reinforcements loosely adhere on the coating, which may reduce the coating properties. Incorporation of 1 wt.% LDH give a modified denser surface than electroless Ni-B coating. Layered materials at boundaries of nickel crystallites can hold them together to form an evener structure. 2 wt.% and 5 wt.% LDH addition produce large quantity of agglomerates within the composite coating as presented in the Figure 3.3e and 3.3f.

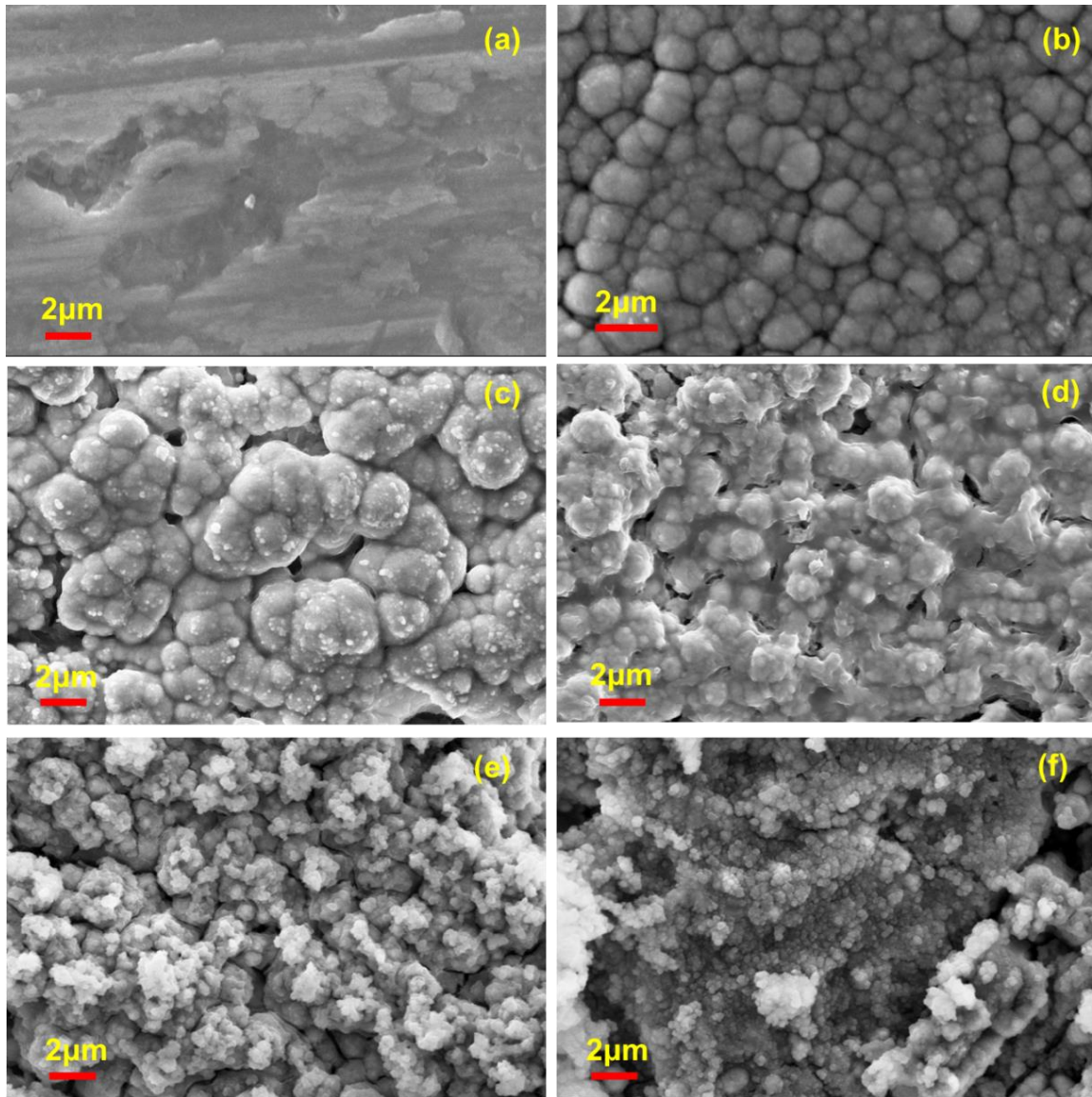


**Figure 3.3:** SEM micrographs of the surface texture of (a) A356 alloy, (b) electroless Ni-B, (c) Ni-B-0.5% LDH, (d) Ni-B-1% LDH, (e) Ni-B-2% LDH and (f) Ni-B-5% LDH composite coatings.

### 3.3.2.2. XRD analysis

X-ray diffraction patterns of prepared Ni-B-1%LDH composite coated aluminium alloy surface and Ni-Al LDH are shown in Figure 3.4. Smaller percentage of reinforcement could not produce identifiable peaks of layered structure. The characteristic reflections of (003), (006) and (012) planes of crystalline LDH are also observed for the composite coated sample, which confirms the presence of LDH in the

composite coating. One more peak at  $2\theta = 28.41^\circ$  is due to the presence of silicon (111) plane which is present in A356 alloy.

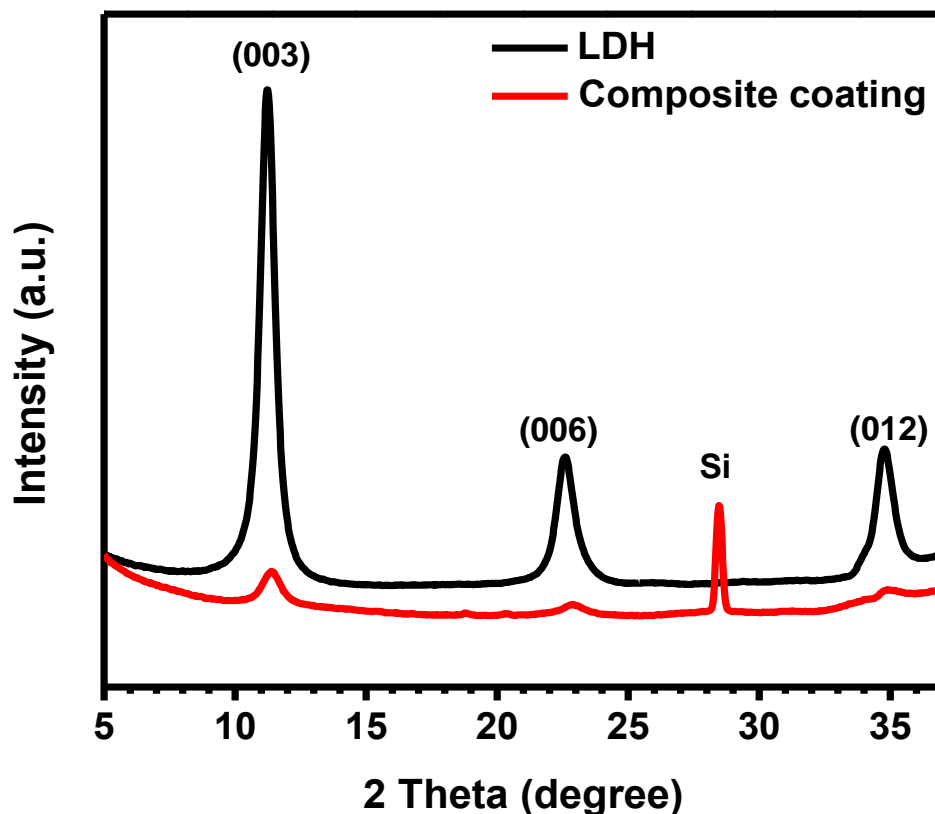


**Figure 3.4:** X-ray diffraction patterns: (a) Ni-Al LDH and (b) Ni-B-LDH coating.

### 3.3.2.3. XPS analysis

The composition of Ni-B LDH composite coating was further studied by X-ray photoelectron spectroscopy (XPS). Presence of Ni, B, Al, N, and O is confirmed from the survey spectrum (Figure 3.5a). Three broad peaks observed between 600 eV to 800 eV denote Ni LMM, Ni LMM1, and Ni LMM2 transitions of Ni auger peaks.<sup>15</sup> An additional peak corresponding to C 1s generated from the background is used as the reference line.

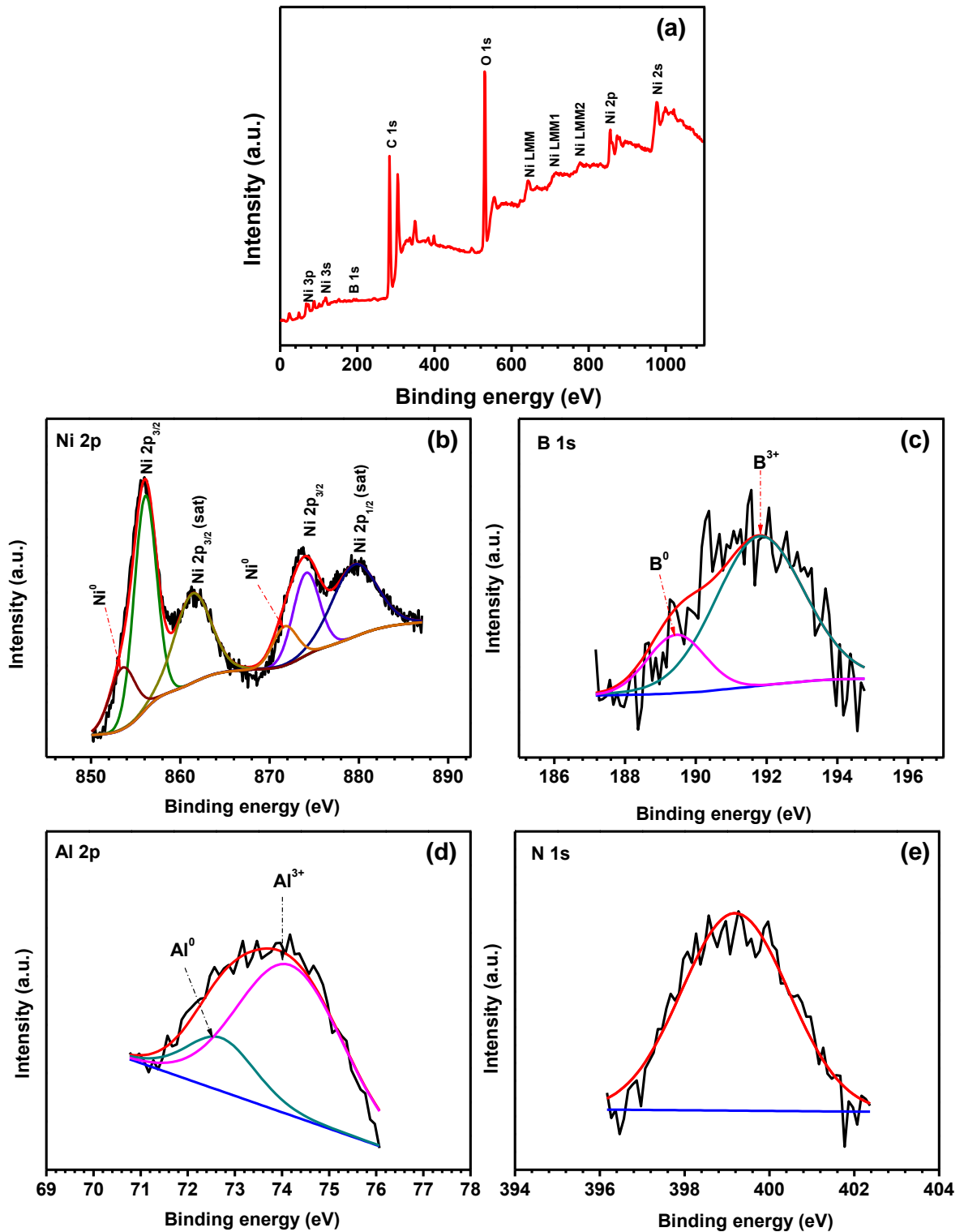


**Figure 3.5:** XPS (a) survey spectrum of Ni-B-LDH and high-resolution spectra of (b) Ni 2p, (c) B 1s, (d) Al 2p, and (e) N 1s.

The high resolution spectrum of Ni 2p (Figure 3.5b) exhibits peaks corresponding to metallic ( $\text{Ni}^0$ ) as well as oxidised state ( $\text{Ni}^{2+}$ ) of nickel. Upon deconvolution, the peaks centred at 853.43 eV and 871.46 eV represents the elemental nickel of amorphous Ni-B alloy.<sup>36</sup> Typical  $\text{Ni}^{2+}$  peaks at 855.96 eV ( $\text{Ni}(\text{OH})_2$ ) and 874.16 eV for Ni 2p<sup>3/2</sup> and Ni 2p<sup>1/2</sup> states were observed along with two satellite bands of complex nickel at 861.56 eV and 879.38 eV.<sup>37</sup> The oxidised nickel is observed due to the incorporated LDH as well as some of the NiO formation on the surface.<sup>36,38</sup> Boron exists as elemental,  $\text{B}^0$ , and oxidized state,  $\text{B}^{3+}$ , resulting from the oxidation by atmospheric oxygen.<sup>39</sup> B 1s spectrum (Figure 3.5c) consists of two bands at 189.2 eV ascribed for  $\text{B}^0$  of NiB alloy and 191.96 eV for  $\text{B}^{3+}$  of boron oxide.<sup>40</sup> The higher energy shift of elemental boron in the composite coating compared to pure boron (187.1 eV) signifying the partial electron transfer from boron to the nickel.<sup>41</sup> The bonding electrons of boron occupy vacant d-orbitals of nickel, making the B electron-deficient and the Ni metal electron-enriched.<sup>36</sup> Deconvoluted Al 2p spectra (Figure 3.5d) exhibit a peak at 74.03 eV for  $\text{Al}^{3+}$  of LDH and another small one at 72.5 eV for  $\text{Al}^0$  of substrate material. Peak corresponding to N 1s (Figure 3.5e) from intercalated nitrate ion of the LDH is observed at 399.26 eV.<sup>42</sup>

#### **3.3.2.4. Surface roughness**

Surface roughness values of the samples are given in Figure 3.6. The composite coatings roughness values are higher than the LDH-free counterpart and aluminium alloy substrate. Presence of bulky layers induces more coarseness to the deposits. Increase in the LDH percentage gradually increases the surface roughness. 5 wt.% of LDH added composite coating exhibit a very high value due to the surface adsorbed agglomerated layered double hydroxides.

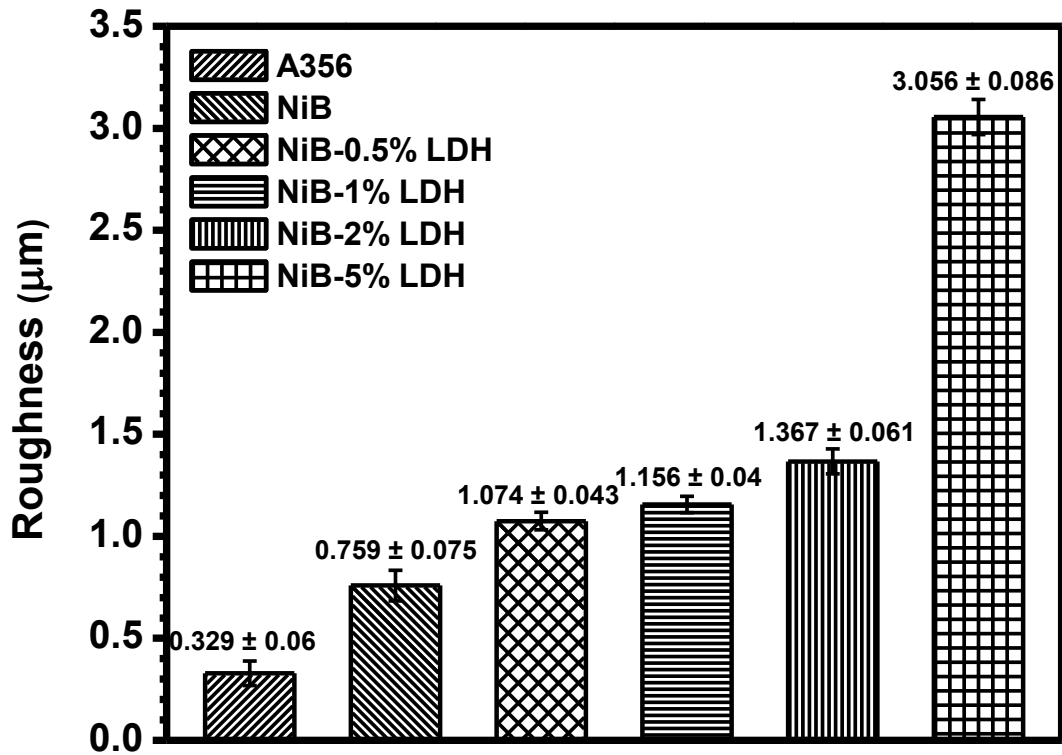


**Figure 3.6:** Average surface roughness of aluminium alloy and composite coatings containing 0 to 5 % of LDH.

### 3.3.2.5. Contact angle measurements

Corrosion resistance of a material highly depends on hydrophobicity owing to the unavailability of electrolytes at the surface. Hence the wettability test by contact angle measurements was done to find out the effect of LDH in Ni-B-LDH composite coatings at different weight percentages of LDH. Figure 3.7 illustrates the water contact angle of Al-alloy, Ni-B coated and composite coated surfaces as deposited condition. The water contact angle of A356 alloy surface is  $84.5 \pm 2^\circ$  and the Ni-B alloy coating give a slight increase to  $96 \pm 3^\circ$ . The Ni-B-LDH composite coating contains 0.5 wt.% LDH shows the highest contact angle of  $120 \pm 2^\circ$ . However, it is observed that the values are decreased in presence of higher amounts of LDHs in the coating. That is, 1 wt.% LDH possesses  $106 \pm 4^\circ$ , 2 wt.% has  $85 \pm 3^\circ$ , and 5 wt.% shows  $46 \pm 4^\circ$ . This suggests that the higher surface roughness offered by the LDH induced grains increases the quantity of air to be trapped between water and solid surface.<sup>43</sup> Further

increase of LDH percentage in the composite coating brings the hydrophilic characteristics of LDHs to the coating instead of surface roughness based hydrophobicity. At very low percentage of LDH, they can be completely covered by thin layer of Ni-B deposit. Increase in LDH wt.% lead to the agglomeration and they may physically adsorb on the surface instead of co-deposition along with nickel boride, which in turn decrease the hydrophobic behaviour.

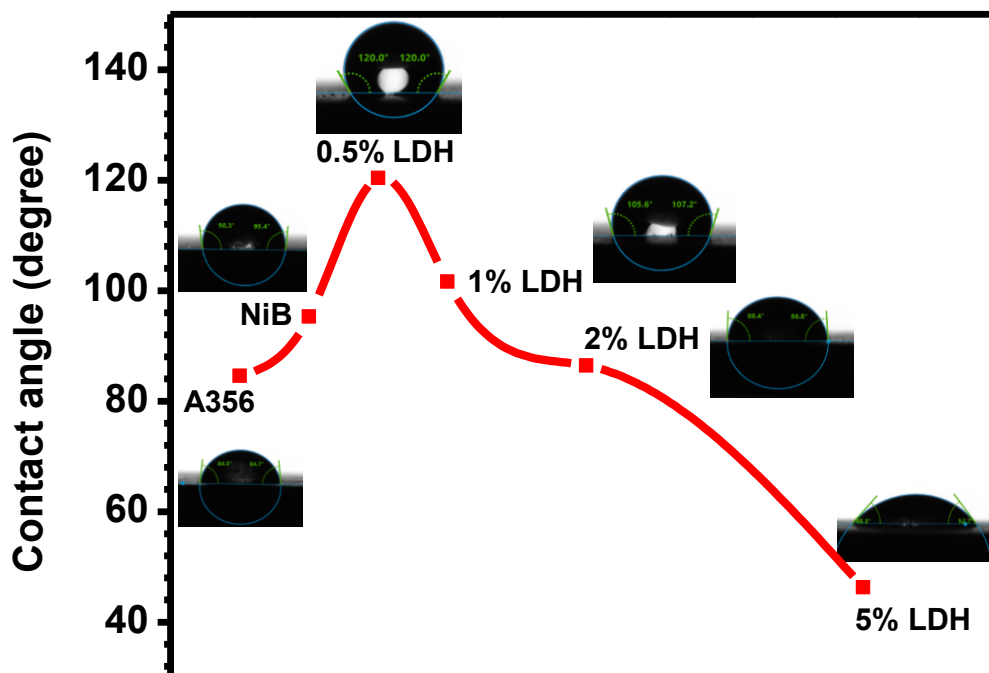


**Figure 3.7:** Water contact angle of aluminium alloy and composite coatings containing 0 to 5 % of LDH.

### 3.3.2.6. Electrochemical corrosion measurements

Electrochemical impedance spectroscopy and potentiodynamic polarization measurements were done to study the electrochemical behaviour of corrosion process of bare aluminium alloy, Ni-B coating and Ni-B-LDH composite coatings. Figure 3.8 shows the potentiodynamic polarization curves (Tafel plots) of samples. The values of corrosion potential,  $E_{corr}$  and corrosion current density,  $i_{corr}$  obtained by extrapolation of cathodic and anodic curves have shown in Table 3.2. The  $E_{corr}$  value of bare aluminium alloy is -0.807 V vs. SCE and the Ni-B coating has a comparable value, while

the composite coated containing 0.5 wt.% of LDH changed slightly to a negative potential. However, more amount of LDH addition shifted the  $E_{corr}$  towards more positive potential and the value increases with increase in LDH percentage. Though the  $E_{corr}$  value shifted to negative side, 0.5 LDH composite exhibited large passivation region compared to higher weight percentages. The breakdown potential ( $E_{break}$ ) values were obtained at -0.676, -0.684 and -0.713 V vs. SCE for 0.5, 1 and 2 wt.% of LDH respectively. This may be due to the effective prevention of aggressive anions by dispersed LDH towards the metal surface, which signifying the self-healing property of the coating by reducing the anodic reactions till the  $E_{break}$  potential.<sup>44</sup> The corrosion resistance of a material is inversely proportional to the  $i_{corr}$  values. The  $i_{corr}$  of 0.5 LDH Ni-B composite coating has the lowest among all the samples with a value of  $3.962 \times 10^{-6} \text{ A cm}^{-2}$ . It is around one order transformation from the corrosion current density of bare aluminium ( $27.86 \times 10^{-6} \text{ A cm}^{-2}$ ). All the coatings show better anticorrosion performance than the aluminium alloy (Table 3.2). Though the LDH addition gives higher corrosion resistance, more weight percentage reduces the performance owing to the LDH agglomeration as well as lower hydrophobicity.

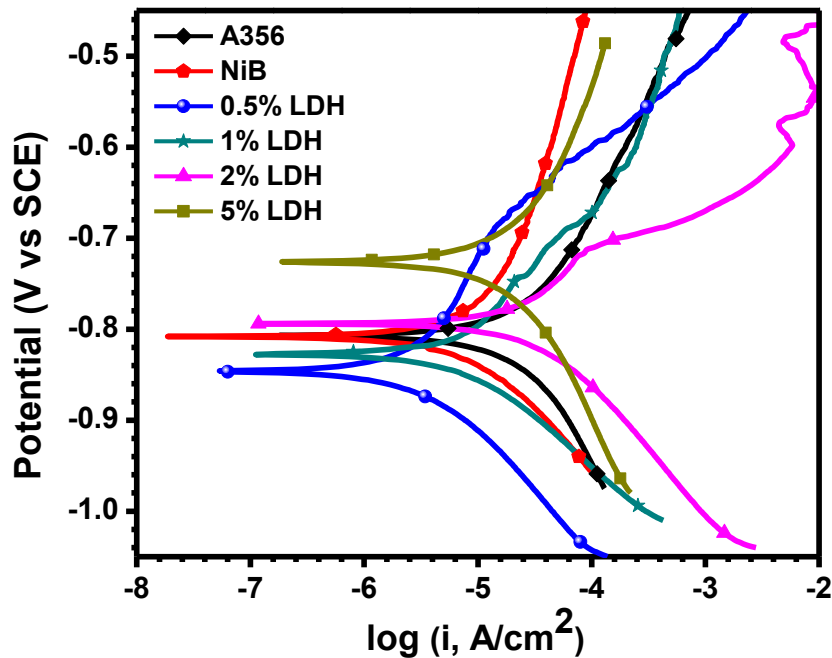


**Figure 3.8:** Tafel plots of aluminium alloy, Ni-B and Ni-B-LDH (0.5 - 5 wt.% of LDH) composite coatings.

**Table 3.2:**  $E_{\text{corr}}$  Vs. SCE and  $i_{\text{corr}}$  values calculated from the Tafel plot.

| Sample ID    | $E_{\text{corr}}$ (V vs. SCE) | $i_{\text{corr}}$ (A cm <sup>-2</sup> ) |
|--------------|-------------------------------|---|
| A356         | -0.807                        | 27.86 x 10 <sup>-6</sup>                |
| NiB          | -0.808                        | 9.970 x 10 <sup>-6</sup>                |
| 0.5 wt.% LDH | -0.846                        | 3.962 x 10 <sup>-6</sup>                |
| 1 wt.% LDH   | -0.828                        | 8.464 x 10 <sup>-6</sup>                |
| 2 wt.% LDH   | -0.794                        | 17.05 x 10 <sup>-6</sup>                |
| 5 wt.% LDH   | -0.726                        | 21.27 x 10 <sup>-6</sup>                |

Nyquist plots of EIS measurements exhibited in Figure 3.9. The graphs corresponding to aluminium alloy and Ni-B coated surface show a capacitive behavior at the high frequency and a Warburg diffusional behavior at the low frequency. However, the charge transfer resistance ( $R_{\text{ct}}$ ) of Ni-B coating (1665  $\Omega$  cm<sup>2</sup>) is slightly greater than the bare material (1152  $\Omega$  cm<sup>2</sup>). For Ni-B-LDH nanocomposite coating, formation of two capacitive loops at high and middle frequencies represents the coating capacitance and the double layer capacitance respectively. The first loop at high to medium frequency region could be attributed to the barrier effect of LDH by ion exchange behavior. The second loop at medium to low frequency relates to the charge transfer resistance. The LDH could also induce zig-zagging of water and ionic transport towards the substrate like any other layered reinforcements.<sup>45</sup> Since, low frequency response is related to corrosion phenomena, probably due to the deformation of coatings; different loop diameters for each sample with the largest by composite coating containing 0.5 wt.% of LDH clearly reveal the improvement in corrosion resistance. The  $R_{\text{ct}}$  values of composite coating concerning the LDH wt.% is in the order of 5% LDH (1539  $\Omega$  cm<sup>2</sup>) < 2% LDH (1911  $\Omega$  cm<sup>2</sup>) < 1% LDH (4320  $\Omega$  cm<sup>2</sup>) < 0.5% LDH (8247  $\Omega$  cm<sup>2</sup>) > 0% LDH (1665  $\Omega$  cm<sup>2</sup>).

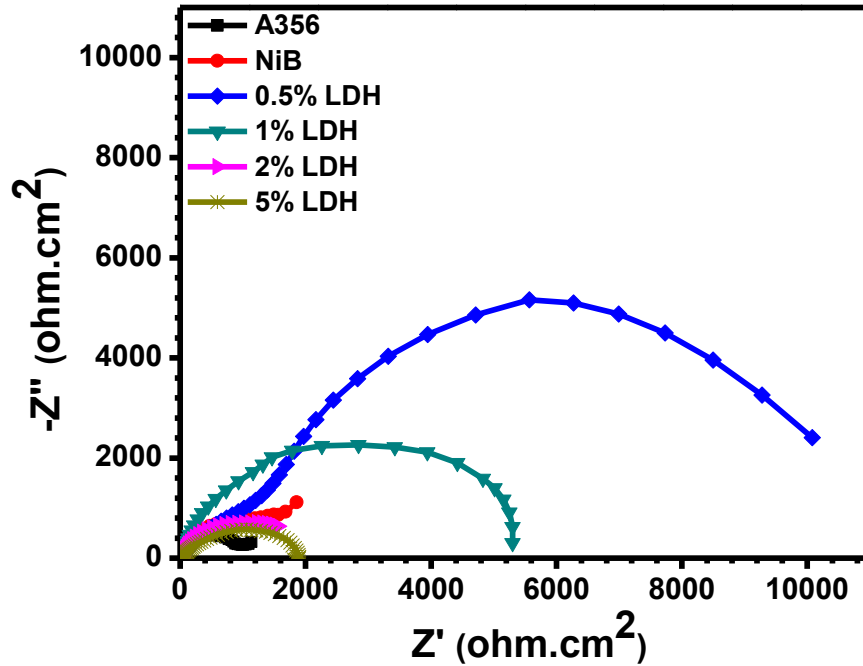


**Figure 3.9:** Nyquist plots of aluminium alloy, Ni-B and Ni-B-LDH (0.5-5 wt.% of LDH) composite coatings.

### 3.3.2.7. Anti-corrosion mechanism

Probable anti-corrosion mechanism of Ni-B-LDH composite coating is given as Figure 3.10. The mechanism includes two stages; firstly, the LDHs can act as an obstacle for aggressive anions as well as water molecules to reach the metal surface and secondly, they can capture corrosive  $\text{Cl}^-$  ions and release  $\text{NO}_3^-$  ions by ion exchange property. Tedim et al.<sup>46</sup> also observed that the nitrate-intercalated LDHs are efficient chloride nanotraps by anion-exchange process. Therefore, the LDHs can delay coating degradation and the corrosion process.

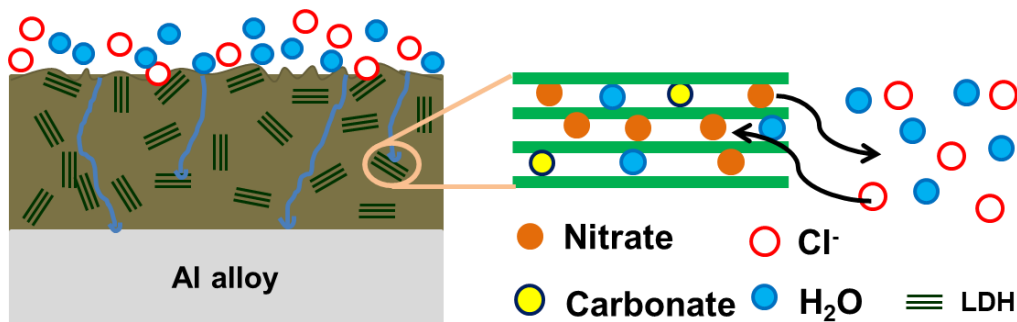


**Figure 3.10:** Schematic demonstration of the anti-corrosion mechanism of Ni-B-LDH composite coating.

### 3.3.2.8. Wear analysis

Specific wear rates of coated and uncoated samples under different loadings are given in Figure 3.11. It is identified that the composite coated systems exhibit lesser wear rate with negligible weight change compared to Ni-B and aluminium alloy. The wear rate of each sample increases by increase of applied load. The debris from the Ni-B-LDH coating and the counter steel disc have resulted in the formation of an intermediate tribolayer, which prevents direct contact of aluminium and counter surface.<sup>47</sup> 0.5 wt.% of LDH itself give considerable improvement of wear resistance. Maximum wear resistance is observed for 1 wt.% LDH reinforced NiB composite coating. Further addition of LDH up to 5 wt.% shows slight reduction in the property, which is due to the delamination of tribolayer by agglomerated layers. The interfacial bonding between nickel matrix and the 1 wt.% LDHs were more compactable as seen in surface morphology (Figure 1).

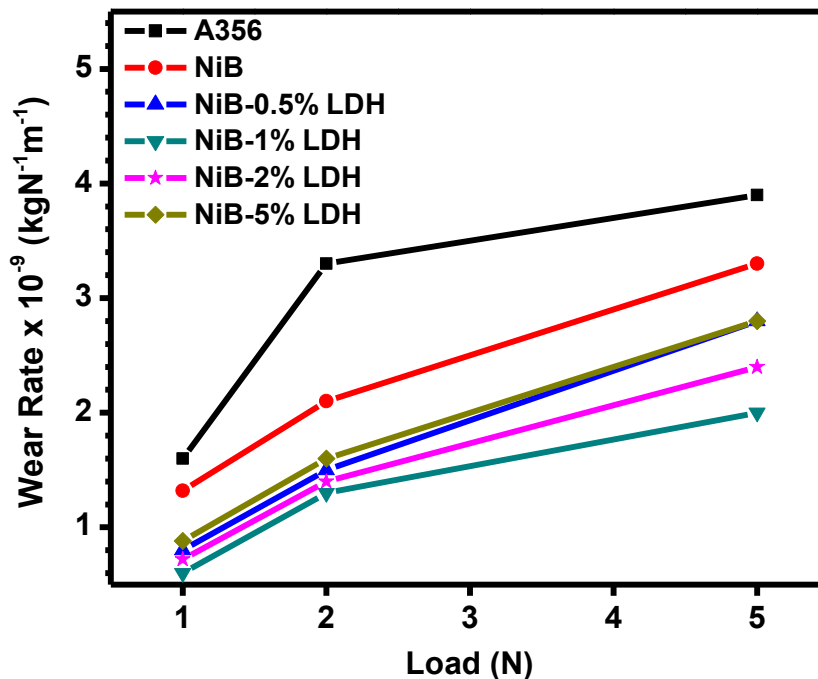


**Figure 3.11:** Wear rates of aluminium alloy and composite coatings containing 0 to 5 % of LDH samples as a function of applied load.

SEM micrographs of wear tracks observed at the sample surface after the wear test with 2N applied load are shown in Figure 3.12. Aluminium alloy exhibited severe wear containing delamination and continuous grooves on the surface. This observation could be attributed to abrasive wearing of comparatively soft aluminium pin by hard steel disc. Ni-B coated sample also show deep grooves on the surface due to the material removal. The material removal produces wear debris and some of them are roughly attached to the Al surface, which is due to the higher wear rate and plastic deformation. The material removal and long grooves formation indicates the bare and Ni-B coated aluminium surface follow the abrasive wear mechanism.<sup>48</sup>

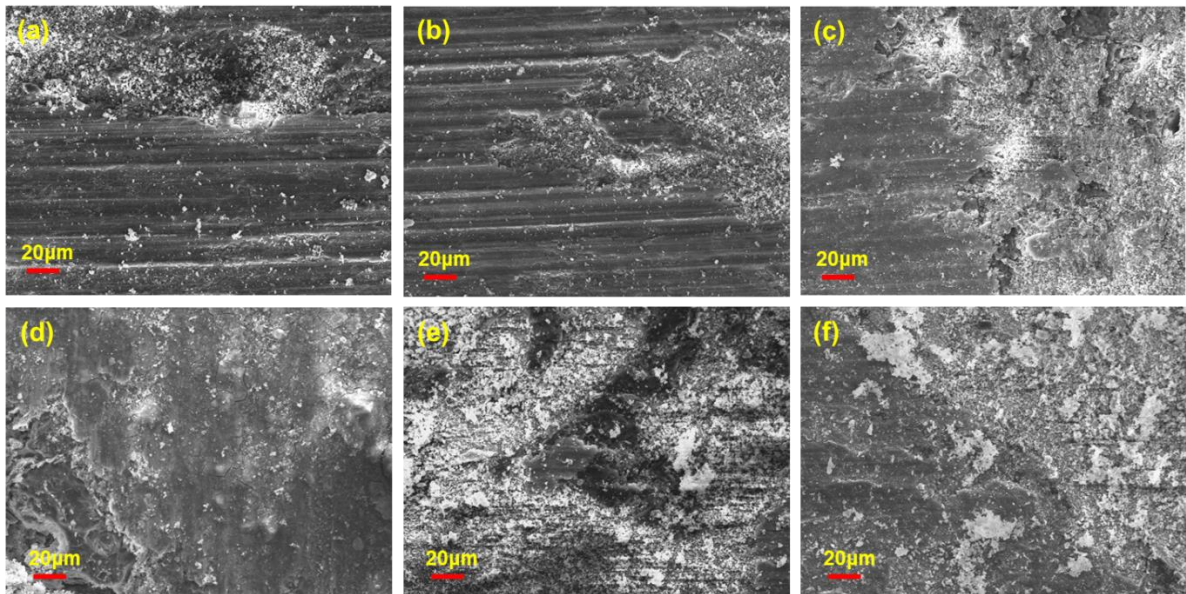


**Figure 3.12:** SEM micrographs of the worn out surface aluminium alloy and composite coatings containing 0 to 5 % of LDH at an applied load 2 N.

The EDS analysis (Figure 3.13) shows the particles are composed of nickel, aluminium and iron as their oxides. On the other hand, the wear tracks are hardly visible for Ni-B-LDH composite coatings. Addition of 0.5 wt.% LDH itself give considerable improvement by showing only shallow grooves formation. Most of the wear debris is remain adhered on the surface to form a compacted mechanically mixed layer (MML). Mechanically mixed composite tribolayer formed by LDH as well as oxides of nickel and aluminium (EDS is given in Figure 3.13) enhances the wear performance. 1% LDH NiB composite coating produced a continuous tribolayer

between two mating surfaces. The tribolayer formation for the composite coatings designates adhesive wear mechanism instead of abrasive wear. Sliding of two surfaces over this layer reduces the wear rate.<sup>49</sup> The EDS analysis clearly shows MML formation with lesser amount of aluminium due to the stable intermediate layer containing LDH. Higher percentage (2 and 5 wt.%) of LDH loading leads to deformed and discontinuous tribolayer owing to the presence of agglomerated layered double hydroxides in the coating. However, the grooves are minor by mild wearing.

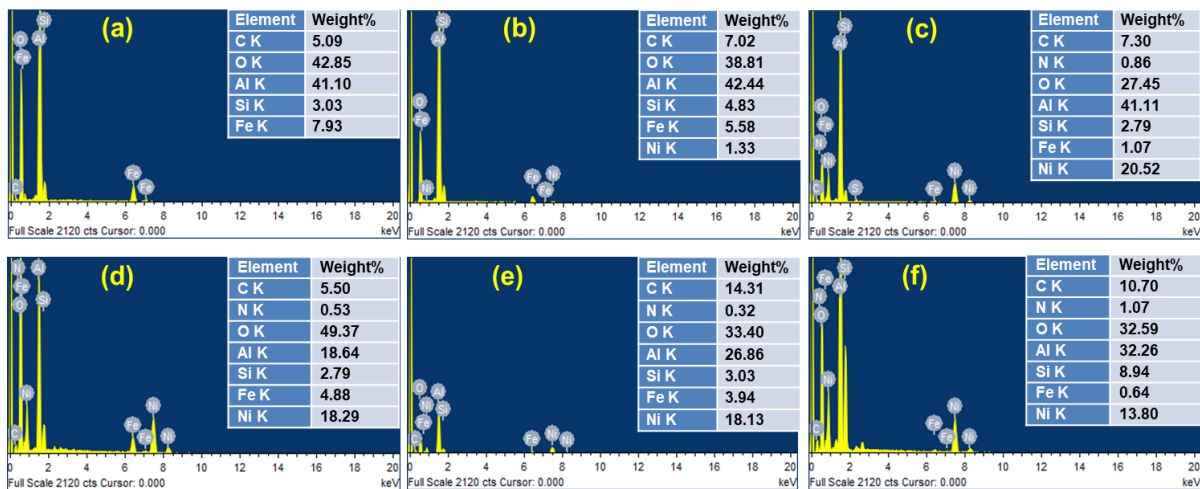


**Figure 3.13:** EDS spectra of the worn out surface aluminium alloy and composite coatings containing 0 to 5 % of LDH at an applied load 2 N.

### 3.4. Conclusions

Ni-B alloy and Ni-B-LDH composite coatings were made effectively on the surface of activated aluminium A356 alloy by autocatalytic reduction mechanism. Uniform nodular surface texture has observed for the coatings. X-ray diffraction patterns show the effective incorporation of LDH into the Ni-B matrix. The corrosion resistance of aluminium alloy has increased significantly for composite coatings compared to Ni-B alloy coating. Better corrosion prevention by the surface layer of LDH added coating may be due to its hydrophobicity and ion exchange capacity in presence of NaCl solution. LDH may enhance the barrier property by zig-zagging the movement of corrosive species towards the metal surface. Maximum corrosion resistance and hydrophobicity were observed for 0.5 wt.% of LDH addition in nickel

matrix. The wear studies on as coated sample showed a considerable improvement in wear resistance compared to that of bare alloy substrate. Maximum wear resistance was observed for 1 wt.% of LDH addition in nickel matrix. The composite coating produced a continuous tribolayer between two surfaces.

## References

- 1 R. J. K. Wood, *Wear*, 2006, **261**, 1012–1023.
- 2 B. Zhang, J. Wang, B. Wu, X. W. Guo, Y. J. Wang, D. Chen, Y. C. Zhang, K. Du, E. E. Oguzie and X. L. Ma, *Nat. Commun.*, 2018, **9**, 2559.
- 3 T. P. Hoar, *Corros. Sci.*, 1967, **7**, 341–355.
- 4 E. Correa, A. A. Zuleta, L. Guerra, M. A. Gómez, J. G. Castaño, F. Echeverría, H. Liu, P. Skeldon and G. E. Thompson, *Wear*, 2013, **305**, 115–123.
- 5 K. Krishnaveni, T. S. N. Sankara Narayanan and S. K. Seshadri, *Surf. Coatings Technol.*, 2005, **190**, 115–121.
- 6 T. S. N. Sankara Narayanan and S. K. Seshadri, *J. Alloys Compd.*, 2004, **365**, 197–205.
- 7 A.-F. Kanta, M. Poelman, V. Vitry and F. Delaunois, *J. Alloys Compd.*, 2010, **505**, 151–156.
- 8 K. N. Srinivasan, R. Meenakshi, A. Santhi, P. R. Thangavelu and S. John, *Surf. Eng.*, 2010, **26**, 153–158.
- 9 T. S. N. S. Narayanan, K. Krishnaveni and S. K. Seshadri, *Mater. Chem. Phys.*, 2003, **82**, 771–779.
- 10 R. S. Dwyer-Joyce, in *Tribology and Interface Engineering Series*, Elsevier, 2005, vol. 48, pp. 681–690.
- 11 K. L. Gilley, J. C. Nino, Y. W. Riddle, D. W. Hahn and S. S. Perry, *ACS Appl. Mater. Interfaces*, 2012, **4**, 3069–3076.
- 12 X. H. Chen, C. S. Chen, H. N. Xiao, H. B. Liu, L. P. Zhou, S. L. Li and G. Zhang, *Tribol.*

- Int.*, 2006, **39**, 22–28.
- 13 H. S. Maharana, A. Basu and K. Mondal, *Surf. Coatings Technol.*, 2018, **349**, 328–339.
  - 14 Y. Fan, Y. He, P. Luo, T. Shi and X. Chen, *J. Electrochem. Soc.*, 2016, **163**, D68–D73.
  - 15 J. K. Pancrecious, J. P. Deepa, V. Jayan, U. S. Bill, T. P. D. Rajan and B. C. Pai, *Surf. Coatings Technol.*, 2018, **356**, 29–37.
  - 16 Z. Yang, X. Liu and Y. Tian, *Colloids Surfaces A Physicochem. Eng. Asp.*, 2019, **560**, 205–212.
  - 17 S. Khorsand, K. Raeissi and F. Ashrafizadeh, *Appl. Surf. Sci.*, 2014, **305**, 498–505.
  - 18 S. Khorsand, K. Raeissi, F. Ashrafizadeh and M. A. Arenas, *Chem. Eng. J.*, 2015, **273**, 638–646.
  - 19 S. Khorsand, K. Raeissi, F. Ashrafizadeh, M. A. Arenas and A. Conde, *Appl. Surf. Sci.*, 2016, **364**, 349–357.
  - 20 Y. Wang, Z. Gu, Y. Xin, N. Yuan and J. Ding, *Colloids Surfaces A Physicochem. Eng. Asp.*, 2018, **538**, 500–505.
  - 21 Y. Liu, X. Yin, J. Zhang, S. Yu, Z. Han and L. Ren, *Electrochim. Acta*, 2014, **125**, 395–403.
  - 22 S. Ding, T. Xiang, C. Li, S. Zheng, J. Wang, M. Zhang, C. Dong and W. Chan, *Mater. Des.*, 2017, **117**, 280–288.
  - 23 D. Iacovetta, J. Tam and U. Erb, *Surf. Coatings Technol.*, 2015, **279**, 134–141.
  - 24 D. Yu, J. Tian, J. Dai and X. Wang, *Electrochim. Acta*, 2013, **97**, 409–419.
  - 25 M. L. Zheludkevich, S. K. Poznyak, L. M. Rodrigues, D. Raps, T. Hack, L. F. Dick, T. Nunes and M. G. S. Ferreira, *Corros. Sci.*, 2010, **52**, 602–611.
  - 26 T. Stimpfling, F. Leroux and H. Hintze-Bruening, *Colloids Surfaces A Physicochem. Eng. Asp.*, 2014, **458**, 147–154.
  - 27 H. Wang, Y. Liu, Z. Chen, B. Wu, S. Xu and J. Luo, *Sci. Rep.*, 2016, **6**, 22748.

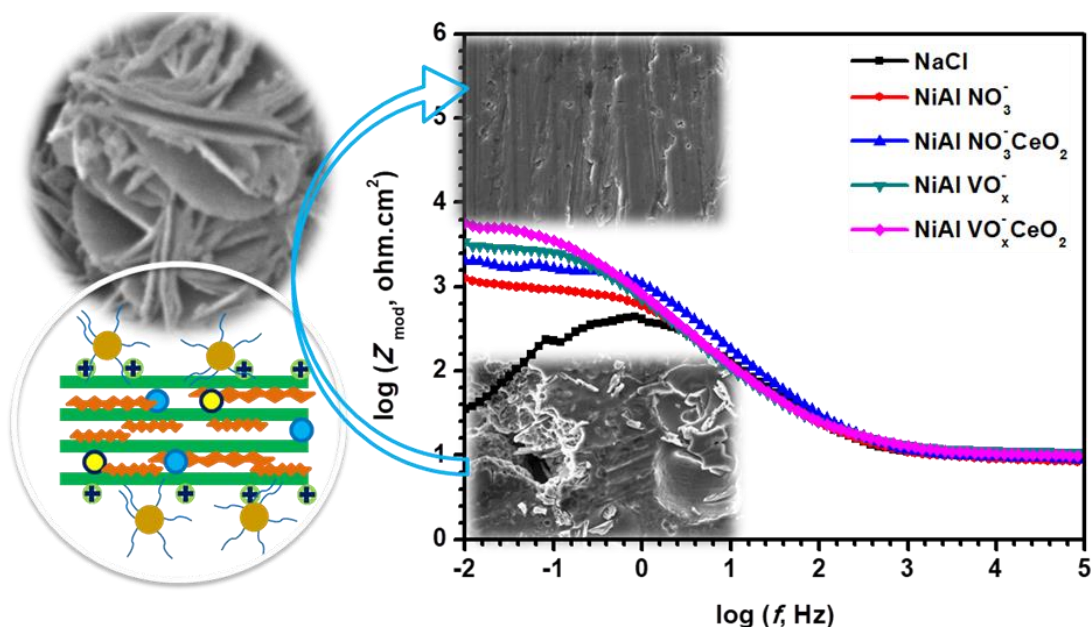
- 28 L. Wang, Q. Zong, W. Sun, Z. Yang and G. Liu, *Corros. Sci.*, 2015, **93**, 256–266.
- 29 R. E. Daugherty, M. M. Zumbach, S. F. Sanders and T. D. Golden, *Surf. Coatings Technol.*, 2018, **349**, 773–782.
- 30 H. Hintze-Bruening, A.-L. Troutier-Thuilliez and F. Leroux, *Prog. Org. Coatings*, 2009, **64**, 193–204.
- 31 B. Pilch-Pitera, M. Kędzierski, E. Olejnik and S. Zapotoczny, *Prog. Org. Coatings*, 2016, **95**, 120–126.
- 32 F. Zhang, L. Guo, S. Xu and R. Zhang, *Langmuir*, 2015, **31**, 6704–6712.
- 33 F. Cavani, F. Trifirò and A. Vaccari, *Catal. Today*, 1991, **11**, 173–301.
- 34 C. A. Antonyraj, P. Koilraj and S. Kannan, *Chem. Commun.*, 2010, **46**, 1902.
- 35 N. Thomas, G. Pradeep Kumar and M. Rajamathi, *J. Solid State Chem.*, 2009, **182**, 592–596.
- 36 W. Zhang, *Int. J. Electrochem. Sci.*, 2018, **13**, 3516–3526.
- 37 F. Muench, M. Oezaslan, M. Rauber, S. Kaserer, A. Fuchs, E. Mankel, J. Brötz, P. Strasser, C. Roth and W. Ensinger, *J. Power Sources*, 2013, **222**, 243–252.
- 38 L. Lv, K. Xu, C. Wang, H. Wan, Y. Ruan, J. Liu, R. Zou, L. Miao, K. (Ken) Ostrikov, Y. Lan and J. Jiang, *Electrochim. Acta*, 2016, **216**, 35–43.
- 39 D. He, L. Zhang, D. He, G. Zhou, Y. Lin, Z. Deng, X. Hong, Y. Wu, C. Chen and Y. Li, *Nat. Commun.*, 2016, **7**, 12362.
- 40 Y. Peng, Q. Chen, J. Xie and W. Lan, *J. Electrochem. Soc.*, 2019, **166**, B521–B523.
- 41 M. Zeng, H. Wang, C. Zhao, J. Wei, K. Qi, W. Wang and X. Bai, *ChemCatChem*, 2016, **8**, 708–712.
- 42 S. Fleutot, J.-C. Dupin, G. Renaudin and H. Martinez, *Phys. Chem. Chem. Phys.*, 2011, **13**, 17564.
- 43 V. Bugatti, S. Livi, S. Hayrapetyan, Y. Wang, L. Estevez, V. Vittoria and E. P. Giannelis, *J. Colloid Interface Sci.*, 2013, **396**, 47–52.

- 44 F. Zhang, C. Zhang, R. Zeng, L. Song, L. Guo and X. Huang, *Metals (Basel)*, 2016, **6**, 85.
- 45 H. Lu, S. Zhang, W. Li, Y. Cui and T. Yang, *ACS Appl. Mater. Interfaces*, 2017, **9**, 4034–4043.
- 46 J. Tedim, A. Kuznetsova, A. N. Salak, F. Montemor, D. Snihirova, M. Pilz, M. L. Zheludkevich and M. G. S. Ferreira, *Corros. Sci.*, 2012, **55**, 1–4.
- 47 J. K. Pancrecius, S. B. Ulaeto, R. Ramya, T. P. D. Rajan and B. C. Pai, *Int. Mater. Rev.*, 2018, **63**, 488–512.
- 48 M. Kök and K. Özdin, *J. Mater. Process. Technol.*, 2007, **183**, 301–309.
- 49 L. Reinert, F. Lasserre, C. Gachot, P. Grützmacher, T. MacLucas, N. Souza, F. Mücklich and S. Suarez, *Sci. Rep.*, 2017, **7**, 42873.

## Chapter 4

### Layered double hydroxide-Ceria hybrid Reinforced

### Epoxy Composite Coating for corrosion resistance



#### Abstract

The present study introduces a modified layered double hydroxide (LDH) based system for corrosion inhibition on dual actions by both active and passive mechanism. Nickel aluminium layered double hydroxide (Ni-Al LDH) intercalated with vanadate ion was further decorated with ceria nanoparticles to enhance the corrosion protection efficiency. The modifications of LDH were confirmed by scanning electron microscopy (SEM), X-ray diffraction (XRD), infrared (IR) and Raman spectroscopy. We have investigated the effect of nanoceria decoration on Ni-Al LDH for the corrosion inhibition efficiency with and without intercalation of vanadate species on A356 aluminum alloy by electrochemical analysis and immersion test. The bare metallic substrates in 3.5 wt % sodium chloride solution containing inhibitor loaded LDH were tested to understand the inhibition mechanism. The presence of stable ceria nanoparticles layer can be an

*effective cathode, which passively protects the metal from corrosive anions and water molecules. The release of vanadate species during anion exchange of LDH with chloride ion in the corrosive environment and formation of polymeric vanadate on the surface actively protects the metal from further corrosion. These results show that an enhancement of the corrosion protection can be achieved by the combination of nanoceria decoration as well as vanadate intercalation on LDH. The modified LDH loaded epoxy composite coatings were also made on A356 alloy to study the corrosion resistance in the real application.*

#### **4.1. Introduction**

Aluminum and its alloys are considered as one of the potential lightweight materials applied in automotive, aerospace, marine, food packaging, electronics and industrial sectors due to their low density, high strength, and economic viability. However, the service durability is limited by their high chemical activity and poor corrosion resistance in the harsh environment. The presence of aggressive ions, surface defects, erosion and mechanical fatigue can trigger the corrosion by removal of the protective oxide layer from the aluminium surface.<sup>1-4</sup> Generally, different coating materials such as polymer coatings, metallic deposits, ceramic and composite coatings are used to enhance the corrosion resistance of Al alloys.<sup>5-7</sup> In the last decade, preparation of inhibitor loaded container based smart composite coatings for controlled releasing of corrosion inhibitors has been established.<sup>8,9</sup> Mesoporous silica,<sup>10,11</sup> polyurethane microcapsules,<sup>12</sup> natural clays<sup>13,14</sup> and layered double hydroxides<sup>15</sup> are widely used as the containers.

Layered double hydroxides (LDH) are synthetic layered materials and commonly known as hydrotalcite or anionic clays. The basic chemical formula can be written as  $[M_{1-x}^{2+}M_x^{3+}(OH^-)_2]^{x+}[(A^{n-})_{\frac{x}{n}}.mH_2O]^{x-}$ , where  $M^{2+}$  is divalent, and  $M^{3+}$  is trivalent cations,  $A^{n-}$  represents anions for charge neutralization.<sup>16,17</sup> The octahedral layers made up of positively charged metal hydroxides and the counter anions as well as water molecules present in the gallery space.<sup>18</sup> Moreover, the flexibility in tuning the metals and anions made the LDH very attractive for different applications.<sup>19</sup> LDH

has been used as an environmental-friendly filler for the preparation of polymer composites to enhance the properties like mechanical strength, UV protection, flame retardancy, dye effluent removal controlled release of antibiotics or drugs and energy storage.<sup>20-26</sup>

The LDH have been widely accepted for corrosion protection by virtue of their unique anion-exchange capacity.<sup>27-31</sup> When LDH is in contact with corrosive medium (sodium chloride solution), two processes can occur. In the first case, the chloride ions exchange with interlayer anions and the other case is water molecule adsorption, which reduces the corrosion process.<sup>32</sup> However, while increasing the immersion time; the anti-corrosion activity can be reduced by the coating deformation due to the diffusion of oxygen and aggressive chloride ions<sup>33</sup> These challenges can be reduced by the use of inhibitor loaded LDH instead of simple carbonate or nitrate-based ones. The release of inhibitors during ion exchange mechanism induces active corrosion protection on the metallic substrate. Significant contributions were made in this area by the groups of Zheludkevich and Tedim, and they have demonstrated that the improvement of corrosion inhibition can be achieved via intercalated active anions such as phosphate, vanadate, 2-mercaptobenzothiazolate and quinaldate in Mg-Al or Zn-Al LDH.<sup>15,34</sup> Depending on the inhibitor anions, the extent of protection action may be varied. Among the different choice of inhibitors, vanadate shows good inhibition efficiency. The vanadate loaded LDH can be an active source of vanadate to provide continuous corrosion protection.<sup>15</sup> On the other hand, oxides of rare-earth elements, in particular ceria, are able to provide corrosion resistance. Cerium salts and oxide nanoparticles have been used to make protective coatings by various methods.<sup>35,36</sup> Stable ceria particles can reduce the penetration of corrosive species towards the substrate material. Additionally, the nonstoichiometric CeO<sub>2</sub> particles can show a passivation behavior with or without change in the corrosion potential region. In the presence of nanoceria the passivity range increases and that reduces the film breakdown process under chloride attack.<sup>37</sup> It was also proposed that the CeO<sub>2</sub> layer can act as a cathode, which involved in the corrosion reaction mechanism.<sup>38</sup> Similarly

our previous work on Ni-B-ceria composite coating indicates the induced corrosion protection in the presence of nanoceria on A356 alloy.<sup>39</sup>

The combinations of two or more corrosion inhibitors have shown a synergistic anticorrosion effect. LDH modification by combining different anionic systems<sup>15</sup> as well as anionic and cerium based systems, cerium salt and cerium molybdate, for preventing aggressive anions have been developed.<sup>40-43</sup> However, a decrease in the activity of organic inhibitors owing to the photodegradation can occur during long term application.<sup>44,45</sup> Though different combinations were tried, a completely inorganic system that explicit the effect of nanoceria decoration as well as vanadate intercalation and their collective mechanistic aspects were not yet been discussed.

Herein, we present a single container system of LDH having intercalated vanadate and decorated ceria nanoparticles as inhibitors. A one step method for ceria nanoparticle decoration on Ni-Al nitrate LDH in addition to inhibitor loaded Ni-Al vanadate LDH for dual action in corrosion protection was investigated. The overall LDH modification process is shown in the schematic (Figure 4.1). For that, Ni-Al NO<sub>3</sub> LDH was prepared first, and ion exchanged with vanadate. Subsequently, sodium dodecyl sulfonate (SDS) dispersed ceria nanoparticles were decorated on the positively charged layer surface. The structure of synthesized LDH was characterized by X-ray diffraction (XRD), Fourier transform infrared spectra (FTIR), Raman spectroscopy, scanning electron microscopy (SEM) and transmission electron microscopy (TEM). The corrosion resistance was measured by potentiodynamic polarization measurements, electrochemical impedance spectroscopy (EIS) and immersion test. The corrosion protection efficiency is increased significantly. Modified LDH added epoxy composite coatings were also made on aluminium A356 alloys to analyze the protection efficiency for practical applications.

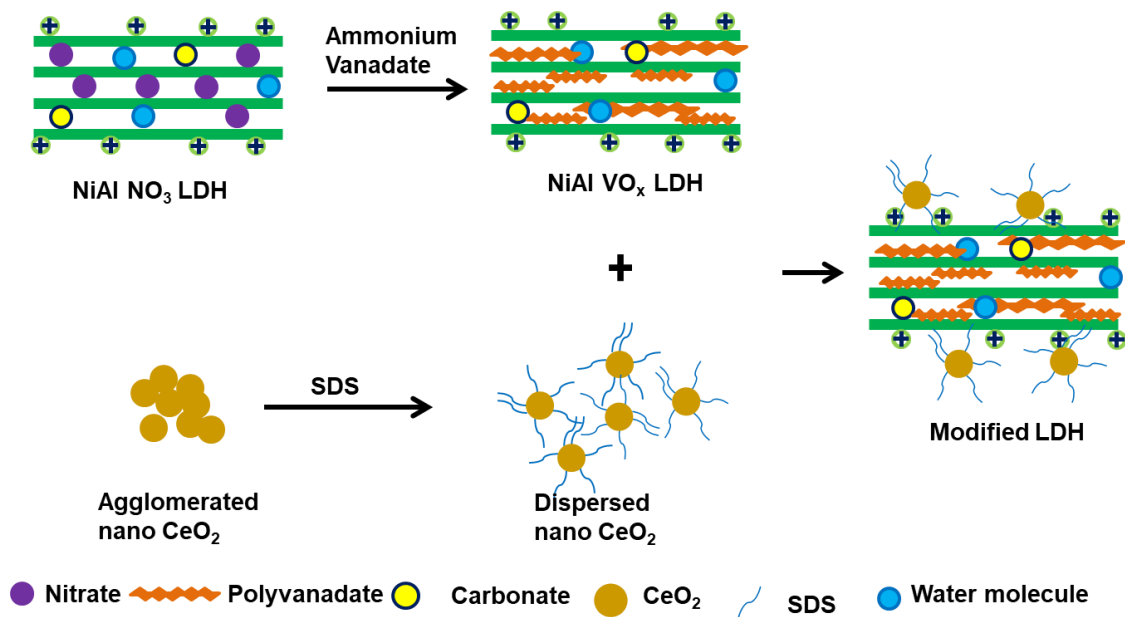


**Figure 4.1:** Schematic representation of inhibitor loaded LDH modification.

## 4.2. Experimental

### 4.2.1. Materials

Metal salts (aluminium nitrate  $\text{Al}(\text{NO}_3)_3 \cdot 9\text{H}_2\text{O}$ , 98.5% and nickel nitrate  $\text{Ni}(\text{NO}_3)_2 \cdot 6\text{H}_2\text{O}$ , 98%), anhydrous 1-Butanol (99.8%) and  $\text{CeO}_2$  particles (99.95%) with 50 nm average particle size were obtained from Sigma-Aldrich Co. Ltd., USA. Urea (99%), ammonium vanadate, NaCl (99%) and sodium dodecyl sulfonate were purchased from Merck, India. Epoxy monomer, diglycidyl ether of bisphenol A (DGEBA), was bought from Thermofisher scientific, India. Vantico, India supplied commercially available hardener, HY951. The chemicals were used as such without purification. Aluminium A356 alloy (Sargam Metals, India) casting with Al-7Si-0.35Mg (in wt.%) composition without any post-treatment was taken for the substrate preparation.

### 4.2.2. Substrate preparation

A356 aluminium alloy strip with 30×20×3 mm dimension was used as the substrate material for the corrosion studies and coatings. The aluminium alloy pieces were polished up to 1000 grit size SiC abrasive paper and washed with acetone under ultrasonication.

### 4.2.3. Ni-Al Nitrate LDH Synthesis

Ni-Al Nitrate LDH (Ni-Al NO<sub>3</sub> LDH) synthesis was done by the co-precipitation process in a round bottom flask connected with a reflux condenser under nitrogen atmosphere. The procedure is given in chapter 3, section 3.2.2.

### 4.2.4. Vanadate intercalation

The ion exchange was carried out in a round bottom flask under the nitrogen atmosphere at ambient conditions. Dried LDH powder was added to the ammonium vanadate salt solution in the weight ratio of 2:1. The mixture was stirred for 24 h, and the final precipitate was washed, and then dried in a vacuum oven.

### 4.2.5. Ceria decoration

Firstly, ceria nanoparticles were dispersed in SDS and sonicated for 1 h for better distribution. LDH was taken in a round bottom flask and ceria dispersion was added into it (LDH: Ceria::10:1). The mixture was stirred for 24 h under nitrogen flow at room temperature. The final precipitate was washed, dried, and used for the corrosion analysis.

### 4.2.6. Epoxy LDH composite coating

0.2 g of LDH powder was dispersed in 10 mL butanol, the solvent used for epoxy resin dilution. 10 g of the DGEBA (monomer) added to it and stirred well for 10 min to obtain a uniform distribution of LDH. Then 10 g of HY951 (hardener) was mixed with epoxy and stirred for 5 min. Dip coating was carried out using this 1 wt% LDH mixture on A356 alloy surface. The coated samples were cured for one week.

### 4.2.7. Characterizations

#### 4.2.7.1. Structural analysis

The surface morphology, chemical analysis, and structure of prepared LDH were determined by different techniques as given in section 2.2.3.1 (chapter 2).

#### 4.2.7.2. Electrochemical measurements

Corrosion behavior of the alloy in different electrolytes was carried out by the electrochemical system with a conventional three-electrode cell (CHI608E). The aluminium alloy was taken as the working electrode (1 cm<sup>2</sup> exposed surfaces); saturated calomel electrode as the reference and a platinum grid was used as the

counter electrode. Different electrolytes made of dispersed LDHs (0.1 wt%) in 3.5 wt% NaCl solution was taken in the cell. The samples were kept in the electrolytes for 20 min to attain stable open circuit potential (OCP). Impedance was measured at the OCP with peak-to-peak amplitude of 10 mV in the frequency range from  $10^5$  to  $10^{-2}$  Hz. The data were fitted by EC-Lab software with equivalent circuits and the corresponding values of circuit elements were obtained. The potentiodynamic scan was done from -200 mV to +200 mV with reference to the OCP values at a rate of 1 mV/s. The corrosion current density ( $i_{\text{corr}}$ ) and corrosion potential ( $E_{\text{corr}}$  vs. SCE) of each electrolyte were calculated from the Tafel plot.

#### 4.2.7.3. Immersion Test

A356 aluminium alloy with 10×10×3 mm dimension was used for immersion test. The polished samples were hung in the 3.5 wt% NaCl solution taken in a 250 mL beaker for 32 days without any disturbance. The electrolytes were varied for five different samples by introducing 0.1 wt% of Ni-Al nitrate, Ni-Al vanadate, Ni-Al nitrate-CeO<sub>2</sub>, and Ni-Al vanadate-CeO<sub>2</sub> along with pure NaCl solution. The samples took from the beaker after 32 days and washed with 70% nitric acid to remove the oxides from the surface. Cleaned strips were dried, and weight loss was measured.

### 4.3. Results and Discussion

#### 4.3.1. SEM Analysis

The morphology of the LDHs was examined by SEM and corresponding elemental compositions of the LDH were analyzed by EDS and are presented in Figure 4.2. Typical two-dimensional flake morphology can be seen with a thickness of few tens of nanometers and lateral dimensions of 700-800 nm. Dried powders exhibit agglomerated microstructure and most of the platelets being stacked on top of each other. Presence of vanadium after vanadate intercalation, i.e., V, O, Al and Ni in Ni-Al vanadate LDH, instead of nitrogen indicate the successive modification and which is observed from EDS analysis (Figure 4.2d). The ceria modified samples have LDH layers with nanoparticle deposition at their sides and edges (Figure 4.2e). Ni-Al vanadate-CeO<sub>2</sub> retains more number of particles compared to Ni-Al nitrate-CeO<sub>2</sub>.

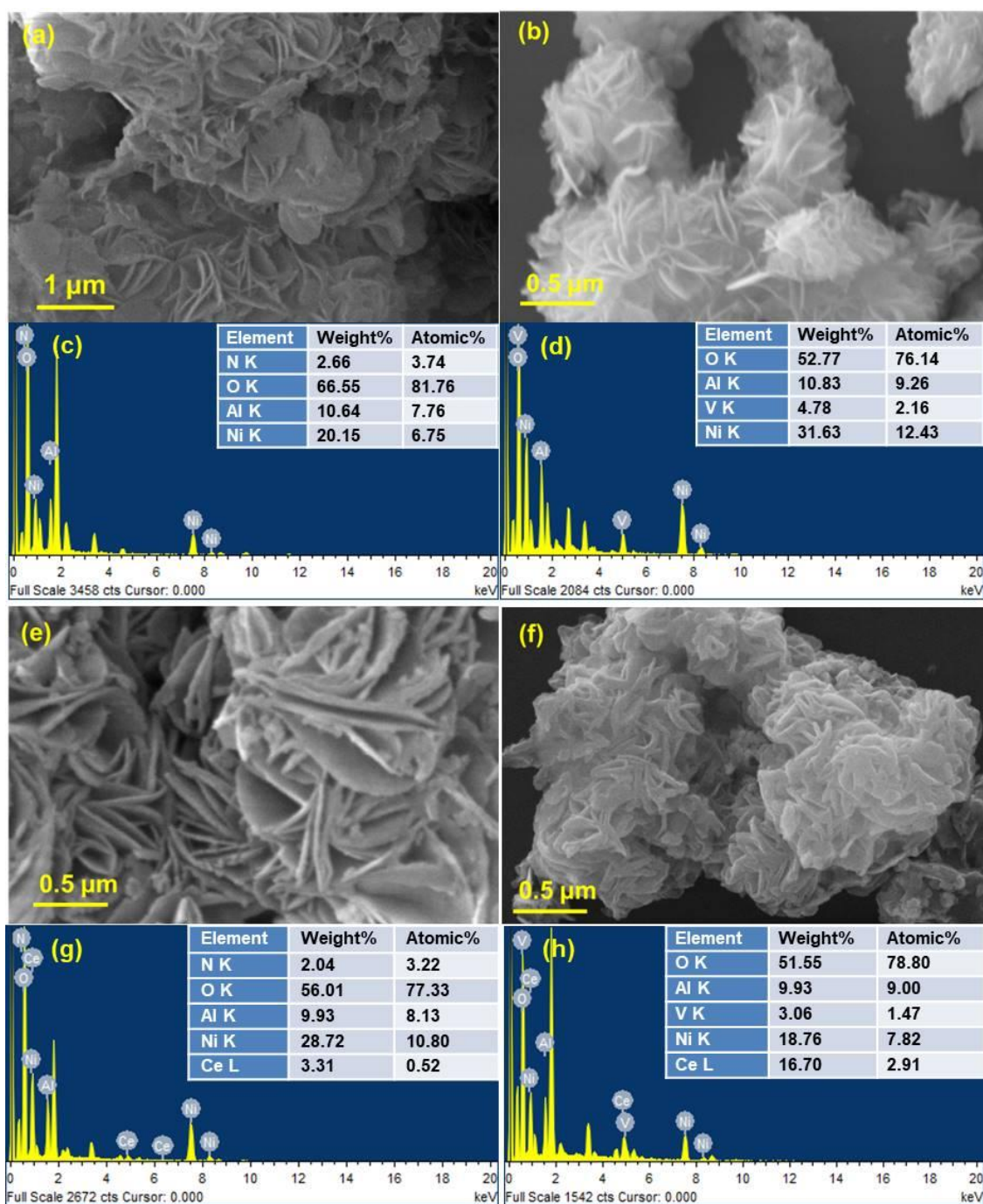


**Figure 4.2:** SEM and EDS analysis of (a,c) Ni-Al nitrate, (b,d) Ni-Al vanadate, (e,g) Ni-Al nitrate-CeO<sub>2</sub> and (f,h) Ni-Al vanadate-CeO<sub>2</sub>.

## 4.3.2. FTIR

The modification of LDH with vanadate is identified by the ATR-FTIR spectra in the range of 450–4000  $\text{cm}^{-1}$  (Figure 4.3). A broad band centered at 3468  $\text{cm}^{-1}$  is assigned to the stretching mode of the hydroxyl group ( $\nu\text{OH}$ ) of the metal hydroxide layer and interlayer water molecules. Broadening of this peak indicates the presence of hydrogen bonding by interlayer water molecules of the hydrotalcite structure. The increase of peak intensity after vanadation is due to the hydrated  $\text{VO}(\text{OH})_3$  and  $\text{VO}(\text{OH})_3(\text{OH}_2)_2$  formation in the aqueous medium during ion exchange.<sup>46</sup> The peak at 1630  $\text{cm}^{-1}$  corresponds to the H-O-H bending vibration of water molecules.<sup>47</sup> The presence of nitrate group can be observed as the sharp peak at 1383  $\text{cm}^{-1}$  for antisymmetric stretching of the nitrate anion present the LDH before vanadate ion exchange. After ion exchange, this peak intensity drastically decreased, which indicates the removal of nitrate anion from the gallery (the enlarged spectrum is shown as inset). However, the shoulder band corresponds to a small amount of interlayer carbonate ion at 1362  $\text{cm}^{-1}$  does not change even after vanadate exchange. An additional band at 903  $\text{cm}^{-1}$  after ion exchange is connected with the  $\nu_1(\text{VO}_x)$  symmetric stretching vibrations.<sup>48</sup> The peak at 600  $\text{cm}^{-1}$  can be attributed to the Al-OH and Ni-Al-OH bending vibrations.<sup>49</sup>

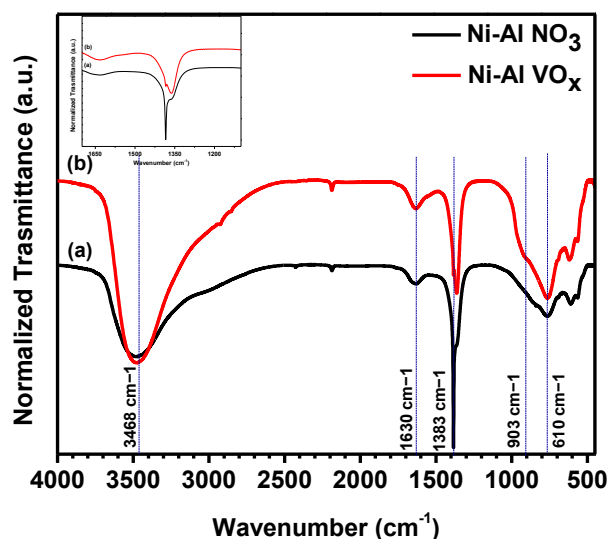


**Figure 4.3:** Infrared spectra of (a) Ni-Al nitrate and (b) Ni-Al vanadate. The enlarged portion of the peaks corresponding to anionic species from 1650  $\text{cm}^{-1}$  to 1150  $\text{cm}^{-1}$  is shown as an inset.

### 4.3.3. Raman analysis

The nature of gallery anions in the LDH samples was characterized by Raman spectroscopy. The spectra taken for  $\text{NH}_4\text{VO}_3$  salt, parent LDH  $\text{NO}_3$ , and LDH  $\text{VO}_x$  are shown in Figure 4.4. The Raman peaks for  $\text{NH}_4\text{VO}_3$  were observed at 928, 896, 648 and 497  $\text{cm}^{-1}$ . The bands are assigned to free V=O symmetric and asymmetric stretching as well as bridged V-O-V asymmetric and symmetric stretching vibrations, respectively.<sup>50</sup> Based on the Raman bands, it is speculated here that a chain like  $(\text{VO}_3)_n^{n-}$  anions are present instead of monomeric  $\text{VO}_3^-$  ion. The parent LDH  $\text{NO}_3$  shows only one peak at 1035  $\text{cm}^{-1}$  with a shoulder corresponding to the nitrate and small quantity of carbonate symmetric stretching vibrations.<sup>51</sup> For the vanadate modified LDH sample, a broad band at 680-900  $\text{cm}^{-1}$  was obtained and it is due to the V-O-V stretching vibrations of two-dimensional distorted polymeric vanadates.<sup>52</sup> Therefore, the vanadates are intercalated as their polymerized form. However, the band is shifted to the low-frequency region comparing with polyvanadates formation on the metallic surfaces as per previous reports.<sup>53</sup> This band shift may be due to the feasibility to stabilize the vanadates by forming hydrogen bonding between oxygen present in the vanadate and hydroxyl group of the positively charged layers.

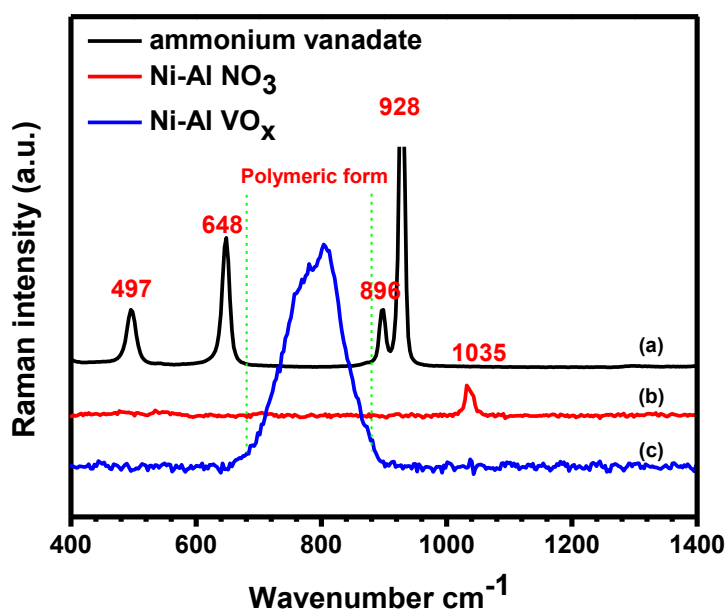


**Figure 4.4:** Raman spectra of (a) ammonium vanadate, (b) Ni-Al Nitrate and (c) Ni-Al Vanadate.

#### 4.3.4. XRD analysis

The X-ray diffraction patterns of Ni-Al NO<sub>3</sub> (as synthesized), Ni-Al VO<sub>x</sub> (after anion exchange) and Ni-Al NO<sub>3</sub>-CeO<sub>2</sub> (after ceria modification) are shown in Figure 4.5. The patterns show the characteristic reflections for single-phase LDH. According to Bragg's law, the *d*-spacing was calculated as 0.76 nm from the position of the (003) reflection. Two-dimensional distorted polymeric vanadate intercalated sample shows only small increase in the *d*-value (0.04 nm) to 0.80 nm. A similar observation was noticed by Tedim et al.<sup>15</sup> and Guo et al.<sup>54</sup> for vanadate intercalated Zn-Al and Mg-Al LDHs. However, some of the polymeric vanadates may adsorb on the layer surface. The ion-exchanged LDH has a broad and low-intensity peak compared to the parent Ni-Al NO<sub>3</sub>, which could be attributed to some disorder in the lamellar structure and higher atomic scattering factor of vanadium.<sup>54</sup> There is no peak (110) shifting was observed for both the parent LDH-nitrate and LDH-vanadate indicating that the ion exchange has not affected the structure of the hydroxide layers.<sup>40</sup> The ceria decorated samples have additional peaks of (111), (200) and (311) corresponding to ceria nanoparticles which confirm the formation of CeO<sub>2</sub> modified LDH.

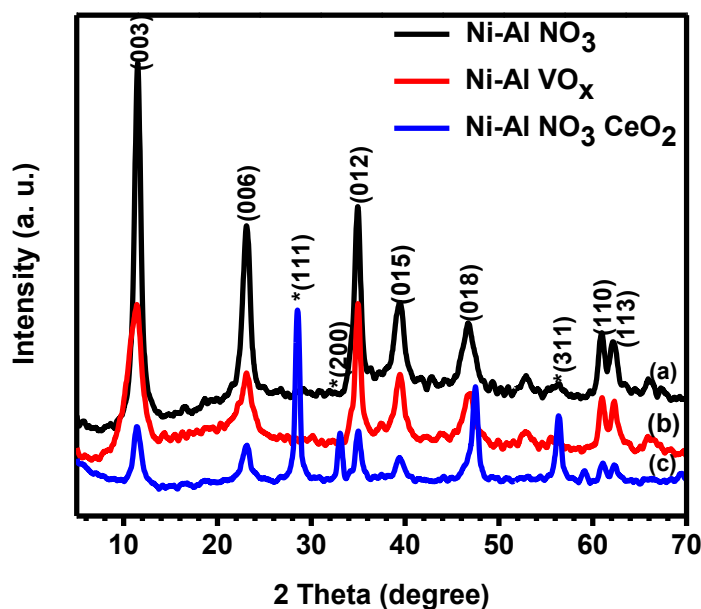


**Figure 4.5:** X-ray diffractions patterns of (a) Ni-Al Nitrate, (b) Ni-Al Vanadate and (c) Ni-Al Nitrate -CeO<sub>2</sub> LDHs.

### 4.3.5. Corrosion analysis

#### 4.3.5.1. Effect of ceria nanoparticles decoration on Ni-Al Nitrate LDH

The electrochemical behavior of A356 alloy in 3.5 wt. % NaCl solution containing Ni-Al nitrate LDH, ceria nanoparticles, a physical mixture of Ni-Al nitrate LDH & ceria particles and CeO<sub>2</sub> decorated Ni-Al nitrate LDH after 24 h of immersion was carried by potentiodynamic polarization measurements. Figure 4.6 shows the Tafel plots of the samples by plotting the logarithm of current density Vs. the applied potential with reference to the OCP. Corrosion potential ( $E_{\text{corr}}$ ) as well as corrosion current density ( $i_{\text{corr}}$ ) values are given in Table 4.1. The presence of ceria nanoparticles resulted in a significant increase in the  $E_{\text{corr}}$  values indicates their noble behavior. Corresponding shift of the graph towards the upper side was observed. The passive corrosion protection of nanoceria reduces the tendency for corrosion reaction on the metal surface. On the other hand, the presence of LDH resulted in the reduction of  $i_{\text{corr}}$  values indicates the decreased ionic diffusion on the surface during the corrosion process. The physical mixture of LDH and ceria nanoparticles showed lower corrosion performance, which might be due to the self-agglomeration of both the dispersoids. The ceria decorated one is more cathodic to the other samples and possesses excellent corrosion protection due to the influence of nanoparticles on LDH.

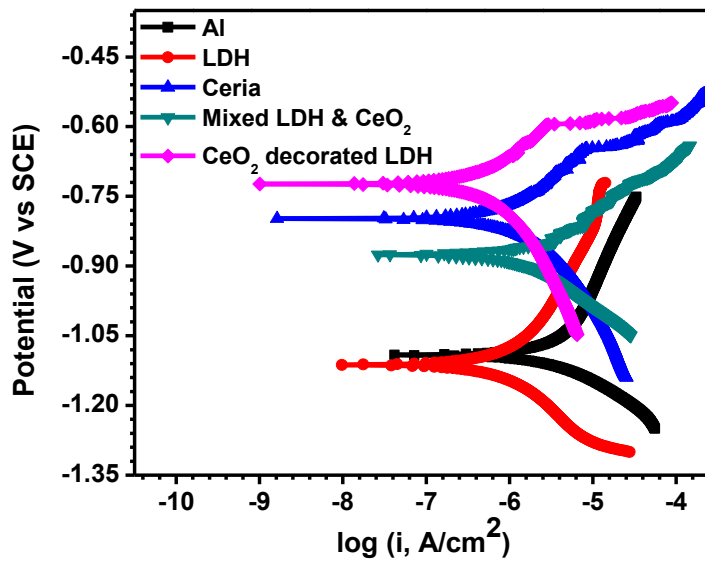


**Figure 4.6:** Tafel plots of A356 alloy in different inhibitor added 3.5% NaCl solution at a scan rate of 1mV/s.

**Table 4.1:**  $E_{\text{corr}}$ , and  $i_{\text{corr}}$  values obtained from potentiodynamic polarization scan.

| Sample ID                      | $E_{\text{corr}}$ (V vs. SCE) | $i_{\text{corr}}$ (A cm <sup>-2</sup> ) |
|--------------------------------|-------------------------------|---|
| A356                           | -1.091                        | 4.574 x 10 <sup>-6</sup>                |
| LDH                            | -1.113                        | 1.130 x 10 <sup>-6</sup>                |
| Ceria                          | -0.798                        | 1.191 x 10 <sup>-6</sup>                |
| Mixed LDH & CeO <sub>2</sub>   | -0.876                        | 2.041x 10 <sup>-6</sup>                 |
| CeO <sub>2</sub> decorated LDH | -0.726                        | 0.737 x 10 <sup>-6</sup>                |

#### 4.3.5.2. Effect of nanoceria decoration on Ni-Al vanadate LDH

The electrochemical behavior of as prepared and modified samples was carried out by electrochemical impedance spectroscopy. Since EIS provides more reasonable indication of active inhibition mechanism and effectiveness. Figure 4.7 shows the Nyquist representations of EIS measurements. The loop corresponds to aluminium alloy surface in 3.5 wt% NaCl solution alone (without LDH) shows a capacitive arc at high and intermediate frequencies followed by an inductive arc at low frequencies. The diameter of the loop denotes the charge transfer resistance ( $R_{\text{ct}}$ ) at the metal-solution interface. At higher frequencies, the resistance is ascribed to the electrolyte bulk resistance ( $R_{\text{s}}$ ). The inductance loop at very low frequency may be due to the pit formation on the metal surface.<sup>55</sup> The equivalent electrical circuit to represent the electrochemical characteristics of aluminium alloy in NaCl alone is given in Figure 4.8a. In this circuit, CPE is the constant phase element of the electrical double layer to fit the impedance behavior of non-homogeneous capacitance. It is used when a non-ideal frequency response is present instead of a pure capacitor to compensate the non-homogeneity in the system.<sup>56</sup> Inductive behavior is given as 'L'. Corresponding fitted values of every element in the equivalent circuit from EC-Lab software are given in Table 4.2.

The Nyquist plots (Figure 4.7) observed for the specimen in contact with electrolytes containing LDH have two capacitive loops at high and medium frequencies followed by a Warburg element. The two capacitive elements present in the fitted electrical circuit represent the presence of two loops (Figure 4.8b). The first loop from high to medium frequency regions could be attributed to a protective film formation with the LDH nanolayers on the alloy surface during the analysis. The parallel combination of film resistance ( $R_f$ ) and film capacitance ( $CPE_f$ ) represents impedance with the interface reaction between the electrolytic solution and the adsorbed LDH film as an additional barrier property. The second one from medium to low frequency might be attributed to the charge transfer resistance. Warburg element represents a kind of resistance to mass transfer due to the oxide layer formed on the metal surface. Since, the low-frequency response is related to corrosion phenomena, probably due to the deterioration of coatings; different loop diameters for each system with the largest by vanadate as well as ceria modified LDH reveal the improvement in corrosion resistance.

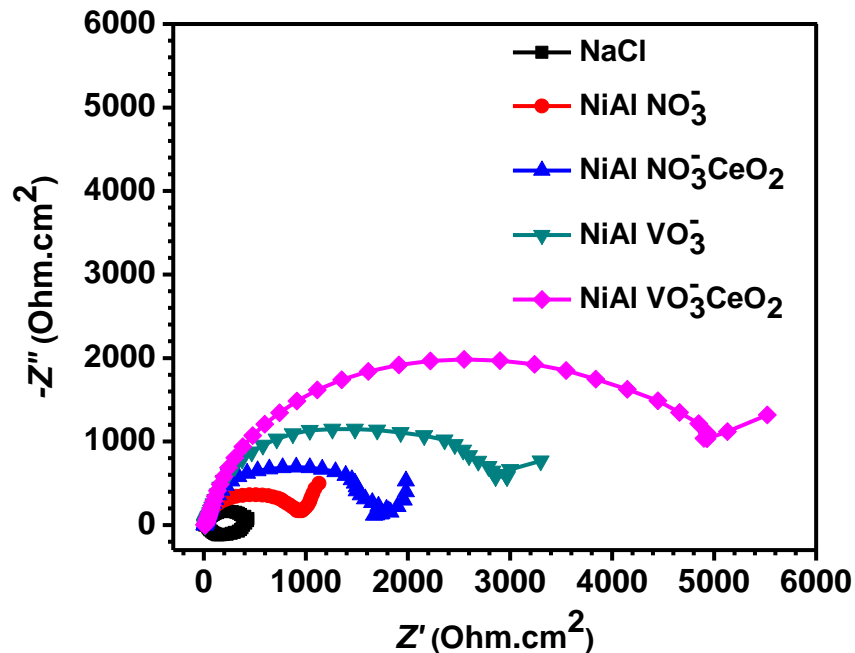


**Figure 4.7:** Nyquist plots of the samples at their open circuit potential with a peak-to-peak amplitude of 10 mV in the frequency range from  $10^4$  to  $10^{-2}$  Hz.

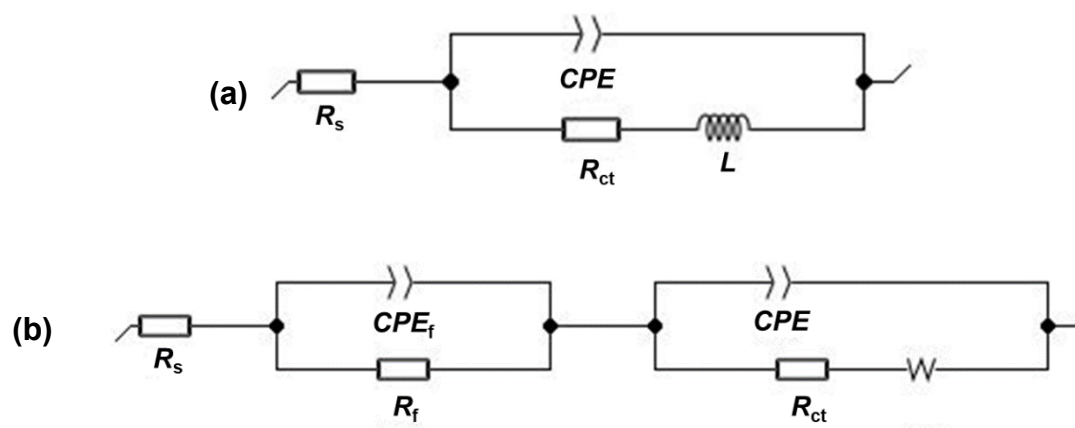


**Figure 4.8:** Equivalent electrical circuit for A356 corrosion behavior in 3.5 wt% NaCl alone (a) and LDH added solution (b).

**Table 4.2:** The fitted values of the samples corresponding to the equivalent circuits given as Figure 4.8.

| Sample ID                          | NaCl                   | Ni-Al NO <sub>3</sub> | Ni-Al NO <sub>3</sub> -<br>CeO <sub>2</sub> | Ni-Al VO <sub>x</sub> | Ni-Al VO <sub>x</sub> -<br>CeO <sub>2</sub> |
|------------------------------------|------------------------|-----------------------|---|-----------------------|---|
| $R_s(\Omega \text{ cm}^2)$         | 11.84                  | 11.37                 | 10.72                                       | 12.35                 | 12.78                                       |
| $R_{ct}(\Omega \text{ cm}^2)$      | 389                    | 669                   | 864   | 1657                  | 3101  |
| $CPE(S^n / \Omega \text{ cm}^2)$   | $13.21 \times 10^{-6}$ | $26.1 \times 10^{-6}$ | $25.4 \times 10^{-6}$                       | $14.7 \times 10^{-5}$ | $5.43 \times 10^{-5}$                       |
| n                                  | 0.919                  | 0.966                 | 1   | 0.922                 | 0.943                                       |
| $W(\Omega \text{ cm}^2)$           | -                      | $1.60 \times 10^4$    | $4.54 \times 10^4$                          | $2.54 \times 10^5$    | $6.17 \times 10^5$                          |
| $R_f(\Omega \text{ cm}^2)$         | -                      | 530                   | 1454  | 1801                  | 2801  |
| $CPE_f(S^n / \Omega \text{ cm}^2)$ | -                      | $2.2 \times 10^{-4}$  | $2.76 \times 10^{-4}$                       | $4.91 \times 10^{-4}$ | $4.46 \times 10^{-4}$                       |
| n                                  | -                      | 0.892                 | 0.926                                       | 1                     | 1   |
| L (H)                              | 368                    | -                     | -   | -                     | -   |

The bode plots are shown in Figure 4.9;  $\log Z$  vs.  $\log f$  (a) and phase angle vs.  $\log f$  (b). The resistance spectra of Bode plots depicts an increase in impedance ( $\log Z$ )

value in the order of Ni-Al vanadate-CeO<sub>2</sub> > Ni-Al vanadate > Ni-Al nitrate-CeO<sub>2</sub> > Ni-Al nitrate > NaCl alone. The phase angle plots are similar to each other except for the sample in solution without LDH. For NaCl alone, the spectrum has one phase maximum at the medium frequency and an inductive shift towards negative phase angle at the lower frequency. The inductance may be offered by the pitting corrosion or the detachment of the protective oxide layer from the metal surface. The presence of LDH in the solution prevents the pit formation even at lower frequency region. In addition to that, the LDHs with different modifications do not change the corrosion mechanism. But the frequency range was shifted to the smaller value owing to the existence of relatively noble CeO<sub>2</sub> and vanadate inhibitor. Vanadate intercalated solution exhibited the capacitance behavior for a wide frequency range at the medium and low-frequency region, which indicates the polyvanadate itself give considerable improvement. The peak may compose of two relaxation processes due to LDH and double layer capacitance overlapped each other. The overlapping of these time constants may be originated from similar values of capacitances of both the capacitance offered by the modified LDH and the double electrochemical layer in the areas where direct contact of the electrolyte.

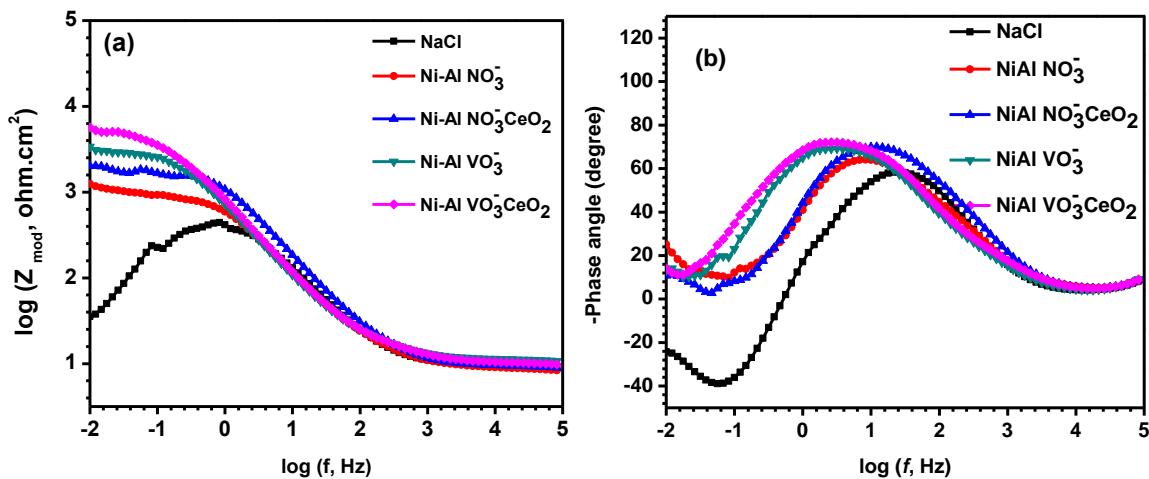


**Figure 4.9.** Bode plots of A356 corrosion behaviour in 3.5 wt% NaCl alone and LDH added solutions (a)  $\log Z$  vs.  $\log f$  and (b) phase angle vs.  $\log f$ .

## 4.3.5.3. Immersion test

Long term immersion test provides more reliable information about corrosion resistance in a real aggressive environment. Figure 4.10 represents the average corrosion rates of aluminium samples in LDH dispersed 3.5 wt% NaCl solutions calculated after 32 days of immersion. The average corrosion rate values are 0.399, 0.313, 0.258, 0.094, 0.078 mm/y for samples kept in NaCl, NaCl with Ni-Al NO<sub>3</sub>, NaCl with Ni-Al NO<sub>3</sub>-CeO<sub>2</sub>, NaCl with Ni-Al VO<sub>x</sub>, and NaCl with Ni-Al VO<sub>x</sub>-CeO<sub>2</sub>, respectively. Presence of unmodified LDH itself gives a considerable decrease in corrosion rate. Further, each of the modifications gives additional performance towards anticorrosive effect. Active vanadium species significantly influences the property than the nanoparticles when they are present in the electrolyte. However, the electrolyte having LDHs after both the modifications gave the lowest corrosion rate with more than 80% enhancement in anti-corrosion performance.

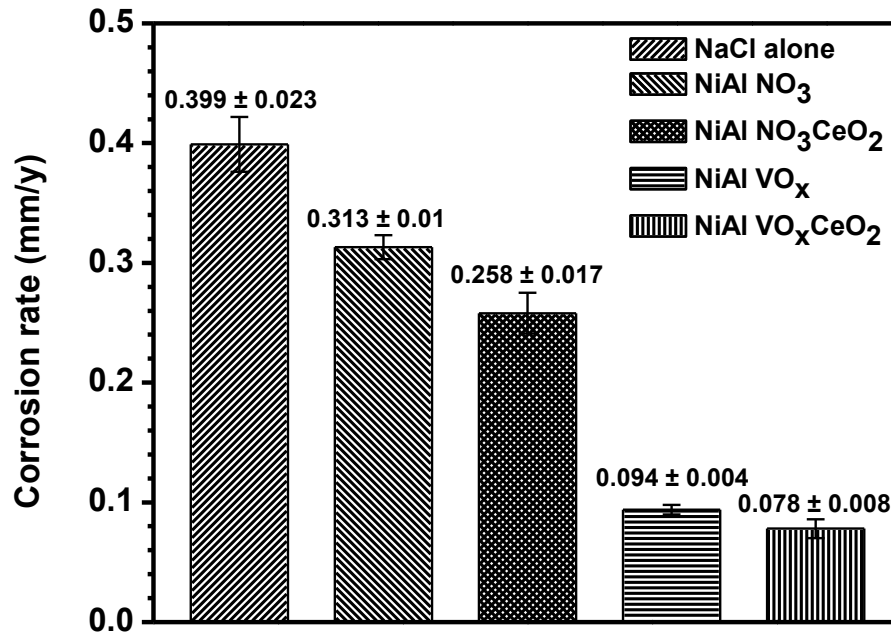


**Figure 4.10:** Corrosion rate of A356 alloy in different electrolytes calculated from weight loss measurement after 32 days immersion test.

Figure 4.11 shows the SEM images of metallic surfaces (Inset: photograph of the immersed samples after the test) after cleaning of corrosion products. Aluminium immersed in NaCl suffered from severe localized pitting corrosion, which led to a large

quantity of material removal. As a result, bigger pores are seen on the surface. The samples kept in Ni-Al nitrate and Ni-Al nitrate-CeO<sub>2</sub> produced smaller pits and ceria deposited LDH had lesser number of pits comparing to the particle-free counterpart. The vanadate loaded LDHs did not allow the material loss from the surface except a few tiny pores. Presence of ceria nanoparticle further improved the stability of the material.

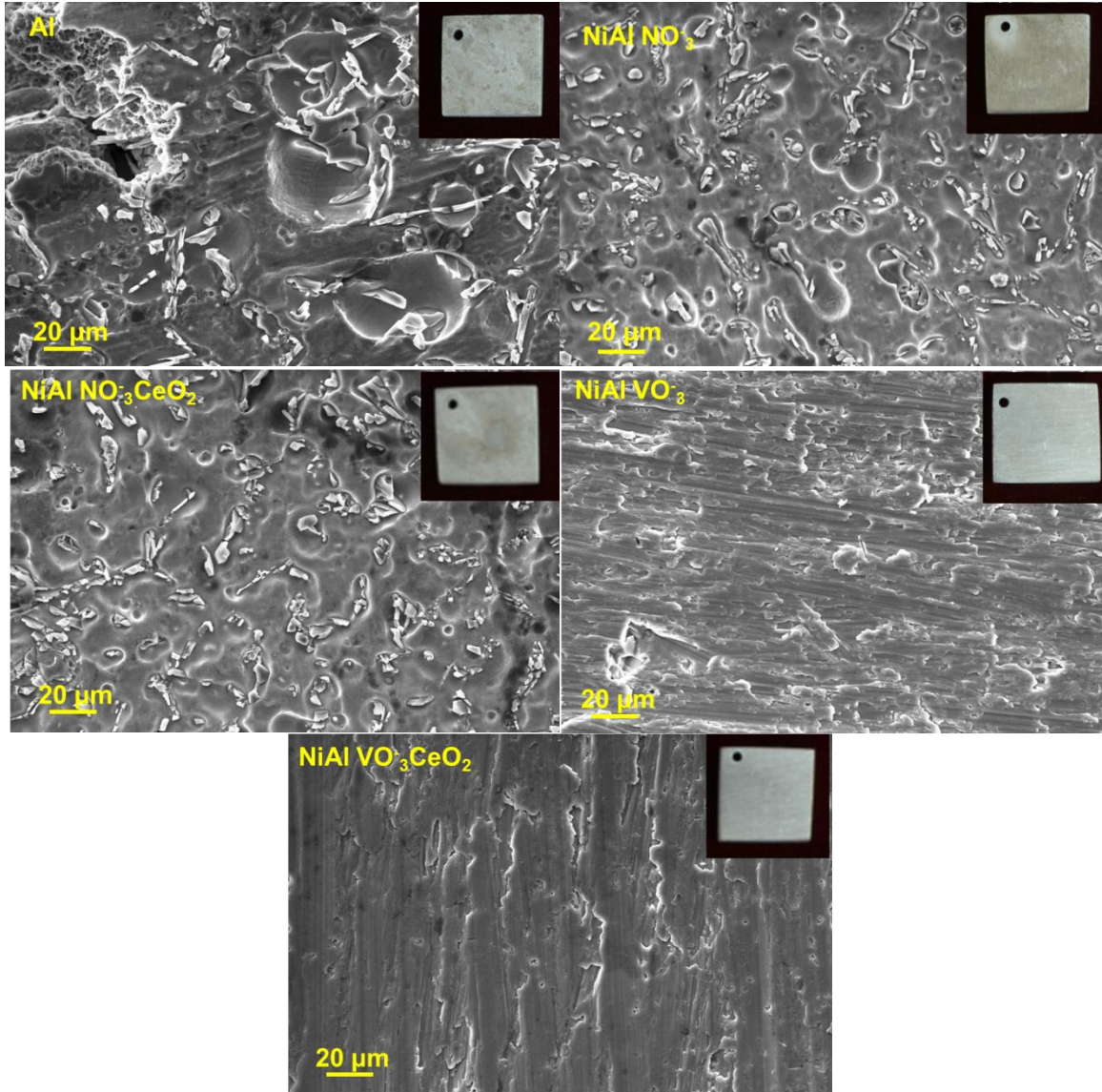


**Figure 4.11:** SEM images of the A356 surface after Immersion test for 32 days (after the removal of corrosion products).

#### 4.3.5.4. Raman analysis

The Raman spectra consist of vanadate modified LDH and aluminium substrate after immersion test are given in Figure 4.12. Both the systems exhibit broad bands corresponding to the polymeric vanadate. However, the band for LDH was observed between  $680\text{ cm}^{-1}$  and  $900\text{ cm}^{-1}$  as explained in section 4.3.3. Whereas, the band for polyvanadate on the metal surface was obtained between  $870\text{ cm}^{-1}$  to  $1000\text{ cm}^{-1}$  consistent with the previous reports<sup>53</sup>. The two-dimensional distorted polymeric vanadates consists of nonstoichiometric mixed oxidation states of vanadium, which are responsible for the parallel oxidation reaction instead of metal corrosion reactions to improve the anticorrosion property<sup>52,57</sup>.

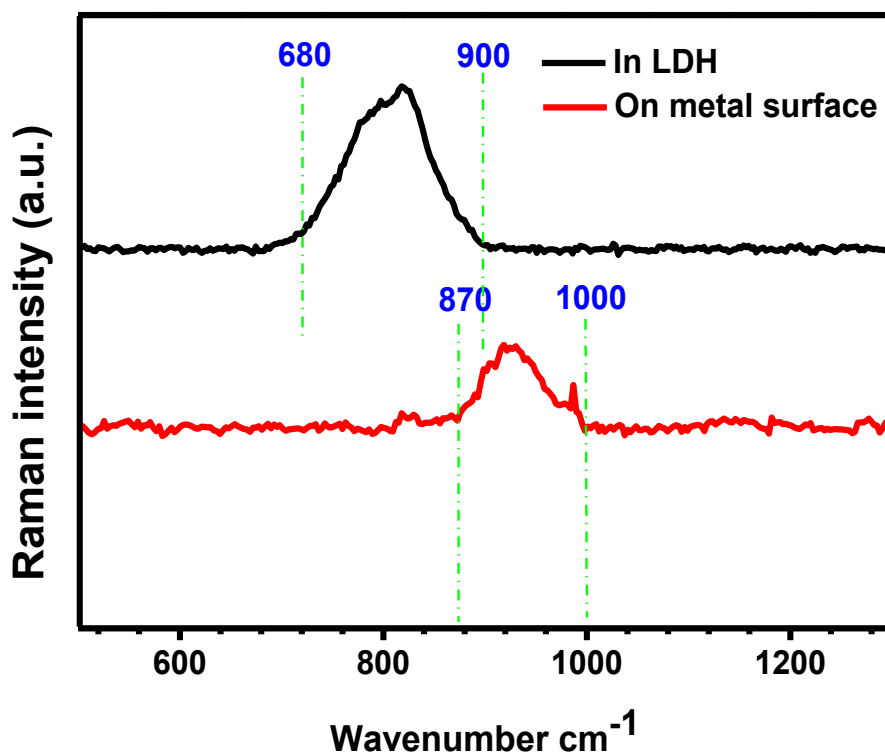


**Figure 4.12:** Raman spectra of (a) NiAl-Vanadate and (b) A356 alloy surface after immersion.

#### 4.3.6. Corrosion Mechanism

When the surface of a metal is in contact with an electrolyte, redox reactions will occur and the corrosion can happen. In the presence of sodium chloride solution, the chloride ion triggers the oxidation process. The anion-exchange property of LDH

can be used to immobilize the chloride ion and act as an anionic scavenger. For inhibitor loaded LDHs, the release of anionic inhibitors can be activated by chloride ion exchange and thereby playing a dual action: entrapment of aggressive chloride ions and release of inhibitors as shown in Figure 4.13. The released anionic inhibitors then reach the metal surface and actively protect the surface delamination. Here the vanadium species reduce the cathodic reaction rate by decreasing the oxygen reduction reaction at neutral pH. Correspondingly, the metal oxidation reaction also diminishes.<sup>57</sup> The vanadate ions are in the polymeric form on the aluminium surface after immersion test. A thin layer of aluminium oxide formation during corrosion analysis holding the polyvanadate and prevents further corrosion.<sup>46</sup> Ceria nanoparticles decorated on the LDH surface can act as a physical barrier to the corrosive medium towards the metal surface. The nanoparticles layer can also be an effective cathode, which protects the metal from corrosive anions and water molecules. This property could be attributed to the inert behavior of the nano-ceria in the corrosive environment. Moreover, ceria nanoparticles behave like an obstacle to induce zig-zagging of corrosive ionic movement towards the substrate.<sup>58</sup>

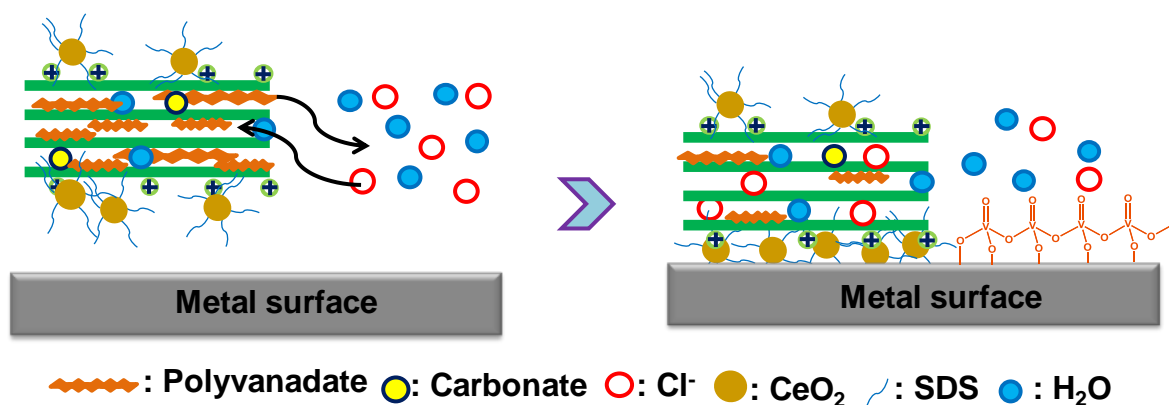


**Figure 4.13:** Schematic representation of the proposed corrosion protection mechanism.

#### 4.3.7. Corrosion Protection of Epoxy-LDH Composite Coatings on A356 alloy

The influence of LDH modification for corrosion resistance in a coating application was measured by preparing epoxy composite coating on the A356 alloy

surface. Composite coating was obtained with a uniform thickness, which is reliable for anticorrosive applications. Figure 4.14 shows the SEM images of epoxy alone (a) and LDH epoxy composite coating (b) cross-section. Both of them have a comparable thickness of  $\sim 22 \mu\text{m}$  and  $\sim 19 \mu\text{m}$  for polymer and composite coating respectively. Good coating adhesion on the metal substrate and less porosity can enhance the corrosion protection behavior.

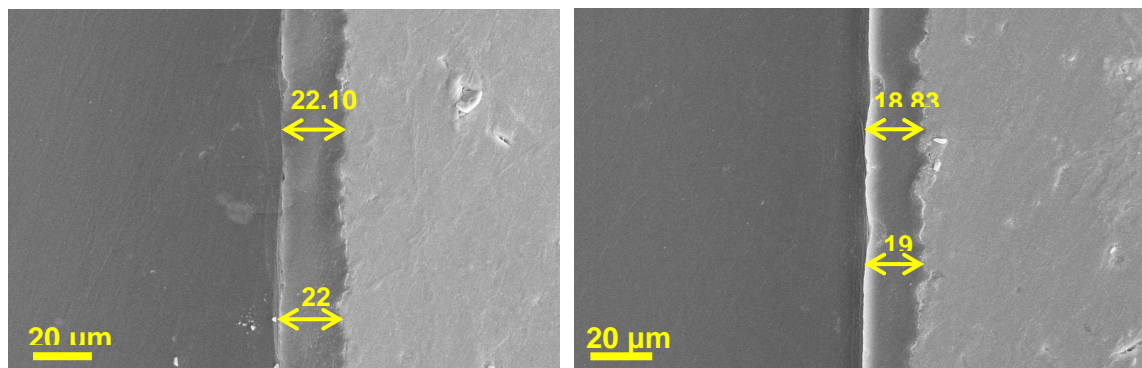


**Figure 4.14:** Cross-sectional SEM image of (a) Epoxy and (b) Epoxy LDH composite coating.

Modified LDH nanocontainers loaded with vanadate and ceria dispersed in epoxy and the corrosion resistance was measured. Bode plots of EIS studies with pure epoxy, epoxy-Ni-Al nitrate, epoxy-Ni-Al vanadate, epoxy-Ni-Al nitrate-CeO<sub>2</sub>, epoxy-Ni-Al vanadate-CeO<sub>2</sub> are given in Figure 4.15. The pure epoxy coating shows the lowest impedance. The addition of LDH to the coating layer increases the corrosion resistance matching with the order of inhibitor's performance. Thus, the combining effect of different inhibitors in LDH exhibited the highest impedance value.

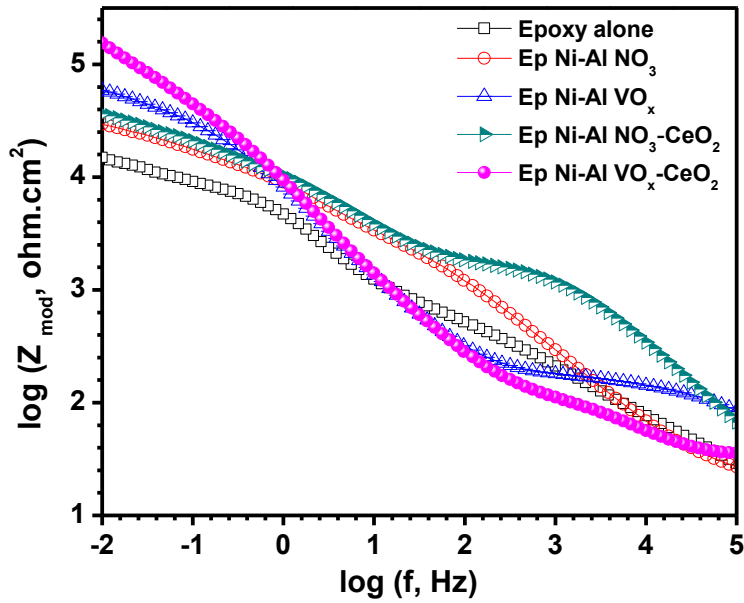


**Figure 4.15:** Bode plots of epoxy composite coated A356 alloy corrosion behaviour in 3.5 wt% NaCl solution.

#### 4.4. Conclusions

Ni-Al NO<sub>3</sub> LDH was synthesized successfully by co-precipitation method and it was further modified by vanadate via ion exchange method. Ceria nanoparticles were decorated on the layers by simple one step method. SEM images show the platelet-like structure of synthesized LDH. FTIR and Raman spectroscopy analyses confirm the effective ion exchange and vanadate inhibitor loading as their polymeric form into the Ni-Al LDH. X-ray diffraction patterns demonstrate the LDH formation as well as ceria decoration. The corrosion resistance of aluminium alloy has increased significantly in the presence of LDH in the electrolyte by order of Ni-Al VO<sub>x</sub>-CeO<sub>2</sub> > Ni-Al VO<sub>x</sub> > Ni-Al NO<sub>3</sub>-CeO<sub>2</sub> > Ni-Al NO<sub>3</sub> > NaCl without LDH. Better corrosion prevention of LDH added coating might be due to its ion exchange capacity with Cl<sup>-</sup> ion and the active corrosion prevention by the formation of polymeric vanadate on the metal surface. Ceria added LDH again enhance the barrier property by zig-zagging the movement of corrosive species towards the metal surface as well as their passive behaviour. The combined effect of active and passive corrosion inhibition gave the best anticorrosion property.

## References

- 1 B. Zhang, J. Wang, B. Wu, X. W. Guo, Y. J. Wang, D. Chen, Y. C. Zhang, K. Du, E. E. Oguzie and X. L. Ma, *Nat. Commun.*, 2018, **9**, 2559.
- 2 T. P. Hoar, *Corros. Sci.*, 1967, **7**, 341–355.
- 3 R. J. K. Wood, *Wear*, 2006, **261**, 1012–1023.
- 4 N. O. Larrosa, R. Akid and R. A. Ainsworth, *Int. Mater. Rev.*, 2018, **63**, 283–308.
- 5 M. W. Kendig and R. G. Buchheit, *CORROSION*, 2003, **59**, 379–400.
- 6 M. L. Auger and V. K. Sarin, *Surf. Coatings Technol.*, 1997, **94–95**, 46–52.
- 7 D. Snihirova, S. V. Lamaka and M. F. Montemor, in *Smart Composite Coatings and Membranes*, Elsevier, 2016, pp. 85–121.
- 8 E. V. Skorb, A. G. Skirtach, D. V. Sviridov, D. G. Shchukin and H. Möhwald, *ACS Nano*, 2009, **3**, 1753–1760.
- 9 D. G. Shchukin, *Polym. Chem.*, 2013, **4**, 4871.
- 10 D. Borisova, H. Möhwald and D. G. Shchukin, *ACS Nano*, 2011, **5**, 1939–1946.
- 11 E. V. Skorb, D. Fix, D. V. Andreeva, H. Möhwald and D. G. Shchukin, *Adv. Funct. Mater.*, 2009, **19**, 2373–2379.
- 12 V. V. Gite, P. D. Tatiya, R. J. Marathe, P. P. Mahulikar and D. G. Hundiwale, *Prog. Org. Coatings*, 2015, **83**, 11–18.
- 13 E. Abdullayev, R. Price, D. Shchukin and Y. Lvov, *ACS Appl. Mater. Interfaces*, 2009, **1**, 1437–1443.
- 14 A. Ghazi, E. Ghasemi, M. Mahdavian, B. Ramezanzadeh and M. Rostami, *Corros. Sci.*, 2015, **94**, 207–217.
- 15 J. Tedim, S. K. Poznyak, A. Kuznetsova, D. Raps, T. Hack, M. L. Zheludkevich and M. G. S. Ferreira, *ACS Appl. Mater. Interfaces*, 2010, **2**, 1528–1535.
- 16 V. R. L. Constantino and T. J. Pinnavaia, *Inorg. Chem.*, 1995, **34**, 883–892.

- 17 S. P. Newman and W. Jones, *New J. Chem.*, 1998, **22**, 105–115.
- 18 C. Barriga, W. Jones, P. Malet, V. Rives and M. A. Ulibarri, *Inorg. Chem.*, 1998, **37**, 1812–1820.
- 19 Q. Wang and D. O'Hare, *Chem. Rev.*, 2012, **112**, 4124–4155.
- 20 P. Guoxiang, X. Xinhui, L. Jingshan, C. Feng, Y. Zhihong and F. Hongjin, *Appl. Clay Sci.*, 2014, **102**, 28–32.
- 21 F. Z. Mahjoubi, A. Khalidi, M. Abdennouri and N. Barka, *Desalin. Water Treat.*, 2016, **57**, 21564–21576.
- 22 S. Hasan, H. Al Ali, M. Al-Qubaisi, M. Zobir Hussein, M. Ismail, Z. Zainal and M. Nazrul Hakim, *Int. J. Nanomedicine*, 2012, **7**, 3351–63.
- 23 S. Barik, A. Khandual, L. Behera, S. K. Badamali and A. Luximon, *Cellulose*, 2017, **24**, 1107–1120.
- 24 M. Chakraborti, J. K. Jackson, D. Plackett, S. E. Gilchrist and H. M. Burt, *J. Mater. Sci. Mater. Med.*, 2012, **23**, 1705–13.
- 25 C. M. Becker, A. D. Gabbardo, F. Wypych and S. C. Amico, *Compos. Part A Appl. Sci. Manuf.*, 2011, **42**, 196–202.
- 26 B. Nagendra, A. M. Joseph, B. Sana, T. Jana and E. B. Gowd, *ACS Appl. Nano Mater.*, 2018, **1**, 111–121.
- 27 J. Tedim, A. Kuznetsova, A. N. Salak, F. Montemor, D. Snihirova, M. Pilz, M. L. Zheludkevich and M. G. S. Ferreira, *Corros. Sci.*, 2012, **55**, 1–4.
- 28 L. Wang, Q. Zong, W. Sun, Z. Yang and G. Liu, *Corros. Sci.*, 2015, **93**, 256–266.
- 29 T. Stimpfling, F. Leroux and H. Hintze-Bruening, *Colloids Surfaces A Physicochem. Eng. Asp.*, 2014, **458**, 147–154.
- 30 M. L. Zheludkevich, S. K. Poznyak, L. M. Rodrigues, D. Raps, T. Hack, L. F. Dick, T. Nunes and M. G. S. Ferreira, *Corros. Sci.*, 2010, **52**, 602–611.
- 31 M. Zhou, L. Yan, H. Ling, Y. Diao, X. Pang, Y. Wang and K. Gao, *Appl. Surf. Sci.*,

- 2017, **404**, 246–253.
- 32 S. P. V. Mahajanam and R. G. Buchheit, *CORROSION*, 2008, **64**, 230–240.
- 33 X. Luo, S. Yuan, X. Pan, C. Zhang, S. Du and Y. Liu, *ACS Appl. Mater. Interfaces*, 2017, **9**, 18263–18275.
- 34 S. K. Poznyak, J. Tedim, L. M. Rodrigues, A. N. Salak, M. L. Zheludkevich, L. F. P. Dick and M. G. S. Ferreira, *ACS Appl. Mater. Interfaces*, 2009, **1**, 2353–2362.
- 35 N. S. Qu, W. H. Qian, X. Y. Hu and Z. W. Zhu, *Int. J. Electrochem. Sci.*, 2013, **8**, 11564–11577.
- 36 E. Stoyanova and D. Stoychev, in *Corrosion Resistance*, 2012, pp. 241–271.
- 37 M. F. Montemor, W. Trabelsi, S. V. Lamaka, K. A. Yasakau, M. L. Zheludkevich, A. C. Bastos and M. G. S. Ferreira, *Electrochim. Acta*, 2008, **53**, 5913–5922.
- 38 E. Stoyanova, D. Nikolova, D. Stoychev, P. Stefanov and T. Marinova, *Corros. Sci.*, 2006, **48**, 4037–4052.
- 39 J. K. Pancreicious, J. P. Deepa, V. Jayan, U. S. Bill, T. P. D. Rajan and B. C. Pai, *Surf. Coatings Technol.*, 2018, **356**, 29–37.
- 40 J. Carneiro, A. F. Caetano, A. Kuznetsova, F. Maia, A. N. Salak, J. Tedim, N. Scharnagl, M. L. Zheludkevich and M. G. S. Ferreira, *RSC Adv.*, 2015, **5**, 39916–39929.
- 41 M. F. Montemor, D. V. Snihirova, M. G. Taryba, S. V. Lamaka, I. A. Kartsonakis, A. C. Balaskas, G. C. Kordas, J. Tedim, A. Kuznetsova, M. L. Zheludkevich and M. G. S. Ferreira, *Electrochim. Acta*, 2012, **60**, 31–40.
- 42 D. Ho, N. Brack, J. Scully, T. Markley, M. Forsyth and B. Hinton, *J. Electrochem. Soc.*, 2006, **153**, B392.
- 43 S. Kallip, A. C. Bastos, K. A. Yasakau, M. L. Zheludkevich and M. G. S. Ferreira, *Electrochem. commun.*, 2012, **20**, 101–104.
- 44 D. Snihirova, S. V. Lamaka and M. F. Montemor, in *Smart Composite Coatings and*

- Membranes*, Elsevier, 2016, pp. 85–121.
- 45 M. Serdechnova, V. L. Ivanov, M. R. M. Domingues, D. V. Evtuguin, M. G. S. Ferreira and M. L. Zheludkevich, *Phys. Chem. Chem. Phys.*, 2014, **16**, 25152–25160.
- 46 B. M. Weckhuysen and D. E. Keller, *Catal. Today*, 2003, **78**, 25–46.
- 47 G. A. Caravaggio, C. Detellier and Z. Wronski, *J. Mater. Chem.*, 2001, **11**, 912–921.
- 48 S. Onodera and Y. Ikegami, *Inorg. Chem.*, 1980, **19**, 615–618.
- 49 M. Z. bin Hussein, Z. Zainal, A. H. Yahaya and A. binti A. Aziz, *Mater. Sci. Eng. B*, 2002, **88**, 98–102.
- 50 S. Onodera and Y. Ikegami, *Inorg. Chem.*, 1980, **19**, 615–618.
- 51 I. D. Dobrea, C. E. Ciocan, E. Dumitriu, M. I. Popa, E. Petit and V. Hulea, *Appl. Clay Sci.*, 2015, **104**, 205–210.
- 52 B. Kilos, A. T. Bell and E. Iglesia, *J. Phys. Chem. C*, 2009, **113**, 2830–2836.
- 53 B. L. Hurley, S. Qiu and R. G. Buchheit, *J. Electrochem. Soc.*, 2011, **158**, C125.
- 54 L. Guo, F. Zhang, J.-C. Lu, R.-C. Zeng, S.-Q. Li, L. Song and J.-M. Zeng, *Front. Mater. Sci.*, 2018, **12**, 198–206.
- 55 Y. Liu, G. Z. Meng and Y. F. Cheng, *Electrochim. Acta*, 2009, **54**, 4155–4163.
- 56 J. Jayaraj, S. Amruth Raj, A. Srinivasan, S. Ananthakumar, U. T. S. Pillai, N. G. K. Dhaipule and U. K. Mudali, *Corros. Sci.*, 2016, **113**, 104–115.
- 57 D. S. Kharitonov, J. Sommertune, C. Örnek, J. Ryl, I. I. Kurilo, P. M. Claesson and J. Pan, *Corros. Sci.*, 2019, **148**, 237–250.
- 58 H. Ashassi-Sorkhabi and M. Es'haghi, *Corros. Sci.*, 2013, **77**, 185–193.

## Chapter 5

### Layered double hydroxide for corrosion sensing applications on light metal alloys

---



#### Abstract

The precise corrosion monitoring can be achieved by the controlled release of corrosion sensing compounds from a container by indicating the pH change associated with the cathodic or anodic reaction that accompanies corrosion. Layered double hydroxide (LDH) is a versatile material for loading the corrosion sensing compounds. In the present study, Zn-Al LDH was used as the container to load phenolphthalein for corrosion sensing applications on light alloys. The synthesized Zn-Al phph LDH was characterized by SEM, FT-IR, EDS, XPS, and XRD analysis, which confirm the formation of phenolphthalein modified LDH. Corrosion resistance investigations in NaCl solution by potentiodynamic polarization analysis and electrochemical impedance spectroscopy (EIS) indicate that the phenolphthalein loaded LDH can be utilized to make composite coatings on metals without prompting the corrosion. During the corrosion analysis the pink coloration on the cathodic reaction sites on metal surface indicate the feasibility of phenolphthalein loaded LDH as corrosion sensing material on magnesium AZ31 alloy (Mg-2.83Al-0.98Zn-0.108Mn), while the corrosion sensing on aluminium alloy could not be achieved in presence of Zn-Al phph LDH. The modified LDH dispersed acrylic coated AZ31 alloy also shows pink colour formation upon corrosion.

## **5.1. Introduction**

Corrosion is a destructive process by which the metallic materials are converted to their more stable oxides, hydroxides or sulphides. It is a major challenge on the safety and economic aspect. Various methodologies have been adopted to control the corrosion, such as selecting corrosion resistant materials, anodizing, galvanization and applying protective coatings. However, metal deterioration is an inevitable mechanism. Recently, coatings that can sense the early stages of corrosion process have developed as an additional precaution. The corrosion sensing can improve the functionality, performance and average life span of the metallic materials by providing timely maintenance. Corrosion monitoring can be achieved by the coatings containing organic or inorganic additives having the ability to response towards different types of environmental stimuli.<sup>1</sup> Change in pH or temperature, mechanical action, radiation, redox reactions and presence of heavy metals or chemicals can be act as external stimuli to induce an easily detectable colour or fluorescence change.<sup>2</sup>

Corrosion is an electrochemical process that influences local pH change on the material.<sup>3</sup> Incorporation of pH indicators in the coatings is an easy method for detecting early state corrosion to ensure change in colour by change in localized pH owing to the oxidation or reduction reaction. The anodic regions possess lower pH and the cathodic regions exhibit higher pH. Both color and fluorescent pH indicators have been incorporated into coating systems for corrosion sensing applications.<sup>4,5</sup> The pH-sensing compounds are mainly used to detect the pH increase associated with cathodic reaction that accompanies the anodic corrosion reaction.<sup>6</sup> In the coating, the sensing compound should be homogeneously dispersed as well as compatible without compromising the barrier properties. Zhang and Frankel<sup>5</sup> made pH sensing acrylic coating on aluminum by incorporating phenolphthalein, bromothymol blue, 7-hydroxycoumarin and coumarin compounds. The former two are colour changing and other two are fluorescent compounds. Phenolphthalein is an acid-base indicator which begins to show pink colour at the alkaline pH of 8.2 onwards and exhibit a bright purple in very high pH. However, the direct contact between pH indicators and the

matrix could reduce the coatings properties and trigger the corrosion. Additionally, deactivation or untimely sensing may occur by the interaction with coating matrix. Incorporation of active compounds into coating after its encapsulation or immobilization in micro or nano capsule helps to overcome the drawbacks of direct incorporation.<sup>7</sup>

Container based composite coating system developed by encapsulation of active corrosion sensing compounds in a container that can provide a sensible on-time response. Phenolphthalein encapsulations have been carried out with different containers such as urea-formaldehyde, melamine-formaldehyde, porous silica and polyurea microcapsules. The micro-sized polyurea capsules could load 12 wt% of phenolphthalein and were able to indicate corrosion initiation processes by a pink coloration at the cathodic areas on aluminium and magnesium alloys.<sup>4</sup> Mesoporous silica containers were synthesized for active compound loading in the coating formulation, since the silica shell reduces the damaging interaction of phenolphthalein with the coating.<sup>8,9</sup> Li et al.<sup>10</sup> prepared a corrosion sensing urethane coating by incorporating high-pH responsive polymer based oil-core and water-core microcapsules encapsulated with phenolphthalein indicator.

Layered double hydroxides are a class of lamellar compounds that consist of positively charged brucite like host layers and hydrated exchangeable anions located in the interlayer gallery for charge balance. LDH has been widely accepted as the container for different types of anions/molecules by the reason of the prominent anion-exchange capacity. The functional ions loaded LDH are used for better catalytic activity,<sup>11</sup> higher supercapacitive behavior,<sup>12</sup> precise drug delivery,<sup>13,14</sup> etc. owing to their stability, low toxicity and biocompatibility. LDH were also investigated as reinforcements in anticorrosion coatings or as polymer composites. Super hydrophobic laurate intercalated LDH film provides corrosion protection of the coated metal substrate.<sup>15</sup> However, LDH has not yet been considered as the container for corrosion sensing compound.

In the present investigation, phenolphthalein modified Zn-Al layered double hydroxide was synthesized to understand their corrosion sensing properties.

Chemical and structural analyses were done to determine the interaction of phenolphthalein with layered double hydroxides. Influence of phenolphthalein in the structural characteristics, corrosion performance and corrosion sensing behavior on AZ31 magnesium alloy substrates were studied. The modified LDH based acrylic composite coating on metallic substrates was intended for applications in structural and engineering components.

## **5.2. Experimental**

### **5.2.1. Materials**

Zn(NO<sub>3</sub>)<sub>2</sub>·6H<sub>2</sub>O (98%), Al(NO<sub>3</sub>)<sub>3</sub>·9H<sub>2</sub>O (98.5%) and phenolphthalein were bought from Sigma-Aldrich Co. Ltd., USA. NaOH (97%), were procured from SD Fine chemicals, India. NaCl (99%) were purchased from Merck, India. The chemicals as obtained were used for the synthesis and coatings.

### **5.2.2. Zn-Al phph LDH synthesis**

Zn(NO<sub>3</sub>)<sub>2</sub>·6H<sub>2</sub>O and Al(NO<sub>3</sub>)<sub>3</sub>·9H<sub>2</sub>O in 2:1 weight ratio were dissolved in distilled water to get 5 mM and 10 mM solutions, respectively. 5 wt% of phenolphthalein powder was added to 1:1 ethanol-water mixture and made the solution. The phenolphthalein solution was added to the salt solution slowly under vigorous stirring at room temperature for 24hr. The reaction was carried out in a round bottom flask under nitrogen atmosphere by co-precipitation method at different pH values; pH8, pH10 and pH12. pH of the reacting mixture was maintained by adding NaOH solution. The precipitate gained was washed with hot distilled water until the solution become neutral. The neutral precipitate was again washed with ethanol to remove unreacted phenolphthalein and dried.

### **5.2.3. Acrylic-LDH composite coating**

A356 aluminium (Al-7Si-0.35Mg wt.%) and AZ31 magnesium alloys were taken as the substrate materials for corrosion sensing and corrosion resistance studies. The strips were polished using SiC abrasive paper up to 1000 grit size and cleaned with

acetone by ultra-sonication. The cleaned and dried strips were used for the coating. Modified LDH dispersed in commercially available acrylic monomer and dip coated on the polished substrate.

#### 5.2.4. Sample analysis

##### 5.2.4.1. Zn-Al phph LDH characterization

Structural and morphological studies of modified LDH were done by SEM, XRD, EDS, XPS, and FTIR. The details of instrumental methods are given in chapter 2, section 2.2.3.1.

##### 5.2.4.2. Corrosion analysis

Corrosion performance of A356 alloy and AZ31 alloy samples at ambient conditions was measured by a conventional three-electrode cell in 3.5 wt% NaCl and 1 wt% NaCl solutions, respectively. The instrumentation set up measurement parameters are same as explained in chapter 2, section 2.2.3.2. The measurements were conducted on bare alloys in the electrolyte containing dispersed LDH to analyze the electrochemical behavior. The samples were exposed to electrolyte (3.5/1 wt.% NaCl or 0.05 wt % of LDH +3.5/1 wt.% NaCl) for about 30 minutes to stabilize the OCP.

##### 5.2.4.3. Corrosion sensing

Corrosion sensing of the phenolphthalein loaded LDH was carried out in three different ways. First, the activity on bare A356/AZ31 alloy in NaCl solution: the strips were immersed in 3.5/1wt % NaCl solution containing dispersed Zn-Al phph LDH. Second, on Zn-Al phph LDH loaded acrylic paint in 1wt % NaOH solution and third on Zn-Al phph LDH-acrylic composite coated AZ31 alloy in 1wt % NaCl solution. The colour change was observed visually and captured by a digital camera.

### 5.3. Results and Discussion

#### 5.3.1. SEM Analysis

SEM images and EDS spectra of Zn-Al LDH and Zn-Al phph LDH synthesized by co-precipitation method at pH10 is given in Figure 5.1. The SEM images show an aggregated LDH structure, since the nucleation is very fast in presence of strong base (NaOH).<sup>16</sup> Adsorption of bulky phenolphthalein molecule at the sides and edges of the layers leads to produce less agglomerations for Zn-Al phph LDH compared to the nitrate intercalated LDH.<sup>17</sup> Elemental composition analysis indicates the presence of Zn, Al, N and O in the prepared Zn-Al LDH. The weight percentages are given in the table as inset. The elemental composition of Zn-Al phph LDH comprises of Zn, Al, N, O and C. Sharp decrease in the weight percentage of nitrogen and the presence of carbon in the modified LDH designate successive removal of nitrate group and phenolphthalein incorporation.

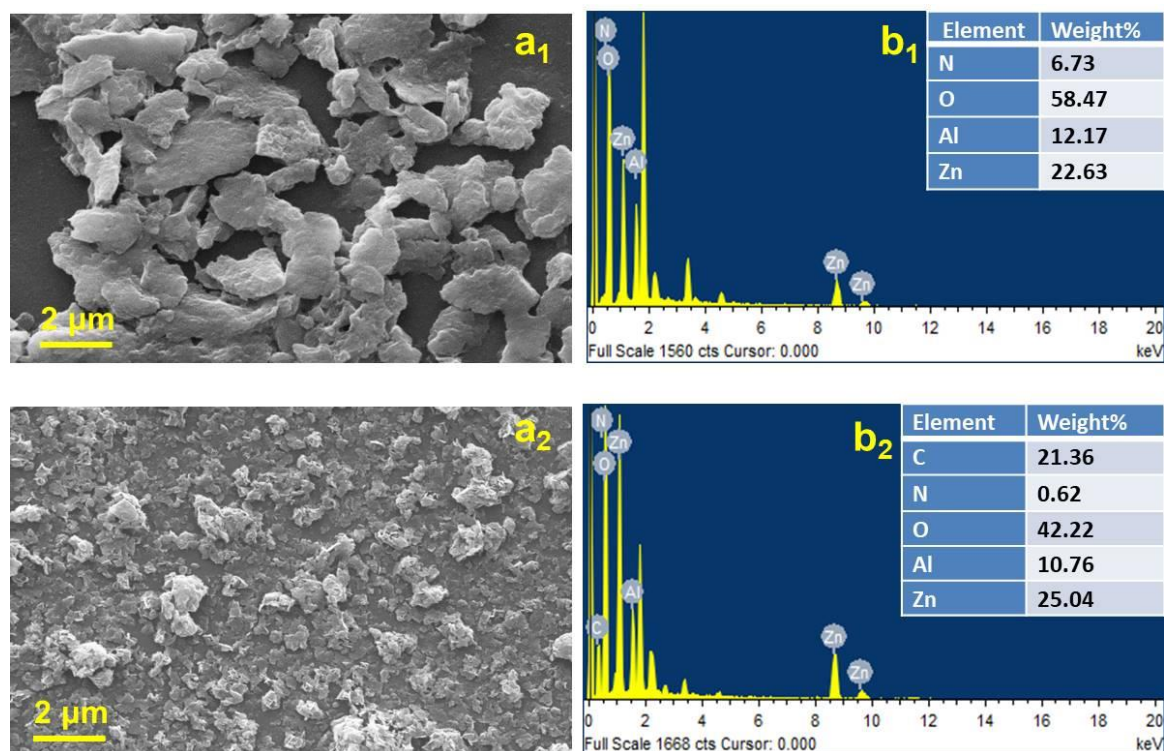


**Figure 5.1:** SEM image and EDS spectra of Zn-Al LDH (a<sub>1</sub>&b<sub>1</sub>) and Zn-Al phph LDH (a<sub>2</sub>&b<sub>2</sub>).

### 5.3.2. XRD Analysis

Figure 5.2 shows the X-ray diffraction patterns of Zn-Al LDH, Zn-Al phph LDH prepared at different pH condition. The unmodified LDH has peaks at  $2\theta = 9.89^\circ$ ,  $19.97^\circ$  and  $34.45^\circ$  corresponding to (003), (006) and (012) planes, respectively; typical reflections for nitrate intercalated Zn-Al LDH with d-spacing of 0.89 nm.<sup>18,19</sup> Phenolphthalein modified LDH possess an upshift in peak position compared to the unmodified one. At pH8 and pH10 the modified LDHs have peaks at  $2\theta = 10.16^\circ$ ,  $20.13^\circ$  and  $34.45^\circ$  analogous to the (003), (006) and (012) planes, respectively. The d-spacing calculated based on (003) plane by Bragg's equation is reduced from 0.89 nm to 0.87 nm. An additional small peak at  $11.55^\circ$  is generated and its intensity is increased with increase in alkaline pH. This could be attributed the layer collapse by removal of water from the interlayer space at very higher pH. When phenolphthalein is present, the intensity of (003) peak increased while, full width at half maximum (FWHM) decreased. Small FWHM after the modification indicates the more crystalline nature of LDH.<sup>20</sup>

At pH12 Zn-Al phph LDH exhibit (003), (006) and (012) planes reflections at  $2\theta = 11.65^\circ$ ,  $23.71^\circ$  and  $34.45^\circ$ , consistently. The d-spacing again decreased to 0.759 nm. If metal hydroxide layer thickness is 0.477 nm,<sup>21</sup> the gallery height can be estimated as 0.293 nm, which is lesser than the phenolphthalein diameter (0.6 nm). This is resulted from the strong interaction between the layers and the guest molecule. It also indicates that the phenolphthalein does not distribute as free molecule/ion in the interlamellar spacing while, it may grafted or hydrogen bonded to the metal hydroxide framework. The d-spacing of grafted system is comparable to that described for carbonate-LDH.<sup>22,23</sup>

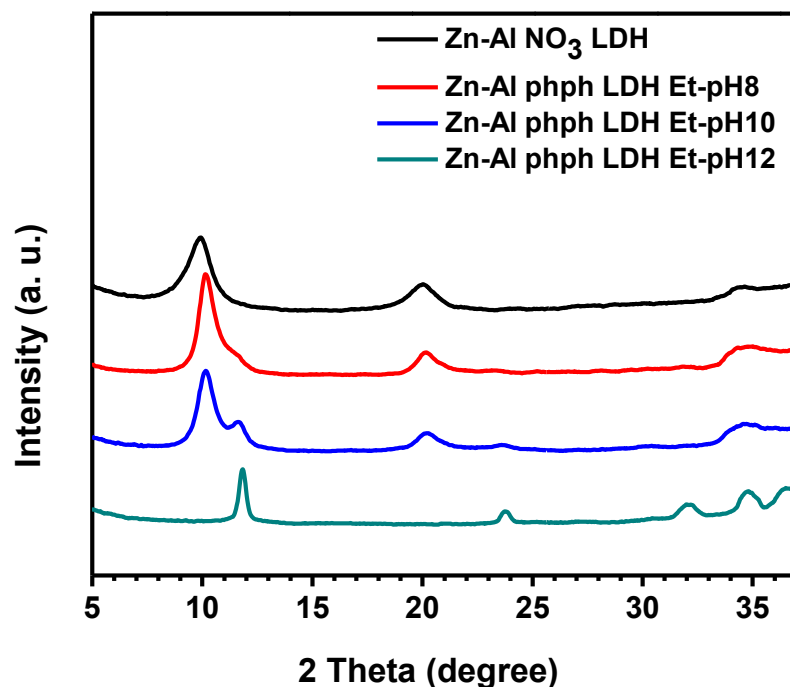


**Figure 5.2:** XRD pattern of Zn-Al LDH and Zn-Al phph LDH synthesized at different pH.

### 5.3.3. FTIR Analysis

ATR-FTIR spectra of Zn-Al LDH and Zn-Al phph LDH are given in Figure 5.3. A broad band centered at  $3440\text{ cm}^{-1}$  is assigned to the stretching mode of hydroxyl group (-OH) on the LDH host layers and interlayer water molecules. Broadening of this peak indicates the presence of hydrogen bonding by interlayer water molecules of the hydrocalcite structure. The peak at  $1630\text{ cm}^{-1}$  corresponds to the H-O-H bending vibration of water molecules.<sup>24</sup> The spectra for Zn-Al phph LDH provide a clear evidence of phenolphthalein modification by showing additional peaks than the pure LDH. However, washing with ethanol removed most of the weakly adsorbed phenolphthalein molecules from the sample. Strong peak at  $764\text{ cm}^{-1}$  is due to the stretching vibrations of aromatic C-H bond. Bands representing C=O bond and C-O bond, appear in the region  $1741\text{ cm}^{-1}$  and  $1218\text{ cm}^{-1}$  respectively. The C=O absorption band for phenolphthalein modified LDH possess a higher value comparing to pure phenolphthalein ( $1731\text{ cm}^{-1}$ ). This change may be due to the increases the strain of

lactone ring generated by the interaction with the LDH.<sup>25</sup> The peak at  $1550\text{ cm}^{-1}$  is corresponding to aromatic C=C stretching vibrations. Strong peak at  $1345\text{ cm}^{-1}$  may be due to the symmetric stretching of carboxylate ion formed in the alkaline medium. Different peaks generated between  $500\text{-}1000\text{ cm}^{-1}$  is due to the presence of aromatic structure.<sup>26</sup>

As the pH increased the contraction of peak at  $3,440\text{ cm}^{-1}$  (-OH stretching) and diminishing of peak at  $1630\text{ cm}^{-1}$  (H-O-H bending) were observed, which indicates the removal of water at high pH.<sup>27</sup> Additionally, the water molecules may replace by phenolphthalein molecule.<sup>28</sup> The intermolecular hydrogen bonding can still remain with phenolphthalein and small quantity of water molecules that maintain the -OH vibration at  $3,440\text{ cm}^{-1}$ .<sup>29</sup>

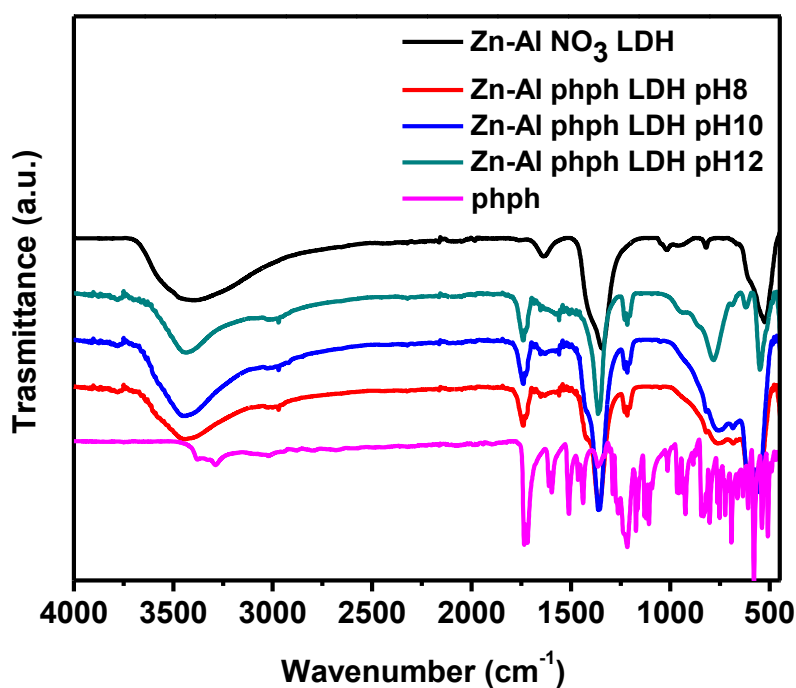


**Figure 5.3:** FTIR spectra of Zn-Al LDH, Zn-Al phph LDH synthesized at different pH and phenolphthalein.

#### **5.3.4. XPS Analysis**

The chemical composition of Zn-Al phph LDH was analyzed by X-ray photoelectron spectroscopy (XPS). The survey spectrum given in Figure 5.4a confirmed that the modified LDH was mainly composed of Zn, Al, C and O. The high resolution Zn 2p spectra of LDH shown in Figure 5.4b can be divided into two peaks located at 1021.5 eV and 1044.59 eV, representing Zn 2p<sub>3/2</sub> and Zn 2p<sub>1/2</sub> of Zn<sup>2+</sup>, respectively. The XPS spectrum of Al 2p (Figure 5.4c) was observed at the binding energy of 74.65 eV corresponding to Al<sup>3+</sup>. The results represent the formation of LDH as given in previous reports instead of simple physical mixture.<sup>30,31</sup>

The deconvoluted C1s peak (Figure 5.4d) consists of three kinds of carbon at different environments. The peak at 284.64 eV for C-C/C-H, 286.6 eV for C-OH and 288.8 eV for O-C=O of the phenolphthalein group. A broad and asymmetric O1s spectrum (Figure 5.4e) comprises three components corresponding to the -OH at 531.4 eV, -C=O at 529.9 eV and hydrogen bonded -O-H--O group.<sup>32</sup> The hydrogen bonding may be resulted by the grafting of phenolphthalein on LDH layers as well as water molecule interaction.

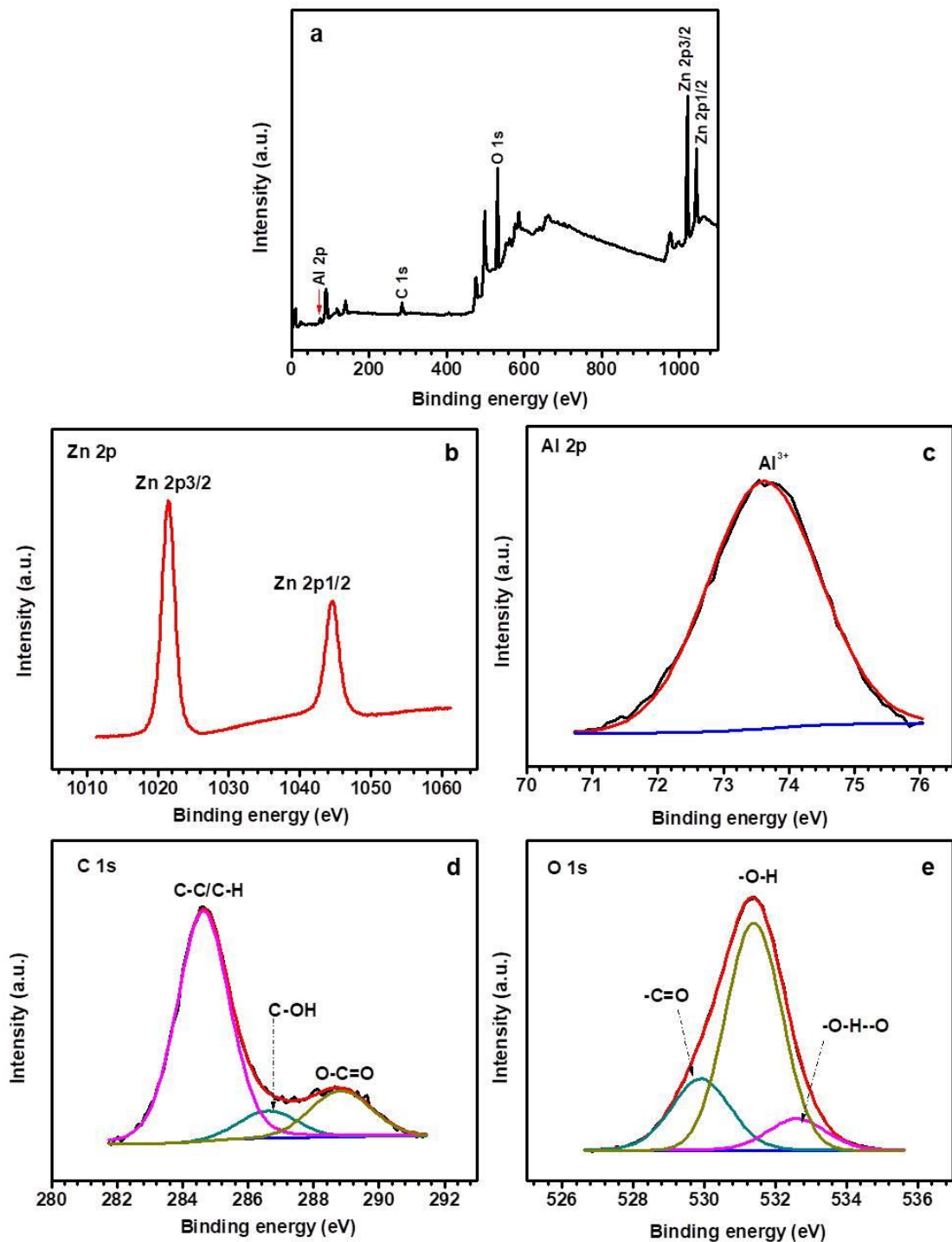


**Figure 5.4:** XPS survey spectrum of (a) Zn-Al phph LDH, high-resolution spectrum of (b) Zn 2p, (c) Al 2p, (d) C 1s, and (e) O 1s.

### 5.3.5. Corrosion Studies

#### 5.3.5.1. Potentiodynamic polarization measurements

Corrosion analysis was carried out to find out the feasibility of Zn-Al phph LDH for the sensing applications, without altering the barrier properties. The LDH particles were dispersed in NaCl solution, which was used as the electrolyte for the test on both aluminium A356 alloy (in 3,5 wt% NaCl) and magnesium AZ31 alloy (in 1 wt% NaCl). The potentiodynamic polarization curves for all the samples scanned from cathodic side to anodic side with reference to their OCP (open circuit potential) values are shown in Figure 5.5a (A356) and Figure 5.5b (AZ31). Tafel plot is obtained by plotting the logarithm of current density Vs. Potential behavior. The corrosion current density ( $i_{\text{corr}}$ ) and corrosion potential ( $E_{\text{corr}}$ ) were measured from the plot with reference to the standard calomel electrode, which are presented in Table 5.1. The  $i_{\text{corr}}$  value of A356 in NaCl solution alone is  $27.79 \times 10^{-6} \text{ Acm}^{-2}$  that is reduced to  $5.960 \times 10^{-6} \text{ Acm}^{-2}$  and  $3.322 \times 10^{-6} \text{ Acm}^{-2}$  for Zn-Al LDH in NaCl and Zn-Al phph LDH in 3.5 wt% NaCl solution, respectively. For AZ31 alloy, the  $i_{\text{corr}}$  value in NaCl solution alone is  $44.46 \times 10^{-6} \text{ Acm}^{-2}$  that is reduced to  $8.023 \times 10^{-6} \text{ Acm}^{-2}$  and  $31.86 \times 10^{-6} \text{ Acm}^{-2}$  for Zn-Al LDH in NaCl and Zn-Al phph LDH in 1 wt% NaCl solution, respectively. Lower corrosion current density indicates the corrosion resistance by the addition of LDH particles. The decrease in current intensity is due to the low chemical reaction in LDH added solution. It can be concluded that the corrosion resistances of LDH in NaCl solution are higher than that of NaCl alone<sup>33</sup>. This may be due to the ion exchange behavior of LDH between intercalated anion and the chloride ion present in the electrolyte.<sup>34</sup>

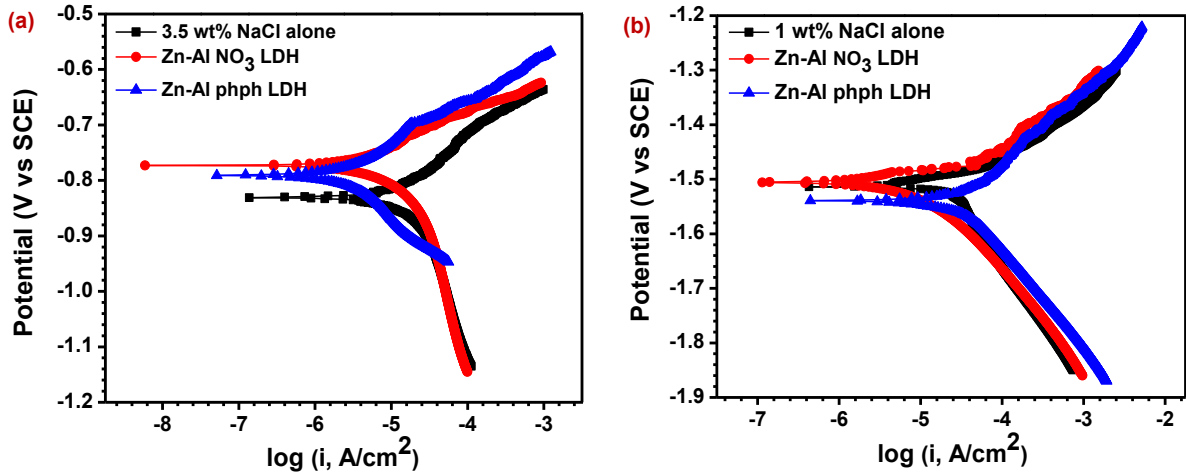


**Figure 5.5:** Tafel plot of (a) A356 alloy in 3.5 wt% and (b) AZ31 alloy in 1wt% NaCl alone, NaCl solution containing 0.05 wt% of Zn-Al LDH, and NaCl solution containing 0.05 wt% of Zn-Al phph LDH.

**Table 5.1:**  $E_{\text{corr}}$  and  $i_{\text{corr}}$  values obtained from potentiodynamic polarization scan given in Figure 5.5.

| Sample ID                 | A356 Alloy                    |   | AZ31 Alloy                    |   |
|---------------------------|-------------------------------|---|-------------------------------|---|
|                           | $E_{\text{corr}}$ (V vs. SCE) | $i_{\text{corr}}$ (A cm <sup>-2</sup> ) | $E_{\text{corr}}$ (V vs. SCE) | $i_{\text{corr}}$ (A cm <sup>-2</sup> ) |
| NaCl alone                | -0.831                        | 27.79 x 10 <sup>-6</sup>                | -1.514                        | 44.46 x 10 <sup>-6</sup>                |
| Zn-Al NO <sub>3</sub> LDH | -0.773                        | 5.960 x 10 <sup>-6</sup>                | -0.534                        | 8.023 x 10 <sup>-6</sup>                |
| Zn-Al phph LDH            | -0.791                        | 3.322 x 10 <sup>-6</sup>                | -1.506                        | 31.86 x 10 <sup>-6</sup>                |

### 5.3.5.2. Electrochemical Impedance Spectroscopy (EIS)

Figure 5.6 shows the Nyquist representations of EIS measurements done on A356 alloy (a) and AZ31 alloy (b). The loops corresponding to aluminum alloy surface in all the solutions (3.5 wt% NaCl alone, Zn-Al LDH and Zn-Al phph LDH) show a capacitive arc at the given frequency range. The capacitive arc observed by the combined effect of double layer capacitance and metal dissolution, and its diameter

represents the charge transfer resistance ( $R_{ct}$ ) at the metal-solution interface. For magnesium alloy, an inductive loop at very low frequency is observed due to the pitting corrosion<sup>35</sup>. The increase in loop diameter by the addition of LDH indicates better corrosion protection the electrolyte than the pure NaCl solution. The presence of phenolphthalein could not increase the corrosion performance instead it was slightly decreased and the difference is more visible on AZ31 alloy. This may be due to the lower ion exchange capacity of bulky phenolphthalein molecule anchored LDH with corrosive chloride ions. However, the corrosion inhibition efficiencies are comparable.

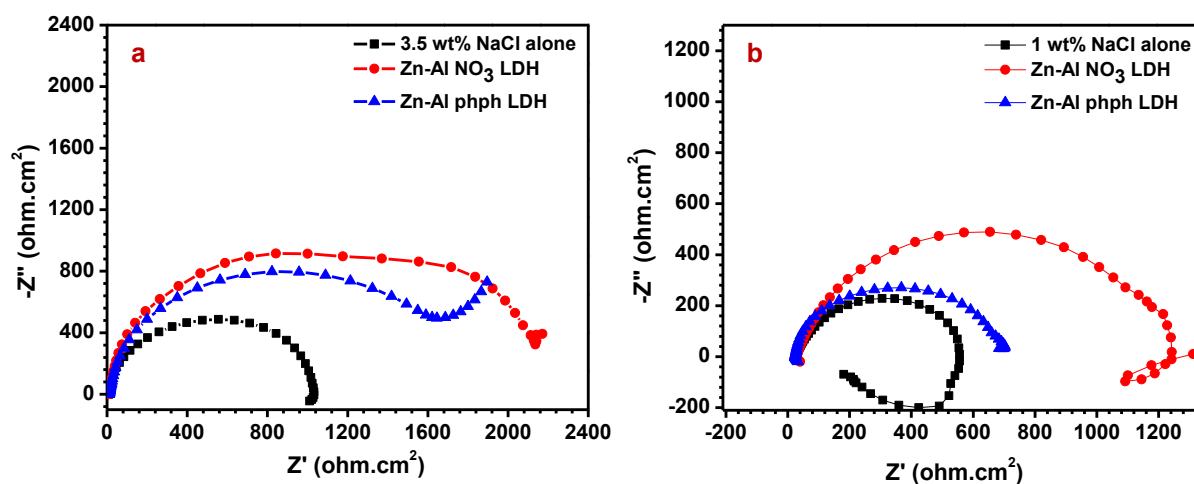


**Figure 5.6:** Nyquist plots of the samples at their open circuit potential with a peak-to-peak amplitude of 10 mV in the frequency range from (a)  $10^4$  to  $10^{-2}$  Hz for A356 and (b)  $10^4$  to  $10^{-1}$  Hz for AZ31.

The bode plots between  $\log Z$  and  $\log f$  are given in Figure 5.7a for A356 and Figure 5.5b for AZ31 alloy. The resistance spectra of Bode plots depicts the increase in impedance ( $\log Z$ ) values are in the order of NaCl alone < Zn-Al phph LDH < Zn-Al LDH as explained above.

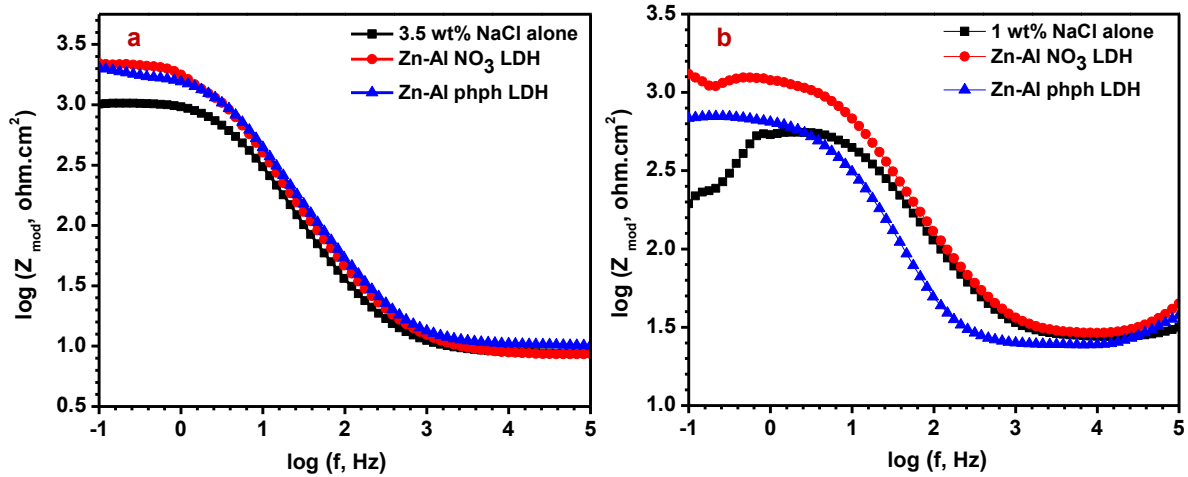
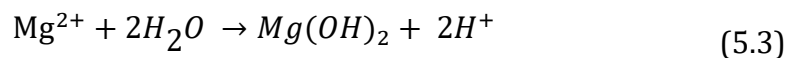
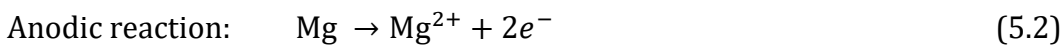
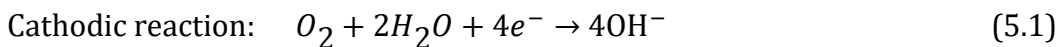


**Figure 5.7:** Bode plots of (a) A356 corrosion behaviour in 3.5 wt% NaCl and (b) AZ31 in 1 wt% NaCl alone and LDH added solutions (log  $Z$  vs. log  $f$ )

### 5.3.6. Corrosion Sensing

The strips of aluminium A356 and magnesium AZ31 alloys were polished with SiC paper up to 1000 grit size and cleaned with acetone under ultrasonication. The cleaned samples were immersed in a solution containing Zn-Al phph LDH in 3.5 wt% NaCl solution.

For AZ31 alloy, the dried strip was kept in the 1wt % NaCl solution taken in a petri dish for ten minutes. Within 30 seconds magnesium starts corroding and produces pink coloration. Figure 5.8 shows the colour change after 2 minutes (a) and 10 minutes (b) on the metal. The pink colour is observed at the cathode and the anodic site becomes colourless that can be explained as equations 5.1-5.3 that representing the corrosion reaction. The local pH at the anode will decrease and at the cathode will increase. Hence, increase in pH at cathode will produce pink coloration in presence of phenolphthalein released from the LDH container.



For A356 alloy, the colored spots were not appeared even after 24 hours of immersion (Figure 5.8c), while the corrosion has been started by that time. This suggests that the slow corrosion rate of aluminium alloy could not specifically spot the cathodic reaction site by the pink coloration due to the diffusion of hydroxyl ions in the NaCl solution.<sup>4</sup>

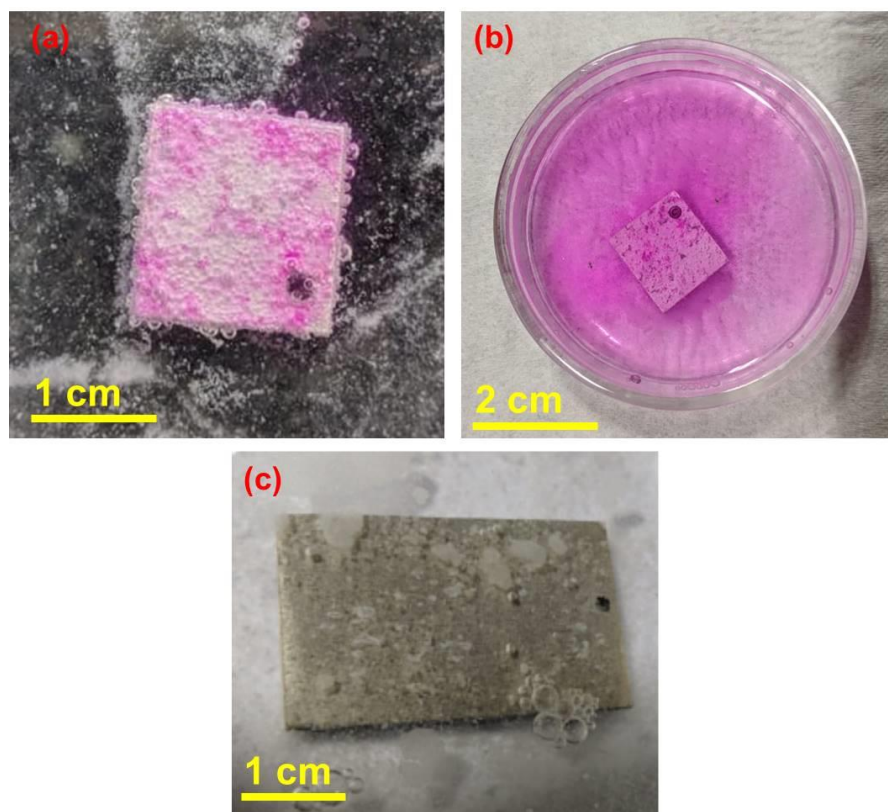


**Figure 5.8:** Photographs of corroding surfaces of AZ31 alloy after (a) 2 minutes (b) 10 minutes and (c) A356 alloy after 24 hours.

The pH sensitivity of Zn-Al phph LDH loaded acrylic paint was checked with 1wt % NaOH solution (Figure 5.9a and 5.9b). Addition of a drop of NaOH clearly produces a pink colouration on the paint. More quantity of NaOH could turn pink more areas on the surface. However, after 5 minutes, the entire phenolphthalein becomes leached out in the presence of strong alkali and the paint turns colourless. The corrosion sensing on Zn-Al phph LDH-acrylic composite coated AZ31 alloy was done for 48 hours in 1wt % NaCl solution. After 48 hours the coating started to show colour

change owing to the corrosion happened on the metal surface beneath the coating. Figure 5.9c shows the corresponding colour change.

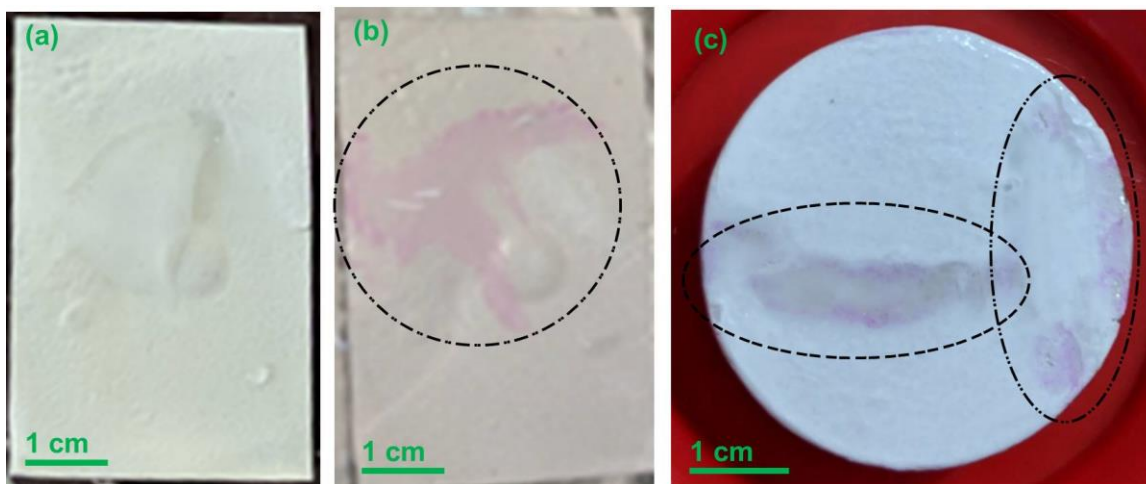


**Figure 5.9:** Acrylic paint in 1% NaOH solution: (a) 0 minutes, (b) 5 minutes, and (c) acrylic coating on AZ31 in 1% NaCl solution: After 48 hours.

#### 5.4. Conclusion

The corrosion indicator, phenolphthalein, was incorporated in Zn-Al LDH container. SEM, EDS, FTIR, XPS and XRD studies show the corresponding LDH modification by phenolphthalein adsorption onto the LDH. The corrosion experiments indicate that, an increase in anti-corrosion behaviour of both A356 aluminium and AZ31 magnesium alloys was observed in the presence of Zn-Al LDH as well as Zn-Al phph LDH. The improvement in corrosion resistance may be due to the barrier properties and chloride ion exchange capacity of LDH. However, phenolphthalein modification slightly reduced the corrosion inhibition property. The phenolphthalein modified LDH was successfully used to detect corrosion on the AZ31 magnesium alloy surface. The spot of colour change on different sites is observed due to increase in pH associated with the local cathodic reaction on the alloy in sodium chloride solution. The corrosion sensing on A356 aluminium alloy could not be achieved in presence of Zn-Al phph LDH owing to the slow corrosion rate and hydroxyl ion diffusion.

## References

- 1 W. Feng, S. H. Patel, M.-Y. Young, J. L. Zunino and M. Xanthos, *Adv. Polym. Technol.*, 2007, **26**, 1–13.
- 2 A. Augustyniak and W. Ming, *Prog. Org. Coatings*, 2011, **71**, 406–412.
- 3 F. J. Maile, T. Schauer and C. D. Eisenbach, *Prog. Org. Coatings*, 2000, **38**, 111–116.
- 4 F. Maia, J. Tedim, A. C. Bastos, M. G. S. Ferreira and M. L. Zheludkevich, *RSC Adv.*, 2014, **4**, 17780.
- 5 J. Zhang and G. S. Frankel, *CORROSION*, 1999, **55**, 957–967.
- 6 S. B. Ulaeto, R. Rajan, J. K. Pancrecius, T. P. D. Rajan and B. C. Pai, *Prog. Org. Coatings*, 2017, **111**, 294–314.
- 7 D. Raps, T. Hack, J. Wehr, M. L. Zheludkevich, A. C. Bastos, M. G. S. Ferreira and O. Nuyken, *Corros. Sci.*, 2009, **51**, 1012–1021.
- 8 T. L. P. Galvão, I. Sousa, M. Wilhelm, J. Carneiro, J. Opršal, H. Kukačková, V. Špaček, F. Maia, J. R. B. Gomes, J. Tedim and M. G. S. Ferreira, *Chem. Eng. J.*, 2018, **341**, 526–538.
- 9 F. Maia, J. Tedim, A. C. Bastos, M. G. S. Ferreira and M. L. Zheludkevich, *Nanotechnology*, 2013, **24**, 415502.
- 10 W. Li, J. W. Buhrow, S. T. Jolley, L. M. Calle, J. S. Hanna and J. W. Rawlins, .
- 11 K. Klemkaitė-Ramanauskė, A. Žilinskas, R. Taraškevičius, A. Khinsky and A. Kareiva, *Polyhedron*, 2014, **68**, 340–345.
- 12 T. Stimpfling and F. Leroux, *Chem. Mater.*, 2010, **22**, 974–987.
- 13 M. Wei, Q. Yuan, D. G. Evans, Z. Wang and X. Duan, *J. Mater. Chem.*, 2005, **15**, 1197–1203.
- 14 K. Ladewig, Z. P. Xu and G. Q. (Max) Lu, *Expert Opin. Drug Deliv.*, 2009, **6**, 907–922.
- 15 Y. Cao, D. Zheng, X. Li, J. Lin, C. Wang, S. Dong and C. Lin, *ACS Appl. Mater. Interfaces*, 2018, **10**, 15150–15162.
- 16 A. Faour, V. Prévot and C. Taviot-Gueho, *J. Phys. Chem. Solids*, 2010, **71**, 487–490.
- 17 B. Choudary, *Appl. Catal. A Gen.*, 2003, **251**, 397–409.

- 18 G. G. C. Arizaga, A. S. Mangrich, J. E. F. da Costa Gardolinski and F. Wypych, *J. Colloid Interface Sci.*, 2008, **320**, 168–176.
- 19 A. Cervilla, A. Corma, V. Fornes, E. Llopis, P. Palanca, F. Rey and A. Ribera, *J. Am. Chem. Soc.*, 1994, **116**, 1595–1596.
- 20 Y. Seida, Y. Nakano and Y. Nakamura, *Clays Clay Miner.*, 2002, **50**, 525–532.
- 21 J. Tedim, S. K. Poznyak, A. Kuznetsova, D. Raps, T. Hack, M. L. Zheludkevich and M. G. S. Ferreira, *ACS Appl. Mater. Interfaces*, 2010, **2**, 1528–1535.
- 22 F. Z. Mahjoubi, A. Khalidi, M. Abdennouri and N. Barka, *J. Taibah Univ. Sci.*, 2017, **11**, 90–100.
- 23 C. Vaysse, L. Guerlou-Demourgues, A. Demourgues and C. Delmas, *J. Solid State Chem.*, 2002, **167**, 59–72.
- 24 G. A. Caravaggio, C. Detellier and Z. Wronski, *J. Mater. Chem.*, 2001, **11**, 912–921.
- 25 H.-W. Cao, R.-W. Xu, H. Liu and D.-S. Yu, *Des. Monomers Polym.*, 2006, **9**, 369–382.
- 26 A. Noshirvani Sharifabad and S. H. Bahrami, *IEEE Sens. J.*, 2016, **16**, 873–880.
- 27 J. Zhang, J. Wu, Y. Cao, S. Sang, J. Zhang and J. He, *Cellulose*, 2009, **16**, 299–308.
- 28 T. Tanaka, Y. Kameshima, S. Nishimoto and M. Miyake, *Anal. Methods*, 2012, **4**, 3925.
- 29 L. M. Wu, D. S. Tong, L. Z. Zhao, W. H. Yu, C. H. Zhou and H. Wang, *Appl. Clay Sci.*, 2014, **95**, 74–82.
- 30 P. Liu, D. Liu, Y. Liu and L. Li, *J. Solid State Chem.*, 2016, **241**, 164–172.
- 31 Z. Li, Q. Zhang, X. He and M. Chen, *Appl. Clay Sci.*, 2018, **151**, 201–210.
- 32 S. Fleutot, J.-C. Dupin, G. Renaudin and H. Martinez, *Phys. Chem. Chem. Phys.*, 2011, **13**, 17564.
- 33 L. Guo, W. Wu, Y. Zhou, F. Zhang, R. Zeng and J. Zeng, *J. Mater. Sci. Technol.*, 2018, **34**, 1455–1466.
- 34 J. Tedim, A. C. Bastos, S. Kallip, M. L. Zheludkevich and M. G. S. Ferreira, *Electrochim. Acta*, 2016, **210**, 215–224.
- 35 J. Jayaraj, S. Amruth Raj, A. Srinivasan, S. Ananthakumar, U. T. S. Pillai, N. G. K. Dhaipule and U. K. Mudali, *Corros. Sci.*, 2016, **113**, 104–115.



# Chapter 6

## Summary

---

### Significant observations / contributions

The present study investigated the influence of CeO<sub>2</sub> and LDH particles on the multifunctional behaviour of metallic as well as polymeric composite coatings on light alloys (aluminium and magnesium). Ni-B alloy deposited by the electroless coating technique was considered as the metal matrix and dip coated epoxy/acrylic was the polymer matrix for the composite coating preparation. The surface morphology, chemical composition, structural characteristics, tribology, mechanical properties, anti-corrosion and corrosion sensing behaviour were evaluated.

In first work, metal based Ni-B alloy and CeO<sub>2</sub> nanoparticle co-deposited composite films were developed on aluminium A356 alloy by the electroless technique. The particle addition has induced grain refinement of the deposit, since the nanoparticles could act as the nucleation sites for grain growth. The nanocomposite coating exhibited higher corrosion resistance with an average current density of  $2.48 \times 10^{-6} \text{ A cm}^{-2}$ , which is smaller than that of particle-free counterpart ( $11.18 \times 10^{-6} \text{ A cm}^{-2}$ ). The corrosion inhibition is resulted by the grain refinement that could induce zig-zagging of the path for aggressive ions/water molecules movement towards the metallic surface. Furthermore, the presence of nonstoichiometric ceria (have both Ce<sup>4+</sup> and Ce<sup>3+</sup>) nanoparticle with Ce<sup>3+</sup> ion in the coating can oxidised to more stable Ce<sup>4+</sup> in the corrosive environment, which can also contribute the anti-corrosion behaviour. Improvement in microhardness ( $\sim 684 \text{ VHN}$  for Ni-B-CeO<sub>2</sub> and  $\sim 424 \text{ VHN}$  for Ni-B) and wear resistance with low friction coefficient were observed for the nanocomposite coating. Grain size reduction and better integrity effect of ceria particle in the matrix has contributed to the coating stability. Ni-B-CeO<sub>2</sub> nanocomposite coatings were uniformly deposited on the centrifugally cast aluminium alloy cylinder liner.

In the second metal based system, electroless Ni-B-LDH composite coatings were made on the aluminium A356 alloy by co-deposition of LDH with Ni-B. Coarse nodular grains were obtained for the coating till the addition of 1wt% of LDH, further increase in the particle percentage to 2 wt% and 5 wt% gave non-uniform surface with agglomerated LDH. The corrosion performance of aluminium alloy has increased significantly for composite coatings compared to Ni-B alloy coating. Better corrosion prevention may be due to its hydrophobicity by LDH induced surface roughness and chloride ion exchange capacity of LDH in the presence of NaCl solution. Moreover, LDH could enhance the barrier property by zig-zagging the movement of corrosive species towards the metal surface. The highest corrosion resistance and hydrophobicity were observed for 0.5 wt% of LDH addition. The tribology analysis showed that the continuous tribolayer formation between coated sample and the counter surface gave a considerable improvement in wear resistance compared to that of bare alloy substrate. Maximum wear resistance was observed for 1 wt% of LDH addition in nickel matrix.

The third experimental chapter dealt with the improvement in corrosion inhibition efficiency of Ni-Al LDH by vanadate intercalation followed by nanoceria decoration. The Ni-Al  $\text{NO}_3$  LDH was synthesized using co-precipitation method and it was modified by vanadate via ion exchange. Ceria nanoparticles were further decorated on the layers by simple one step method. Chemical and elemental characterisations indicate the vanadate inhibitor loaded as their polymeric form. The structural analysis demonstrates the LDH formation as well as ceria decoration. The corrosion resistance of aluminium A356 alloy tested in LDH dispersed electrolyte exhibited inhibition efficiency in the order of Ni-Al  $\text{VO}_x\text{-CeO}_2 > \text{Ni-Al VO}_x > \text{Ni-Al NO}_3\text{-CeO}_2 > \text{Ni-Al NO}_3 > \text{NaCl without LDH}$ . This performance could be attributed to the ion exchange capacity with  $\text{Cl}^-$  as well as the active corrosion prevention by the formation of polymeric vanadate on the metal surface. Ceria decorated LDH again enhance the barrier property by zig-zagging the movement of corrosive species towards the metal surface as well as their passive behaviour. The combined effect of active and passive corrosion inhibition gave the best anticorrosion property among all the analysed

systems. The modified LDH reinforced epoxy coatings with higher corrosion resistance were developed on A356 alloy.

In the last part of the research, Zn-Al LDH modified with phenolphthalein were synthesised for corrosion sensing application. The characterisations confirm that the phenolphthalein was loaded into the LDH. However, the molecule could not be intercalated instead it was adsorbed on the layer surface by grafting or hydrogen bonding. Before the corrosion sensibility measurement, corrosion resistance of Zn-Al phph LDH system on aluminium alloy as well as magnesium alloy were examined. The improvement in corrosion resistance of LDH dispersed solution may be due to their barrier properties by chloride ion exchange capacity. However, phenolphthalein modification slightly reduced the corrosion resistance by slow ion consumption in presence of bulky group. The phenolphthalein modified LDH was successfully used to detect corrosion on the magnesium alloy surface. The spot of pink colouration on different sites were observed due the increase in pH associated with the local cathodic reaction on the alloy in sodium chloride solution. On the other hand aluminium alloy could not show detectable colour change owing to its slow corrosion rate and hydroxyl ion diffusion into the surroundings.

### **Future perspectives**

- The nanoceria decorated LDH reinforced electroless Ni-B coating for high corrosion resistance as well as mechanical properties.
- Role of various nanoparticles in Ni-B/ polymer composite coating can be investigated.
- Development of functionally graded composite coating by combination of LDH and different ceramic particles.
- The influence of different organic/inorganic modifications on LDH for corrosion inhibition can be studied.

- Multifunctional behavior like combination of UV blocking, flame retardancy, mechanical properties, corrosion resistance, etc. of epoxy-LDH coating can be investigated.
- The phenolphthalein based corrosion sensing material development to detect the early stage corrosion on aluminium alloy.

## List of Publications

1. **Pancrecius, J. K.**, Ulaeto, S. B., Ramya, R., Rajan, T. P. D., & Pai, B. C. (2018). Metallic composite coatings by electroless technique-a critical review. *International Materials Reviews*, 63(8), 488-512.
2. **Pancrecius, J. K.**, Deepa, J. P., Jayan, V., Bill, U. S., Rajan, T. P. D., & Pai, B. C. (2018). Nanoceria induced grain refinement in electroless Ni-B-CeO<sub>2</sub> composite coating for enhanced wear and corrosion resistance of Aluminium alloy. *Surface and Coatings Technology*, 356, 29-37.
3. **Pancrecius, J. K.**, Deepa, J. P., Ramya, R., Rajan, T. P. D., Gowd, E. B., & Pai, B. C. (2015). Ultrasonic-Assisted Electroless Coating of Ni-B Alloy and Composites on Aluminum Alloy Substrates. *Materials Science Forum* (Vol. 830, pp. 687-690). Trans Tech Publications.
4. Ulaeto, S. B., Rajan, R., **Pancrecius, J. K.**, Rajan, T. P. D., & Pai, B. C. (2017). Developments in smart anticorrosive coatings with multifunctional characteristics. *Progress in Organic Coatings*, 111, 294-314.
5. Ulaeto, S.B., Nair, A.V., **Pancrecius, J.K.**, Karun, A.S., Mathew, G.M., Rajan, T.P.D. and Pai, B.C. (2019). Smart nanocontainer-based anticorrosive bio-coatings: Evaluation of quercetin for corrosion protection of aluminium alloys. *Progress in Organic Coatings*, 136, p.105276.
6. Lakshmi, V., Raju, A., Resmi, V. G., **Pancrecius, J. K.**, Rajan, T. P. D., & Pavithran, C. (2016). Amino-functionalized breath-figure cavities in polystyrene–alumina hybrid films: effect of particle concentration and dispersion. *Physical Chemistry Chemical Physics*, 18(10), 7367-7373.
7. **Jerin K. Pancrecius**, S. V. Vineetha, Ulaeto Sarah Bill, E. Bhoje Gowd, T. P. D. Rajan and B. C. Pai. Active and Passive Corrosion Inhibition of Modified Ni-Al Layered double hydroxide on A356 alloy. (Manuscript submitted)
8. **Jerin K. Pancrecius**, P.S. Gopika, P. Suja, Sarah Bill Ulaeto, T.P.D. Rajan, E. Bhoje Gowd and B.C. Pai. Role of layered double hydroxide in enhancing the wear and

corrosion performance of hydrophobic Ni-B-LDH composite coatings on A356 aluminium alloy. (To be submitted)

9. **Jerin K. Pancreciuous**, K.N. Savithry, T.P.D. Rajan, E. Bhoje Gowd and B.C. Pai. Phenolphthalein modified Layered Double Hydroxide for Corrosion Sensing Applications on Light Metal Alloys. (Under preparation)

## Book Chapters

1. Ulaeto, S. B., **Pancreciuous, J. K.**, Rajan, R., Rajan, T. P. D., & Pai, B. C. (2018). Role of Nanodispersoids on Corrosion Inhibition Behavior of Smart Polymer Nanocomposite Coatings. In *Advanced Polymeric Materials for Sustainability and Innovations* (pp. 321-366). Apple Academic Press.
2. Ulaeto, S. B., **Pancreciuous, J. K.**, Rajan, T. P. D., & Pai, B. C. (2019). Smart Coatings. In *Noble Metal-Metal Oxide Hybrid Nanoparticles* (pp. 341-372). Woodhead Publishing.
3. Ulaeto, S. B., Suja P., **Pancreciuous, J. K.**, Rajan, T. P. D., & Pai, B. C. (2019). Intelligent Coatings for Anticorrosive Applications. In *Phenomena and Theories in Corrosion Science: Methods of Prevention* (pp. 219-254). Nova Science Publishers.

## List of Conference Presentations

1. **Jerin K. Pancreciuous**, Varanya Jayan, J. P. Deepa, T.P.D. Rajan, E. Bhoje Gowd and B.C. Pai. Influence of Cerium addition in Electroless Ni-B Coating on Aluminum Alloy Substrates, NCMST – 2015.
2. **Jerin K. Pancreciuous**, R. Ramya, Sarah Bill Ulaeto, T.P.D. Rajan, E. Bhoje Gowd and B.C. Pai. Effect of CeO<sub>2</sub> nano particles on structure and corrosion behaviour of electroless Ni-B coating on A356 aluminium alloy, 17th Asian Pacific Corrosion Control Conference, IIT Bombay, Mumbai, 27-30 January, 2016.
3. **Jerin K. Pancreciuous**, Sarah B. Ulaeto, R. Ramya, Jithu Jayaraj, T.P.D. Rajan, E. Bhoje Gowd and B.C. Pai. Structural and Corrosion behaviour of Electroless Ni-B-CeO<sub>2</sub> nanocomposite coatings on A356 alloy, CORCON-2016, New Delhi, September 18-21, 2016.

4. **Jerin K. Pancreciious**, Sarah. B. Ulaeto, R. Ramya, T.P.D. Rajan, E. Bhoje Gowd and B.C. Pai. Studies on wear and corrosion behaviour of electroless Ni-B-CeO<sub>2</sub> nanocomposite coatings on A356 alloy, National Conference on Critical and Strategical Materials for Advanced Technologies, Munnar, Kerala, March 9-11, 2017. **(Best presentation award)**
5. **Jerin K. Pancreciious**, Sarah B. Ulaeto, R. Ramya, T.P.D. Rajan, E. Bhoje Gowd and B.C. Pai. Effect of Layered Double Hydroxide Inhibitors on Corrosion Behaviour of Electroless Ni-B Nanocomposite Coatings on A356 Al Alloy. International Conference on Advanced Materials and Processes, Thiruvananthapuram, Kerala, December 14-16, 2017.
6. **Jerin K. Pancreciious**, Sarah B. Ulaeto, P. Suja, T.P.D. Rajan, E. Bhoje Gowd and B.C. Pai. Smart LDH-Polymer Composite Coatings for Corrosion Resistance Applications, 2<sup>nd</sup> International Conference on Recent Trends in Materials Science and Technology (ICMST 2018) Thiruvananthapuram, October 10-13, 2018.
7. **Jerin K. Pancreciious**, Sarah B. Ulaeto, T.P.D. Rajan, E. Bhoje Gowd and B.C. Pai. Formation of LDH Dispersed Ni-B Composite Coatings on Aluminium Alloys, International Conference on Advanced Materials and Manufacturing Processes for Strategic Sectors (ICAMPS 2018) Thiruvananthapuram October 25-27, 2018
8. **Jerin K. Pancreciious**, P. Suja, Sarah B. Ulaeto, T.P.D. Rajan, E. Bhoje Gowd and B.C. Pai. Role of Ceria and LDH on Morphological Evolution and Anticorrosive Behaviour of Electroless Nickel boride Coatings on Aluminium Alloys, National Conference on Emerging Trends in Science, Technology & Application of Electron Microscopy (STAEM 2018) December 19-21, 2018
9. **Jerin K. Pancreciious**, Sarah B. Ulaeto, T.P.D. Rajan, E. Bhoje Gowd and B.C. Pai. Corrosion Inhibition of Modified Ni-Al-Layered Double Hydroxide on A356 alloy, MRSI trivandrum chapter-Technical Seminar , March 2019, **(Best presentation award)**
10. **Jerin K. Pancreciious**, P. Suja, Sarah B. Ulaeto, T.P.D. Rajan, E. Bhoje Gowd and B.C. Pai. Wear and corrosion performance of Ni-B-Layered double hydroxide composite coatings fabricated by electroless process on A356 aluminium alloy, IIM trivandrum chapter-Technical Seminar , April 2019, **(Best presentation award)**